Institut national de la recherche scientifique
Centre Eau Terre Environnement

Magma fragmentation and juvenile pyroclast shapes, with a focus on lava fountains

Fragmentation magmatique et forme des pyroclastes juvéniles, avec un focus sur les fontaines de lave

By

Pier Paolo Comida

Thesis submitted for the degree of

Philosophiae Doctor (Ph.D.)

In Earth Sciences

Evaluation jury

President of the jury and internal examiner	Pierre Francus INRS-ETE, Canada
External examiner	Lucy Porritt University of British Columbia, Canada
External examiner	Jacopo Taddeucci Istituto Nazionale di Geofisica e Vulcanologia, Italia
Research supervisor	Pierre-Simon Ross INRS-ETE, Canada

ACKNOWLEDGEMENTS

The following dissertation represents only the mere conclusion of an extraordinary, often incredibly challenging journey revolving around my passion for volcanoes, their complexity and their impact on life on Earth as we know it. None of what I have done over the past four and a half years would have been possible without the help and support of a large cohort of people that helped me to become a better human being and volcanologist.

First and foremost, my gratitude goes to my supervisor Pierre-Simon Ross for choosing me for this project, for the professional guidance and omnipresent support from start to finish. His exceptional expertise in geology and volcanology, scientific writing, and highly efficient reviewing and science-applied critical thinking enabled me to face and overcome any challenge during the development of the methodology, data acquisition and analysis. His continuous support during preparation of posters, oral presentations, scientific papers and this thesis made a crucial difference in the quality of the work, for which I am genuinely grateful. I also thank him for the endless patience during our long discussions over every aspect of the project, which turned out to be far more compelling, broad, mentally and physically challenging than initially envisaged. The whole research was funded by the National sciences and engineering research council of Canada (NSERC) through a Discovery Grant and Accelerator Supplement to P-S Ross, which allowed the two trips to Würzburg in order to perform the fragmentation experiments, the tour at ETH Zürich, the conferences in Portland, Naples and Montreal, and much more.

Beyond the scientific realm, my most profound thanks goes to my love and life Jenny for the unconditional love, the continuous support and patience throughout all these years, I could not have done all of this without her in my life. Thank you for listening to all my doubts and for tolerating my mental rollercoasters. Thank you for always being there for me when I needed it the most, for constantly reminding me to eat, sleep, and to take pauses. Thanks for always taking care of me and for believing I could do anything, achieve anything. Thanks for waiting for me all these years, I cannot wait to start the new chapter of our life together. I also thank my parents, my great aunts, my family-in-law, for always believing in me and for the genuine support along the way.

A genuine thanks goes to one of my best friends Nicolò, for the continuous personal and professional support, for the profound friendship and help whenever I need it. Thank you for being an essential part of my daily life, for the fruitful and never boring discussions on the most disparate

topics, for listening to my rants even after a long working day, and for the material help without which my experience in Quebec would have been quite different. Our coffee times together at Pekoe, the long walks and all the other spontaneous chats will be greatly missed.

Another great thanks also goes to Benjamin, for the genuine friendship, the professional support and the constant pushes to face and overcome any problems. Thanks for your volcanological support, for being the best unofficial French teacher a person could desire. Thanks for the long culinary conversations, and for the fruitful discussions towards a more sustainable lifestyle. A special thanks for the falafels and the dinners together, which I greatly miss.

A genuine thanks goes to Valentina for the friendship, the support, the fruitful discussions, and for being the best Italian grammar checker in the world. A special thanks goes to my friends Charlie and Laurie for their genuine friendship and support when I needed it, for the nice times together and for being the eco-sustainability flag bearers of Quebec society. A profound gratitude goes to Gaetano and Michela for the huge help during my first years in Quebec, for their friendship and help, which truly made a difference. My gratitude also goes to Charis, Filippo and Silvia, for their friendship and support, especially during my limited-mobility times. Really, thanks.

A great thanks goes to Shiva and Ali, Quentin, Aurélie, Pier-Luc, Arnaud F., Julia and William, Laura M., Mira, Cecilia, Felix Girard, Alexandre, Simon and all the other friends and colleagues for their support and friendship. A thanks goes to Philippe-Edwin Bélanger, Patricia Muñoz, Linda Aubert, Gilles Guerin and André St-Hilaire for caring and providing support during difficult times.

An acknowledgement goes to Philippe Girard and Arnaud De Coninck for the logistic support during the development of the methodology. We also acknowledge Bernd Zimanowski, Ralf Büttner and Nico Spitznagel during the experiment sessions. My gratitude goes to Felix Gagnon, Caroline Belanger and Sarah Galloway for their great support in the laboratory analyses, image preparation and processing. A great thanks goes to Nathalie Lefebvre for providing the Ukinrek samples and for showing us many ticks on juvenile pyroclasts. A thanks to Wendy Cockshell, Sebastian Mueller and Bruce Houghton for providing the Kilauea Iki samples.

Finally, I want to dedicate the whole PhD thesis to María Isabel, a great friend whose passing left an unbridgeable void in my life and that of many others. To you, dear María, I dedicate this long-awaited achievement. I wish we had more time to spend together, and for me to visit your Colombia and its astounding volcanoes, spend time with your amazing family and engage in long conversations about sustainability and conservation. Fear not, I will continue the fight for environmental justice in your honor and memory.

ABSTRACT

Explosive fragmentation of ultramafic and mafic magmas can be magmatic or phreatomagmatic, and each mode can result in different eruption styles and form different juvenile pyroclasts. Strombolian pulses and lava fountains are a common example of magmatic fragmentation in basalts, driven by magma decompression and vesiculation. When magma meets external water, rapid magma cooling and the violent conversion of water into steam leads to phreatomagmatic eruptions, such as those forming maar-diatremes. Beyond the eruption style, fragmentation mechanisms can be either hydrodynamic or brittle. The former consists in the ductile breakup of magma into smaller liquid drops and filaments, like the achneliths observed from lava fountain deposits. Brittle fragmentation is caused by very high stresses, resulting in juvenile pyroclasts with specific external shapes, internal textures and surface features.

Linking juvenile pyroclast characteristics and primary magma fragmentation requires a standardized methodology of analysis. In this thesis, magmatic and phreatomagmatic pyroclasts from the 1977 eruption of Ukinrek volcano (Alaska) were used to select the best size fraction (coarse ash from 0.71 to 0.5 mm) for the analysis of juvenile pyroclasts in comparative studies of magma fragmentation. Moreover, it was found that SEM image acquisition for this fraction should be performed for at least 50 juvenile grains, each with a pixel density of at least 20 000 pixels per particle. The software PASTA was developed to facilitate image processing and measurement of morphometric and textural parameters. The chosen coarse ash size fraction allows representative quantification of 2D vesicularity and crystallinity in cross-sections without significant post-fragmentation changes. A very fine ash fraction (88–63 µm), on the other hand, is ideal for morphometric measurements and crucial for the study of surface characteristics, but special care must be taken during sample preparation and juvenile grains have to be confirmed using a dual mounting technique.

Hydrodynamic magma fragmentation was investigated through laboratory experiments involving remelted volcanic rocks, at the *Physikalisch Vulkanologisches Labor* (PVL) in Germany. About 200–250 g of magma at 1200°C was generated within 1 hour, using an induction furnace. Magma fragmentation was triggered through the injection of compressed argon at 3 MPa or 10 MPa, and recorded by high-speed cameras between 2000 and 5000 frames per second. The three volcanic materials used in the experiments are an olivine-melilite (Hohenstoffeln, ~ 38% SiO_2), an alkali basalt (Billstein, ~ 45% SiO_2), and a basaltic-trachyandesite (Sommata, ~ 54% SiO_2). All magmas

produced glassy, bubble- and crystal-poor, fluidal juvenile pyroclasts. The experimental pyroclasts were compared to natural juvenile pyroclasts from the 1959 eruption of Kīlauea Iki (~ 49% SiO_2) in Hawaii, which consist of glassy fluid particles, scoria and golden pumice. Juvenile pyroclasts from experiments and lava fountains were analyzed using the steps in the standardized methodology. Hydrodynamic fragmentation of magmas in the experiments is similar to the breakup of industrial liquid jets. Different breakup regimes are controlled by the balance of magma viscosity and surface tension, the ejection velocity and external aerodynamic effects. On one hand, ultramafic magmas of low viscosity ejected at high velocity (Hohenstoffeln 10 MPa) form a spray (regime IV), dominated by surface tension and aerodynamic forces. In contrast, intermediate magmas expelled at lower velocities (Sommata 3 MPa) are barely fragmented at the crucible exit (regime II), as higher viscosity causes stretching into multiple filaments before fragmentation. Similar regimes are observed in natural lava fountains. A modified Ohnesorge diagram (Reynolds number versus Weber number) has the potential to distinguish different breakup regimes, and future work is advised to improve this diagram.

Hydrodynamic magma fragmentation in the experiments generated a panoply of fluidal juvenile pyroclasts. For coarse ash-sized particles, ultramafic magma ejected at the lowest velocity (Hohenstoffeln 3 MPa) mainly formed spheres (~ 50%), with high values of axial ratio and solidity (> 0.7 and > 0.9 respectively). Efficient hydrodynamic fragmentation was dominated by surface tension and rapid contraction (< 1 ms). In contrast, the intermediate magma ejected at high velocity (Sommata 10 MPa) primarily formed Pele's hairs, with lower values of axial ratio and solidity (0.4 and 0.7, respectively). Final fluidal morphologies result from the competition between viscosity and surface tension, ultimately preserved by the fast cooling process. In ultramafic magmas, stretching is minor and relaxation times are short, resulting in compact morphologies. For intermediate magmas, the higher viscosity and stretching prevents contraction, allowing elongated shapes to be maintained. These fluidal particles are morphologically similar to achneliths generated during the 1959 eruption of Kīlauea Iki.

Keywords: primary magma fragmentation, juvenile pyroclasts, fluidal, lava fountains, experiments, morphology, internal texture, standardized methodology

RÉSUMÉ ÉTENDU

Ce projet de doctorat analyse les processus de fragmentation primaire du magma et le lien avec les pyroclastes juvéniles, pour les magmas ultramafiques à mafiques. Les connaissances sur la fragmentation du magma sont encore incomplètes, mais les pyroclastes juvéniles pourraient comporter des caractéristiques clés permettant la distinction entre différents styles éruptifs. Cet aspect est crucial pour mieux comprendre les éruptions passées et aider à prédire l'activité future.

Cette thèse comprend trois articles. Le premier contribue au développement d'une méthodologie standardisée pour l'analyse des pyroclastes juvéniles, pour les études comparatives ayant pour but de comprendre la fragmentation du magma. Les deuxième et troisième articles traitent respectivement de la fragmentation hydrodynamique (ductile) du magma dans les fontaines de lave et des caractéristiques des pyroclastes juvéniles associés.

Ce résumé étendu commence par décrire brièvement les connaissances actuelles sur la fragmentation du magma, les styles éruptifs et les pyroclastes associés. Puis il aborde la problématique, les objectifs et la méthodologie. Ensuite les résultats principaux et les interprétations des trois articles seront présentés, suivis d'une conclusion générale.

Fragmentation magmatique, phréatomagmatique et styles éruptifs pour les magmas ultramafiques à mafiques

Les éruptions explosives impliquant des magmas ultramafiques à mafiques sont parmi les phénomènes volcaniques les plus fréquents (Taddeucci et al. 2015 ; Houghton et al. 2016). Bien qu'elles soient moins dangereuses que les éruptions pliniennes, elles représentent néanmoins une source de danger significative (Heggie 2009 ; Calvari et al. 2018 ; Neal et al. 2019). Par exemple, les coulées et les fontaines de lave de style hawaïen du volcan Kīlauea (Hawaï, États-Unis), de l'Etna (Italie) et du Fagradalsfjall (Islande), visitées par des milliers de personnes chaque année (Houghton et al. 2016), présentent un risque pour la sécurité des visiteurs. Au-delà du danger immédiat, les fontaines de lave avec une haute production de cendres comme à l'Etna (Italie) et/ou les coulées de lave actives des volcans Fogo (Cap-Vert) et Nyiragongo (République Démocratique du Congo) ont fréquemment un impact sur les activités et la vie même des populations voisines (Sigurdsson 2015 ; Andronico et Del Carlo 2016 ; Cappello et al. 2016).

Les différents styles éruptifs explosifs observés dans la nature sont produits par la fragmentation primaire du magma, et forment des pyroclastes juvéniles avec différentes caractéristiques

(Heiken 1974 ; Fisher et Schmincke 1984). On distingue la fragmentation magmatique et phréatomagmatique, selon la présence ou non d'eau externe pendant la fragmentation.

La fragmentation magmatique est régie par la décompression et la vésiculation du magma (Cashman 2004 ; Parfitt 2004 ; Parfitt et Wilson 2009 ; Cashman et Scheu 2015). En l'absence d'eau externe, la fragmentation est dominée par la décompression rapide et l'effet des volatiles présents dans le magma (Cashman et Scheu 2015). Lorsque le magma remonte vers la surface, différentes phases gazeuses commencent à se séparer de la phase liquide, formant des bulles qui s'agrandissent et coalescent progressivement. La formation de bulles réduit la densité du magma, augmentant sa vitesse d'ascension (Parfitt et Wilson 2009). En fonction du couplage entre la phase volatile et la phase liquide du magma, différentes styles éruptifs se produisent (Cashman et Scheu 2015). Deux styles éruptifs magmatiques sont pertinents pour ce projet de thèse : i) le style Strombolien, qui consiste en la décompression cyclique de grosses bulles de gaz dans le magma, créant des impulsions discrètes séparées par des pauses de quelques minutes à quelques heures (Blackburn et al. 1976; Ripepe et al. 2008; Del Bello et al. 2015; Pering et al. 2015); ii) le style Hawaiien, caractérisé par le couplage optimal des bulles de gaz et du magma, résultant en des fontaines de lave soutenues durant des heures à quelques jours. Ces styles éruptifs peuvent former des cônes de scories, des anneaux de spatter, etc.

Lorsque le magma rencontre de l'eau externe, la fragmentation phréatomagmatique se produit par le refroidissement rapide du magma et la conversion violente de l'eau en vapeur (Heiken et Wohletz 1991 ; Sohn 1996 ; Zimanowski et al. 1997 ; Wohletz et al. 2013 ; Cioni et al. 2014). Le style Taalien a été considéré dans ce projet, caractérisé par une interaction magma-eau discontinue se produisant sous terre, résultant en l'excavation du conduit et le remplissage ultérieur avec du matériel volcanoclastique (Moore et al. 1966 ; White et Ross 2011). Le style Taalien forme des maars et des anneaux de tuf.

Physique de la fragmentation du magma

Au-delà de la distinction génétique entre fragmentation magmatique et phréatomagmatique, le mécanisme de fragmentation est de deux types. Le premier est la fragmentation hydrodynamique, caractérisée par la rupture ductile du magma en gouttes liquides plus petites ou en filaments (Zimanowski et al. 1991, 1997 ; Shimozuru 1994 ; Caffier 1998 ; Porritt et al. 2012 ; Jones et al. 2019), comme observé dans les fontaines de lave de style hawaïen. Ce processus aboutit à la formation de particules fluidales allant des sphères aux larmes et cheveux de Pelé (Walker et Croasdale 1971). Le second mécanisme de fragmentation est fragile, et consiste en la fracturation

du magma sous des contraintes internes très élevées (Büttner et al. 2006 ; Gonnermann 2015 ; Namiki et al. 2021). La fragmentation fragile produit des fragments anguleux s'ils sont refroidis rapidement.

Le mécanisme hydrodynamique des fontaines de lave est le plus important pour la présente thèse. En fonction de leur taille, de leur histoire de refroidissement et de leur parcours vers le sol, les premières gouttes de magma peuvent continuer se fragmenter en plusieurs gouttelettes de plus en plus petites jusqu'à ce qu'une taille critique soit atteinte (Birouk et Lekic 2009 ; Lefebvre et McDonell 2017). La désintégration hydrodynamique des magmas dans les fontaines de lave ressemble à la rupture de jets liquides dans des applications industrielles (Eggers et Villermaux 2008). En fonction de la vitesse d'éjection croissante et/ou de la rhéologie du liquide, quatre régimes de rupture ont été définis pour caractériser l'apparence d'un jet liquide émis d'un tube (Reitz et Bracco 1986 ; Birouk et Lekic 2009 ; Lefebvre et McDonell 2017).

Nonobstant le régime de rupture du jet liquide, le mécanisme de fragmentation d'une goutte initiale en deux gouttelettes différentes est responsable des différentes formes de pyroclastes générées. Le processus de fragmentation et de changement de forme d'une goutte est régi par la tension de surface et équilibré par la viscosité, l'inertie du fluide et l'élasticité (Shimozuru 1994 ; Clasen et al. 2012). Lorsqu'une goutte de liquide commence à se diviser, un col se forme entre les deux masses. Si le processus d'amincissement au niveau du col est dominé par la tension superficielle (c'est le cas des liquides à faible viscosité), les échelles de temps d'amincissement seront suffisamment courtes pour provoquer la rupture précoce de la masse initiale en deux gouttelettes relativement compactes, en particulier à faible vitesse d'émission (Clasen et al. 2012). À des vitesses d'éjection plus importantes, l'inertie du liquide s'opposera à la tension de surface, prolongeant l'amincissement du filament et retardant la rupture. Pour les liquides viscoélastiques, la viscosité et l'élasticité s'opposent efficacement à la tension de surface, en particulier à des vitesses d'éjection élevées. Les temps d'amincissement seront longs, entraînant la génération de longs filaments liquides (Eggers et Villermaux 2008 ; Clasen et al. 2012).

Contrairement aux liquides industriels, les mécanismes de fragmentation du magma sont plus complexes, en raison : i) du refroidissement rapide du magma amenant la formation de verre volcanique ; ii) de la présence de bulles et de cristaux à l'intérieur du magma, qui introduisent une complexité supplémentaire pendant la déformation et la fragmentation (Mader et al. 2013 ; Cashman et Scheu 2015 ; Jones et al. 2019).

Les pyroclastes juvéniles

Les pyroclastes juvéniles ont des caractéristiques variées en termes de textures internes (cristaux, vésicules), formes externes, et détails de leur surface. Ces variations sont liées aux différents processus de formation et aux différents styles éruptifs. L'identification et l'étude des pyroclastes primaires juvéniles sont donc cruciales pour comprendre la dynamique des éruptions, interpréter l'histoire éruptive des volcans et aider à prévoir leur comportement futur. Cette thèse s'intéresse aux caractéristiques primaires obtenues après la fragmentation, et non à leur éventuelle modification ultérieure due aux processus de transport et de dépôt.

La **morphologie** d'un nouveau pyroclaste juvénile est directement déterminée par la déformation du magma pendant la fragmentation (Heiken 1972, 1974 ; Porritt et al. 2012). Celle-ci, à son tour, est fonction de plusieurs paramètres tels que la composition chimique, la vésicularité, la teneur en cristaux, la température d'éruption, etc. (Stovall et al. 2011 ; Porritt et al. 2012 ; Liu et al. 2015). Dans les fontaines de lave par exemple, la vésicularité faible à modérée (sensu Houghton et Wilson 1989) du magma et la fragmentation hydrodynamique donnent lieu à des pyroclastes à formes fluidales, appelés achnélithes (Walker et Croasdale 1971 ; Porritt et al. 2012). Les achnélithes vont de fragments sphériques à des fragments en forme de larmes et de filaments (Walker et Croasdale 1971 ; Duffield 1977 ; Shimozuru 1994 ; Porritt et al. 2012 ; Cannata et al. 2019). Lorsque les volatiles sont plus abondants, les achnélithes sont progressivement transformées en fragments scoriacés puis ponceux, produits par la rupture fragile des bulles voisines (Stovall et al. 2011, 2012 ; Porritt et al. 2012 ; Andronico et al. 2014 ; Jones et al. 2019). Les lapilli de scories et de ponces sont couramment observés dans les événements stromboliens, dû à l'abondance de cristaux et de bulles qui renforce la fragmentation fragile (Self et al. 1980 ; Polacci et al. 2006 ; Taddeucci et al. 2015 ; Houghton et al. 2016 ; Jones et al. 2019).

Lorsque de l’eau externe est présente, un refroidissement plus rapide du magma et une fragmentation phréatomagmatique peuvent aboutir à des particules présentant des morphologies angulaires à sub-angulaires dans toutes les fractions granulométriques (Büttner et al. 1999 ; Ort et al. 2018). La fragmentation phréatomagmatique produit des particules appelés « interactives » et « passives » (Büttner et al. 2002 ; Dellino et al. 2012). Les particules interactives sont normalement anguleuses et retrouvées principalement dans les fractions de cendres très fines (Büttner et al. 1999 ; White et Houghton 2006). Les formes passives vont des achnélithes produits par la rupture ductile aux scories et aux ponces.

Les **textures internes** des pyroclastes juvéniles dépendent de la quantité, la taille, la distribution et l'orientation des cristaux et des vésicules. Ces caractéristiques sont liées à l'histoire pré-

fragmentation du magma, fournissant des informations indirectes sur la vitesse d'ascension, les conditions de stockage temporaire et une éventuelle interaction avec l'hydrosphère (Cashman 2004 ; Wallace et al. 2015). Comme indiqué plus haut, les cristaux et les bulles peuvent exercer un contrôle sur la forme globale des fragments juvéniles, lorsqu'ils sont abondants (Jones et al. 2019). Ce contrôle augmente lorsque que la taille des particules diminue, provoquant l'apparition des faces des bulles et des coins des cristaux à la surface du grain (Porritt et al. 2012).

La fragmentation du magma primaire peut laisser des **marques distinctes à la surface** des fragments obtenus. Si les particules fluidales produites par la fragmentation magmatique dans les fontaines de lave ont des surfaces lisses (Zimanowski et al. 2015), la fragmentation fragile dans les éruptions phréatomagmatiques génère des cendres juvéniles très fines caractérisées par des caractéristiques de surface uniques (Büttner et al. 1999 ; Zimanowski et al. 2015).

Problématique

Cette thèse aborde trois problématiques. D'abord, l'absence d'une méthodologie standardisée pour l'analyse des pyroclastes juvéniles. Différents laboratoires ciblent différentes fractions granulométriques, utilisent différentes techniques et différents paramètres analytiques. Cela limite la comparaison des données entre les volcans, avec des répercussions sur la capacité à comprendre les événements passés et à prévoir les paramètres des éruptions futures.

Les deuxième et troisième problèmes traitent de la fragmentation hydrodynamique dans les fontaines de lave et des pyroclastes juvéniles associés. Les fontaines de lave sont similaires à la désintégration des jets liquides dans l'industrie, mais les connaissances sur les jets industriels n'ont pas été appliquées aux magmas jusqu'à maintenant. Contrairement aux liquides industriels, les magmas sont des matériaux plus complexes, qui se refroidissent avec le temps. Les particules juvéniles fluidales sont le produit direct de la fragmentation hydrodynamique, présentant une grande variété de morphologies et de textures internes. Néanmoins, ce qui contrôle ces caractéristiques n'est pas complètement compris.

Objectifs

L'objectif global du projet est d'améliorer nos connaissances sur la fragmentation hydrodynamique du magma par des expériences de fragmentation en laboratoire et par l'analyse de pyroclastes juvéniles. Ceci sera réalisé en travaillant sur trois objectifs spécifiques, correspondant chacun à un article.

(i) Il faut d'abord développer une méthodologie standardisée pour l'analyse des pyroclastes juvéniles, qui servira non seulement pour ce projet mais pour tout futur travail similaire. Cette partie de l'étude permettra de déterminer quels sont les meilleures fractions granulométriques à analyser, combien de pyroclastes juvéniles sont nécessaires et quelle est la résolution d'image optimale pour obtenir des données statistiquement fiables sur la morphologie et la texture interne des particules (Chapitre 2 et Annexe I).

(ii) Le second objectif spécifique est d'obtenir une meilleure compréhension du processus de fragmentation hydrodynamique dans les fontaines de lave. Quelles sont les propriétés et les paramètres qui influencent la fragmentation et le type de jet (Chapitre 3) ?

(iii) L'objectif spécifique final est de cerner les paramètres contrôlant la morphologie des pyroclastes juvéniles fluidaux dans les fontaines de lave et les évènements stromboliens (Chapitre 4).

Méthodologie

La première étape du projet était le développement de la méthodologie standardisée pour l'analyse des pyroclastes juvéniles. Ce développement a été réalisé par une équipe internationale incluant l'auteur, et le protocole complet est présenté à l'annexe I. La contribution de cette thèse porte sur les étapes de laboratoire du protocole. Des pyroclastes magmatiques et phréatomagmatiques provenant de l'éruption du volcan Ukinrek (Alaska) en 1977 (Kienle et al. 1980 ; Ort et al. 2018) ont été utilisés pour développer et tester différentes étapes du protocole. Spécifiquement, il s'agissait de déterminer quelle fraction granulométrique est la plus souhaitable pour l'étude des cendres en section polie au microscope électronique à balayage (MEB), combien de grains sont nécessaires, etc. Un logiciel, nommé PASTA (Comida et Ross 2021), a été développé pour faciliter le traitement d'image et la mesure des paramètres morphométriques, de la cristallinité 2D et de la vésicularité 2D sur les pyroclastes juvéniles.

La fragmentation hydrodynamique du magma a été étudiée grâce à des expériences de laboratoire impliquant la fragmentation de roches volcaniques refondues, réalisées au *Physikalisch Vulkanologisches Labor* (PVL) en Allemagne. Environ 200–250 g de magma à 1200°C a été généré à l'intérieur d'un creuset en acier de 5 cm (diamètre intérieur) à l'aide d'un four à induction. Puis le magma a été éjecté du creuset et fragmenté grâce à l'injection d'argon comprimé à 3 MPa ou à 10 MPa. Ceci produit des jets de magma qui ont été filmés par une caméra à haute vitesse à une cadence variant entre 2 000 et 5 000 images par seconde. Les trois matériaux volcaniques utilisés dans les expériences sont une mélilitite à olivine

(Hohenstoffeln, ~ 38% SiO_2), un basalte alcalin (Billstein, ~ 45% SiO_2) et une trachyandésite basaltique (Sommata, ~ 54% SiO_2) (Zimanowski et al. 1997 ; Zimanowski et al. 2004 ; Hobiger et al. 2011). Tous les magmas ont produit des pyroclastes juvéniles vitreux, pauvres en bulles et en cristaux, de formes fluidales.

Les pyroclastes expérimentaux ont été comparés aux pyroclastes juvéniles naturels de l'éruption de 1959 du Kīlauea Iki à Hawaii (Ritcher et al. 1970 ; Stovall et al. 2011 ; Porritt et al. 2012 ; Mueller et al. 2018). Les pyroclastes juvéniles basaltiques (~ 49% SiO_2) de Kīlauea Iki sont constitués de particules fluidales vitreuses, de scories et de ponces. Ces pyroclastes juvéniles provenant des expériences et des fontaines de lave naturelles ont été analysés selon les étapes de la méthodologie standardisée.

Résultats et interprétations : méthodologie standardisée

La fraction des cendres grossières (0.71–0.5 mm) a été identifiée comme étant la plus adaptée pour les mesures sur des sections polies de pyroclastes juvéniles, dans les études comparatives de la fragmentation du magma. De telles sections polies – montrant l'intérieur de fragments juvéniles préalablement sélectionnés à la loupe binoculaire – permettent de mesurer la forme des fragments en 2D, de quantifier les textures internes, et aussi de déterminer la chimie du verre volcanique. Toutefois, le polissage doit être réalisé très soigneusement pour préserver la forme des particules. Le test sur les pyroclastes juvéniles d'Ukinrek montre que l'acquisition d'image au MEB doit être effectuée pour au moins 50 grains juvéniles, et aboutir à au moins 20 000 pixels par particule, pour cette fraction. La fraction granulométrique des cendres grossières permet une quantification représentative de la vésicularité et de la cristallinité en 2D sans modifications post-fragmentation importantes. La préparation des particules en sections polies et l'acquisition d'image sont relativement plus rapides et faciles que pour les fractions plus grossières ou plus fines (Chapitre 2).

La fraction des cendres très fines (88–63 µm) est en revanche idéale pour les mesures morphométriques et cruciale pour l'étude des caractéristiques de surface des particules juvéniles. Ces caractéristiques peuvent être mesurées sur des images des grains en 3D au MEB, réalisées grâce à un montage sur ruban de carbone. Toutefois un tel montage ne permet pas de voir l'intérieur des grains, pour s'assurer que les particules mesurées sont bel et bien juvéniles. C'est pourquoi une procédure de « double montage » des particules a été développée. Les particules provenant de la fraction brute (sans tentative de tri des grains juvéniles au binoculaire) sont montées sur ruban de carbone et imagées au MEB. Puis le montage est converti en section polie

en ajoutant de l'époxy et en érodant la moitié de la taille de la plus petite particule. Cette section polie est imagée de nouveau au MEB, et les particules juvéniles sont identifiées. Elles sont ensuite repérées sur l'image miroir provenant du montage sur ruban de carbone. Enfin, les mesures morphométriques et de surface peuvent être effectuées (Annexe I).

Résultats et interprétations : Fragmentation hydrodynamique du magma dans les fontaines de lave

Le chapitre 3 suggère que la fragmentation hydrodynamique des magmas dans les expériences pourrait être partiellement similaire avec la fragmentation des jets liquides dans l'industrie. Une attention particulière a été porté à ce qui arrive au magma juste à la sortie du creuset. Le régime de fragmentation est contrôlé par l'équilibre des forces dans le liquide et des forces aérodynamiques à la surface du jet. Ces forces sont influencées par la viscosité du magma, la tension de surface et la vitesse d'éjection. Parmi les six expériences considérées en détail, on peut distinguer deux pôles aux extrémités d'un spectre. D'un côté, les magmas ultramafiques de faible viscosité éjectés à haute vitesse (Hohenstoffeln 10 MPa) sont pulvérisés (régime IV de fragmentation d'un jet liquide). La fragmentation est dominée par la tension de surface et les forces aérodynamiques. À l'opposé, les magmas intermédiaires expulsés à plus faible vitesse (Sommata 3 MPa) sont à peine fragmentés à la sortie du creuset (régime II). La viscosité plus élevée de ces magmas domine le processus, caractérisé par l'étirement en filaments multiples avant et après la fragmentation. Des expériences avec des conditions entre ces deux extrêmes ont aussi montré un comportement de régime III, où le jet se désintègre assez proche de la sortie.

Du à la similarité du mécanisme de fragmentation entre les expériences et les phénomènes volcaniques naturels, les mêmes trois régimes pourraient être présents dans les fontaines de lave. Un diagramme de Ohnesorge modifié est esquissé (nombre de Reynolds versus nombre de Weber) pour montrer les conditions des trois régimes de fragmentation des jets liquides, mais ce diagramme devra être raffiné lors de travaux futurs. Des expériences supplémentaires avec des matériaux analogues et/ou des modèles numériques pour mieux aborder le comportement du magma à un nombre de Weber élevé devraient être inclus lors d'études futures.

Résultats et interprétations : morphologie des pyroclastes juvéniles dans les fontaines de lave

La fragmentation hydrodynamique des magmas dans les expériences a généré un assemblage varié de pyroclastes juvéniles de formes fluidales, avec des proportions variables de différentes formes selon la composition du magma et la vitesse d'éjection (Chapitre 4). Le magma

ultramafique éjecté à la vitesse la plus faible (Hohenstoffeln 3 MPa) a principalement formé des sphères (environ 50%). La population de pyroclastes juvéniles a des valeurs élevées de rapport axial et de solidité (> 0,7 et > 0,9 respectivement). Ces valeurs reflètent une fragmentation hydrodynamique efficace dominée par la tension de surface et une contraction en moins de 1 ms observée dans la vidéo haute résolution de l'expérience. Ce temps de contraction est beaucoup plus court que le temps de refroidissement de 10 ms obtenu pour les particules de la taille des cendres grossières à partir de 1200°C jusqu'à la température de transition vitreuse. À l'opposé, le magma intermédiaire éjecté à haute vitesse (Sommata 10 MPa) a principalement formé des cheveux de Pelé, avec des valeurs plus faibles de rapport axial et de solidité (0,4 et 0,7 respectivement).

La morphologie finale des particules fluidales est produite par la compétition entre la viscosité et la tension de surface, mais dépend aussi du processus de refroidissement qui « gèle » la forme. Dans les magmas ultramafiques, l'étirement est mineur et les temps de relaxation sont courts, résultant en des morphologies compactes. Pour les magmas intermédiaires, la plus forte viscosité et l'étirement empêchent la contraction, permettant de conserver des formes allongées.

Les particules fluidales formées pendant les expériences de laboratoire sont morphologiquement similaires à leurs homologues générés lors de l'éruption du Kīlauea Iki en 1959. Néanmoins, la plus grande vésicularité des magmas naturels et la durée des fontaines ont amené la génération de scories et de ponces en plus des achnélithes, résultant en des valeurs moyennes de solidité beaucoup plus faibles dans les cendres grossières. Dans les cendres très fines, la rupture post-fragmentation est responsable d'une forte présence des parois de vésicules cassées.

Conclusion

Cette thèse de doctorat a permis de mieux comprendre les processus de fragmentation des magmas ultramafiques à mafiques et a renforcé la pertinence des pyroclastes juvéniles comme éléments clés dans l'investigation de ces processus.

Le premier résultat principal du projet est la nouvelle méthodologie standardisée pour l'analyse des pyroclastes juvéniles dans les études comparatives de la fragmentation du magma, dont l'application et les améliorations futures favoriseront la comparaison des données entre différents volcans et différents groupes de recherche. La définition des fractions granulométriques optimales, les étapes détaillées de préparation d'échantillons, ainsi que la semi-automatisation du traitement d'image et de la mesure de paramètres de forme et texture, aideront les chercheurs à obtenir des données reproductibles. Des travaux futurs sont recommandés afin de créer de

nouveaux diagrammes de fragmentation pour la discrimination de différents modes de fragmentation et de différents styles éruptifs.

Les deuxième et troisième résultats principaux concernent la fragmentation hydrodynamique dans les fontaines de lave et l'importance des pyroclastes juvéniles. Les expériences de fragmentation en laboratoire imitent la fragmentation hydrodynamique qui se produit pendant les impulsions des fontaines mais aussi dans les événements stromboliens, montrant des similarités avec les jets de liquides industriels. L'étude combinée des séquences vidéo à haute vitesse et l'analyse des pyroclastes juvéniles a permis de contraindre les paramètres physiques pertinents. D'un côté, les magmas ultramafiques sont pulvérisés, car la tension de surface est le paramètre dominant. Ceci forme notamment des pyroclastes sphériques. À l'opposé, la fragmentation des magmas intermédiaires est davantage contrôlée par la viscosité, générant principalement des pyroclastes allongés et une fragmentation moins intense. Les expériences futures de fragmentation et les modèles numériques devraient se concentrer sur le comportement du magma à des taux de déformation élevés, pour lesquels la littérature actuelle en volcanologie et dans l'industrie fait défaut. L'exploration de ces conditions extrêmes améliorerait encore la compréhension de la dynamique des fontaines de lave. Enfin, les expériences montrent leur pertinence au-delà du domaine de la volcanologie. Un exemple est la production de fibres minérales, actuellement produite principalement à partir de roches basaltiques. La génération de cheveux de Pelé dans presque toutes les expériences suggère que, avec la juste combinaison de composition, température et vitesse d'éjection, la laine minérale pourrait être générée pour toutes les compositions.

TABLE OF CONTENTS

ACKNOWLEDGEMENTS ..... **III**
ABSTRACT ..... **V**
RÉSUMÉ ÉTENDU ..... **VII**
TABLE OF CONTENTS ..... **XVII**
LIST OF FIGURES ..... **XXV**
LIST OF TABLES ..... **XXVII**
1 GENERAL INTRODUCTION **1**
1.1 EXPLOSIVE VOLCANISM INVOLVING ULTRAMAFIC AND MAFIC MAGMAS 1
1.1.1 Magmatic explosive styles *3*
1.1.2 Phreatomagmatic explosive styles *3*
1.2 PHYSICS OF MAGMA FRAGMENTATION 5
1.2.1 Magmatic fragmentation *5*
1.2.2 Phreatomagmatic fragmentation *5*
1.2.3 Mechanisms of magma breakup in lava fountains *6*
1.3 JUVENILE PYROCLASTS 8
1.3.1 External morphologies *9*
1.3.2 Internal textures *10*
1.3.3 Surface features *11*
1.4 PROBLEMS TO BE SOLVED 11
1.4.1 Standardized methodology to characterize juvenile pyroclasts for comparative studies of primary fragmentation *11*
1.4.2 Liquid jet breakup in lava fountains *12*
1.4.3 Achnelith morphologies *12*
1.5 AIMS 12
1.5.1 Standardized methodology to characterize juvenile pyroclasts for comparative studies of primary fragmentation *12*
1.5.2 Liquid jet breakup in lava fountains *13*
1.5.3 Achnelith morphologies *13*
1.6 METHODOLOGY OVERVIEW 14
1.6.1 Standardized methodology to characterize juvenile pyroclasts for comparative studies of primary fragmentation *14*
1.6.2 Magma fragmentation experiments *16*
1.6.3 Artificial pyroclasts *19*
1.6.4 Natural pyroclasts from Hawaii *20*

1.7 THESIS ORGANIZATION 20
1.8 CONTRIBUTION OF THE AUTHORS TO THE PUBLICATIONS 21
2 FIRST ARTICLE: STANDARDIZED METHODOLOGY 23
2.1 ABSTRACT 25
2.2 INTRODUCTION 25
2.3 BACKGROUND 28
2.3.1 Imaging methods and strategies 28
2.3.2 Sample preparation 28
2.3.3 Number of particles to image 29
2.3.4 Image preparation and analysis 29
2.4 METHODS 30
2.4.1 Origin of tested material 30
2.4.2 Overview of the standardized protocol and of the present study 31
2.4.3 Preparing the size fractions 32
2.4.3.1 Sieving 32
2.4.3.2 Ultrasonic cleaning 33
2.4.3.3 Juvenile clast selection 33
2.4.4 Polished epoxy grain mounts 33
2.4.5 Image acquisition 35
2.4.6 Image preparation and measurements 36
2.4.6.1 Image preparation stage 36
2.4.6.2 Processing and measurement stage 38
2.4.7 Finding the best image resolution and magnification 40
2.4.8 Choice of parameters to find the optimum size fractions 40
2.5 RESULTS 41
2.5.1 Optimum pixel density for image analysis 41
2.5.2 The role of scan speed in image acquisition 41
2.5.3 Number of grains to measure 44
2.5.4 Rejection rate 48
2.5.5 How morphometric and textural parameters vary with particle size 48
2.6 DISCUSSION 50
2.6.1 Choice of the optimum size fraction for particle cross-sections 50
2.6.1.1 Theoretical and empirical considerations 52
2.6.1.2 Practical considerations 52
2.6.1.3 Final choice for particle cross-sections 54
2.6.2 Number of pixels for combined morphometric and textural measurements 54
2.6.3 Number of juvenile grains for particle cross-section studies 54
2.6.4 Importance of sample preparation and imaging 55

2.6.4.1 PEGM manufacture 55
2.6.4.2 SEM image acquisition 55
2.7 Conclusions 56
2.8 Acknowledgements 57
2.9 Online resource 2.1: Making polished epoxy grain mounts of juvenile particles 57
2.9.1 List of recommended tools/equipment 58
2.9.2 Mounting 58
2.9.2.1 Preliminary sample conditions 58
2.9.2.2 Preparation of the mounting support 59
2.9.2.3 Placement of the grains 60
2.9.3 Epoxy casting and curing 61
2.9.4 Manual grinding and polishing 62
2.9.4.1 Preliminary step 64
2.9.4.2 Grinding pressure test 64
2.9.4.3 Grinding steps 65
2.9.4.4 Polishing steps 65
2.10 Online Resource 2.2: Measurement data spreadsheets 66
2.11 Online Resource 2.3: Axial ratio versus pixel density plots 66
3 SECOND ARTICLE: BREAKUP REGIMES IN LAVA FOUNTAINS 67
3.1 Abstract 69
3.2 Introduction 69
3.3 Review of liquid jet breakup in industrial and commercial applications 70
3.3.1 Why liquid jets break up 71
3.3.2 Jet breakup regimes 71
3.3.2.1 Jet stability curve classification 72
3.3.2.2 Ohnesorge classification 72
3.3.2.3 The four jet breakup regimes 74
3.4 Methods 75
3.4.1 Tested materials 75
3.4.2 Experiment setup and timeline 77
3.4.3 Video footage analysis 78
3.5 Experimental parameters and physical properties of the magmas 78
3.5.1 Temperature 78
3.5.2 Ejection velocity 78
3.5.3 Surface tension 79
3.5.4 Bubble-free density 81
3.5.5 Viscosity 81
3.6 Magma breakup in experiments 81

3.6.1 In-crucible magma fragmentation ... 82
3.6.2 Free-air expansion and final fragmentation ... 83
3.6.2.1 Preamble ... 83
3.6.2.2 Early stage of the jet ... 90
3.6.2.3 Intermediate and final stages of the jet ... 91
3.7 DISCUSSION ... 92
3.7.1 Jet breakup regimes in the experiments ... 92
3.7.2 Jet breakup regimes in Hawaiian eruptions ... 94
3.7.3 Controls on natural lava fountains ... 96
3.7.3.1 Ejection speed ... 96
3.7.3.2 Conduit size ... 96
3.7.3.3 Viscosity ... 96
3.7.3.4 Bubbles and density ... 97
3.7.3.5 Surface tension ... 97
3.8 CONCLUSIONS AND OUTLOOK ... 97
3.9 DECLARATION OF COMPETING INTEREST ... 98
3.10 ACKNOWLEDGMENTS ... 98
4 THIRD ARTICLE: PYROCLAST SHAPES IN LAVA FOUNTAINS ... 99
4.1 ABSTRACT ... 101
4.2 INTRODUCTION ... 101
4.3 METHODS ... 104
4.3.1 Experiments and samples ... 104
4.3.2 Analysis of samples ... 105
4.4 RESULTS ... 106
4.4.1 Grainsize distribution ... 106
4.4.2 Detailed juvenile componentry of the coarse ash fraction ... 108
4.4.3 3D morphology of juvenile particles from the very fine ash fraction ... 110
4.4.4 Internal textures and morphometry of the coarse ash fraction ... 112
4.4.4.1 Experimental juvenile particles ... 112
4.4.4.2 Natural juvenile particles ... 115
4.4.5 Morphometry of the very fine ash fraction ... 115
4.4.5.1 Experimental juvenile particles ... 115
4.4.5.2 Natural juvenile particles ... 118
4.5 DISCUSSION ... 118
4.5.1 Summary of magma fragmentation during a typical experimental run ... 118
4.5.1.1 In-crucible fragmentation ... 118
4.5.1.2 Magma fragmentation in the atmosphere ... 120
4.5.2 What controls juvenile particle morphologies in experiments? ... 121

4.5.2.1 Thinning and clast formation 121
4.5.2.2 Cooling and morphology preservation 127
4.5.3 Kīlauea Iki 1959 versus experiments 128
4.5.4 Limits of very fine juvenile ash in studies of primary magma fragmentation for lava fountains 129
4.6 Conclusions 130
4.7 Acknowledgements 132
4.8 Online Resource 4.1: Detailed methodology 132
4.8.1 Tested materials 132
4.8.1.1 Experimental samples 132
4.8.1.2 Natural samples 132
4.8.2 Experiment setup and timeline 134
4.8.2.1 Collection of the experimental pyroclasts 136
4.8.3 Particle characterization 136
4.8.3.1 Overview of the work done at INRS 136
4.8.3.2 Pre-cleaning, dry hand sieving and ultrasonic treatment 137
4.8.3.3 Selection of juvenile particles 137
4.8.3.4 Detailed componentry and 3D morphology study of juvenile particles 138
4.8.3.5 2D morphometric and internal texture measurements 139
4.9 Online Resource 4.2: High-speed video recordings 141
4.10 Online Resource 4.3: Measurement data spreadsheets 142
5 GENERAL CONCLUSIONS 143
5.1 Summary of the main outcomes 143
5.1.1 Standardized methodology for comparative studies of primary magma fragmentation using juvenile pyroclasts 143
5.1.2 Hydrodynamic breakup regimes in lava fountains 144
5.1.3 What achneliths can tell about primary magma fragmentation 146
5.2 Linking the main outcomes: juvenile pyroclasts and primary magma fragmentation in basaltic eruptions 147
5.2.1 Importance of the standardized methodology 147
5.2.2 An improved understanding of lava fountains 148
5.2.3 Building a fragmentation diagram for mild basaltic eruptions 150
5.3 Future directions 151
5.3.1 Distinguishing magmatic from phreatomagmatic fragmentation through the analysis of juvenile pyroclasts 151
5.3.2 Understanding magma breakup at high deformation rates 152
5.3.3 From volcanology to industry: future work on Pele's hairs 153
6 REFERENCES 155

APPENDIX I: STANDARDIZED METHODOLOGY 171

ABSTRACT 173

INTRODUCTION 173

OVERVIEW OF THE WORKFLOW AND TARGET USERS 176

Who should use standardized analysis of juvenile pyroclasts? *177*

Overview of standard outputs *177*

Overview of recommended outputs *180*

Organization of the paper *181*

FIELDWORK AND PYROCLASTIC SAMPLING 181

Fieldwork (standard) *181*

Sampling pyroclastic deposits for particle size, morphologies, surface features and internal textures (standard) *181*

GEOCHEMICAL ANALYSIS (STANDARD) 184

Why geochemistry is needed *184*

Whole-rock analysis of juvenile pyroclasts *186*

Groundmass geochemistry *186*

SIEVING (STANDARD) 187

Particle-size distributions *188*

Is 'complete' grainsize distribution needed? *188*

Sieving techniques *189*

OUR CHOICE OF SIZE FRACTIONS 189

Coarse ash fraction (standard) *189*

Very fine ash fraction (standard) *190*

ULTRASONIC CLEANING (STANDARD) 191

BASIC COMPONENTRY (STANDARD) 192

JUVENILE PARTICLE SELECTION (STANDARD) 194

Coarse ash fraction (standard) *194*

Very fine ash fraction (standard) *194*

SAMPLE PREPARATION FOR QUANTITATIVE 2D MORPHOLOGICAL AND INTERNAL TEXTURE ANALYSIS (COARSE ASH FRACTION) (STANDARD) 194

DUAL MOUNTING OF THE VERY FINE ASH FRACTION (STANDARD) 195

Carbon tape grain mount *195*

Polished epoxy grain mount *197*

QUANTITATIVE MORPHOLOGY ANALYSIS 197

Overview of possible imaging methods *197*

Imaging strategy for the coarse ash fraction *198*

Imaging strategy for the very fine ash fraction *200*

Choice of morphometric parameters *200*
Imaging details for the coarse ash fraction *201*
Imaging details for the very fine ash fraction *203*
Measuring the morphometric parameters *204*
Excluding grains that are too small (post-processing) *205*
INTERNAL TEXTURES (COARSE ASH FRACTION) 205
Standard textural parameters *205*
Preparing the SEM images *205*
Textural measurements *205*
ASH SURFACE FEATURES (VERY FINE ASH FRACTION) (STANDARD) 205
Interactive particles *206*
Secondary surface features *210*
ARCHIVING THE IMAGES AND DATA 210
DATA ANALYSIS 211
DISCUSSION AND CONCLUSIONS 211
ACKNOWLEDGEMENTS 212
ONLINE RESOURCE A1.1: RECOMMENDED AND OPTIONAL STEPS 212
Density, porosity, connectivity and permeability measurements *213*
Dense rock equivalent density (recommended) 213
Porosity (recommended) 213
Vesicle connectivity (recommended) 213
Clast permeability (optional) 214
Grain-size distribution *214*
Complete grain size analysis (recommended) 214
Total grain size distribution (optional) 215
Familiarization (recommended) *215*
Choice of size fractions: adding medium lapilli *215*
Detailed componentry of glassy juvenile particles (recommended) *216*
Componentry classes 216
How many grains? 217
Juvenile particle selection and preparation for internal texture analysis (medium lapilli and coarse ash) *217*
Image analysis of cross-sectioned single particles (three fractions) *218*
Crystallinity and vesicularity for the medium lapilli fraction (recommended) 218
Other shape measurements for the coarse ash fraction (optional) 218
Morphology and textural parameters for the very fine ash fraction (recommended) 218
Internal textures: optional measurements 219
Dual mounting for the very fine ash fraction *219*
3D morphological classification of the very fine ash fraction (recommended) *219*

Fluidal particles 220
Vesicle-dominated particles 222
Angular particles 223
Practical details 224
Quantitative shape analysis: alternative methods *224*
ONLINE RESOURCE A1.2: METHODOLOGY STEPS TEMPLATES 225
ONLINE RESOURCE A1.3: SIEVING OF PYROCLASTIC DEPOSITS 225
Blocks and bombs *225*
Drying and splitting *225*
Manual dry sieving *225*
Cleaning the sieves *226*
Dealing with aggregates *227*
ONLINE RESOURCE A1.4: DUAL MOUNTING OF THE VERY FINE ASH FRACTION 227
Carbon tape grain mount *227*
Preparing the mounting surface 227
Quick particle transfer methods 227
Grain-by-grain transfer method 228
Final steps 228
Polished epoxy grain mount 229
ONLINE RESOURCE A1.5: SEM IMAGING SETTINGS 229
Coarse ash fraction *229*
Very fine ash fraction *230*
REFERENCES 230
APPENDIX II: CONFERENCE ABSTRACTS 251
POSTER SESSION AT IAVCEI (2017), PORTLAND, USA 251
POSTER SESSION AT COV10 (2018), NAPLES, ITALY 253
ORAL SESSION AT GAC-MAC-IAH (2019), QUEBEC CITY, CANADA 255
ORAL SESSION AT IUGG (2019), MONTREAL, CANADA 257
ORAL SESSION AT IUGG (2019), MONTREAL, CANADA 259

LIST OF FIGURES

Figure 1.1: The Walker (1973) classification of explosive eruptions. 2
Figure 1.2: Examples of magmatic and phreatomagmatic fragmentation processes. 5
Figure 1.3: Traditional Ohnesorge classification of breakup regimes. 7
Figure 1.4: Mix of juvenile morphologies, internal textures and surface features. 10
Figure 1.5: Standard steps of the standardized methodology. 15

Figure 2.1: Expanded version of the standard steps. 27
Figure 2.2: Representative images of juvenile particles from Ukinrek. 31
Figure 2.3: Preparing a polished epoxy grain mount. 34
Figure 2.4: Image preparation in Photoshop. 37
Figure 2.5: Final image outputs of the PASTA script for Fiji. 38
Figure 2.6: Pixel number test for 2D crystallinity and 2D vesicularity. 42
Figure 2.7: Pixel number test for convexity and solidity. 43
Figure 2.8: SEM-BSE images of the same particle cross-section but different scan speeds. 44
Figure 2.9: Optimum number of grains for each size fraction, strombolian. 45
Figure 2.10: Optimum number of grains for each size fraction, phreatomagmatic. 46
Figure 2.11: Rejection rate for the Ukinrek examples. 48
Figure 2.12: Convexity and 2D crystallinity versus solidity plots. 49
Figure 2.13: 2D crystallinity versus 2D vesicularity and the Büttner et al. (2002) plots. 51
Figure 2.14: Illustration of recommended tools for PEGM manufacturing. 59
Figure 2.15: Mounting the juvenile particles. 60
Figure 2.16: Printable directions for manual grinding and polishing of PEGMs. 63

Figure 3.1: The four liquid jet breakup regimes. 73
Figure 3.2: Magma compositions and experimental setups. 76
Figure 3.3: Physical properties of the tested magmas. 80
Figure 3.4: Initial movement of the magma plug and in-crucible fragmentation. 83
Figure 3.5: Time-lapse of the Hohenstoffeln 10 MPa run. 84
Figure 3.6: Time-lapse of the Hohenstoffeln 3 MPa run. 85
Figure 3.7: Time-lapse of the Billstein 10 MPa run. 86
Figure 3.8: Time-lapse of the Billstein 3 MPa run. 87
Figure 3.9: Time-lapse of the Sommata 10 MPa run. 88
Figure 3.10: Time-lapse of the Sommata 3 MPa run. 89
Figure 3.11: Modified “Ohnesorge” diagram applied to the early stage of the jet. 93

Figure 3.12: Potential examples of breakup regimes in lava fountains. 95

Figure 4.1: Lava fountains and melt ejection experiments. 103
Figure 4.2: Grain size distributions of the nine tested samples. 106
Figure 4.3: Binocular microscope and SEM-BSE images of natural and experimental pyroclasts. 107
Figure 4.4: Detailed juvenile componentry proportions for the narrow + 1ϕ (710–500 μm) fraction. 109
Figure 4.5: 3D morphology proportions for the + 4ϕ (88–63 μm) fraction. 111
Figure 4.6: SEM-BSE images of cross-sections of experimental juvenile pyroclasts..... 113
Figure 4.7: Axial ratio and vesicularity versus solidity for the narrow + 1ϕ (710–500 μm). 114
Figure 4.8: SEM-BSE images of particle cross-sections of the Kīlauea Iki juvenile pyroclasts..... 116
Figure 4.9: Axial ratio and convexity versus solidity for the narrow + 4ϕ (88–63 μm) fraction. 117
Figure 4.10: Schematic drawing of magma fragmentation in the experiments..... 119
Figure 4.11: Endmember behaviors for the thinning and breakup of magma. 125
Figure 4.12: Time lapse of liquid thinning and breakup of a thread into four droplets..... 126
Figure 4.13: Total Alkalis vs. Silica diagram of the studied materials experiment setups. 133
Figure 4.14: Hierarchical classification. 139

Figure 5.1: Modified Ohnesorge diagram for the identification of the breakup regimes. 145
Figure 5.2: Sketch of potential basalt fragmentation diagrams..... 151

Figure A1.1: Flowchart of the standard steps. 178
Figure A1.2: Flowchart of the standard and recommended steps. 179
Figure A1.3: Characteristics of fallout deposits from different eruptive styles. 182
Figure A1.4: Field work, ultrasonic cleaning, and basic componentry..... 185
Figure A1.5: Dual mounting procedure for the very fine ash fraction. 196
Figure A1.6: Definitions of the standard morphometric parameters. 202
Figure A1.7: Stability test for morphology measurements of particle silhouettes. 204
Figure A1.8: Secondary electron SEM images of stepped features and hackle marks. 208
Figure A1.9: SEM images of two types of interactive particles. 209
Figure A1.10 SEM images of some typical 3D particle shapes. 222
Figure A1.11: Sieving and cleaning the sieves. 226

LIST OF TABLES

Table 2.1: Optimum values of pixel density for SEM image processing of particle cross-sections 44

Table 2.2: Number of juvenile fragments needed to reach a stable average in morphometric and textural parameters 47

Table 2.3: Pros and cons of different ash size fractions 53

Table 2.4: Thickness to erode during grinding/polishing 64

Table 3.1: Physical parameters of the magma plug among different experiments. 79

Table 4.1: Relevant physical parameters of the magmas in the experiments and the Kīlauea Iki. 123

Table 4.2: Breakdown of the hierarchical classification. 140

Table A1.1: Correspondence between the ϕ scale and mm, for half-ϕ sieving columns. 175

Table A1.2: Comparison of three particle mounting methods for SEM imaging. 199

1 GENERAL INTRODUCTION

This PhD thesis explores the link between the external morphology of juvenile pyroclasts and primary magma fragmentation processes. Magma fragmentation represents the conversion of a coherent magma mass into a hot mixture of gas and pyroclasts (± liquid water) ejected from a volcanic vent (Parfitt and Wilson 2009; Cashman and Scheu 2015). Different fragmentation mechanisms and eruption intensities result in a broad variety of explosive eruptive styles ranging from “mild” Hawaiian-style fire fountains to global-scale catastrophic phreatoplinian eruptions driven by magma-water interaction (Parfitt and Wilson 2009; Cioni et al. 2015; Houghton et al. 2015; Taddeucci et al. 2015; Zimanowski et al. 2015). Magma fragmentation remains incompletely understood but juvenile pyroclasts should inherit characteristics that can be used to discriminate among eruptive styles (Walker and Croasdale 1971; Heiken 1974; Fisher and Schmincke 1984; Büttner et al. 1999; Andronico et al. 2009; Liu et al. 2015). This information is important in order to better predict what a volcano might do in the future based on the study of deposits of past, often unwitnessed, eruptions.

This chapter begins with an outline of the current knowledge on the dynamics involving mildly-explosive eruption styles for basalts and similar magmas, and the associated pyroclastic products. A description of both magmatic and phreatomagmatic fragmentation mechanisms follows. Because this thesis deals in large part with lava fountains, the hydrodynamic breakup of magmas is compared with industrial liquid jet breakup. Next comes a description of the link between breakup mechanisms, magma composition and juvenile particle shapes. Later, the problems to be solved, the aims and the methodology are presented. Finally, the structure of the thesis is outlined, and the contribution of the authors to the different publications is explained.

1.1 Explosive volcanism involving ultramafic and mafic magmas

More than 800 million people live within 100 km of an active volcano, often attracted by the fertile soils (Gottsmann et al. 2019). Relatively mild explosive eruptions involving ultramafic to mafic magmas are among the most frequent and iconic volcanic phenomena (Taddeucci et al. 2015; Houghton et al. 2016). Despite being less dangerous when compared to devastating plinian eruptions, they are nonetheless a relevant source of hazard (Heggie 2009; Calvari et al. 2018; Neal et al. 2019). For example, recent hawaiian style eruptions at Kīlauea volcano (Hawaii, USA), Mount Etna (Italy) and Fagradalsfjall (Iceland), with their fast-moving lava flows and spectacular lava fountains, attract thousands of visitors each year (Houghton et al. 2016). Beyond the

immediate danger of being too close to an active lava field, more intense ash-dominated lava fountains such as at Mount Etna (Italy) and/or active lava flows of Fogo (Cape Verde) and Nyiragongo (Democratic Republic of the Congo) volcanoes frequently become a threat to the livelihood of nearby towns, resulting in direct deaths, crop failure, disruption of transportation services and buildings, etc. (Sigurdsson 2015; Andronico and Del Carlo 2016; Cappello et al. 2016).

A range of explosive eruptive styles can be distinguished between magmatic and phreatomagmatic (Fig. 1.1). Here the focus is on relatively mild eruption styles involving ultramafic to mafic magmas.

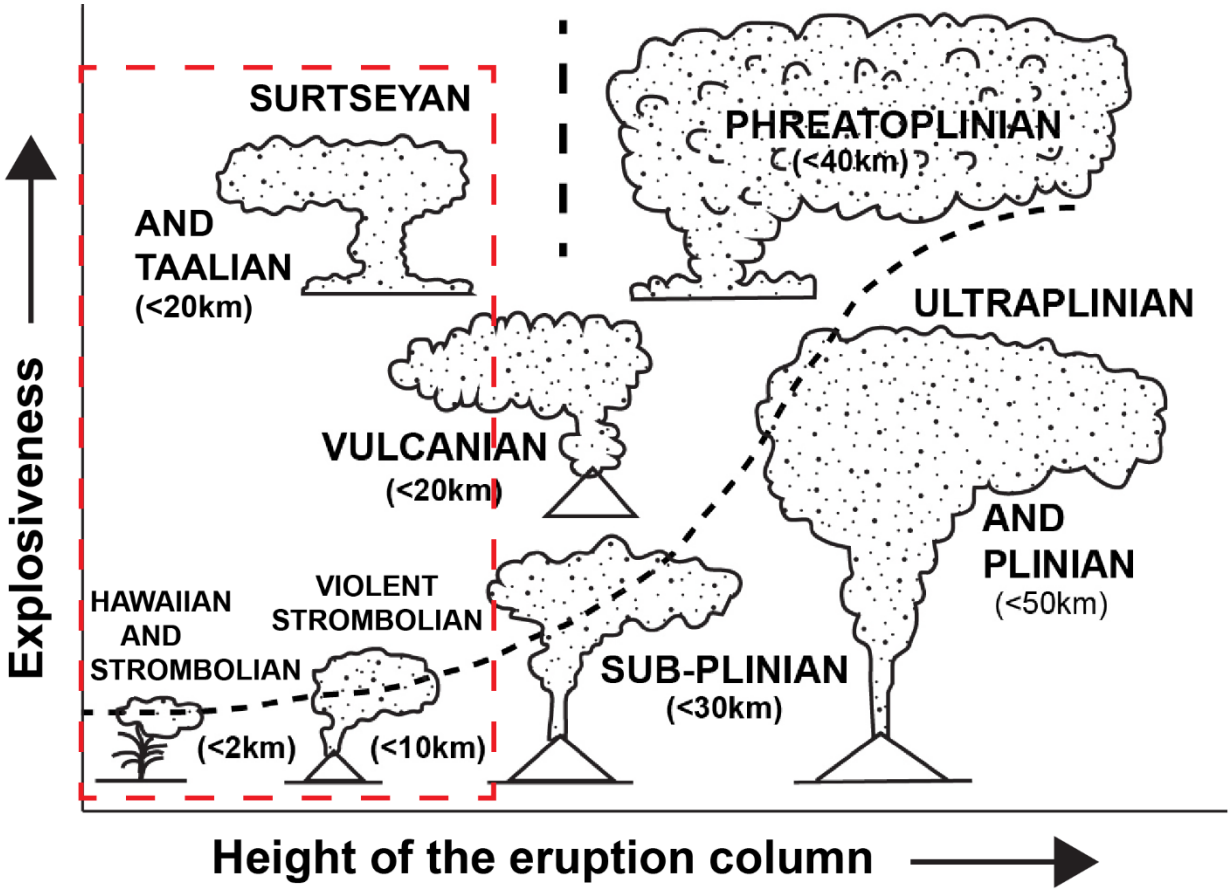

Figure 1.1: The Walker (1973) classification of explosive eruptions showing the magnitude (expressed by the surface area of a certain isopach, a proxy for the height of the eruption column) versus the explosiveness (expressed by the proportion of ash finer than 1 mm at a certain isopach). The dashed red box emphasizes the eruption styles considered in this study. Modified from Cas and Wright (1987) to include the taalian style. Also, the hawaiian and classic strombolian styles might better fall within the same field in the lower left corner of the diagram, while violent strombolian activity (e.g. Paricutin) would replace the "strombolian" field in the original diagram.

1.1.1 Magmatic explosive styles

In the absence of external water, explosive eruptions are caused by the growth of gas bubbles and by rapid magma decompression (Cashman and Scheu 2015). Parameters that control the different styles of magmatic explosive eruptions include bulk magma composition, viscosity, crystallinity, vesicularity, ascent velocity, etc. (Cashman 2004; Parfitt 2004; Parfitt and Wilson 2009; Cashman and Scheu 2015; Jones et al. 2019). The following comparatively mild styles can be distinguished.

- The classic Strombolian style consists of brief explosive pulses individually separated by pauses of minutes to hours (Taddeucci et al. 2015; Houghton et al. 2016). Fragmentation is triggered by the cyclical explosive decompression of large coalesced gas bubbles (gas slugs) trapped near the top of a mafic magma column (Blackburn et al. 1976; Ripepe et al. 2008; Del Bello et al. 2015; Pering et al. 2015). The typical products are scoriaceous lapilli and bombs, along with lithic blocks and ash (Polacci et al. 2006; Rosi et al. 2013; Andronico et al. 2015);
- Hawaiian style pulses are instead so closely-spaced that they form a single, sustained event lasting for hours to days (Taddeucci et al. 2015; Houghton et al. 2016). Hawaiian eruptions create lava fountains and fissural fountaining (a.k.a. curtains of fire). The largest pyroclasts are still hot when they land, deforming upon impact. Rapid accumulation of molten magma clots can feed secondary, clastogenic lava flows (Sumner 1998; Andronico et al. 2008; Mueller et al. 2018). A portion of the smaller pyroclasts are lofted in a column above the fountain, forming a fallout sheet (Ritcher et al. 1970; Stovall et al. 2011; Calvari et al. 2018; Mueller et al. 2018).
- Violent strombolian activity produces more ash than the first two magmatic explosive styles (Pioli et al. 2008; Valentine and Gregg 2008). The higher mass flux and fragmentation efficiency lead to formation of sustained eruption columns up to 10 km high, setting this style apart from both classic strombolian and hawaiian styles. In this regard, violent strombolian activity is beyond the scope of this thesis.

The edifices built by such activity include spatter ramparts and rings, scoria cones, etc. (Taddeucci et al. 2015).

1.1.2 Phreatomagmatic explosive styles

When magma meets external water, explosive eruptions are called phreatomagmatic. Some eruptions that would have been effusive become explosive because of phreatomagmatism

(Wohletz et al. 2013). In addition, magmatic explosive eruptions can become enhanced by phreatomagmatism to produce more intense fine fragmentation (Cioni et al. 2014). For ultramafic to mafic magmas, two comparatively mild styles can be distinguished (Sohn 1996).

- The Surtseyan style (after the 1963 eruption of Surtsey in Iceland, Thorarinsson 1967) is characterized by abundant liquid water driving the fragmentation process (White and Houghton 2000). Magma being erupted through shallow seas results in the important generation of steam to produce silent, collapsing fountains known as tephra jets (Schipper et al. 2015). Typical volcanic constructs are tuff cones (White et al. 1991; Agustín-Flores et al. 2015). The pyroclastic products span from lapilli to fine juvenile ash and subordinate ballistic bombs. Hyaloclastite is produced in the initial stage of shallow submarine activity, turning into more scoriaceous juvenile clasts in the subaerial environment (but vesicularity is highly variable) as the active fragmentation zone approaches the sea surface, with less than 10% lithic fragments (Cole et al. 2001; Murtag and White 2013);
- The Taalian style (after the 1965 eruption of Taal volcano in the Philippines, Moore et al. 1966) is normally associated with a more discontinuous or less abundant water supply during fragmentation. This occurs, for example, when rising magma passes through a water-saturated rock formation, or surface water accessing an active vent. In the first case, underground phreatomagmatic fragmentation promotes excavation of the conduit and subsequent infill by volcaniclastic material (White and Ross 2011). In the latter case, there is less underground excavation. For both sources of water, convective plumes and pyroclastic density currents are produced, characterized by abundant moisture and relatively low pyroclast concentration. Typical volcanic constructs are maars and tuff rings (White and Ross 2011). The pyroclastic products range from bombs to fine ash of variable vesicularity and crystallinity, with an abundant but variable portion made by lithic material (up to 90%) (Self et al. 1980; White 1989; White et al. 1991; White and Ross 2011; Latutrie and Ross 2019). Vesicularity and crystallinity of juvenile materials are also widely variable, from mostly glassy scoria with large open vesicles, to markedly tachylitic grains with closed vesicularity (Ort et al. 2018). If vesiculation is arrested early by contact with external water, the juvenile pyroclasts can be dense and blocky.

1.2 Physics of magma fragmentation

1.2.1 Magmatic fragmentation

In the absence of external water, fragmentation is dominated by rapid decompression and the effect of the volatiles present in the magma (Cashman and Scheu 2015). As a certain magma batch rises toward the surface, different gas phases start to exsolve from the melt, forming bubbles that progressively expand and coalesce. This reduces the bulk density of the magma, increasing its ascent velocity (Parfitt and Wilson 2009). Ultimately, it is the ability of the bubbles to decouple and escape from the melt that governs fragmentation (Cashman and Scheu 2015). At one extreme, bubbles rising faster than the surrounding melt result in lava effusion at the surface. If bubbles coalesce into gas slugs, strombolian eruptions occur (Blackburn et al. 1976; Parfitt 2004). If the bubbles and melt are more coupled, the magma will accelerate and come out as a lava fountain (Parfitt 2004; Taddeucci et al. 2015) (Fig. 1.2a). Magma fragmentation in lava fountains is often a type of hydrodynamic (ductile) fragmentation, as will be discussed in section 1.2.3. Still more violent styles of magmatic explosive eruptions involving basalts are possible (violent strombolian, sub-plinian and even plinian, Fig. 1.1), but are beyond the scope of the present thesis.

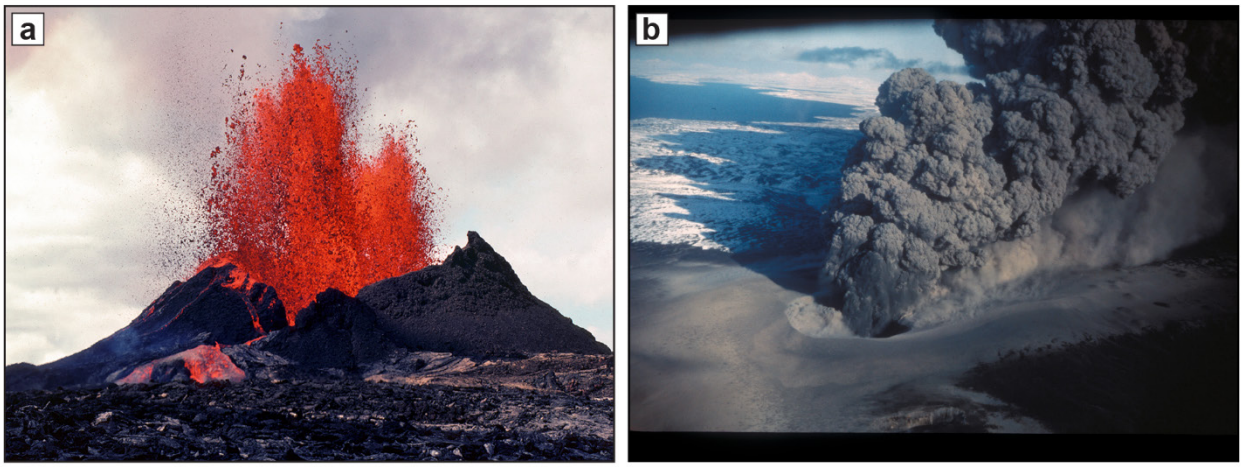

Figure 1.2: Examples of magma fragmentation processes. (a) Magmatic fragmentation of a weak lava fountain from the Pu'u 'Ō'ō eruption (Kīlauea), September 6, 1983 (Hawaii, U.S.A). Credit: U.S. Geological Survey/photo by J.D. Griggs. (b) Phreatomagmatic activity during the 1977 Ukinrek Maars eruption, April 6 1977. Credit: ADF&W/photo by R. Russell.

1.2.2 Phreatomagmatic fragmentation

The encounter between rising magma and the hydrosphere can also result in explosive eruptions (Fig. 1.2b). The thermal energy stored in the magma is transferred to the water, then released as

mechanical energy. The resulting phreatomagmatic fragmentation is intense (Heiken and Wohletz 1991) and more ash is typically produced than in magmatic eruptions (Zimanowski et al. 1997; Dellino et al. 2012; Liu et al. 2017). The details of how this happens in nature are not entirely clear and the processes may vary between surtseyan and taalian styles (or not). A popular model is called the molten fuel-coolant interaction (MFCI), based on industrial accidents and magma fragmentation experiments in the laboratory. MFCI consists of four steps (Büttner et al. 2002; Zimanowski et al. 1997, 2015):

1. Premix-phase. The rising magma comes into contact with external water and coarsely mixes with it. A stable vapor film is established between the domains of magma and water.
2. Trigger-phase. The vapor films collapse within 1 ms, allowing direct contact between magma and water. The trigger comes in the form of a pressure wave that can be produced by different sources, such as seismic activity, hydraulic fracturing, etc.
3. Direct contact phase. Heat is rapidly transferred from the magma to the water. This cools and fractures a portion the magma in a brittle fashion. The very small angular glassy fragments with specific surface features produced during this stage are known as ‘interactive’ particles.
4. Expansion phase. As water is converted into steam, the system violently expands to ambient pressure, converting the surrounding coherent magma mass into fragments propelled upward along with vapor and volcanic gases, as commonly observed during phreatomagmatic eruptions. The additional juvenile fragments produced during this stage tend to form from ductile stretching and are known as ‘passive’ particles.

1.2.3 Mechanisms of magma breakup in lava fountains

Beyond the type of driving force responsible for the overall fragmentation process, magma breaks up in two different fashions: i) hydrodynamic breakup; ii) brittle fragmentation. These two mechanisms are not mutually exclusive, and both might occur within the same explosive pulse (Zimanowski et al. 1997; Jones et al. 2019).

Hydrodynamic fragmentation consists in the ductile breakup of a coherent liquid magma mass into multiple smaller drops and/or threads (Zimanowski et al. 1991, 1997; Shimozuru 1994; Caffier 1998; Porritt et al. 2012; Jones et al. 2019). One place where this occurs is a lava fountain, which can be thought of as a fragmenting magma jet. Depending on their size, cooling history and travel time, the first magma drops might undergo further breakup, forming progressively smaller droplets until a critical size is reached (Birouk and Lekic 2009; Lefebvre and McDonell 2017). The

hydrodynamic disintegration of magmas in lava fountains resembles the breakup of liquid jets issued from a nozzle, a topic that has been extensively studied in industrial applications (Eggers and Villermaux 2008). As will be discussed in detail in Chapter 3, a liquid can exit the nozzle as a coherent jet or a fully atomized spray, depending on several parameters such as the issuing velocity and internal liquid properties (Chigier and Reitz 1996; Birouk and Lekic 2009). Four breakup regimes were defined to characterize the appearance of a liquid jet issued at increasing ejection velocity (Reitz and Bracco 1986; Birouk and Lekic 2009; Lefebvre and McDonell 2017) (Fig. 1.3): i) Rayleigh regime; ii) first wind-induced regime; iii) second wind-induced regime; iv) atomization regime.

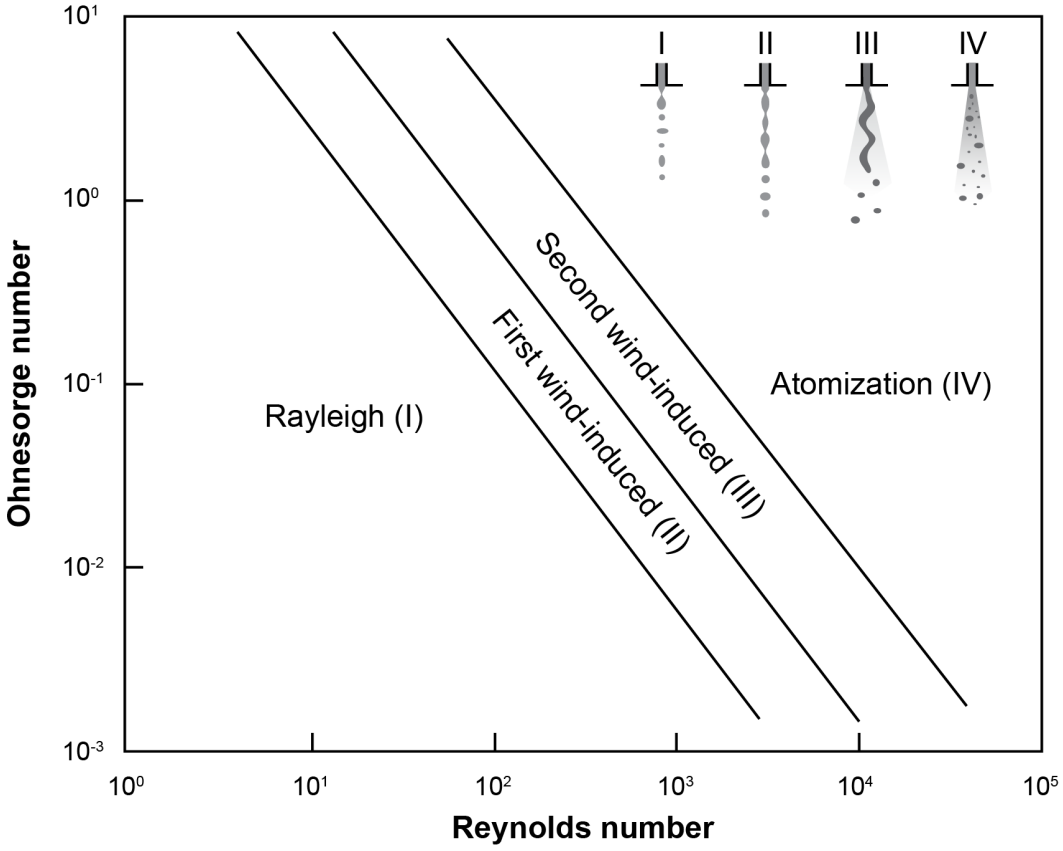

Figure 1.3: Traditional Ohnesorge classification of the four modes of breakup of a liquid jet issued from a nozzle as function of the increasing velocity (from left to right). The four fields were obtained from experiments on diesel fuels. The Ohnesorge ($Oh = \frac{\eta}{\sqrt{\rho\sigma d}}$) and Reynolds ($Re = \frac{\rho u d}{\eta}$) dimensionless numbers relate viscous, inertial and surface tension forces, where σ, η, ρ and u are respectively the surface tension, dynamic viscosity, density and velocity of the issued liquid, while d is the diameter of the nozzle. Redrawn from Lefebvre and McDonell (2017).

Beyond the overall description of the liquid jet, it is the breakup mechanism of each single drop into two parting masses that controls the overall shapes of the future droplets. The process is

governed by surface tension and balanced by viscosity, fluid inertia and elasticity (Shimozuru 1994; Clasen et al. 2012). As a liquid drop start splitting, a neck forms between the two masses. If the thinning process at the neck is dominated by surface tension (this is the case of low viscosity liquids), thinning timescales will be short enough to cause early breakup of the initial mass in two relatively compact droplets, especially at low issuing velocity (Clasen et al. 2012). Liquid contraction toward a minimum energy configuration (i.e. a sphere) will occur at both ends of the neck (Eggers and Villermaux 2008). For sufficiently long tails, contraction will lead to the creation of one or more small satellite droplets (Clasen et al. 2012). At larger ejection velocities, liquid inertia will oppose surface tension, extending filament thinning and delaying breakup. For viscoelastic liquids, viscosity and elasticity efficiently oppose surface tension, especially at high ejection velocity. Thinning timescales will be large, resulting in the generation of long liquid filaments. When finally breakup occurs, only partial contraction of the long thread will be allowed, with virtually no satellite droplet formation (Eggers and Villermaux 2008; Clasen et al. 2012).

Unlike industrial liquids, thinning and breakup mechanisms involving magma are more complex, due to: i) the fact that the magma mass is approaching the glass transition temperature due to rapid cooling from initial eruption temperature values, especially for small pyroclasts; ii) the presence of bubbles and crystals within the magma, which introduce further complexity during deformation and breakup (Mader et al. 2013; Cashman and Scheu 2015; Jones et al. 2019).

When shear rates become larger than the stressed magma can tolerate, transition from viscous to elastic behavior occurs, causing solid-like breakage known as brittle fragmentation (Zimanowski et al. 2003; Büttner et al. 2006; Jones et al. 2019). This transition might occur i) by approaching the glass transition temperature, which involves a dramatic increase in viscosity (Gonnermann 2015), ii) because of a large abundance of crystals and bubbles within the melt (Cassidy et al. 2018; Jones et al. 2019), and/or iii) by extreme stresses and shear rates induced by explosive magma-water interaction. These factors are not mutually exclusive, and might act simultaneously to cause brittle failure. Some lava fountains allow brittle failure to happen, for example at Etna (La Spina et al. 2021).

1.3 Juvenile pyroclasts

The result of both magmatic and phreatomagmatic eruption styles is a virtually endless panoply of juvenile pyroclasts (Heiken 1974; Fisher and Schmincke 1984). Their external morphology, surface features and internal textures reflects specific eruption conditions, as they represent the fragmented magma (Walker and Croasdale 1971; Dellino and La Volpe 1996; Büttner et al. 1999,

2006; Dürig et al. 2012a, 2012b; White and Houghton 2006; Jordan et al. 2014; Liu et al. 2015, 2017). The identification and study of primary juvenile pyroclasts is therefore crucial to understand eruption dynamics, interpreting history and to help forecast future behavior of volcanoes around the world (Dürig et al. 2020a). After primary fragmentation, transport and deposition processes might partially or totally obliterate primary morphological characteristics, but this thesis is only concerned with those primary characteristics, not their possible later modification.

1.3.1 External morphologies

The morphology of a newly formed juvenile pyroclast is directly determined by the deformation response of the magma during fragmentation (Heiken 1972, 1974, Porritt et al. 2012). This, in turn, is a function of several parameters such as the chemical composition, vesicularity, crystal content, eruption temperature, etc. (Stovall et al. 2011; Porritt et al. 2012; Liu et al. 2015). Ultramafic and mafic juvenile pyroclasts can display a vast cohort of morphologies (Fig. 1.4a, b).

In **lava fountains**, low to moderate magma vesicularity (*sensu* Houghton and Wilson 1989) and hydrodynamic fragmentation results in fluidal pyroclasts, also known as achneliths (Walker and Croasdale 1971; Porritt et al. 2012). Achneliths range from spherical to tear-shaped and filamentous fragments (Walker and Croasdale 1971; Duffield 1977; Shimozuru 1994; Porritt et al. 2012; Cannata et al. 2019). When volatiles are abundant, within larger clasts, bubbles grow in size and number, progressively converting achneliths into scoriaceous and then pumiceous fragments (Stovall et al. 2011, 2012; Porritt et al. 2012; Andronico et al. 2014). This occurs in well-established fountains like at Kilauea volcano. In the case of prolonged vesiculation, expansion of nearby bubbles results in the thinning and brittle failure of the melt film between them (Jones et al. 2019). Pumice fragments and glass shards are the main fragments generated this way (Kameda et al. 2008; Stovall et al. 2012; Cashman and Scheu 2015). Brittle fragmentation has also been described to happen during late stages of Hawaiian eruptions, resulting in the generation of angular, blocky morphologies (Polacci et al. 2019, Namiki et al. 2021).

In **strombolian events** (Taddeucci et al. 2015; Houghton et al. 2016), scoria and pumice lapilli are commonly observed (Self et al. 1980). Their formation is favored by abundant crystals and bubbles, whose presence enhances brittle fragmentation (Polacci et al. 2006; Jones et al. 2019).

If external water comes into play, faster cooling and **phreatomagmatic fragmentation** can result in particles displaying blocky, angular to sub-angular morphologies in all the size fractions (Büttner et al. 1999; Ort et al. 2018). However, abundant vehicles can modify the external shapes of phreatomagmatic particles. Phreatomagmatic fragmentation, as already discussed, produces

both interactive and passive particles (Büttner et al. 2002; Dellino et al. 2012). The interactive ones are normally blocky, mostly found in the very fine ash fractions (Büttner et al. 1999; White and Houghton 2006) (Fig. 1.4c, d, e). The passive ones range from achneliths produced by ductile breakup to scoria and pumice.

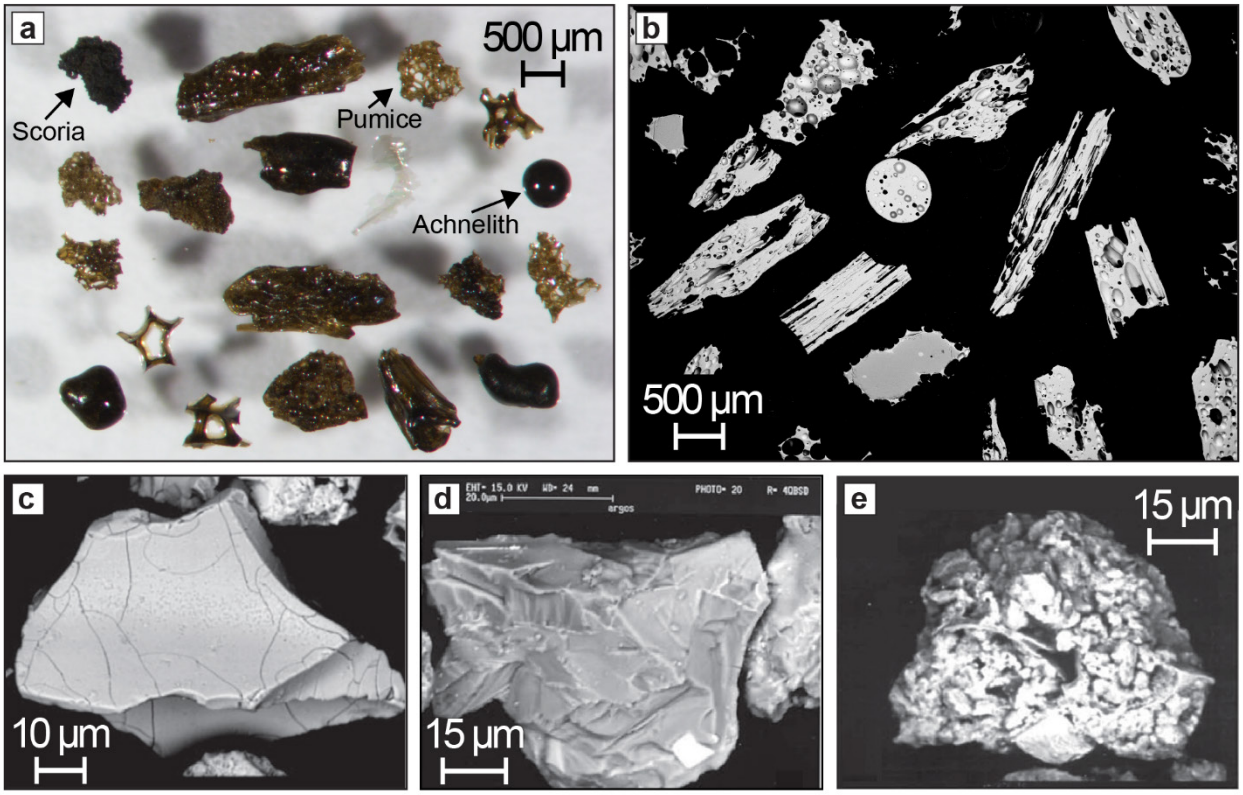

Figure 1.4: (a) Mix of juvenile morphologies from the 1959 Kīlauea Iki eruption, Hawaii, USA. (b) Mix of internal textures for the same juvenile material (SEM-BSE image). (c-d-e) SEM images of interactive particles with specific surface features (from Zimanowski et al. 2015): (c) quenching cracks; (d) stepped features; (e) mosslike pattern.

1.3.2 Internal textures

The most common internal textures of juvenile pyroclasts revolve around the quantity (expressed in volume %), size, distribution and orientation of crystals and vesicles (Fig. 1.4b). These features are linked to the pre-fragmentation history of the magma, providing indirect information on ascent velocity, temporary storage conditions and possible interaction with the hydrosphere (Cashman 2004; Wallace et al. 2015).

As introduced in the previous section, crystals and bubbles might exert a control on the overall shape juvenile fragments when abundant (Jones et al. 2019). The same effect is obtained as particle size decreases, with faces of bubbles and corners of crystals appearing on the surface of

the grain (Porritt et al. 2012). Crystals and bubbles indirectly control the resistance and way of fragmentation of a particle. Thin bubble walls and faces of the crystals act as planes of weakness inside the fragment, reducing their resistance to breakage (Jones et al. 2019).

1.3.3 Surface features

Primary magma fragmentation can leave distinct marks on the surface of the resulting fragments. Fluidal particles have smooth surfaces (Zimanowski et al. 2015), whereas blocky juvenile grains typically display conchoidal fractures acquired through brittle deformation (Dürig and Zimanowski 2012). Unique features are generated during phreatomagmatic fragmentation, as observed over two decades of studies on natural pyroclasts and comparison with experimental analogues (Dellino and La Volpe 1995, 1996; Büttner et al. 1999, 2006; Dürig et al. 2012a, 2012b; Zimanowski et al. 2003). Interactive particles are characterized by unique surface traits like branching quench cracks (Fig. 1.4c), stepped features (Fig. 1.4d), and mosslike patterns (Fig. 1.4e) (Zimanowski et al. 2015). Features of this kind, observed in the fine ash size fraction, are totally absent to very rare in particles produced during magmatic fragmentation (Zimanowski et al. 1997).

1.4 Problems to be solved

Primary juvenile pyroclasts constitute the direct result of magma fragmentation processes occurring within an active vent (or just above). These processes are therefore not generally accessible. Even at well monitored volcanoes, observations of fragmentation mechanisms are impossible during a paroxysm. Therefore, our understanding of primary magma fragmentation greatly relies on the information preserved within juvenile pyroclasts, especially for unwitnessed eruptions. This thesis will address three main problems.

1.4.1 Standardized methodology to characterize juvenile pyroclasts for comparative studies of primary fragmentation

At present, it is challenging to directly link specific features observed on or in juvenile pyroclasts to specific fragmentation mechanisms and associated eruption styles. Only a limited number of cases where the eruption has been observed had their pyroclasts analyzed for this purpose (Porritt et al. 2012; Liu et al. 2015, 2017; Avery et al. 2017; Polacci et al. 2019; Dürig et al. 2020b, 2020c). This issue is compounded by the lack of a widely accepted standardized methodology of investigation for juvenile pyroclasts: there is no agreement on which grain size to use, which parameters to measure and how, or which analyses should be essential for comparative studies

of primary fragmentation. This currently limits comparison among different volcanic events and their products, curbs collaboration among different research groups and slows the journey toward a more complete understanding of magma fragmentation and the dynamics of explosive eruptions. Ultimately, these shortcomings partly prevent volcanologists from using existing pyroclastic deposits to better predict possible future behavior at dangerous active volcanoes.

1.4.2 Liquid jet breakup in lava fountains

In hawaiian style lava fountains, hydrodynamic fragmentation is one of the main processes converting coherent magma into a cloud of liquid droplets. The detailed understanding on how this process works is relevant to link related pyroclastic deposits with the mechanism that generated them. A broad literature exists on the hydrodynamic breakup of industrial and commercial liquids, and four liquid jet breakup regimes have been defined (Fig. 1.3) but these concepts have yet to be applied to magmas. Compared with industrial liquids, magmas are complex and potentially dangerous to experiment on. Also, the balance between internal physical parameters such as viscosity, surface tension and density are composition-, time- and temperature-dependent in magmas, making modelling more challenging.

1.4.3 Achnelith morphologies

In lava fountains, achneliths are the type of juvenile fragment most directly linked with magma fragmentation (Porritt et al. 2012). The fascinating variety of achnelith morphologies (from spheres to Pele's hairs) represents the complexity and variability of the fragmentation process and pyroclast behavior. The parameters controlling these shapes are not completely understood.

1.5 Aims

1.5.1 Standardized methodology to characterize juvenile pyroclasts for comparative studies of primary fragmentation

The first aim of this study is to develop a standardized methodology for the analysis of juvenile pyroclasts in comparative studies of magma fragmentation. This standardized methodology represents the backbone of the entire investigation; it is presented briefly in section 1.6 and fully in a two-part manuscript found in Appendix I (Part 1, by Ross et al. 2021) and Chapter 2 (Part 2, by Comida et al. 2021a).

Some of the questions that need to be answered for developing the standardized methodology include:

- What kind of analyses are essential for studying primary magma fragmentation?
- What are the best size fractions to be analyzed?
- How many juvenile pyroclasts are needed in order to obtain statistically reliable data?
- Which image resolution is required for the accurate quantification of particle morphologies and internal textures?

A standardization of the methodology for comparative studies of primary magma fragmentation will benefit the volcanological community as a whole, making data from different research groups, volcanoes and eruptions directly comparable. The use of a same size fraction, analyzed using the same key steps in the protocol, will generate highly comparable data. This has important implications on the advancement of volcanological knowledge and for hazard mitigation purposes, as insights from a well-known eruption could be used to predict and assess other volcanoes where data are scarce and investigations are limited.

1.5.2 Liquid jet breakup in lava fountains

The second aim of the study is to better understand hydrodynamic fragmentation in lava fountains. This will rely on high-speed movies from laboratory experiments involving magmas expelled violently from a crucible, and an exploration of the similarities between these experiments and industrial liquid jet breakup, as well as natural lava fountains (Chapter 3).

Some of the questions around the investigation of hydrodynamic fragmentation are:

- How does magma break up during hydrodynamic fragmentation?
- What physical properties control thinning and breakup?
- What are the similarities (and differences) between industrial liquids and magmas during breakup?
- What can the experiments tell us about magma breakup in natural lava fountains?

1.5.3 Achnelith morphologies

The third aim of the study is to better understand what controls the shape of fluidal juvenile pyroclasts in lava fountains. This will rely on the same laboratory experiments, but focusing on characterizing the artificial juvenile pyroclasts, using the standardized methodology developed in Chapter 2 and Appendix I. Ash-sized juvenile particles from the experiments will be compared with those from the 1959 Kīlauea Iki eruption at Kilauea volcano (Hawaii, USA) (Ritcher et al. 1970; Mueller et al. 2018) (Chapter 4).

Some of the questions around the comparison between artificial and natural juvenile pyroclasts are:

- What properties control the morphology of juvenile pyroclasts in lava fountains?
- What are the limits of the very fine ash fractions for the purposes of investigating eruption dynamics?

Due to the discrete nature of the experimental runs and the absence of any transport, the collected juvenile pyroclasts are the direct unmodified product of primary fragmentation. Their morphological characteristics and variety are an ideal reference for comparing and understanding natural deposits, allowing to reconstruct past events.

1.6 Methodology overview

Each chapter contains its own detailed methodology and the present section only provides a general overview, to help the reader understand the links between the chapters.

1.6.1 Standardized methodology to characterize juvenile pyroclasts for comparative studies of primary fragmentation

The lack of a standardized methodology to characterize juvenile pyroclasts for comparative studies of primary fragmentation was established early on during this project. It became clear that detailed steps from sample collection in the field to data acquisition and analysis of juvenile particles were needed. Therefore a multinational team of experts was brought together, and three years of work produced workflows characterized by standard, recommended and optional steps, for which a brief summary is provided below. Only steps from the standard workflow (Fig. 1.5) are presented here.

The workflow starts with fieldwork and the collection of pyroclastic material, opting for those deposits that underwent the least amount of disturbance by transport, deposition and remobilization processes. For this reason, fallout deposits are preferred whenever available. Fresh juvenile lapilli or bombs can be selected for a geochemical characterization. Pyroclastic samples from representative layers are collected and brought back to the laboratory. Gentle hand sieving allows to generate a complete grain size distribution, and to extract the two main half-ϕ (ϕ = $-\log_2 d$, where d is the particle diameter in mm, Krumbein and Sloss 1963) size fractions of interest: i) a 0.71–0.5 mm (+ 0.5 to + 1ϕ or “narrow + 1ϕ”) coarse ash fraction; ii) a 88–63 µm (+ 3.5 to + 4ϕ or “narrow + 4ϕ”) very fine ash fraction.

After cleaning these fractions using an ultrasonic bath, steps differ for each size fraction. For the coarse ash, basic componentry and juvenile particle selection is carried out at the binocular microscope, leading to the selection of > 50 juvenile grains. The selected particles are converted into a polished epoxy grain mount (PEGM). Images of the mounted juveniles are acquired at the scanning electron microscope (SEM), to be ultimately prepared and processed for the measurement of morphometric parameters, 2D crystallinity and 2D vesicularity on particle cross-sections.

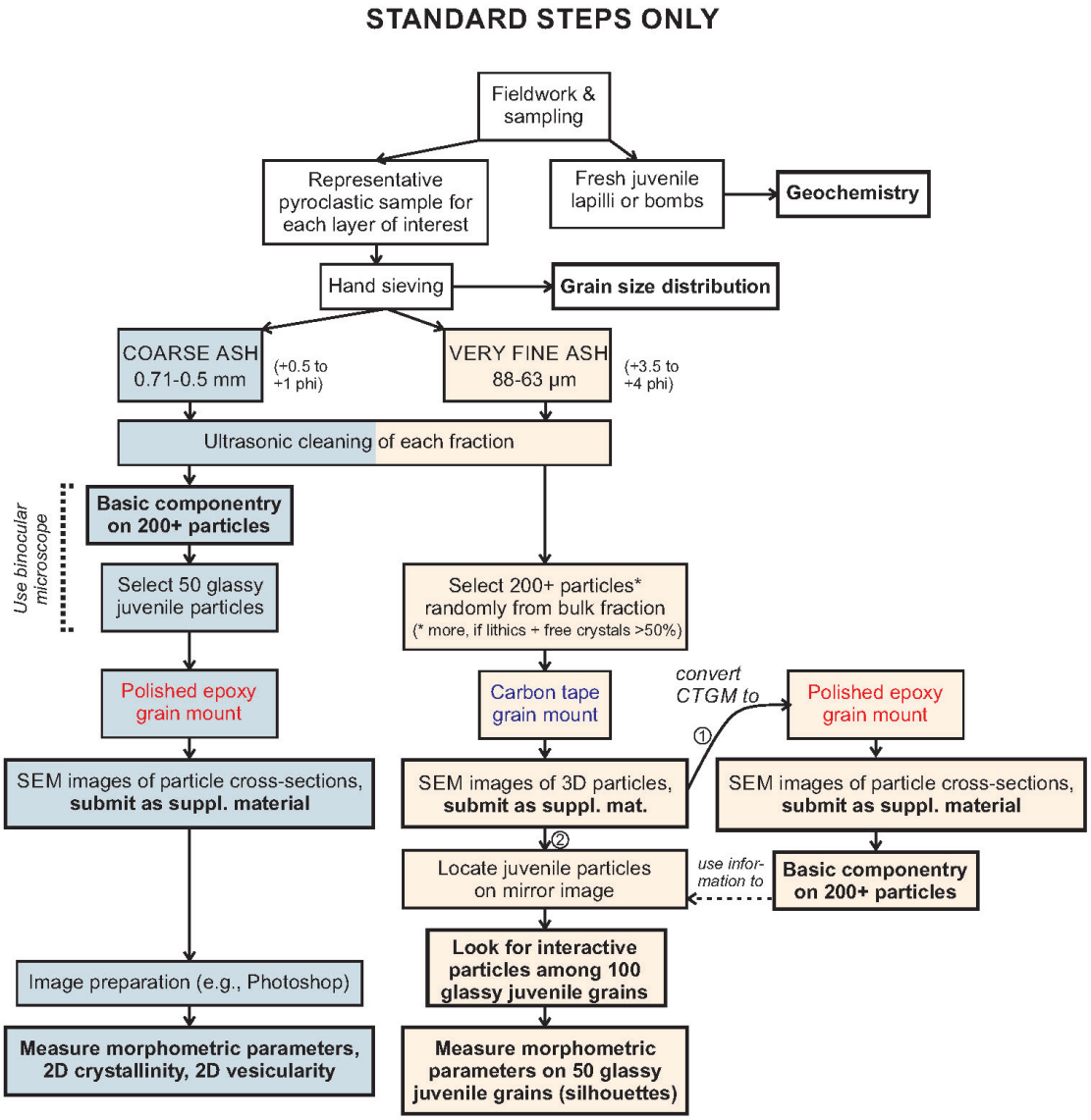

Figure 1.5: Standard steps of the standardized methodology (from Appendix I).

For the very fine ash fraction, the small size requires the identification of juveniles at the SEM. A double mounting technique was therefore developed. At least 200 particles from the bulk fraction

are first prepared into a carbon tape grain mount (CTGM), then SEM images of the 3D particles are acquired. For an accurate juvenile selection, the CTGM is converted into a PEGM in order to see the grain interiors. Basic componentry is done on the SEM images of the grain cross-sections. Then 100 juvenile grains are observed for interactive particles on the CTGM images, and 50 grains are used for the measurement of morphometric parameters on silhouettes.

Material was needed to develop and test each step of the standardized methodology. Magmatic and phreatomagmatic pyroclasts from the 1977 Ukinrek maars eruption (Alaska, USA) (Kienle et al. 1980; Ort et al. 2018) was used. This eruption lasted for about 11 days and formed two maars (West and East, Kienle et al. 1980; Ort et al. 2018). The magma was an alkaline basalt (Kienle et al. 1980). Samples from both a strombolian and a phreatomagmatic style were chosen from very proximal units belonging to the initial stage of an eruptive episode, in order to minimize recycling and transport effects. The strombolian sample was produced during the initial fissural activity (F1 unit, Ort et al. 2018) (Fig. 1.6a). It is characterized by brown to black fallout ash, incipiently to moderately vesicular (5–60%) with a glassy (sideromelane) groundmass. The phreatomagmatic sample is part of the East Maar ejecta ring (EM1 unit of Ort et al. 2018) (Fig. 1.6b). The lithic-rich deposit contains sub-compact, poorly to highly vesicular juvenile clasts characterized by a tachylitic groundmass and high crystallinity (> 50%).

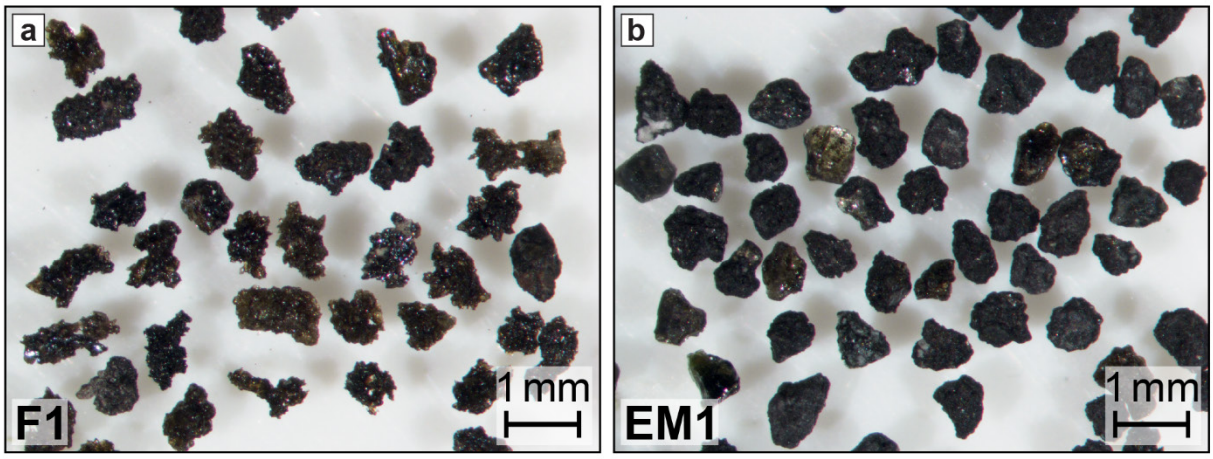

Figure 1.6: Juvenile particles extracted from (a) strombolian and (b) phreatomagmatic samples from the 1977 Ukinrek Maars eruption.

1.6.2 Magma fragmentation experiments

The study of magma fragmentation processes in this PhD project was centered on laboratory experiments involving fragmentation of remelted volcanic rocks (Zimanowski et al. 1991, 1997; Caffier 1998; Büttner et al. 1999). The complete control on the experimental setup and the up-

close video recording of the fragmentation process provide a unique insight on a phenomenon difficult to observe. The breakup mechanism observed in the experiments was linked to the generated artificial juvenile material, then compared to the natural juvenile clasts from the 1959 Kīlauea Iki eruption (Hawaii, USA) (Ritcher et al. 1970; Stovall et al. 2011; Porritt et al. 2012; Mueller et al. 2018).

The great difficulty to witness magma fragmentation dynamics during explosive natural volcanic eruptions has fostered a multitude of laboratory and even large scale experiments since the 1980s (Wohletz and McQueen 1984; Büttner and Zimanowski 1998; Büttner et al. 1999, 2002, 2006; Zimanowski et al. 1991, 1997, 2015). For this PhD project, laboratory experiments on magmatic fragmentation were performed at the *Physikalisch Vulkanologisches Labor* (PVL) of Würzburg University, Germany. The facility consists of many elements, enabling to perform several types of experiments and measure a multitude of physical parameters (Sonder et al. 2006; Austin-Erickson et al. 2008; Ross et al. 2008; Hobiger et al. 2011; Dürig and Zimanowski 2012; Dürig et al. 2012a). Below, only those elements relevant to the experiment setup used in the investigation are mentioned (Fig. 1.7):

- A magma analog is produced in an induction furnace. This consists of a water-cooled base support, on which a 5 cm (inner diameter) steel crucible is mounted. An induction coil powered by a 100kW AC power generator surrounds the crucible, which hosts the granulated volcanic material, providing the heat required to remelt the sample within about one hour (Fig. 1.7a);
- Once ready, the magma is fragmented by violently injecting compressed argon gas to simulate a lava fountain;
- About above and beyond the induction furnace, a partial containment system is placed, consisting of metal panels. This is designed to protect the experiment room and minimize the dispersion of the fragmented material (Fig. 1.7b);
- The separate control room hosts the experiment control unit, the data acquisition system and the most expensive video recording devices that capture the fragmentation process (Fig. 1.7c, d). Cheaper cameras can be placed directly in the experiment room to film from different angles.

The first experimental session was carried out over two weeks in February 2017, using the “blowout type” setup (Büttner et al. 2006). In this configuration, compressed argon (500 cc at 10 MPa) initially blocked by a solenoid valve was suddenly allowed through a hole at the base of the crucible. The gas pressure buildup pushed the ~ 200 g magma mass upwards,

triggering fragmentation both inside and outside the crucible by various processes (Büttner et al. 2006) (Fig. 1.8a). A high speed camera recorded the free-air expansion of the fragmented magma at 2000 frames per second (fps).

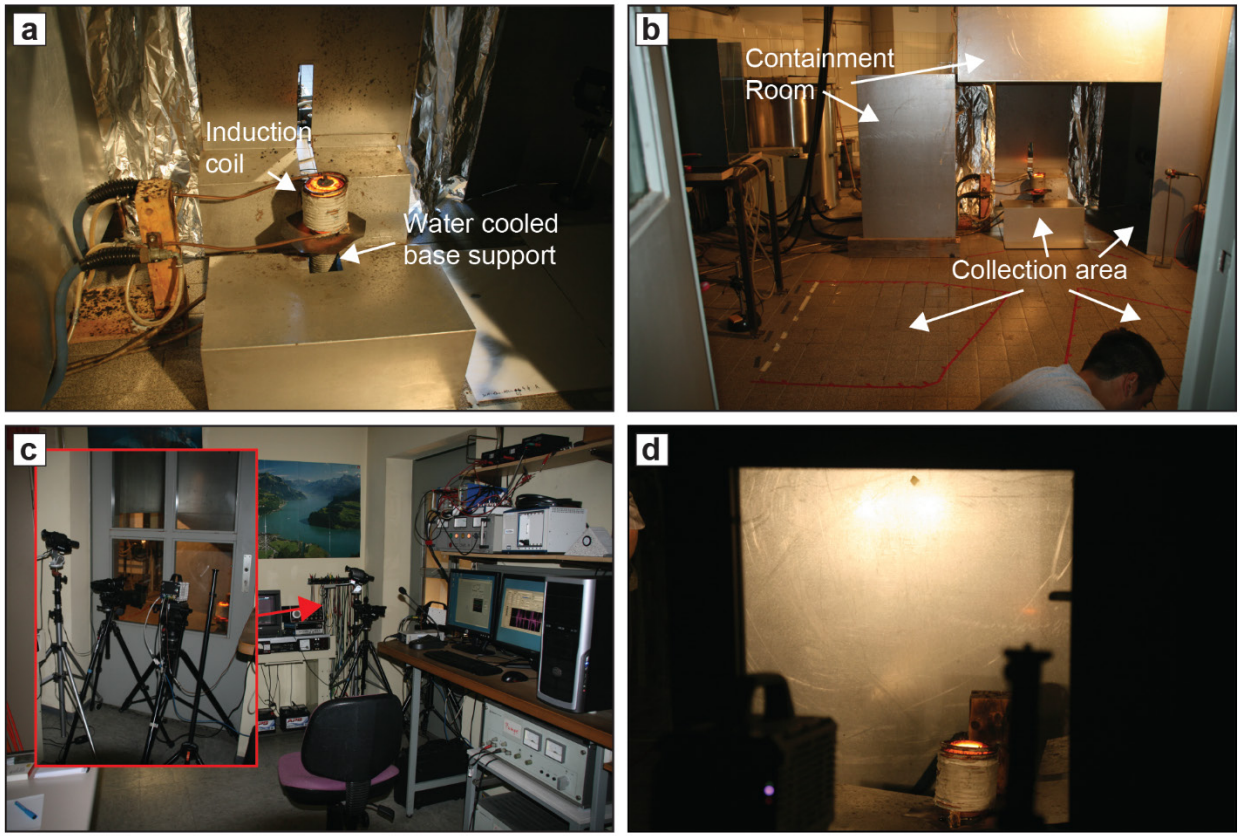

Figure 1.7: Main elements of the experimental facility: (a) Induction furnace; (b) Containment room and collection area; (c) Control room with close up of the video recording system; (d) View of the crucible area from the control room.

The second experimental session lasted two weeks in July 2017, using the “injection type” setup (Zimanowski et al. 1997). In each run, about 250 g of the granulated sample was placed inside the steel crucible, which in this setup had no hole at the bottom. Once the material was completely molten, pressurized argon at 3 MPa was injected directly inside the magma through a J-shaped steel pipe operated by a linear servo drive, resulting in a rapid expulsion and fragmentation similar to the blowout-type (Fig. 1.8b), but at lower pressure (and exit velocity). The free-air expansion phase was recorded by the high speed camera at 5000 fps.

For both setups, a range of sensors recorded the repulsion force, seismic waves, etc. with a very high sampling rate. Artificial pyroclasts were very careful collected after each experiment.

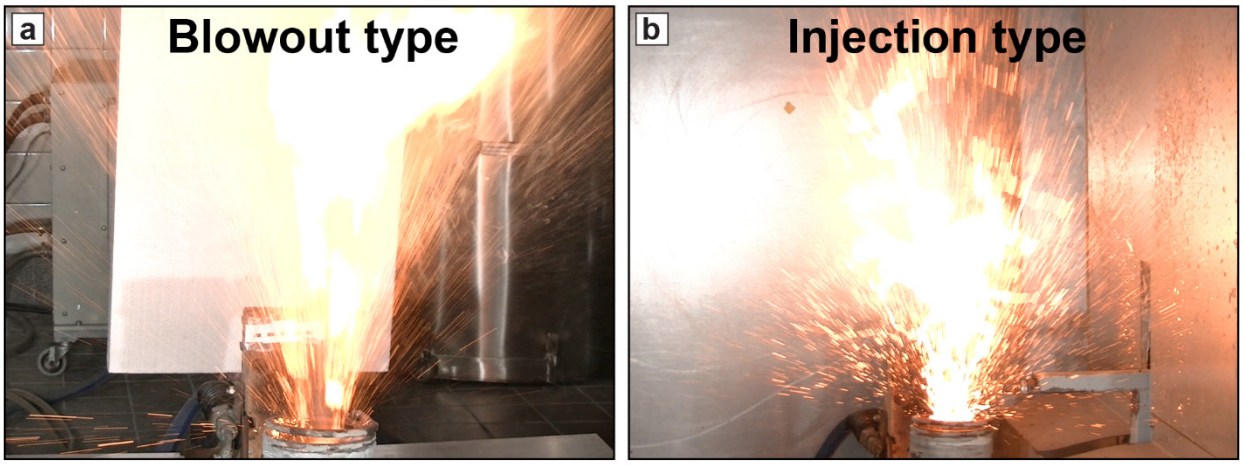

Figure 1.8: Expulsion and fragmentation of the magma during the experiments: (a) blowout type setup used in the first session; (b) injection type setup used in the second session. For scale, the diameter of the induction coil is about 12 cm.

1.6.3 Artificial pyroclasts

The pyroclastic material of six successful runs was selected to be used in the study of primary fragmentation in lava fountains (Fig. 1.9).

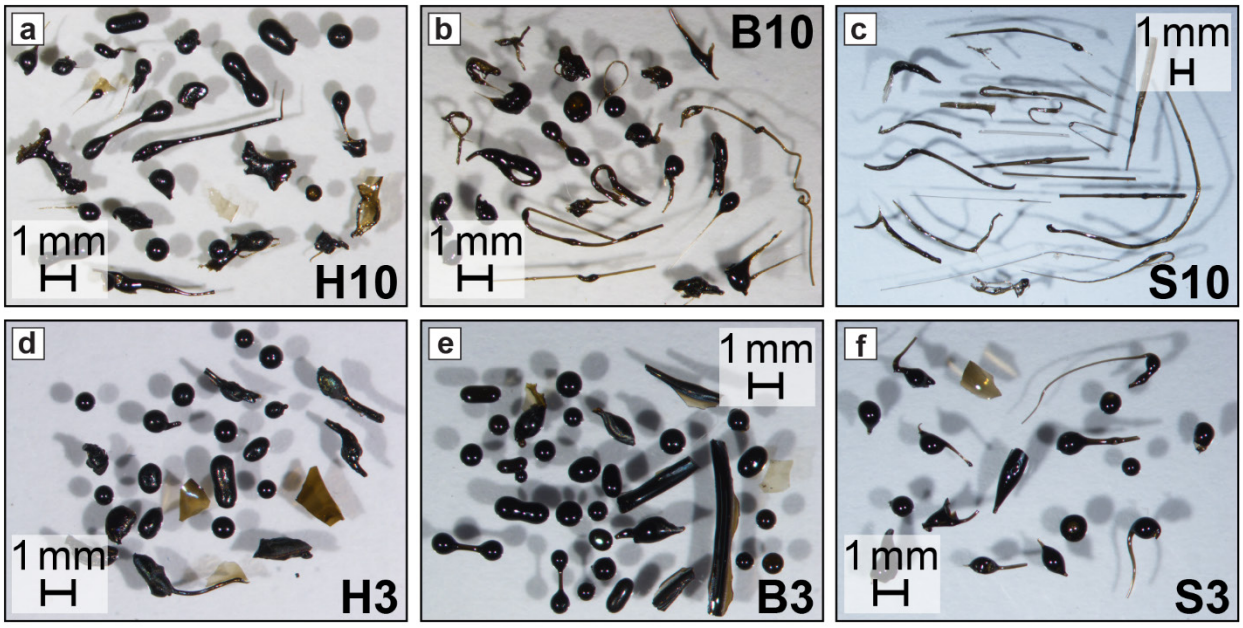

Figure 1.9: Selection of artificial pyroclasts generated from the experiments: (a) Hohenstoffeln 10 MPa run; (b) Billstein 10 MPa run; (c) Sommata 10 MPa run; (d) Hohenstoffeln 3 MPa run; (e) Billstein 3 MPa run; (f) Sommata 3 MPa run.

The tested volcanic material spans from ultramafic to intermediate in composition: i) Hohenstoffeln, a dense olivine-melilitite with ~ 38 wt.% SiO_2 from the homonymous lava lake in the Tertiary Hegau volcanic field, Germany (Zimanowski et al. 1997; Hobiger et al. 2011); ii)

Billstein, a thick and dense alkaline basalt lava flow with ~ 45 wt.% SiO_2 from the Rhön volcanic field, Germany (Zimanowski et al. 2004); iii) Sommata, a basaltic trachyandesite lapilli-size scoria deposit with ~ 54 wt.% SiO_2 from the island of Vulcano in the Aeolian archipelago, Italy (Büttner et al. 2002; Hobiger et al., 2011; De Astis et al. 2013). For each composition there is a high and low ejection speed endmember sample, the 10 MPa (Fig. 1.9a, b, c) produced during the first experimental session and the 3 MPa (Fig. 1.9d, e, f) produced during the second experimental session. Regardless of the run, all samples consist of non- to poorly-vesicular achneliths, either because the magmas were always dense since the starting material was itself dense and water-free, or because bubbles were lost during the remelting process.

1.6.4 Natural pyroclasts from Hawaii

The natural pyroclasts used for comparison with the experiments come from the 1959 Kīlauea Iki eruption. This eruption was characterized by 17 episodes of lava fountaining (Ritcher et al. 1970; Stovall et al. 2011; Porritt et al. 2012; Mueller et al. 2018). Initial fissural activity at ten vents gradually focused to one main vent, forming the > 60 m-high, Pu‘u Pua‘i cone. Lava fountains reached up to 580 m in height (Stovall et al. 2011), accompanied by lava flows which filled the Kīlauea Iki pit crater with a thick lava lake. The three pyroclastic samples used in this study (Fig. 1.10) come from the fallout blanket dispersed SW from the active vents by prevailing winds. The samples are a combination of different episodes, characterized by glassy achneliths, scoria and pumiceous juvenile pyroclasts with a sub-alkaline basalt composition (~ 49 wt.% SiO_2).

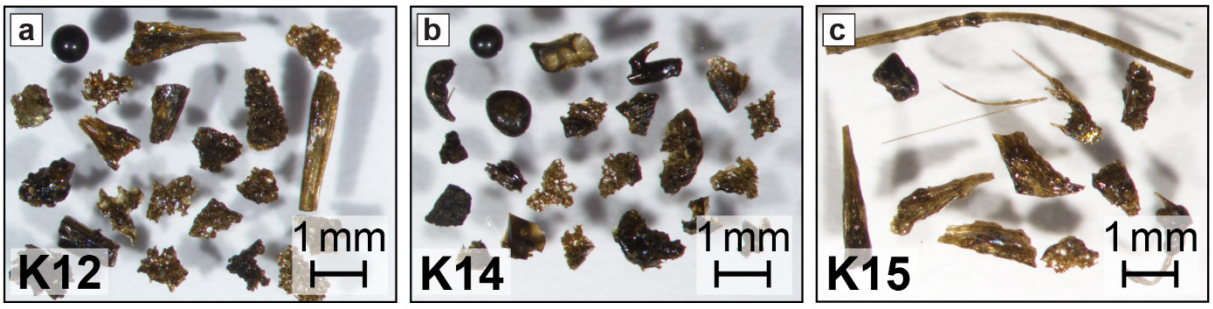

Figure 1.10: Selection of natural pyroclasts from the 1959 Kīlauea Iki eruption: (a) sample Ki-03-12, (b) sample Ki-03-14, (c) sample Ki-03-15.

1.7 Thesis organization

Five main chapters compose the dissertation. The present Chapter 1 is the general introduction, while chapters 2, 3 and 4 are the three journal manuscripts. Chapter 5 is the general conclusion, connecting the findings from each manuscript, as well as highlighting the wider relevance of the

study of juvenile morphologies and primary magma fragmentation processes. Since chapters 2–4 were each conceived to be standalone journal manuscripts, there is a small degree of repetition, mostly in the methods sections. Due to the limited number of words allowed for submission of manuscripts to journals, two papers have supplementary materials, which are inserted at the end of the relevant chapters, where possible.

Chapter 2, to be read in conjunction with Appendix I, is a contribution to the development of a standardized methodology for comparative studies of juvenile pyroclasts. It deals with the choice of the best size fraction for studying juvenile pyroclasts in cross-section, the manufacture of PEGMs, imaging parameters, and the presentation of the newly developed Particle Shapes & Textures Analyzer (PASTA) package (Comida and Ross 2021). Chapter 3 focuses on hydrodynamic magma breakup in the experiments, specifically the different regimes of liquid jet breakup. It compares experiments to natural lava fountains. Chapter 4 explores what controls primary juvenile morphologies in lava fountains, linking magma breakup processes and the cooling history to the pyroclasts collected in the experiments as a way to understand the more complex heterogeneity observed in nature.

1.8 Contribution of the authors to the publications

Chapter 2 has been accepted by Bulletin of Volcanology with the title “Standardized analysis of juvenile pyroclasts in comparative studies of primary magma fragmentation; 2. Choice of size fraction and method optimization for particle cross-sections”, by P.P. Comida (PPC), P.-S. Ross (PSR), T. Dürig (TD), J.D.L. White (JW) and N. Lefebvre (NL). It is part 2 of a group of two manuscripts on juvenile pyroclasts. Part 1 by Ross et al. is entitled “Standardized analysis of juvenile pyroclasts in comparative studies of primary magma fragmentation; 1. Overview and workflow” and is presented in Appendix I. PSR, TD and NL developed the early concept of the standardized methodology, with contributions of PPC, JW, Daniele Andronico, Simon Thivet, Julia Eychenne, and Lucia Gurioli.

For chapter 2, PPC carried out hand sieving and ultrasonic cleaning with the help of Caroline Belanger (CB). PPC performed juvenile particle selection, imaging at the binocular microscope, image refinement and processing. PPC developed the procedure to manufacture the PEGMs with initial input from Ikbel Mouedhen and Philippe Girard, and the conversion from CTGM to PEGMs for the very fine ash fraction. PPC performed both PEGM and CTGM preparation and imaging at the SEM, as well as the EDS chemistry. PPC developed the PASTA package for the processing of SEM images of juvenile particle cross-sections and silhouettes, with revision and improvements

by PSR. PPC, Felix Gagnon (FG), CB and Sarah Galloway performed image processing on the SEM images. PSR, TD, NL and JW revised and improved the manuscript.

Chapter 3 is ready to submit to Journal of Volcanology and Geothermal Research with the title "Liquid jet breakup regimes in lava fountains" by PPC, PSR, Bernd Zimanowski (BZ), Ralf Büttner (RB) and Ingo Sonder (IS). BZ and RB designed and performed the fragmentation experiments, with the help of Nico Spitznagel (NS). PPC and PSR investigated the video recordings, and reviewed the literature on jet breakup, with an early input from IS. PPC and PSR wrote the manuscript. BZ, RB and IS revised and improved the manuscript.

Chapter 4 is ready to submit to Bulletin of Volcanology with the title "Controls on juvenile ash morphologies in lava fountains: insights from laboratory experiments" by PPC, PSR, BZ, RB, and Tobias Dürig (TD). BZ and RB designed and performed the fragmentation experiments, with the help of NS. PPC collected the samples after each experiment run, with the help of PSR. PPC prepared the samples, carried out mounting of PEGMs and CTGMs, and subsequent imaging and chemistry check at the SEM-EDS. PPC and FG carried out juvenile selection and imaging at the binocular microscope of the coarse ash for componentry. PPC performed image acquisition at the SEM. PPC and FG prepared particle images which were then processed by PPC. PPC and PSR performed data analysis, data interpretation and worked on several versions of the manuscript. BZ, RB and TD reviewed and improved the manuscript.

2 FIRST ARTICLE: STANDARDIZED METHODOLOGY

Standardized analysis of juvenile pyroclasts in comparative studies of primary magma fragmentation; 2. Choice of size fraction and method optimization for particle cross-sections

Analyse standardisée des pyroclastes juvéniles dans les études comparatives de la fragmentation primaire du magma; 2. Choix de la fraction granulometrique et optimisation de la méthode pour les sections polies

Authors:

Pier Paolo Comida[1], Pierre-Simon Ross[1], Tobias Dürig[2], James D.L. White[3], Nathalie Lefebvre[4]

1. Institut national de la recherche scientifique, 490 rue de la Couronne, Québec (Qc), G1K 9A9, Canada

2. Institute of Earth Sciences, University of Iceland, Sturlugata 7, 101 Reykjavík, Iceland

3. Department of Geology, University of Otago, 360 Leith Street, Dunedin 9016, New Zealand

4. ETH Zurich, Institute of Geochemistry and Petrology, Clausiusstrasse 25, 8092 Zurich, Switzerland

Title of the journal:

Bulletin of volcanology

Accepted: 16 November 2021

DOI: 10.1007/s00445-021-01517-5

This chapter is the accepted version of the research article:

Comida PP, Ross P-S, Dürig T, White JDL, Lefebvre N (2021) Standardized analysis of juvenile pyroclasts in comparative studies of primary magma fragmentation; 2. Choice of size fractions and method optimization. Bull Volc.

2.1 Abstract

The morphological and textural features of juvenile pyroclasts record crucial details on magma conditions at the time of fragmentation. Their study is therefore essential to better understand the dynamics of explosive eruptions. Unfortunately, the absence of a standardized protocol of investigation hinders data reproducibility and comparison among different laboratories. Here we focus on morphometric parameters, 2D crystallinity and 2D vesicularity resulting from cross-section analysis of juvenile particles using backscattered electron imaging, and address the following questions: i) how to prepare polished epoxy grain mounts; ii) which pixel density to be used; iii) how to facilitate image preparation and image analysis; iv) which sample size is necessary to obtain statistically robust results; v) what is the optimum size fraction for analysis. We test juvenile particles in grain size bins ranging from 2–1 mm (- 1 to 0ϕ) to 88–63 µm (+ 3.5 to + 4ϕ), using samples from the 1977 Ukinrek eruption. We find that the required resolution ranges from 10 000 to 75 000 pixels per particle, depending on the size fraction, higher than previously postulated. In the same size ranges, less than 50 grains per size fraction and sample are needed to get robust averages. Based on theoretical, empirical and practical considerations, we propose 0.71–0.5 mm (+ 0.5 to + 1ϕ) as the optimum size fraction to be analyzed as particle cross-sections in standardized comparative studies of magma fragmentation. We provide a detailed guide for preparing polished epoxy grain mounts and introduce a software package (PASTA) for semi-automated image preparation, image processing and measurement of morphological and textural parameters.

2.2 Introduction

Juvenile particles in pyroclastic deposits preserve key information on fragmentation mechanisms (e.g., Dellino and La Volpe 1996; Zimanowski et al. 1997; Cioni et al. 2014; Jordan et al. 2014; Rausch et al. 2015; Verolino et al. 2019; Dürig et al. 2020a, 2020b, 2020c) and on the state of magma at the time of fragmentation (e.g., Heiken 1972; Heiken and Wohletz 1985; Freundt and Rosi 1998; Lautze and Houghton 2007; Rust and Cashman 2011; Dürig and Zimanowski 2012; Liu et al. 2017). This knowledge is important for understanding eruptive processes, including those that produce hazardous activity (Dellino et al. 2012; Leibrandt and Le Pennec 2015; Avery et al. 2017). Specific morphological features, particle surface features and internal textures (related to crystals and bubbles) can be measured, and the ash range is typically targeted (e.g., Dellino and La Volpe 1996; Büttner et al. 1999; Bagheri et al. 2015; Liu et al. 2017). Yet, despite decades of research on juvenile particles, a standard methodology of analysis does not yet exist

for comparative studies. Differences between laboratories include the choice of imaging device (scanning electron microscope (SEM), micro-CT, automated particle imager, other microscope or device), which particle size to use, whether to use silhouettes or particle cross-sections, which morphometric parameters are best, what statistical methods to perform, etc. (e.g., Dellino and La Volpe 1996; Büttner et al. 2002; Leibrandt and Le Pennec 2015; Liu et al. 2015; Dürig et al. 2018; Dürig et al. 2021). Also, particle shapes have often been measured independently of particle surface features and internal textures (Cioni et al. 1992; Rausch et al. 2015; Liu et al. 2017).

The lack of a standardized methodology to study juvenile particles means that data from different laboratories and different volcanoes cannot be integrated and directly compared. We therefore propose, in two papers, a standardized methodology for comparative studies, which can be discussed and refined during an international workshop. In the first paper, Ross et al. (2021) (Appendix I) give an overview of the whole workflow, which includes standard steps and recommended steps (Figs. A1.1 and A1.2 in Appendix I). Initial standard steps include fieldwork, sampling, geochemistry and sieving (Fig. 2.1). Further standard steps are tailored for each recommended cleaned size fraction, as follows: i) for the 0.71–0.5 mm ash size fraction (+ 0.5 to + 1ϕ) (see White and Houghton 2006 for definition of grain size terms), basic componentry, juvenile selection, preparation of polished epoxy grain mounts (PEGMs), imaging of the particle cross-sections with an SEM and measurements of morphometric parameters, 2D vesicularity, and 2D crystallinity; ii) for the 88–63 µm (+ 3.5 to + 4ϕ) grains, dual mounting (both carbon tape and polished epoxy) of the bulk size fraction, imaging twice at the SEM, basic componentry on particle cross-sections, searching for interactive particles, and measurement of morphometric parameters on juvenile particle silhouettes.

This paper focuses on particle cross-sections imaged with an SEM and completes the standardized methodology proposal by providing information on the following topics not covered in detail in Appendix I (Fig. 2.1):

(1) The method for preparing a standard PEGM;
(2) The SEM magnification and image resolution needed to obtain enough pixels per particle, to ensure stable average values of morphometric parameters, 2D crystallinity and 2D vesicularity;
(3) The minimum number of particles required to obtain statistically robust averages for morphometric parameters, vesicularity and crystallinity;
(4) The process for automating image preparation and image analysis as much as possible, and which manual steps are still needed to obtain good results;

(5) The rationale for choosing the 0.71–0.5 mm (+ 0.5 to + 1ϕ) size fraction as the best compromise for determining both morphometric parameters and internal textures.

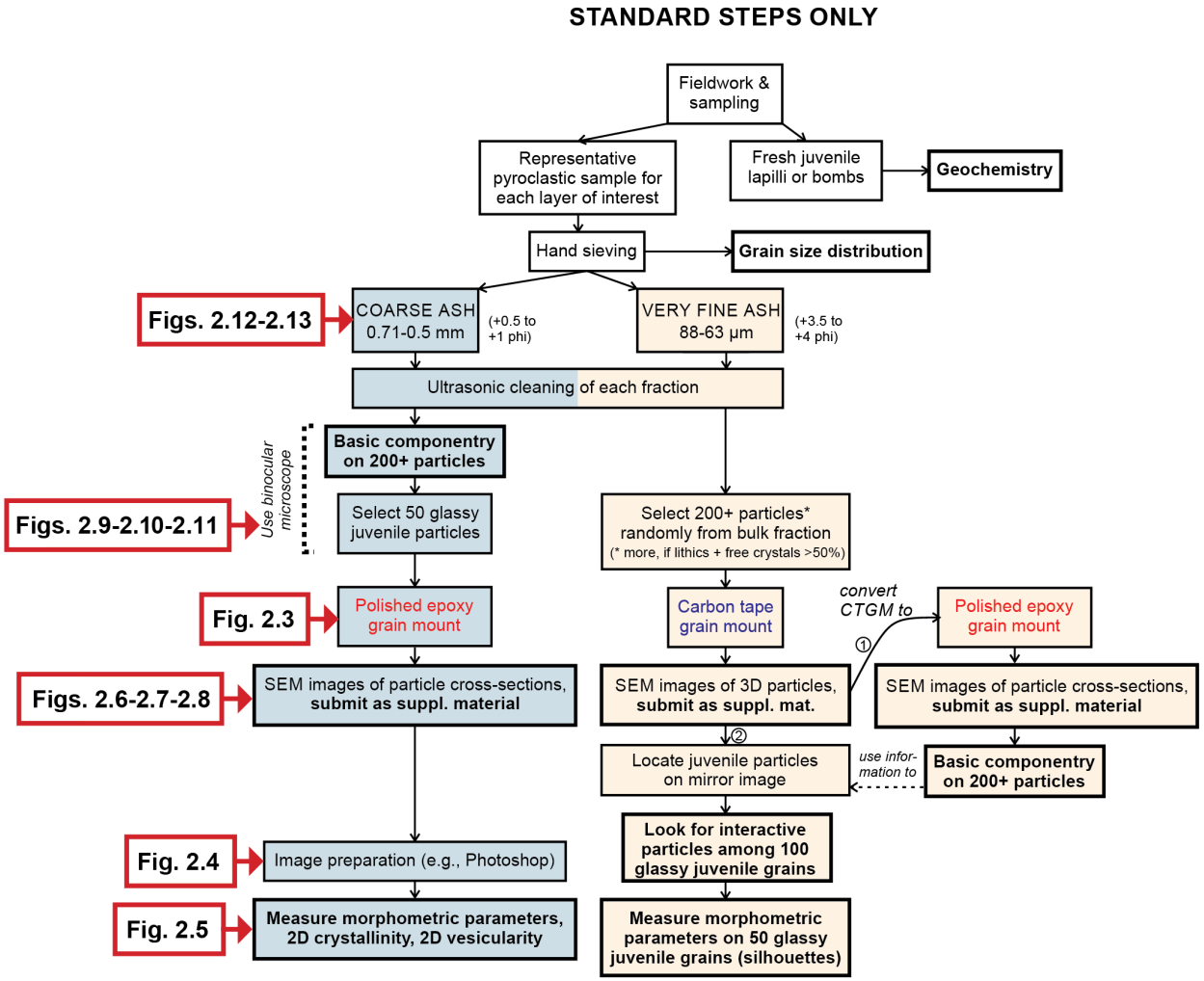

Figure 2.1: Expanded version of the standard steps from Appendix I highlighting the contributions detailed in this work.

In order to assess the best size fraction to use for juvenile particle cross-sections in fragmentation studies, we measured morphometric parameters and internal features on size fractions from 2–1 mm (- 1 to 0ϕ) to 88–63 µm (+ 3.5 to + 4ϕ), on natural basaltic samples, derived from both magmatic and phreatomagmatic fragmentation. As detailed in the manuscript, the investigation ultimately led to the choice of the 0.71–0.5 mm (+ 0.5 to + 1ϕ) as one of the three size fractions proposed in the standardized methodology (Appendix I). Image preparation and analysis has many steps, and details have often been lacking in previous publications. We explain our methods in detail and present semi-automated scripts to save the user as much time as possible.

2.3 Background

2.3.1 Imaging methods and strategies

The study of shapes and textures of juvenile pyroclasts is carried out on particle images. These images can be obtained with particle sizing and imaging devices, with a SEM, or with micro-CT methods (Schipper et al. 2013; Vonlanthen et al. 2015; Dioguardi et al. 2017; Mele and Dioguardi 2018; Mele et al. 2018). Unfortunately, results based on different imaging systems may not be comparable (Appendix I and references therein). The present contribution focuses on SEM-BSE (backscattered electron) imaging of particle cross-sections, which allow both morphometric parameters and internal textures to be assessed from the same images.

The resolution and magnification of a SEM-BSE image are critical parameters to obtain reliable and comparable measurements. Previous workers have recommended 750 to 5000 pixels per particle for shape measurements, mainly in the 125–63 μm (+ 3 to + 4ϕ) size fraction (Dellino and La Volpe 1996; Dürig et al. 2012; Liu et al. 2015). The larger value has also been considered optimum for coarse ash grains (Mele et al. 2011). We show below that this range is probably insufficient for obtaining stable values for the combination of crystallinity, vesicularity, and morphometric parameters.

Two imaging strategies are possible when internal textures are important: (1) collect images at a high enough resolution or (2) progressively increase the magnification in a nesting strategy (Shea et al. 2010a). In this study, we determine the imaging settings that are sufficient to quantify both the shape and internal texture from one image, preferably containing multiple particles, to minimize total SEM time.

2.3.2 Sample preparation

To acquire SEM-BSE images of particle cross-sections, the grains are usually embedded in epoxy resin, ground down to expose the grain interiors. This ground epoxy 'briquette' can be mounted to a glass slide, thinned and polished to make a polished thin section, or it can simply be polished to produce the grain mount (PEGM). Published papers rarely describe sample preparation in detail, but there are several steps in the manufacture of PEGMs/polished thin sections, and these play a critical role in obtaining a 2D cross-section representative of the whole particle. Particularly important are the orientation of a grain relative to the polishing surface, and the extent of grinding/polishing which controls the area size of the grain exposed. Moreover, under pressure

and/or under vacuum embedding may be necessary for vesicular grains with fine vesicles, as epoxy-filled vesicles will have a better chance to be preserved during grinding and polishing.

2.3.3 Number of particles to image

Another important parameter to be assessed is the number of grains needed to obtain statistically robust results for morphometric and textural measurements, for a given size fraction in a sample. Previous studies have used particle numbers spanning several orders of magnitude (e.g., Durant et al. 2009: 100 000 particles; Cioni et al. 2008: 30 particles), as well as different size fractions and image acquisition systems. For example:

- Liu et al. (2015) suggested 1000–2000 grains for the 125–63 μm (+ 3 to + 4ϕ) fraction as the optimum number to achieve stable morphometric parameter averages. Their test was based on particle cross-sections imaged with an SEM.
- Leibrandt and Le Pennec (2015) recommended 150 and 2000 grains for the 1.0–0.5 mm (0 to + 1ϕ) and 125–63 μm (+ 3 to + 4ϕ) size fractions, respectively, using an automated optical particle analyzer (i.e., a modified version of an optical microscope) to measure morphometric parameters on silhouettes.
- Dürig et al. (2018) suggested a minimum number of 50 grains for obtaining statistically robust averages in morphometric analyses of particle silhouettes, imaged with an SEM.
- Mele and Dioguardi (2018) performed 3D X-ray microtomography on 30 fallout pyroclasts spanning a size range between 16–8 mm (- 4 to - 3ϕ) and 63–31 μm (+ 4 to + 5ϕ), belonging to three different eruptions of Campi Flegrei (Italy). The particles were morphometrically parameterized by using 3-dimensional morphometric parameters, such as fractal dimension, sphericity or (3D) shape factor (Dioguardi et al. 2017).

2.3.4 Image preparation and analysis

The analysis of particle images has benefited from the advancement in computer technology over the last decades. Liu et al. (2015) provided a macro code for the image processing software ImageJ (Schneider et al. 2012) that allows measurement of a set of morphometric parameters on 2D particle cross-sections. The required input is a stitched binary image containing multiple particles.

Another macro code for the same software package was developed by Hornby (2018), which measures both shapes and internal textures. This technique relies on false color QEMSCAN®

multi-particle images, manually converted to one binary image per feature (e.g., vesicles, crystal phase 1, crystal phase 2, glass, etc.).

Dürig et al. (2018) introduced PARTISAN, a script for Matlab© which measures, in its newest version (Dürig and Bowman 2021), 23 non-dimensional morphometric parameters, based on five different morphometric systems by Dellino and La Volpe (1996), Cioni et al. (2014), Leibrandt and Le Pennec (2015), Liu et al. (2015) and Schmith et al. (2017). The required input consists of binarized SEM images acquired from particle silhouettes, with each image containing only one particle.

In all three cases cited above, the codes require “ready to use” binary images of single or multiple particles. Obtaining these images involves either (i) manual stitching and thresholding of several SEM images (for the Liu et al. code); (ii) an expensive and proprietary data acquisition system and some manual processing (for the Hornby code); or (iii) manual separation and generation of single particle images (for the Dürig et al. code). None of the scripts available in the literature enables a quick, automated and inexpensive generation of single particle binary images, neither do they produce single particle image files showing a ready-to-quantify internal texture such as crystallinity or vesicularity.

2.4 Methods

2.4.1 Origin of tested material

The natural juvenile pyroclasts used here come from the Ukinrek Maars (Alaska), which erupted in 1977 and emitted alkaline basalt (Kienle et al. 1980). The whole event lasted for about 11 days and formed two maars (west and east, Kienle et al. 1980) preceded by fissural activity southeast of the west maar (Ort et al. 2018). We selected two end-member samples for this study: a phreatomagmatic one and a strombolian one. Both samples were chosen from very proximal units, to minimize transport effects on particle morphology. They were taken from deposits representing the beginning of an eruptive episode, to avoid recycled pyroclasts.

The strombolian sample comes from a juvenile-rich fallout deposit linked to the initial fissural activity (F1 unit, Ort et al. 2018). Juvenile ash is brown to black scoria, characterized by irregular shapes (Fig. 2.2a). Following the classification of Houghton and Wilson (1989), juvenile clasts are incipiently to moderately vesicular (5–60%). Vesicle sizes range from about 10 µm to over 1 mm across (Fig. 2.2b), and vesicles are often connected in 3D. Crystals (including phenocrysts of all sizes and microlites) are moderately to highly abundant (typically ~ 40–80% in coarse ash-sized

juvenile clasts) (Fig. 2.2b). Olivines are the largest phenocrysts (250 µm – 1.5 mm), have euhedral to anhedral shapes, and are commonly characterized by edge resorption (Fig. 2.2b). Inclusions of glass and oxides are common within the olivines. Magnetite crystals are euhedral, ranging from about 3 to 50 µm across. Anorthite-rich plagioclase microphenocrysts are the second largest population. They are euhedral to subhedral and 15–650 µm across, embedded in a sideromelane-bearing groundmass.

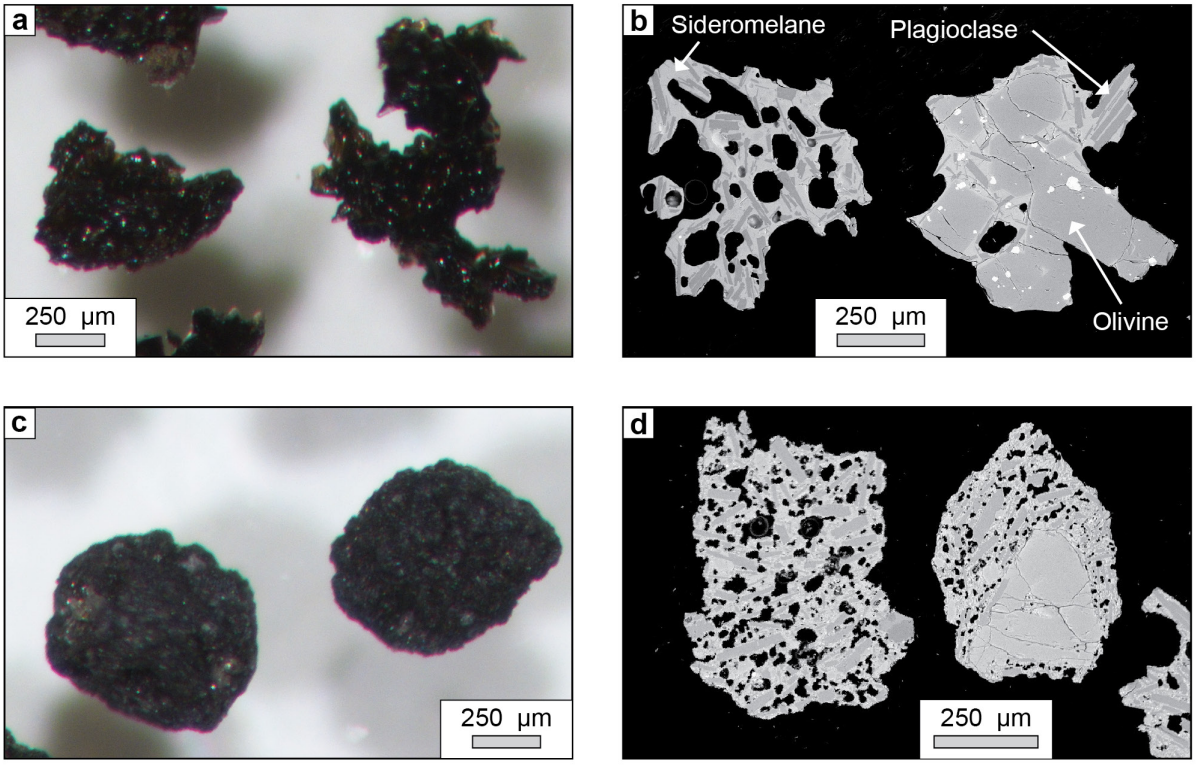

Figure 2.2: Representative images of juvenile particles from the two basaltic Ukinrek test samples. For each sample, both binocular microscope (left) and SEM-BSE particle cross-sections views (right) are presented: (a-b) strombolian; (c-d) phreatomagmatic.

The phreatomagmatic sample comes from the lithic-rich PDC unit at the base of the East Maar ejecta ring (EM1 unit of Ort et al. 2018). Juvenile clasts have generally sub-equant shapes (Fig. 2.2c). Vesicles are isolated, subround to amoeboid (5–600 µm), and the coarse ash-sized juvenile clasts are poorly to highly vesicular (~ 30–60%). Crystallinity is high (> 50%), with similar minerals as in the strombolian sample, and the groundmass is tachylitic (Fig. 2.2d).

2.4.2 Overview of the standardized protocol and of the present study

In the companion paper, Ross et al. (2021) (Appendix I) present a standardized protocol for the analysis of juvenile pyroclasts for comparative studies of primary magma fragmentation, and their

standard steps are shown in Fig. 2.1. Two main size fractions are included in the flowchart: 0.71–0.5 mm (+0.5 to +1ϕ) and 88–63 μm (+ 3.5 to + 4ϕ). Juvenile particles from the 0.71–0.5 mm (+0.5 to +1ϕ) fraction are made into a PEGM, from which morphometric parameters and internal textures can be determined for each grain, based on particle cross-sections. The bulk 88–63 μm (+ 3.5 to + 4ϕ) fraction is prepared as a carbon tape grain mount, imaged, and then converted to a PEGM and imaged again. This allows determination of basic componentry, morphometric parameters, and surface features for juvenile grains. To reach this simplified protocol, we first needed to determine which size fraction is optimal for the joint measurement of morphometric and textural parameters. Therefore, for each of our two samples we prepared PEGMs for five size fractions between 2–1 mm (- 1 to 0ϕ) and 88–63 μm (+ 3.5 to + 4ϕ), and then measured morphometric parameters and internal textures.

This size range includes the most popular size fractions considered in the literature for fragmentation studies (Dellino and La Volpe 1996; Büttner et al. 1999; Cioni et al. 2014; Jordan et al. 2014; Leibrandt and Le Pennec 2015; Liu et al. 2015 and references therein). The particles between 2–1 mm (- 1 to 0ϕ) and 88–63 μm (+ 3.5 to + 4ϕ) should also be small enough to have cooled very rapidly after fragmentation, hence preserving particle shapes related to fragmentation, and crystals and bubbles representing the state of magma at the time of fragmentation (Porritt et al. 2012; D'Oriano et al. 2014).

2.4.3 Preparing the size fractions

2.4.3.1 Sieving

The Ukinrek samples arrived pre-sieved into full ϕ fractions. The 2–1 mm (- 1 to 0ϕ), 0.5–0.25 mm (+ 1 to + 2ϕ) and 0.25–0.125 mm (+ 2 to + 3ϕ) fractions were utilized as is. We further narrowed the other two fractions using half ϕ sieves, yielding 0.71–0.5 mm (+ 0.5 to + 1ϕ) and 88–63 μm (+ 3.5 to + 4ϕ) fractions; unfortunately, other half-phi sieves were not available at INRS when this work was done. While comparing full ϕ and half ϕ fractions in the same study is not ideal, the dataset presented here still allows us to optimize the methodology in terms of image preparation and image analysis, pixel density for each grain, how many grains are needed, and what is the optimum size fraction for analysis. It also allows the demonstration that morphometric and textural parameters vary with grain size, as also shown by previous studies.

2.4.3.2 Ultrasonic cleaning

Particles from each size fraction were cleaned to remove adhering fine dust using an ultrasound bath at low intensity in cycles of 1 minute, for a total time of 3 minutes, using distilled water, and subsequently dried at 60°C. These short cleaning cycles without the use of aggressive chemicals should minimize damage to the grains.

2.4.3.3 Juvenile clast selection

Natural samples contain a mixture of juvenile and lithic clasts, but only juvenile grains are to be used for magma fragmentation studies. In this study we selected hundreds of grains per sample and per size fraction, much more than were eventually needed, since one of the goals was to find out the minimum number grains needed to obtain statistically reliable averages. Manual hand picking of juvenile clasts under the binocular microscope was feasible for the size fractions 2–1 mm (- 1 to 0ϕ) to 0.5–0.25 mm (+ 1 to + 2ϕ), requiring up to 20 minutes for every 50 juvenile grains selected. The 0.25–0.125 mm (+ 2 to + 3ϕ) and 88–63 µm (+ 3.5 to + 4ϕ) juvenile grains were also picked under the binocular microscope, but it was a time-consuming task, taking over 1 hour to yield about 100 juvenile grains. This was due to static electricity and physical limitations of the picking tools, which set a size limit for this kind of technique. Electrostatic charge effects often resulted in unwanted picking of lithics along with juvenile particles. Any remaining lithics were mounted along with the juveniles, only to be excluded later from the analysis, based on SEM imagery. Because of these practical problems with selecting very small juvenile fragments under the binocular microscope, and because it is impossible to be certain that each picked fragment is indeed juvenile, the standardized protocol calls for dual mounting of the bulk fraction for the 88–63 µm (+ 3.5 to + 4ϕ) particles (Appendix I).

2.4.4 Polished epoxy grain mounts

Imaging of particle cross-sections with an SEM necessitates PEGMs or polished thin sections. The PEGM manufacturing procedure developed as part of this study is summarized here and fully explained in Online Resource 2.1.[1]

The juvenile grains were first placed on a very flat surface lined with double-sided tape (Fig. 2.3a), using different methods depending on the size fraction considered. For the coarser fractions 2–1

[1] Online resource 2.1 is inserted at the end of Chapter 2

mm (- 1 to 0ϕ) to 0.5–0.25 mm (+ 1 to + 2ϕ), the grains were mounted one by one on the tape (Fig. 2.3b).

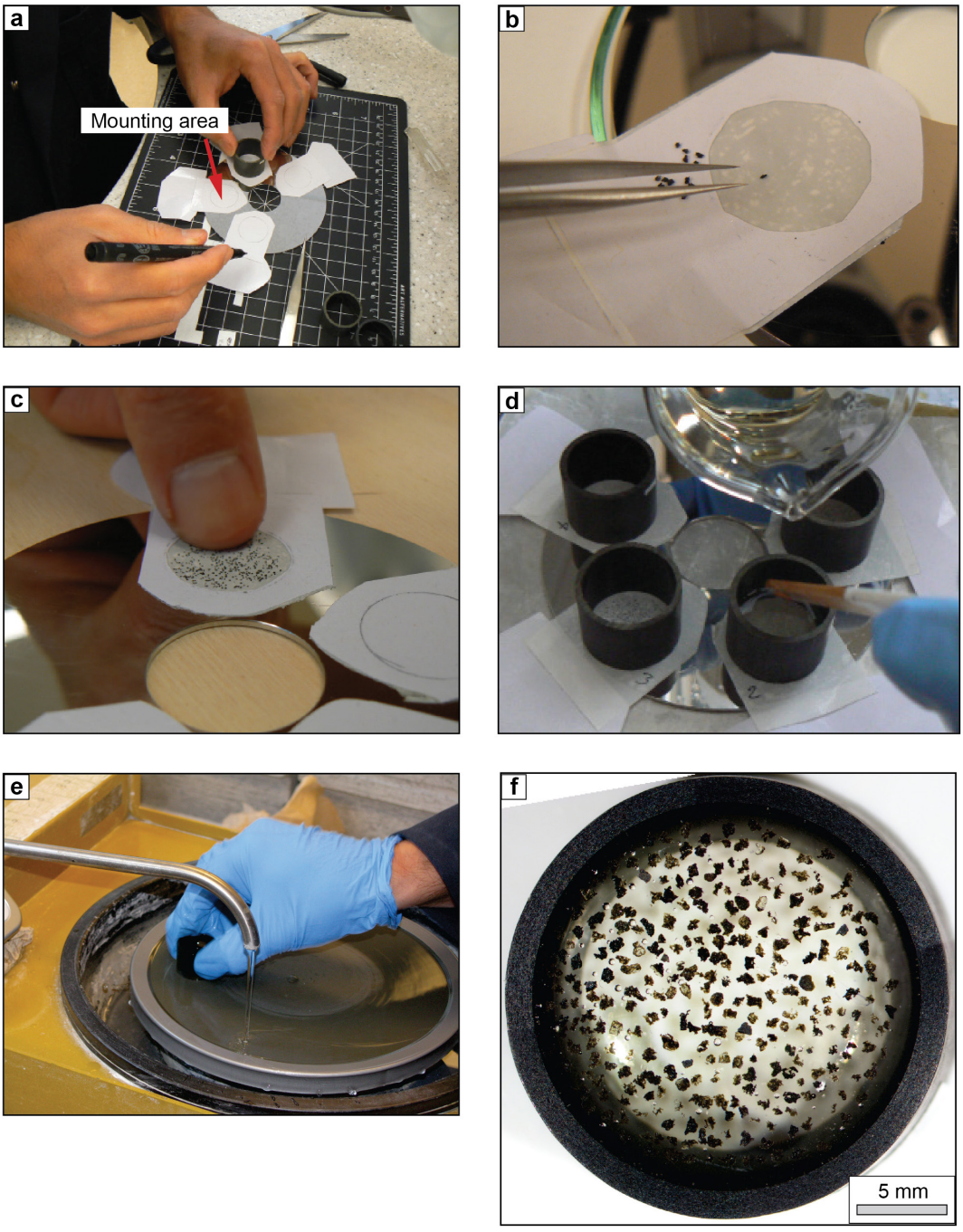

Figure 2.3: Preparing a polished epoxy grain mount. (a) Placing the double-sided tape on a hard drive platter and marking the mounting area. The ringform is 1 inch (2.54 cm) in diameter. (b) View of particle transfer method for coarser particles (size fractions 2–1 mm or - 1 to 0ϕ, to 0.5–0.25 mm or + 1 to + 2ϕ). (c) View of "thumb" particle transfer method for finer particles (size fractions 0.25–0.125 mm or + 2 to + 3ϕ, and 88–63 µm or + 3.5 to + 4ϕ). (d) Pouring the epoxy into the ring form. (e) View of the grinding stage with abrasive paper. (f) The finished PEGM under the binocular microscope (strombolian sample from Ukinrek, 0.71–0.5 mm or + 0.5 to + 1ϕ).

Particles were positioned to have their two longest axes parallel to the PEGM examination surface.

For the finer fractions 0.25–0.125 mm (+ 2 to + 3ϕ) to 88–63 µm (+ 3.5 to + 4ϕ), the material was first spread in a petri dish and then transferred to the mounting area using the “thumb method”. A lightly moistened thumb was very gently pressed on a particle-rich portion of the petri dish, mimicking a fingerprint capture gesture. The movement was repeated on the exposed sticky surface of the mounting support until enough particles were transferred (Fig. 2.3c). In order to avoid contamination and prevent finger marks on the tape, the use of a latex/nitrile finger cot or glove is suggested. The cylindrical molding case was subsequently placed into position, then the blended epoxy mixture was poured into each mold and left to cure overnight within a vacuum chamber in order to ensure vesicle infilling by epoxy needed to avoid breakage during sectioning and imaging (Fig. 2.3d). The flat mounting surface was then detached.

Grinding and polishing of each mount aimed to expose the center of the smallest juvenile fragments in each size fraction. For example, for the 2–1 mm (- 1 to 0ϕ) fraction, we removed 0.5 mm of material, starting from the side on which the grains had been deposited. The grinding and polishing must be done very carefully to preserve the particle shapes in cross-section, as well as to minimize the formation of fractures and ablation of the mounted grains. Based on the equipment available at INRS (Institut national de la recherche scientifique, Canada), we settled on up to three grinding steps and two polishing steps, using a mix of abrasive paper and fine suspensions (Fig. 2.3e). A typical final product is shown in Fig. 2.3f, containing more grains than needed.

2.4.5 Image acquisition

Au/Ir-Pd coated PEGMs were imaged at INRS using a Zeiss EVO 50 SEM in BSE mode. Images for each sample were acquired using an optimum working distance of 8.5 mm, while magnification, image resolution and scan speed were adjusted relative to the size fraction, as explained in a later section. Further focus adjustments were unique to each PEGM because of the slightly different final thicknesses attained during polishing.

The time and number of images that were involved in scanning a whole PEGM increased for finer size fractions, because larger magnifications were necessary to capture finer details, ranging from 20–25 images for 2–1 mm (- 1 to 0ϕ) and up to about 100 images for 88–63 µm (+ 3.5 to + 4ϕ) PEGMs. For the size fraction and the number of grains that we recommend for standardized comparative magma fragmentation studies, i.e. 0.71–0.5 mm (+ 0.5 to + 1ϕ) and 50 juvenile grains (see discussion), about three images would be needed for each sample if all particles were

grouped relatively closely together in the PEGM. In this case, the total imaging time would be about 10 minutes.

Brightness and contrast were set to provide a good separation in terms of greyscale intensity both between the resin and the particle edge, and between the particle groundmass, crystals and vesicles. This is an essential pre-requisite for the image processing methodology developed in this work. All images from the same sample should ideally have comparable grey levels for the same features. For example, olivine crystals should always have a similar darkness. At the SEM, this can be better achieved by disabling the automatic adjustment of brightness and contrast when moving to the next acquisition area. Keeping the initial image open helps the operator ensure that subsequent images look similar. The groundmass often includes both microlites and glass, and it is sometimes difficult to distinguish them from a single particle or multi-particle image. A typical solution would be to zoom on the groundmass, but this is not a standard step in the figure 2.1 flowchart, as we are aiming for a bulk estimate of the crystallinity and therefore we are not using a nesting strategy. The image file format should be non-compressed (e.g., TIFF), to preserve original scan quality.

2.4.6 Image preparation and measurements

Image preparation and analysis was undertaken using a combination of semi-automated processing and manual refinement. An image preparation stage was done in a raster graphics editor (here Adobe Photoshop©). This was followed by a processing and measurement stage in a scientific image analysis software (Fiji, Schindelin et al. 2012). Scripts which partially automate some of the steps were developed for both stages in order to save time and are available online as the PArticle Shapes & Textures Analyzer (‘PASTA’) project (Comida and Ross 2021). The package includes detailed step-by-step user guides for both image preparation in Photoshop© and image processing in Fiji, with a much shorter overview provided below.

2.4.6.1 Image preparation stage

SEM images have to be prepared (enhanced) before morphometric parameters and internal textures can be measured (Shea et al. 2010b). Image preparation accomplishes the following: (1) making sure that the juvenile particle outlines are perfectly selected (Figs. 2.4a–2.4c); (2) keeping only juvenile fragments not touching the edges, eliminating lithic fragments and free crystals that escaped the juvenile selection process, and replacing the inter-particle background with a uniform color (Figs. 2.4d–2.4e); (3) for each multi-particle image, optionally improving the contrast

between different internal features, such as crystals versus groundmass (Figs. 2.4f–2.4g); (4) for each juvenile fragment, blackening the vesicles and “repairing” obvious flaws, such as larger cracks (Figs. 2.4g–2.4h).

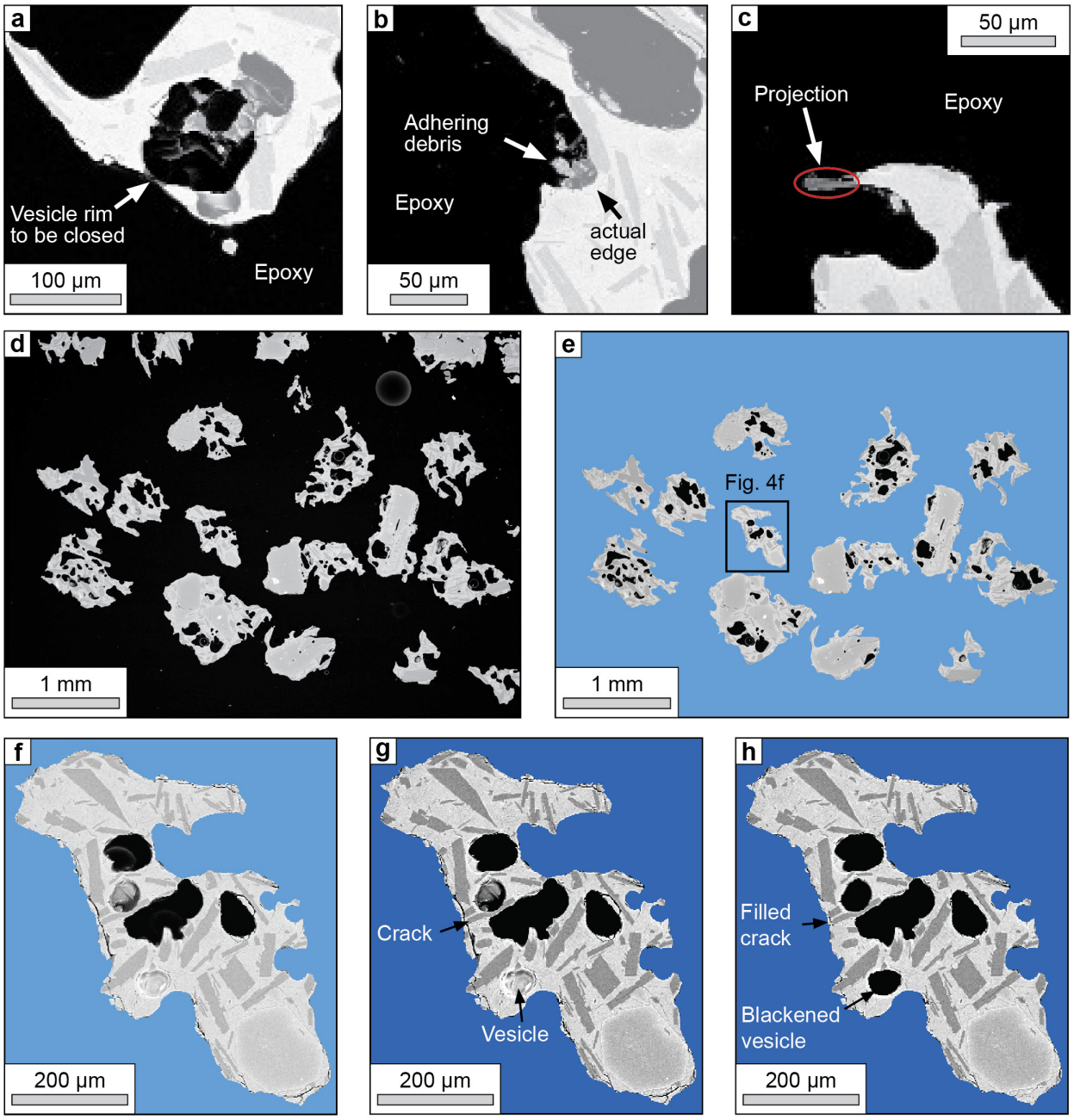

Figure 2.4: Image preparation in Photoshop©. (a) Closing vesicles. (b) Removing adhering debris misinterpreted as particle edge. (c) Including thin projections in the particle outline. (d) A typical image of the 0.71–0.5 mm (+ 0.5 to + 1ϕ) fraction in BSE mode (same Ukinrek strombolian sample as in Fig. 2.2b). (e) Replacing the background with a uniform blue color and deleting particles touching the edge of the image (as well as those that are obviously too small or inferred to be lithics). (f) Zoom on one of the juvenile particles from Fig. 2.4e, internal texture unrefined. (g) Appearance of Fig. 2.4f if the contrast between crystals and glassy groundmass is enhanced on Fig. 2.4e by adjusting the grey levels. (h) Manually blackening vesicles and filling the cracks.

Since certain kind of fractures might be important to recognize specific fragmentation-related processes such as thermal granulation (Colombier et al. 2019), the user could create a copy of the images to optionally study fractures, while using the other copy with repaired cracks to carry out standard textural measurements. The end products of the image preparation stage are multi-particle images containing only complete juvenile particles on a uniform background. These particles are characterized by well-defined edges and well-contrasted internal features.

2.4.6.2 Processing and measurement stage

The Fiji script portion of PASTA allows the semi-automated processing and measurement of morphometric parameters, 2D crystallinity and 2D vesicularity of juvenile particles. Settings are optimized for BSE-SEM images of particle cross-sections, but morphometric parameters can also be measured on particle silhouettes. The code features a Graphical User Interface (GUI) with detailed instructions which results in only a small amount of straightforward user input. The script executes three main steps: (1) isolating single particles; (2) image processing; (3) measurements and saving the results (Fig. 3 in the PASTA user guide, Comida and Ross 2021).

Step 1. Isolating single particles is required for multi-particle images, since processing must be done on images containing one particle only. The script does this automatically for the entire batch of multi-particle images in the input folder.

Step 2. Image processing involves a series of operations that generate images directly suitable for measuring morphometric parameters and/or internal features. For morphometric parameters, a binary image is created, with a single black particle on a white background (Fig. 2.5a).

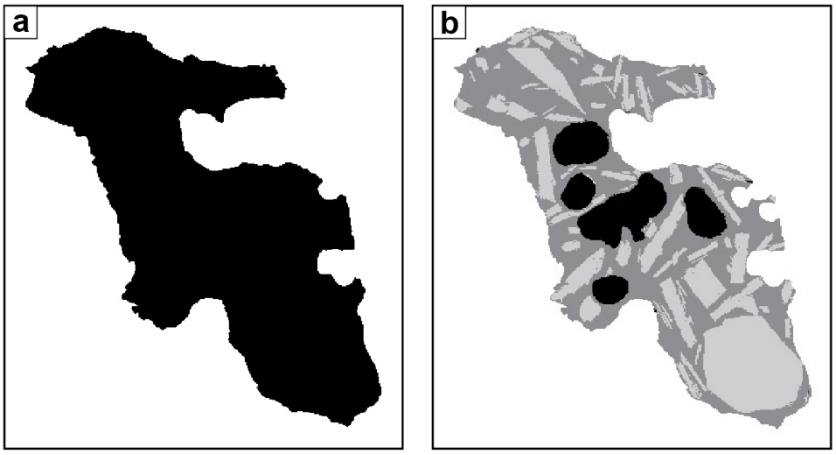

Figure 2.5: Final image outputs of the PASTA script for Fiji. (a) View of the binary image file generated to measure shape parameters. (b) View of the false-color segmented greyscale image generated to measure 2D crystallinity and 2D vesicularity.

For internal features (i.e., crystallinity and vesicularity), false-color segmented images are generated, with arbitrary greyscale intensities identifying the grey levels representing groundmass, crystals and vesicles, on a white background (Fig. 2.5b). During image segmentation, the user selects which internal features are to be extracted, what minimum size to use for each crystal or vesicle, and enters personalized labels (Fig. 7 upper half in the PASTA user guide, Comida and Ross 2021). Based on tests and in general agreement with previous studies (Shea et al. 2010a), we suggest a minimum (default) size of 4 pixels for vesicles and oxides, and 20 pixels for grey crystals. Such minimum values yield relatively clean refined images while accurately depicting internal features without underestimating their relative abundance.

For each selected feature (e.g., vesicles or plagioclase crystals) the minimum and maximum grey levels are identified using a representative area on a representative image (Fig. 8 in the PASTA user guide, Comida and Ross 2021). If a feature is not found on the current image (e.g., no vesicles present), the user can view other images. Once the optimum threshold values are inserted (Fig. 7 lower half in the PASTA user guide, Comida and Ross 2021), the final generation of the segmented images might occur either one particle at a time or as a batch for the whole stack of images, depending on user preference.

Step 3a: measurements. For shape parameters, PASTA uses a modified version of the Liu et al. (2015) code. PASTA batch-processes a stack of single particle binary images (e.g., Fig. 2.5a) for an entire sample. To obtain other morphometric parameters such as those of Dellino and La Volpe (1996), Cioni et al. (2014), Leibrandt and Le Pennec (2015), and Schmith et al. (2017), the PARTISAN script from Dürig et al. (2018) can be used on the single particle binary images extracted by PASTA. These morphometric parameters have been chosen for their capability to highlight different morphological characteristics, and to distinguish ductile from brittle fragmentation, as detailed in Appendix I.

2D vesicularity and 2D crystallinity are calculated as the number of black (vesicle) and grey (crystal) pixels divided by the total surface area of the particle, respectively, on the false-color segmented images (e.g., Fig. 2.5b). In the future, we hope to provide the proportions of different crystal types as well, for each clast. The code could also be expanded to provide vesicle size distributions or crystal size distributions.

Step 3b: save results. Results may be saved as a csv file (by default) and/or exported as a Microsoft Excel© file. The current output parameters include particle area, particle perimeter, area and perimeter of the convex hull bounding the particle, axial ratio, solidity, convexity, form factor, 2D vesicularity (both in pixels and %), and 2D crystallinity (both in pixels and %).

2.4.7 Finding the best image resolution and magnification

The number of pixels per particle (pixel density) needed to get stable values of morphometric parameters and internal textures is a function of both image resolution and SEM magnification. In our tests, we replicated the Liu et al. (2015) approach to determine the necessary pixel density but included 2D crystallinity and 2D vesicularity along with the morphometric parameters. The idea is to define a typical pixel number that stabilizes the values for each morphometric and textural parameter in a number of individual particles. The strombolian sample from Ukinrek was used for these tests. For each size fraction, we selected four juvenile particles spanning the full range of crystallinity and vesicularity (i.e., minimum and maximum vesicularity; minimum and maximum crystallinity). Each particle image was initially acquired at a high magnification using the highest resolution available (i.e., 3072*2304 pixels), then progressively downsampled in Photoshop© by digitally decreasing the resolution by one-third intervals. The full image preparation and analysis described above was run on each resolution, for each endmember particle. A particular effort was made to avoid operator bias related to possible memory effect, alternating different particles after each manual refinement.

2.4.8 Choice of parameters to find the optimum size fractions

To quantify particle morphology, the companion paper (Appendix I) suggests two sets of morphometric parameters: i) three of the shape parameters suggested by Liu et al. (2015) and measured with PASTA: axial ratio, solidity and convexity; ii) the four morphometric parameters introduced as “IPA (image particle analysis) parameters” by Dellino and La Volpe (1996), i.e. circularity, rectangularity, compactness and elongation. The IPA parameters, measured here with PARTISAN (Dürig and Bowman 2021), were compared in pairs following Dürig et al. (2018), that is, for example, as the product of elongation times circularity and rectangularity times compactness. The first pair shows well the deviations from equant shapes, whereas the latter emphasizes morphological and textural roughness variations present in the particle outline. These morphometric parameters, along with 2D crystallinity and 2D vesicularity measurements obtained with PASTA, were used to assess critical aspects in the development of the methodology, as described in the next section. All measurements on the particles used in this study are available in Online Resource 2.2. All raw SEM images are available online from the Zenodo.org data repository (Comida et al. 2021b).

2.5 Results

2.5.1 Optimum pixel density for image analysis

For each clast studied, the measured values of morphometric and textural parameters are dependent on pixel density (number of pixels per particle) (Figs. 2.6, 2.7). For example, 2D crystallinity values of individual grains typically increase with pixel density, stabilizing beyond 70 000 pixels per particle for the 2–1 mm (- 1 to 0ϕ) size fraction, beyond 20 000 pixels for the 0.71–0.5 mm (+ 0.5 to + 1ϕ) fraction, and beyond 10 000 pixels for the finer size fractions (Fig. 2.6, left). The most likely explanation is that small crystals are better resolved if more pixels are available, which is the equivalent of zooming in on the grain while keeping the image resolution constant. The trends for 2D vesicularity are partly similar, presumably because small vesicles are better resolved in better quality images, but typically, fewer pixels are needed to stabilize vesicularity than crystallinity in these samples (Fig. 2.6, right).

Convexity generally decreases when the pixel density increases (Fig. 2.7, left), because convexity depends on the inverse of perimeter, and the perimeter typically lengthens with better images (Liu et al. 2015). Convexity mostly stabilizes beyond 75 000 pixels for the 2–1 mm (- 1 to 0ϕ) grains studied, beyond 20 000 pixels for 0.71–0.5 mm (+ 0.5 to + 1ϕ), and beyond 10 000 pixels for finer size fractions. Other morphometric parameters such as solidity (Fig. 2.7, right) and axial ratio (Online Resource 2.3[2]) stabilize at much lower pixel densities, beyond 40 000 pixels for the 2–1 mm (- 1 to 0ϕ) fraction, beyond 10 000 pixels for 0.71–0.5 mm (+ 0.5 to + 1ϕ), and beyond 5 000 pixels for finer size fractions. In summary, the pixel density needed to get stable values for both morphometric parameters and internal textures ranges from 75 000 for the 2–1 mm (- 1 to 0ϕ) size fraction to 10 000 in the 88–63 μm (+ 3.5 to + 4ϕ) size fraction (Table 2.1).

2.5.2 The role of scan speed in image acquisition

When discussing SEM imaging parameters, previous studies have focused on image resolution and magnification, without mentioning another crucial feature, scan speed. This represents the speed at which the electron beam swings over the examined area of a sample. Slower scan speed means longer imaging time but a finer definition of the details of the image (Fig. 2.8a).

[2] Online Resource 2.3 appears at the end of this chapter.

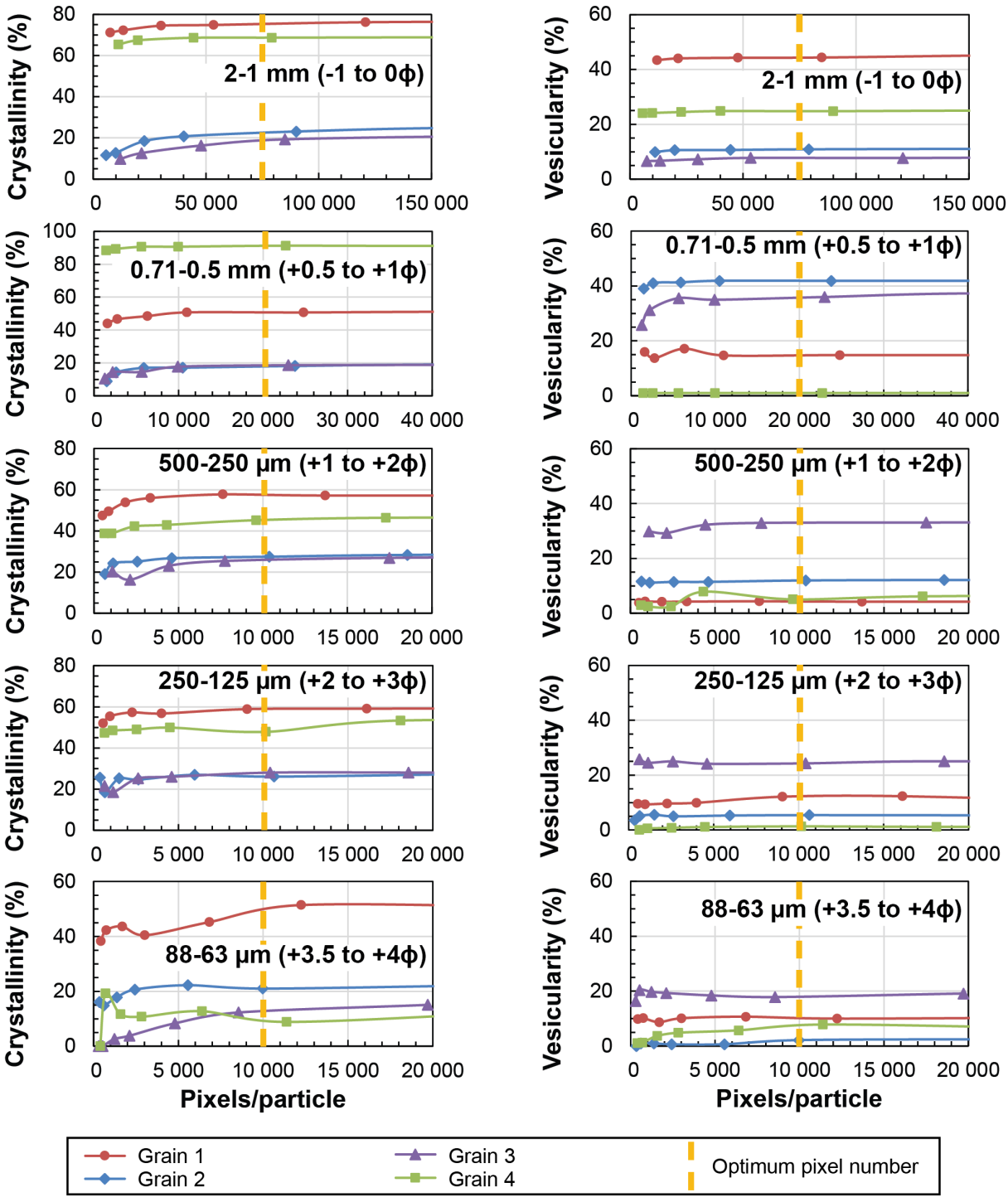

Figure 2.6: Pixel number test for 2D crystallinity and 2D vesicularity, using the Ukinrek strombolian sample. In figures 2.6 and 2.7, four grains were tested for each size fraction, covering the highest and lowest crystallinity as well as the highest and lowest vesicularity. Each trend line corresponds, within a single size fraction, to the same grain. The vertical dashed lines indicate the optimum pixel numbers for each size fraction (all parameters considered, see also Fig. 2.7).

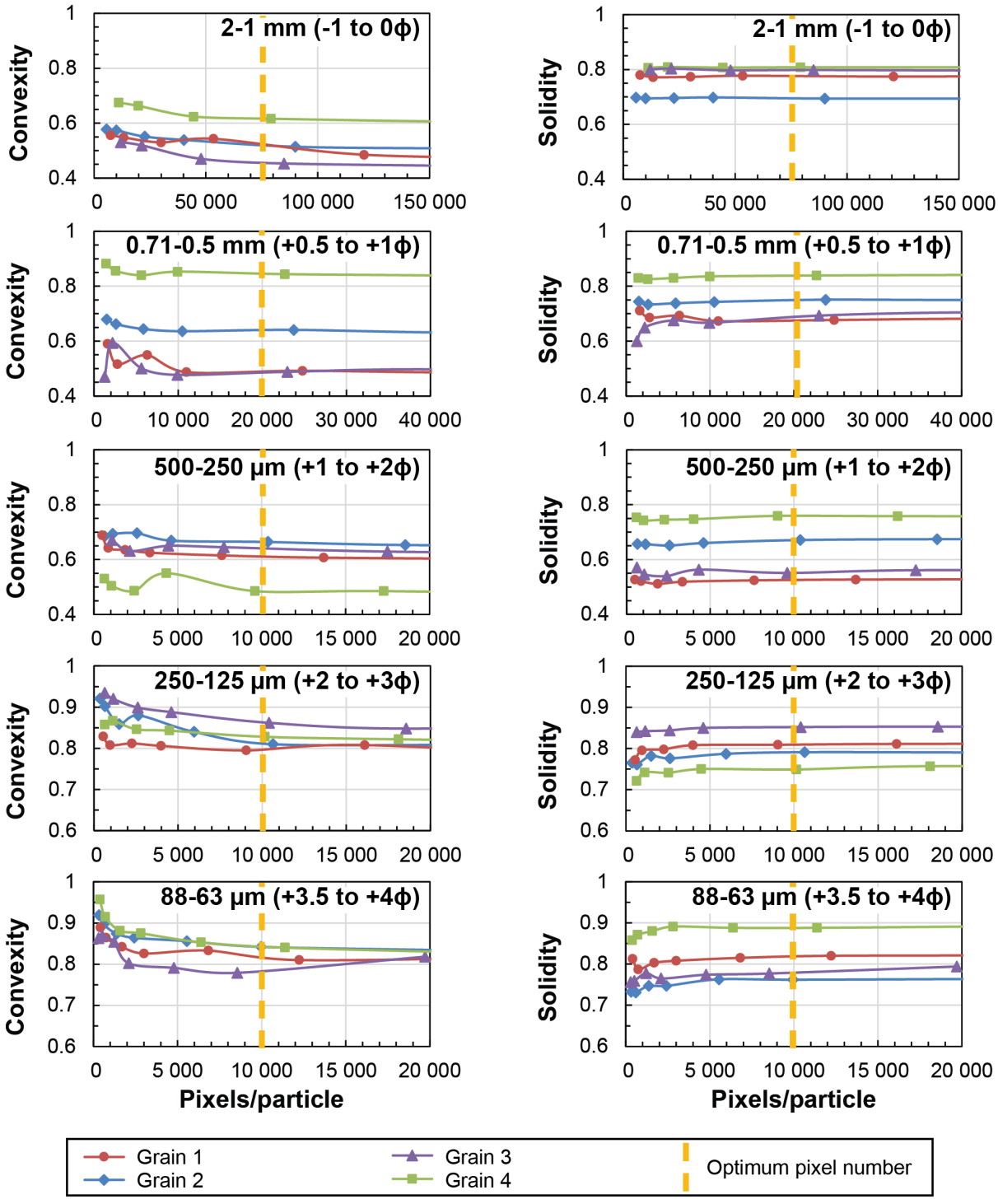

Figure 2.7: Pixel number test for convexity and solidity, using the Ukinrek strombolian sample.

On the contrary, faster scan speed will downgrade the quality of the image, thereby compromising the accuracy of shape and, especially, textural measurements (Fig. 2.8b). The optimum scan

speed provides sharp edge distinction between microlites and the glass in the groundmass, at the magnification and resolution used for the final image acquisition.

Table 2.1: Optimum values of pixels per particle (pixel density) for SEM image processing of particle cross-sections

Size fraction		Pixel density
μm	ϕ	
2000–1000	-1 to 0	75,000
710–500	+0.5 to +1	20,000
500–250	+1 to +2	10,000
250–125	+2 to +3	10,000
88–63	+3.5 to +4	10,000

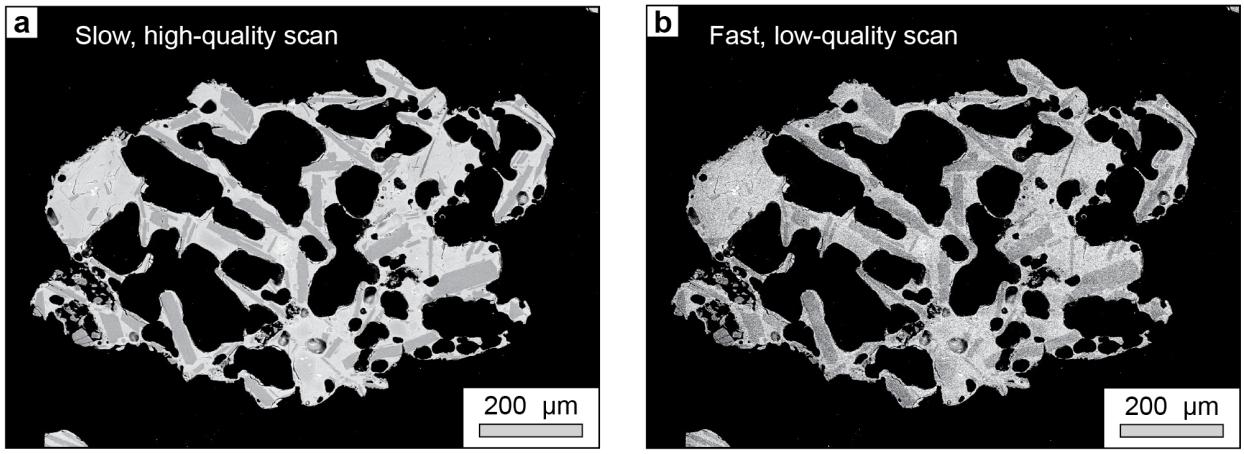

Figure 2.8: SEM-BSE images of the same particle cross-section taken at the same magnification (68X) and resolution (2048 x 1536 pixels), but different scan speeds. (a) Slow, high-quality scan (about 160 sec) (b) Fast, low-quality scan (about 5 sec).

2.5.3 Number of grains to measure

The average values of measured morphometric and textural parameters, and their representativeness, are dependent on the number of grains studied in a sample. Average values will stabilize only when a sufficient number of grains have been analyzed, depending on the heterogeneity of the sample in terms of particle shapes and internal textures. In the strombolian sample from Ukinrek, average vesicularity and crystallinity stabilize at about 20–25 grains in the

2–1 mm (- 1 to 0ϕ) size fraction, whereas it takes only around 10 grains for solidity and convexity to do so (Fig. 2.9, top).

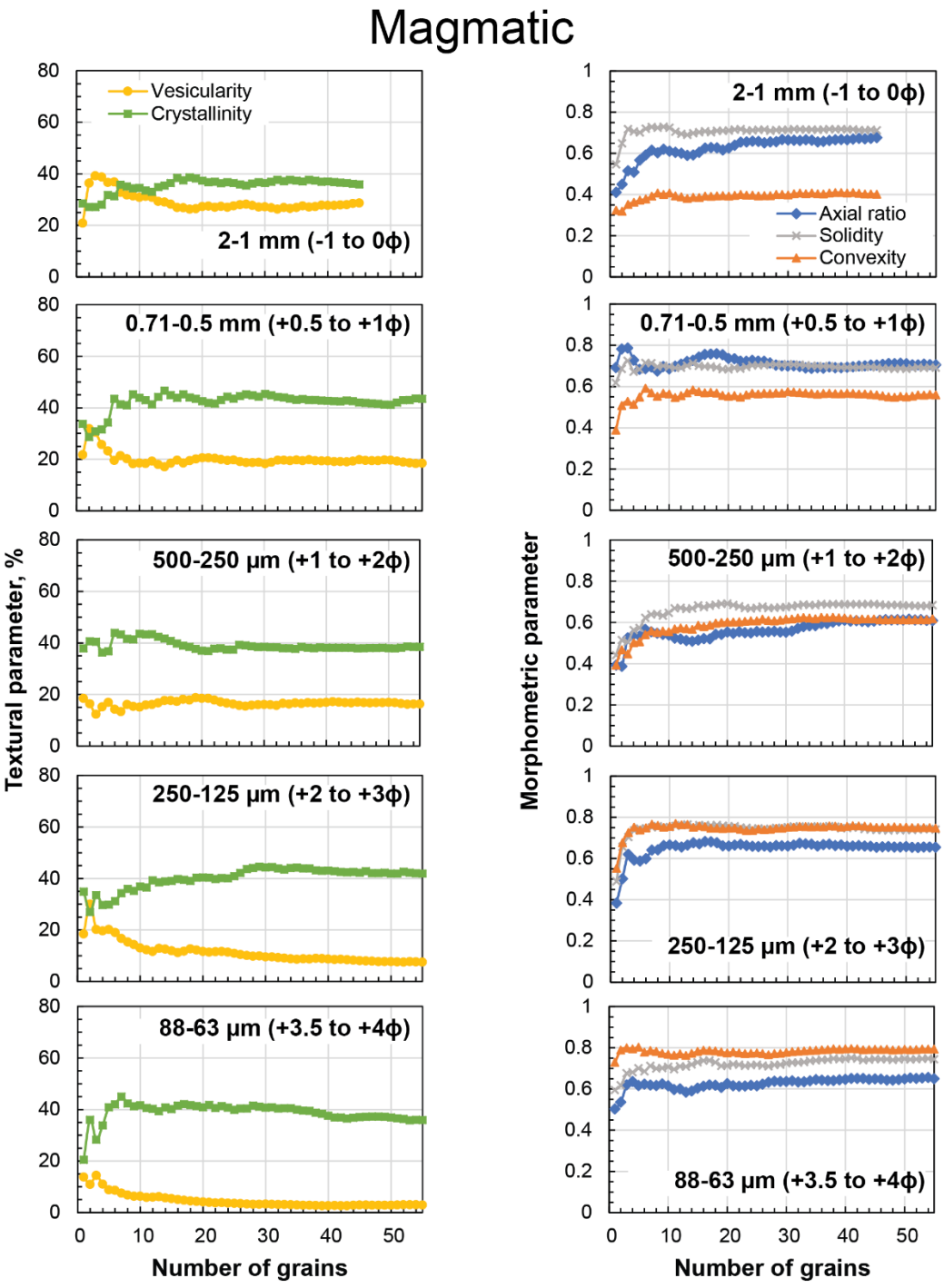

Figure 2.9: Stability test to find the optimum number of grains for each size fraction, using the strombolian sample from Ukinrek. The average values of 2D crystallinity, 2D vesicularity and three morphometric parameters stabilize as more grains are added. After filtering out the grains that were too small, more than 50 grains were measured for each size fraction except for the 2–1 mm (- 1 to 0ϕ) fraction, for which fewer grains had unfortunately been mounted.

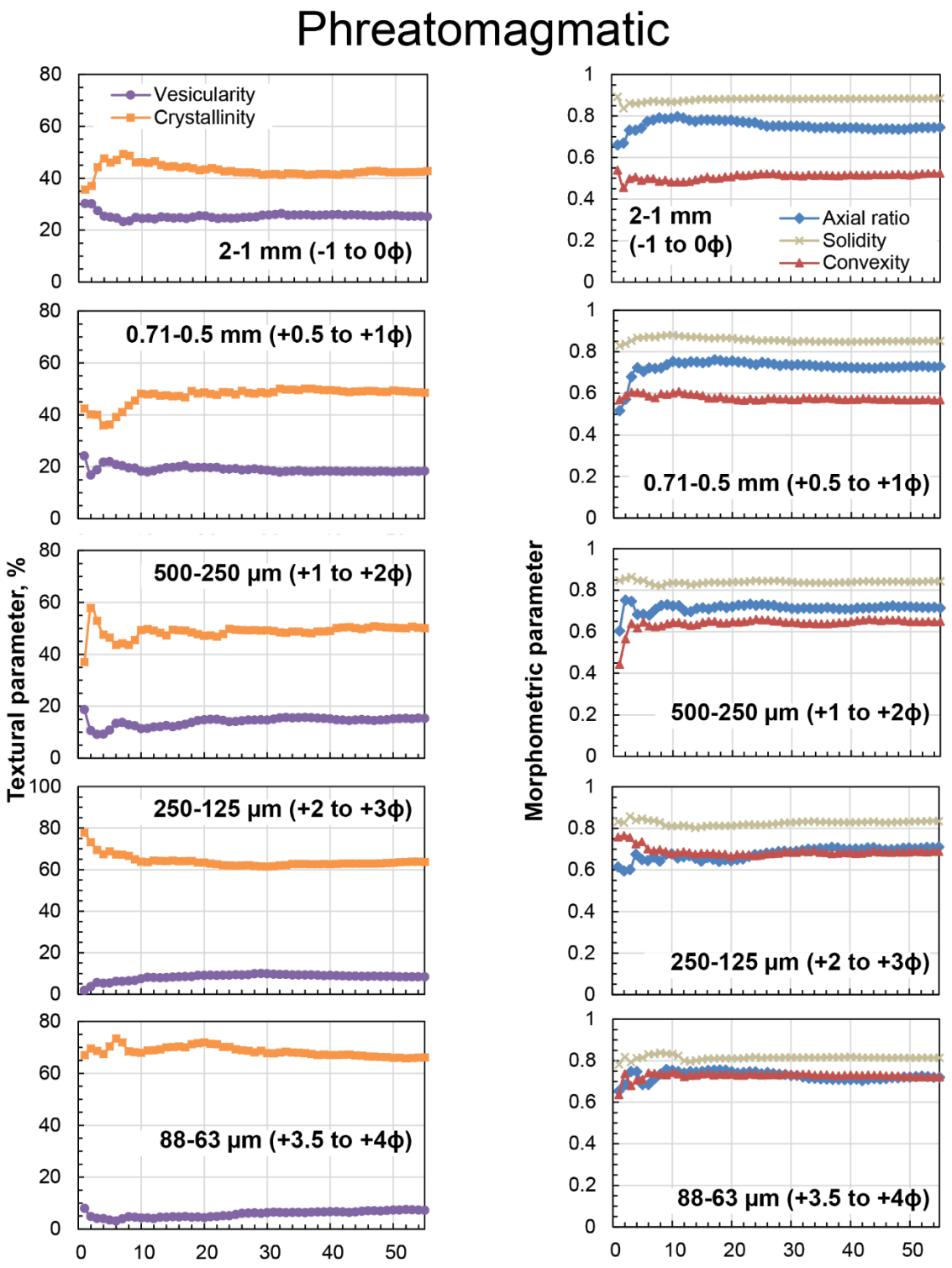

Figure 2.10: Stability test to find the optimum number of grains for each size fraction, using the phreatomagmatic sample from Ukinrek. The average values of 2D crystallinity, 2D vesicularity and three morphometric parameters stabilize as more grains are added.

In progressively finer size fractions, the number of grains generally increases to stabilize the textural parameters, reaching about 40 grains for the 88–63 μm (+ 3.5 to + 4ϕ) fraction (Fig. 2.9, bottom; Table 2.2). In the phreatomagmatic sample, the estimated number of grains needed to get stable averages for all parameters ranges from 20 grains at 2–1 mm (- 1 to 0ϕ) to 30 grains at 88–63 μm (+ 3.5 to + 4ϕ) (Fig. 2.10, Table 2.2).

Another way to estimate these minimum numbers of clasts is the "5% variation" statistical method. For each parameter, grains are progressively added to the average until the effect of adding one more grain becomes less than 5% relative difference. In both samples, this method resulted in smaller cut-offs than the visual estimate (Table 2.2).

Table 2.2: Number of juvenile fragments needed to reach a stable average in morphometric and textural parameters, as a function of grain size, for Ukinrek samples

Size fraction		Strombolian		Phreatomagmatic	
μm	ϕ	Visual estimate on graphs	5% variation cut-off	Visual estimate on graphs	5% variation cut-off
2000–1000	-1 to 0	~25	20	~20	12
710–500	+0.5 to +1	10–15	5	~20	7
500–250	+1 to +2	~20	17	~20	9
250–125	+2 to +3	~30	11	~30	22
88–63	+3.5 to +4	~40	28	~30	22

For reasons that will be explained below, for the standardized methodology (Appendix I), we ultimately selected the 0.71–0.5 mm (+0.5 to +1ϕ) size fraction for particle cross-sections. For this particular fraction, given the modest rejection rates discussed in the next section, a recommendation to analyze 50 grains (Fig. 2.1) seems safe given the much lower minimum numbers reported in Table 2.2. Again, this is the number of particles required to get stable averages, not to characterize different subpopulations. If these different subpopulations are of interest, a larger number of grains should be analyzed, but this is not a standard requirement in the figure 2.1 flowchart.

2.5.4 Rejection rate

We filtered out grains that were too small for each size fraction before compiling data for the stability tests just discussed. Specifically, we fitted a minimum area bounding rectangle around each grain, using PARTISAN. When the short width of the rectangle was smaller than the retaining sieve mesh size, the grain was discarded. For the 2–1 mm (- 1 to 0ϕ) to 0.5–0.25 mm (+ 1 to + 2ϕ) size fractions, the proportion of grains rejected is relatively low, comprising between 11% and 29% out of a total 46–69 grains (Fig. 2.11). For the 0.25–0.125 mm (+ 2 to + 3ϕ) and 88–63 µm (+ 3.5 to + 4ϕ) fractions, the rejection rate becomes severe, spanning between 37% and 58% out of 75–156 grains.

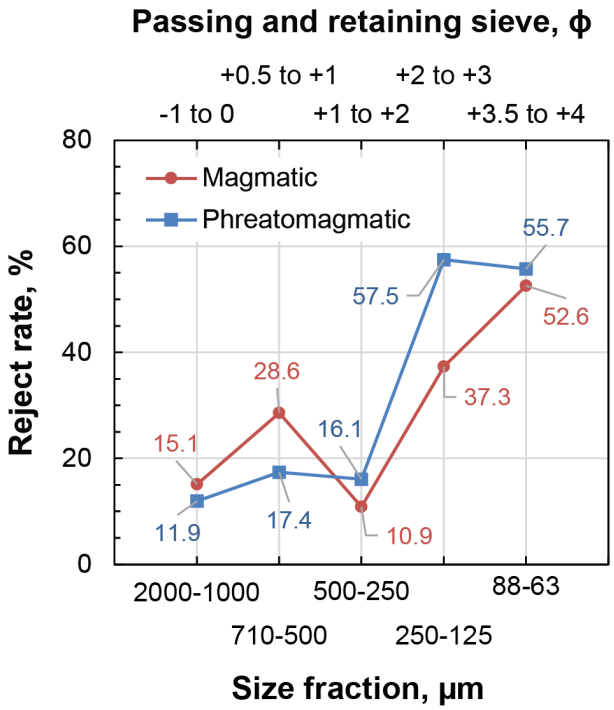

Figure 2.11: Rejection rate for the Ukinrek examples. Particles are discarded when they are too small, more specifically when their width (the short side of the minimum area bounding rectangle; Dürig et al. 2018) is smaller than the diameter of the holding sieve for the respective size fraction.

2.5.5 How morphometric and textural parameters vary with particle size

Morphometric parameters and internal textures of our Ukinrek samples are partly dependent on the size fraction studied. In the strombolian sample for example, median convexity increases from 0.4 to 0.8 as the grain size investigated decreases (Fig. 2.12, left). The change in convexity is more modest in the phreatomagmatic sample.

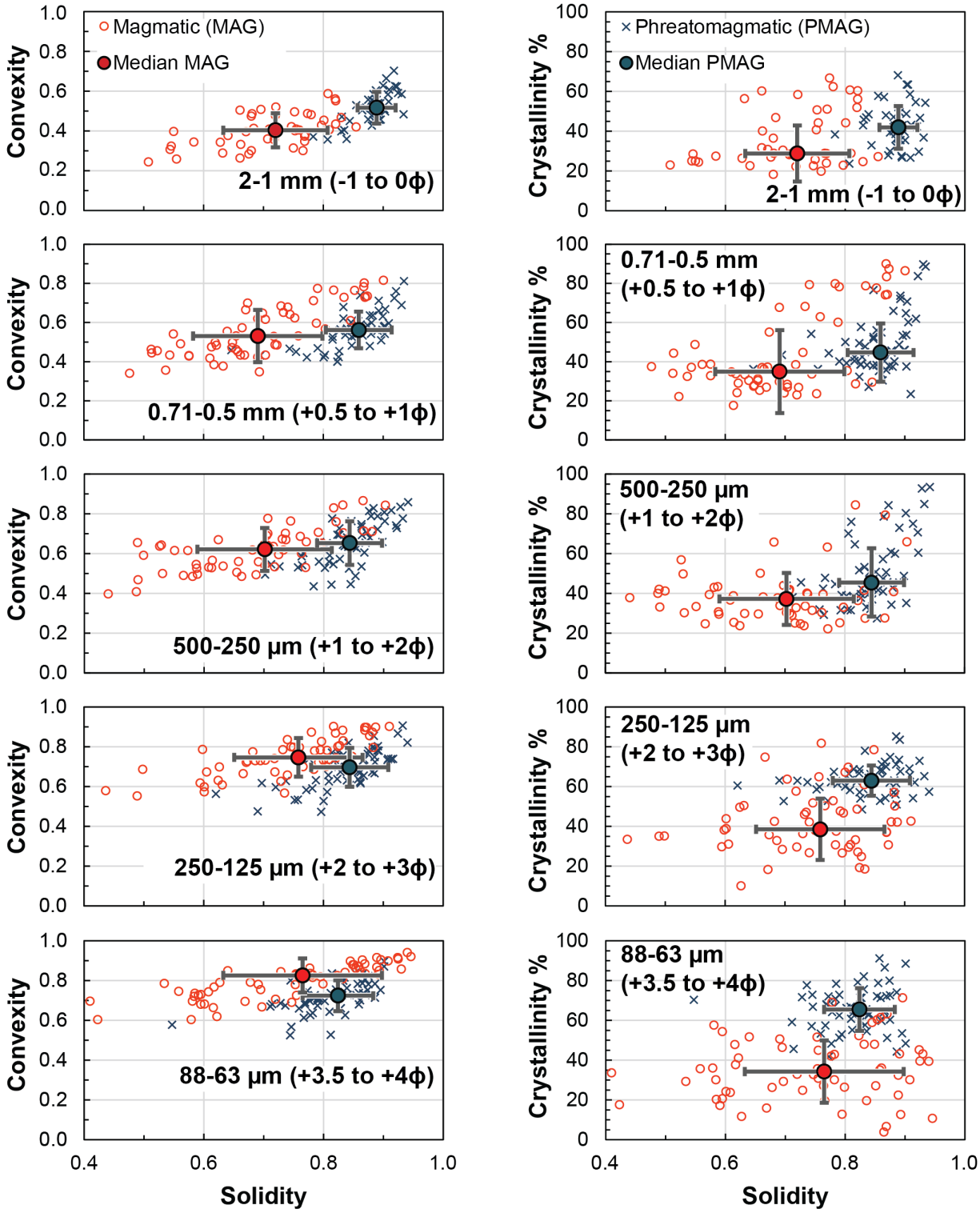

Figure 2.12: Convexity and 2D crystallinity versus solidity for both magmatic and phreatomagmatic samples from Ukinrek. The grey error bars represent one standard deviation in each direction.

Median 2D crystallinity in the phreatomagmatic sample increases from 42% to 65% in progressively finer grains (Fig. 2.12, right). In contrast, 2D crystallinity is more stable in the strombolian sample.

In both samples, 2D vesicularity decreases globally with the size fraction (Fig. 2.13, left), from median values of over 25% for 2–1 mm (- 1 to 0ϕ), to ~ 5% and less at 88–63 μm (+ 3.5 to + 4ϕ). In detail, the strombolian sample is more vesicular (greater vesicle area) than the phreatomagmatic one at 2–1 mm (- 1 to 0ϕ), but the phreatomagmatic sample is more vesicular at 88–63 μm (+ 3.5 to + 4ϕ).

The Büttner et al. (2002) plot, which uses the IPA parameters, was designed to be employed on ash grains 0.25–0.125 mm (+ 2 to + 3ϕ) or smaller, imaged as silhouettes. This diagram separates clasts inferred to have been produced by ductile vs. brittle fragmentation, based on the "Rectangularity x Compactness" product, indicated by a horizontal line. More recently, Dürig et al. (2018) revised this threshold, based on morphometric analyses of silhouettes for rhyolitic ash particles with grain size < 250 μm. Here we present resulting diagrams for all our size fractions, using particle cross-sections, to explore how grain size controls the position of fragments on the plot (Fig. 2.13, right). In our samples, the median values of "Rectangularity x Compactness" are strongly related to grain size.

Looking first at the fine fractions for which the diagram is intended, using the revised brittle-ductile cutoff proposed by Dürig et al. (2018) (purple line), a significant number of phreatomagmatic grains plot in the brittle field for the 0.25–0.125 mm (+ 2 to + 3ϕ) and 88–63 μm (+ 3.5 to + 4ϕ) plots, whereas almost all strombolian grains fall in the ductile field. This suggests that this diagram can also be employed successfully on particle cross-sections, for these fine fractions. The distinction between strombolian and phreatomagmatic based on "Rectangularity x Compactness" progressively breaks down for larger ash particles, with the 2–1 mm (- 1 to 0ϕ) fraction showing no difference between our samples. This was expected since the diagram was not designed for coarse ash.

2.6 Discussion

2.6.1 Choice of the optimum size fraction for particle cross-sections

Particle cross-sections have the advantage of exposing the particle interiors to quantify vesicularity and crystallinity along with particle shape (they also allow measurement of the groundmass and crystal chemistry).

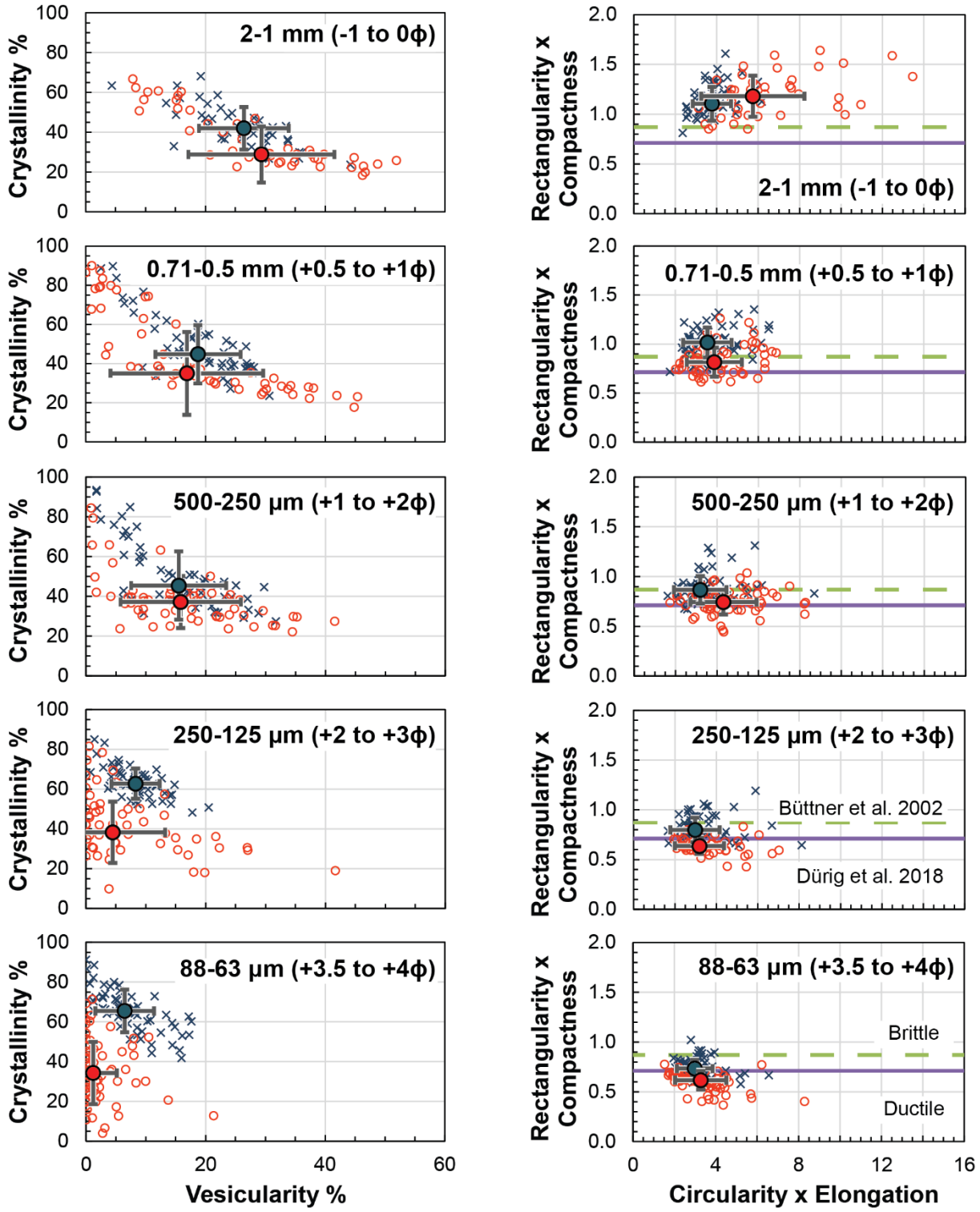

Figure 2.13: 2D crystallinity versus 2D vesicularity and the Büttner et al. (2002) plots for both magmatic and phreatomagmatic samples from Ukinrek. The grey error bars represent one standard deviation in each direction. The dashed green line separates ductile from brittle fragmentation for shoshonite clasts smaller than 130 µm (Büttner et al. 2002). The solid purple line operates the same distinction for rhyolite clasts smaller than 250 µm (Dürig et al. 2018).

Since morphometric and textural parameters depend on particle size, very strongly so for some parameters in some samples (Figs. 2.12, 2.13), it is necessary to select an 'optimal' size fraction for juvenile particle cross-sections in any standardized methodology for comparative studies of primary magma fragmentation. If all researchers use the same size fraction for particle cross-sections, and the same measurement method, results will be directly comparable.

Table 2.3 summarizes the pros and cons of the coarser versus finer size fractions we examined for particle cross-sections. Arguments include theoretical considerations, empirical results (the tests described above), and practical details influencing the time/user effort for different size fractions.

2.6.1.1 Theoretical and empirical considerations

The selected size fraction for particle cross-sections must ideally be found in the vast majority of natural pyroclastic deposits. Some types of pyroclastic deposits are ash-poor (e.g., proximal hawaiian fallout), but the larger ash grains among those studied here (those from the 2–1 mm (- 1 to 0ϕ), to 0.5–0.25 mm (+ 1 to + 2ϕ) fractions) should be found in most deposits.

To get good data on internal textures within the ash, larger grains are theoretically better suited since they more directly reflect the overall crystallinity and vesicularity of the magma prior to fragmentation. We do not think that the observed decrease in 2D vesicularity from 2–1 mm (- 1 to 0ϕ) to 88–63 μm (+ 3.5 to + 4ϕ) (Fig. 2.13) reflects strong post-fragmentation vesiculation in the coarser ash grains. Instead, as the grain size decreases, the large vesicles are progressively cut across during fragmentation, so the smaller grains are less representative.

For 2D crystallinity, the apparent increase of crystallinity in finer fractions for the phreatomagmatic sample reflects the tachylitic groundmass (Fig. 2.2d), as opposed to the glassy groundmass of the strombolian sample (Fig. 2.2d). When acquiring multiple grains simultaneously, groundmass was better imaged in the finer fractions, since smaller particles necessitated higher magnifications. However, if the groundmass texture is of interest, a zoom can optionally be made on large ash grains to get the same information without sacrificing the larger crystals.

2.6.1.2 Practical considerations

Practical laboratory considerations also militate in favor of using relatively coarse ash. Both 0.71–0.5 mm (+ 0.5 to + 1ϕ) and 0.5–0.25 mm (+ 1 to + 2ϕ) size fractions, for instance, can be easily and quickly picked under the binocular microscope and prepared as PEGMs.

Table 2.3: Pros and cons of different ash size fractions for measurement of morphometric and textural parameters on particle cross-sections

Size fractions	2000–1000, 710–500, 500–250 µm (- 1 to 0ϕ, + 0.5 to + 1ϕ, + 1 to + 2ϕ)	250–125, 88–63 µm (+ 2 to + 3ϕ, + 3.5 to + 4ϕ)
Pros	• Size fractions potentially available in more deposits, including ash-poor ones • Distinction between magmatic and phreatomagmatic particles on a solidity versus convexity plot in our test (Fig. 2.12) • Larger fragments means more vesicles and crystals to work with (generally better for textural analysis) • PEGM easier to prepare (i.e., juvenile particle selection, epoxy mounting, grinding and polishing) • SEM images faster to acquire (i.e., lower magnification, and more particles within the same image due to the more controllable mounting process)	• Better observation of the groundmass including small crystals (if present) as the magnification is normally higher* • Büttner et al. (2002) diagram can potentially be applied to assess the prevalence of brittle and ductile fragmentation, even though this diagram was designed for particle silhouettes
Cons	• Image pre-processing in Photoshop takes longer, as more vesicles might need to be blackened and fractures repaired • For 2–1 mm (- 1 to 0ϕ) only, the relatively large size of the grains and the very high number of pixels/particle needed (Table 2.1) result in fewer grains per image and therefore, an overall longer image acquisition time	• Very small grains are difficult to handle, mount and polish, resulting in a high particle rejection rate (Fig. 2.11) • These smaller clasts are missing large crystals and vesicles (vesicularity and crystallinity are not representative) • Imaging becomes long and difficult: o necessitates higher magnification and resolution o long acquisition times due to higher magnification and possibly fewer grains per image due to the trickier mounting process o smaller spot size o extreme brightness and contrast settings, resulting in blurred images

*But if the groundmass is of interest, it can be studied by zooming on the groundmass within grains from a coarser size fraction.

They allow multiple grains per image during acquisition, speeding up the process. In contrast, the 2–1 mm (- 1 to 0ϕ) fraction necessitates significantly more pixels to get stable values (Figs. 2.6, 2.7; Table 2.1), and more time for image preparation prior to textural analysis. It may also cause imaging/distortion problems on some SEMs because the grains are large (L. Gurioli, pers. commun., 2020).

2.6.1.3 Final choice for particle cross-sections

Considering all these aspects, we propose that the 0.71–0.5 mm (+ 0.5 to + 1ϕ) size fraction is optimal for the determination of morphometric and textural parameters using particle cross-sections (Fig. 2.1). The 0.5–0.25 mm (+ 1 to + 2ϕ) fraction would have been equally acceptable, but 0.71–0.5 mm (+ 0.5 to + 1ϕ) is evenly spaced on the ϕ scale between our recommended lapilli fraction (8–4 mm, - 3 to - 2ϕ) and our standard fine ash fraction (88–63 μm, + 3.5 to + 4ϕ; Appendix I).

2.6.2 Number of pixels for combined morphometric and textural measurements

Some previous studies have been focused on the fast measurement of morphometric parameters. This involved a moderate pixel density coupled with a large number of grains, in order to get stable average values for the morphometric parameters. In this study, we measured both textural and morphometric parameters, and determined that relatively high values of pixel density are required. The parameters that needed the most pixels to stabilize are convexity (which never fully stabilizes, since it is a perimeter-based measure) and the textural parameters. Interestingly, the higher pixel density proposed in this study ultimately allowed a much lower number of juvenile grains to be processed, as detailed in the next section.

2.6.3 Number of juvenile grains for particle cross-section studies

Previous morphometric parameter studies have called for large numbers of grains to be analyzed in each sample. There is a perception that thousands of grains might be needed (Durant et al. 2009; Liu et al. 2015). Here we show that using high-quality SEM-BSE images of particle cross-sections for the selected 0.71–0.5 mm (+ 0.5 to + 1ϕ) size fraction, in our samples, analyzing approximately 20 grains would be sufficient to obtain stable averages in morphometric and textural parameters. Taking into account that other samples may be more complex than ours (e.g., polymodal distributions), and that up to a quarter of imaged grains may be rejected due to particle size considerations (Fig. 2.11), we recommend selecting, mounting and imaging 50 juvenile grains per sample (Fig. 2.1). Once again, this value proved to be sufficient to characterize the whole population, but more grains would be needed to characterize each subpopulation in detail, if those subpopulations are of interest.

This number of grains should be tested in future studies with other samples. In these future studies, stability of morphometric and textural parameters can be verified by calculating the

relative differences in the cumulative average shape parameters for the 45th, 46th, 47th, 48th, and 49th grains. If the relative differences exceed 5%, more grains should be imaged and analyzed.

2.6.4 Importance of sample preparation and imaging

In supporting the chain of standard steps (Fig. 2.1), careful manufacture of PEGMs and attention to the quality of SEM images acquired for juvenile particle cross-sections are very important. The quality of the morphometric and textural measurements ultimately depends on the care employed during these steps.

2.6.4.1 PEGM manufacture

Mounting grains with the longest axis parallel to the mounting plane ensures that 2D aspect ratios give a good idea of 3D particle elongations. Other particle orientations, especially for some elongate grains, might produce “too small” cross sectional areas, resulting in the grain being rejected during filtering.

The stages of mounting, grinding and polishing have to be done carefully. It is crucial to mount the grains on a very flat surface; in addition, one must make sure that the liquid epoxy has a low viscosity and does not lift the grains up. Finally, grinding/polishing a PEGM too much (or not enough) may result in the cross-section being discarded during data filtering (Fig. 2.11). Our tests show that with careful PEGM manufacturing, a relatively low rejection rate can be maintained for the 0.71–0.5 mm (+ 0.5 to + 1ϕ) size fraction. In contrast, the high rejection rates observed for the finer ash PEGMs (i.e., 0.25–0.125 mm or + 2 to + 3ϕ, and 88–63 μm or + 3.5 to + 4ϕ) are, in our experience, imputable to difficulties in consistent PEGM preparation that result from interactions of these small grains with epoxy, and electrostatic forces.

In summary, we aim to capture the longest axis of the particle in 2D and expose its center normal to this dimension. These conditions offer the best chances to preserve as much 3D information as possible during the “conversion” of the grains into cross-sectional slices.

2.6.4.2 SEM image acquisition

The most crucial aspect of SEM-BSE image acquisition on particle cross-sections is to obtain an image with sharply contrasted internal phases (i.e., the groundmass relative to the crystal phases). This requires (i) a high enough pixel density (the combination of magnification and image resolution), (ii) an appropriate scan-speed setting, and (iii) optimal adjustment of brightness and

contrast settings within the SEM image acquisition software. Obtaining sharp contrast during acquisition will ease subsequent image preparation by minimizing the need for adjustments of grey levels within the image. Furthermore, this will speed up image segmentation, i.e. greyscale thresholding of each crystal phase and vesicles. A poorly contrasted image, however, will lead to erroneously segmented particle cross-sections, potentially leading to severe underestimation/overestimation of 2D crystallinity and 2D vesicularity of the sample. In addition, features such as groundmass or specific crystal types should ideally have the same grey levels for different clasts within a whole sample, in order to allow batch processing during image segmentation. In our tests, such conditions were easily met for the 0.71–0.5 mm (+ 0.5 to + 1ϕ) size fraction, due to the relatively small magnification and reduced scan time for each image. Reduced scan time minimizes charging, which is probably responsible for observed temporal drifts in brightness. For some magma compositions where crystal density approaches that of the glass in the groundmass (e.g., plagioclase-bearing felsic pyroclasts), extra care should be applied in obtaining the best possible contrast between the two phases.

2.7 Conclusions

Together, this study (Chapter 2) and its companion paper (Appendix I) constitute an initial proposal for a standardized methodology to characterize juvenile pyroclasts for comparative fragmentation studies. A standardized methodology will allow the volcanological community to generate data that is reproducible and can be compared between different volcanoes and different laboratories. Ultimately, we hope that this will lead to the generation of a large database covering all the main eruptive styles and magma compositions, which would allow volcanologists to gain more insights on fragmentation processes. It would therefore also have potential implications for volcano monitoring and eruption forecasting.

This study defines key points of the standardized protocol for the analysis of primary juvenile pyroclasts using polished epoxy grain mounts (PEGMs) and SEM-BSE imaging of particle cross-sections:

(1) It is important to correctly prepare and image the grains in order to obtain high-quality particle images suitable for shape and textural analysis;
(2) Compared to previous studies that analyzed only morphometric parameters, a higher number of pixels per particle between 10 000 and 75 000 is required to also measure 2D crystallinity and 2D vesicularity on each particle cross-section, respectively for 88–63 µm (+ 3.5 to + 4ϕ) and 2–1 mm (- 1 to 0ϕ) size fractions;

(3) Using a specific sieved size fraction and high-quality SEM images, 50 grains are needed in order to obtain stable averages in morphometric parameters, a much lower number compared to suggestions from many previous studies;
(4) We propose that the 0.71–0.5 mm (+ 0.5 to + 1ϕ) size fraction is optimal for joint morphometric and textural studies using particle cross-sections, based on a range of theoretical, empirical and practical considerations.

Moreover, we provide detailed instructions for PEGM preparation. Such information is commonly omitted in publications, but crucial to obtain reproducible data. Finally, we developed the script package “PASTA”, which facilitates image preparation and allows the semi-automated processing of both particle cross-sections and silhouettes, followed by the accurate measurement of 2D morphometric and/or textural parameters.

2.8 Acknowledgements

This study was funded by a Discovery Grant to PSR from the Natural Sciences and Engineering Research Council of Canada (NSERC) (RGPIN-2015-06782). TD is supported by the Icelandic Research Fund (Rannís), grant Nr. 206527-051. We thank Ikbel Mouedhen, Philippe Girard and Arnaud De Coninck for the support during the development of the polishing technique. We acknowledge Caroline Bélanger, Sarah Galloway and Félix Gagnon for the support in sample preparation and data processing. We thank Lucy Porritt, Jacopo Taddeucci and Pierre Francus for their comments on a draft of this paper. We thank Erin Fitch, an anonymous reviewer and associate editor Benjamin J. Andrews for constructive journal reviews.

2.9 Online resource 2.1: Making polished epoxy grain mounts of juvenile particles

This supplementary document describes the manufacturing of polished epoxy grain mounts (PEGMs) of juvenile particles required for the analysis of particle cross-sections. For the sake of completeness, we present instructions for making PEGMs for fractions between 2–1 mm (- 1 to 0ϕ) and 125–63 µm (+ 3 to + 4ϕ). For simplification, the following instructions assume that the user is mounting clean loose juvenile grains from a specific size fraction. Such a mounting procedure is described as a standard step for the 0.71–0.5 mm (+ 0.5 to + 1ϕ) size fraction in our standardized methodology for studies of primary magma fragmentation (Appendix I; Fig. 2.1). For the 88–63 µm (+ 3.5 to + 4ϕ) fraction, however, a dual mounting procedure is suggested: the user will first manufacture a carbon tape grain mount of the bulk size fraction (see Appendix I), and

then convert it to a PEGM. The instructions presented here can, however, easily be adapted for that procedure as well.

To lighten the text, in the rest of this supplement, size fractions will be designated by the ϕ size of the retaining sieve, for example the 2–1 mm (- 1 to 0ϕ) size fraction will now be called 0ϕ. We recognize that this creates an ambiguity as to whether "0ϕ" refers to a half-ϕ or a full-ϕ fraction, but for the purposes of preparing PEGMs, it does not matter: the instructions are the same for a half-ϕ or a full-ϕ size fraction. Refer to Table A1.1 in Appendix I for a conversion table of ϕ to mm.

2.9.1 List of recommended tools/equipment

Several tools are recommended for the mounting-casting process (Fig. 2.14), such as: i) wide glass petri dish (Ø 10–15 cm); ii) microspatula, spoon and dissecting needle; iii) wood sticks to stir uncured epoxy mixture; iv) ultra-fine point tweezers; v) 1-inch circular plastic ring forms (molds); vi) clear, low viscosity, low shrinkage, epoxy mixture (preferably curing at room temperature); vii) very flat mounting surface (we use a 3.5 inch hard disk drive platter); viii) strong and wide double-sided tape for placing the grains (e.g., carpet tape); ix) ml-range beakers for epoxy handling; x) wax paper; xi) binocular microscope for placing the grains on the sticky mounting surface; xii) cutting mat and art knife, xiii) coarse abrasive sand paper (400–600 GRIT); xiii) very fine permanent marker; xiv) brush.

2.9.2 Mounting

2.9.2.1 Preliminary sample conditions

The sample to be mounted contains only juvenile particles extracted from a discrete size fraction obtained through dry hand sieving, then cleaned in an ultrasonic bath in cycles of 1 minute, for a total of 3 minutes (see Appendix I). Vacuum impregnation of the grains (to fill vesicles) before mounting is not suitable for this methodology, for several reasons: i) the small particle size of the material would make difficult to preserve the loose state of the particles after impregnation, which is an essential condition for mounting; ii) lack of control on how to deliver the epoxy onto the grains and to extract it once impregnation is completed; iii) increase in time and complexity of the whole PEGM preparation.

2.9.2.2 Preparation of the mounting support

Before the sample can be embedded in epoxy, the mold (ringform) and the support need to be appropriately prepared. First, using the sandpaper, polish the ring form on the flat end chosen as the base of the PEGM (to make it very flat and smooth), as well as on the external sides (to make writing easier). Second, for each sample, glue a piece of double-sided tape, significantly larger than the ringform, on the mounting surface (here, the hard drive platter) (Fig. 2.15).

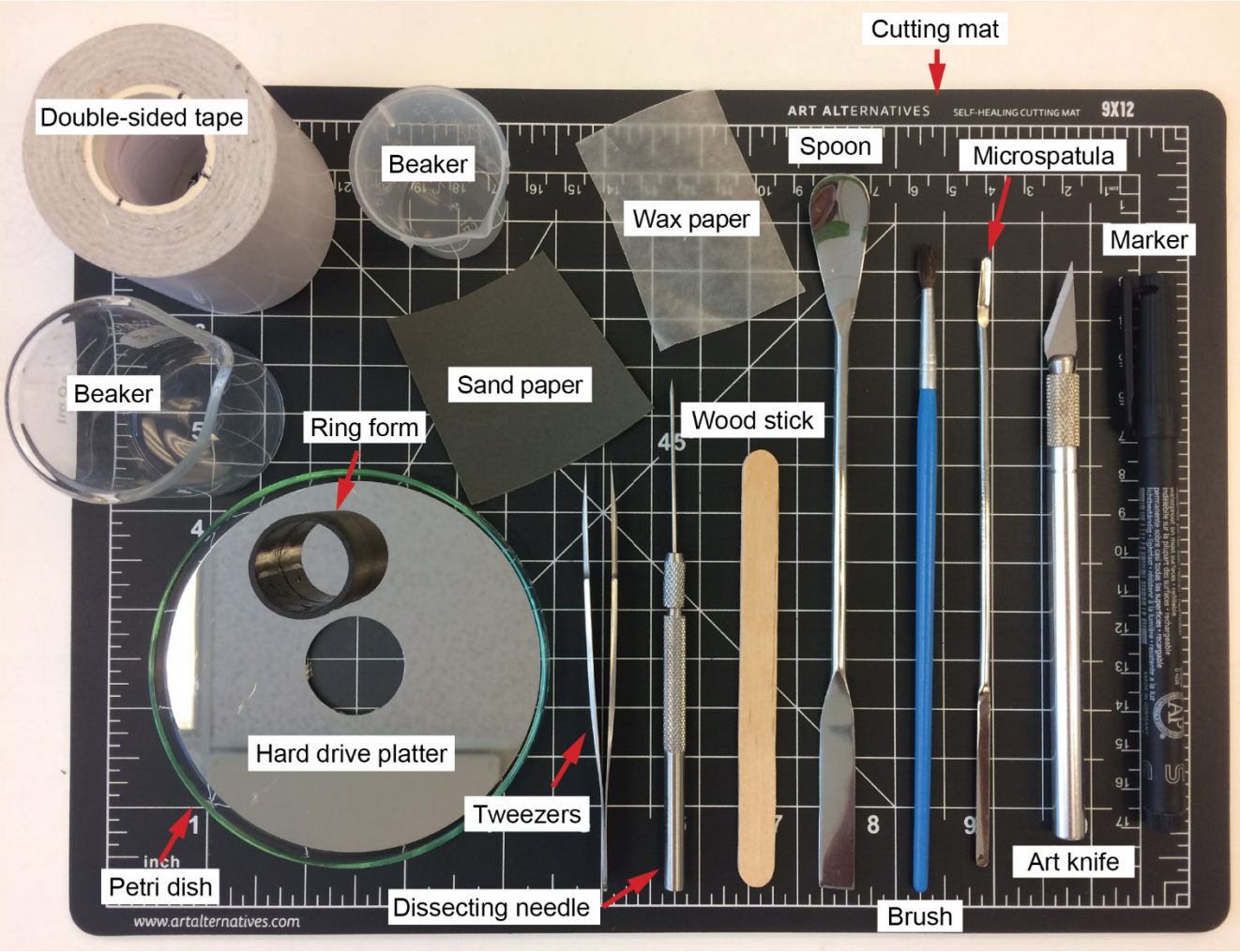

Figure 2.14: Illustration of recommended tools for PEGM manufacturing.

Five samples can easily be mounted simultaneously on a hard drive platter. The tape strips should be cut in one go in order to minimize bending and wrinkling of the future mounting surface. With the non-stick covers still present on the upper side, press the tape surfaces with a blunt flat object (avoid fingers as they leave fingerprints) in order to have a tape surface as flat as possible. To trace the mounting area, place the ring form at the center of each tape strip, and mark a circle

inside the mold using the permanent marker, which will correspond to the deposition area (Fig. 2.3a).

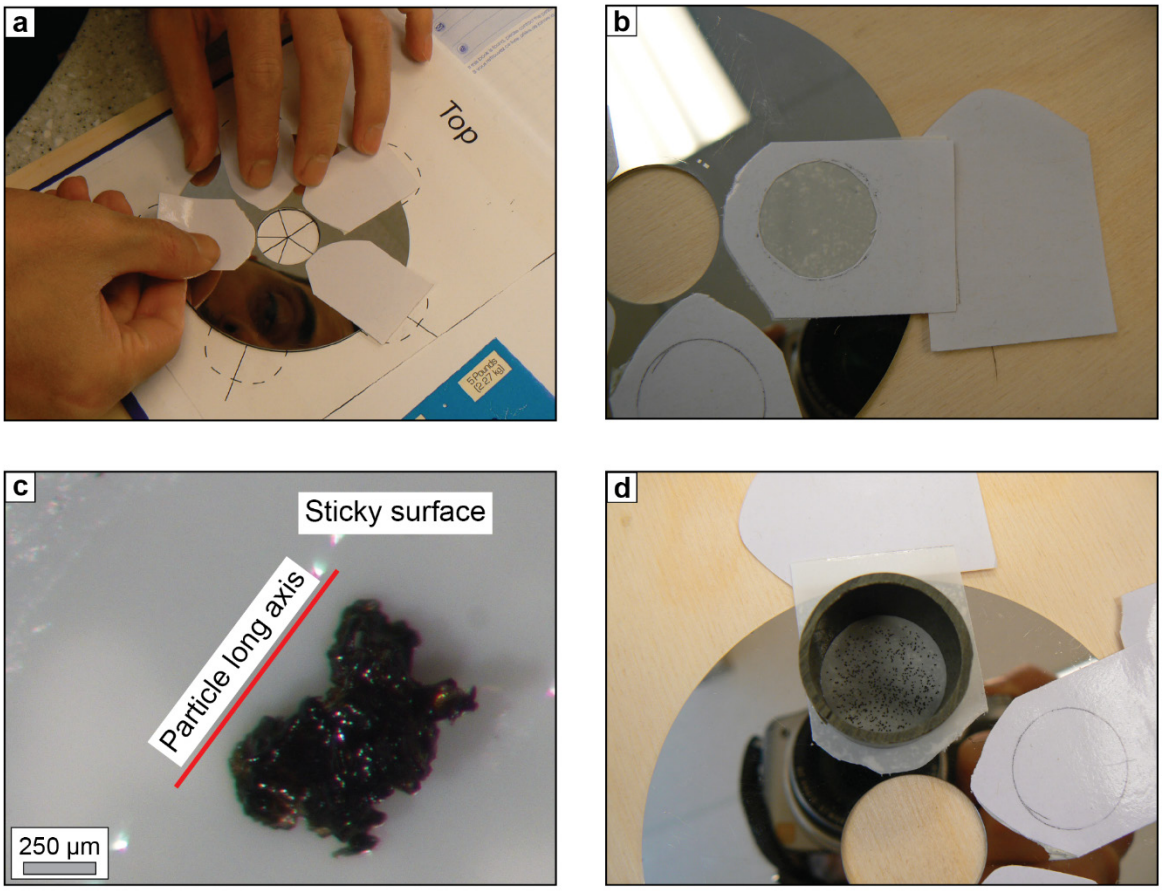

Figure 2.15: Mounting the juvenile particles. a) Sticking the double-sided tape on the flat support. b) Sticky area of the tape exposed for particles placement. c) Detail of a grain oriented with the longest axis parallel to the sticky surface (top-down view). d) Ring form placed into position around juvenile particles (black dots), ready for casting.

2.9.2.3 Placement of the grains

For each sample, lift up the entire non-stick cover by using the art knife and place it temporarily on the cutting mat. There, cut a circle out of the non-stick cover, staying inside the marked line. Place the cover (minus the cut circle) back in position on the tape, pressing all around the rim with the back of the art knife (Fig. 2.15b).

For size fractions from 0ϕ to + 2ϕ, the juvenile grains are transferred one by one, as follows. Transfer the mounting support inside the large petri dish (Fig. 2.14). Take the vial containing the juvenile grains and swirl it to homogenize the sample. Using the microspatula, take a small portion of material at a time (about 20 grains) and place it on the non-stick tape cover surrounding the

circular area of exposed tape (Fig. 2.3b). Working under the binocular microscope, pick and drop the grains on the sticky surface, one by one, using the tweezers. Use the needle/probe to orient the particles with the long axes parallel to the mounting surface (Fig. 2.15c). The goal is to have the grains relatively close together (to require as few SEM images as possible) but clearly separated from each other, with the longest axis parallel to the sticky surface.

For the + 3ϕ and + 4ϕ size fractions, if mounting large numbers of grains, use the “thumb method” instead:

- Sprinkle a small quantity of juvenile grains on different areas of an empty petri dish. Gently shake the dish sideways in order to displace and separate (as much as possible) the grains, creating a single layer;
- Wet your thumb’s fingertip with distilled water, preferably rubbing it on a saturated paper tissue in order to avoid excess water. Very gently rub the moist fingertip over the grains to collect them, then gently transfer the grains on the sticky surface, mimicking the gesture used to take fingerprints (Fig. 2.3c);
- Clean the non-stick cover around the circle and other parts of the disk platter from excess particles in order to collect them back for potential future use.

Once grains are mounted, gently remove the holed non-stick cover (exposing the entire tape surface), then firmly place the ring form into position (Fig. 2.15d). If are you mounting multiple samples at once, cover the top of the ring form in order to avoid cross-contamination. Placing the ring form after each sample is deposited on the tape also prevents cross-contamination.

2.9.3 Epoxy casting and curing

We successfully tested the EpoThin 2 epoxy castable system from Buehler®. It consists in a very low viscosity (350 mPa·s), low shrinkage clear epoxy mixture that cures at room temperature. This epoxy system is composed by a resin (R) and a hardener (H), which need to be mixed using a ratio of 2R : 1H by volume (or 100R : 45H by weight). Once mixed, the compound cures within 9 hours producing a hard, clear epoxy polymer, reaching a low peak exotherm up to 40°C during the curing process.

To proceed, cover the working area (countertop) with wax paper. For safety, it is recommended to wear gloves and a face mask when handling the epoxy, or work under a ventilation hood. Use three beakers and stirrers to handle the epoxy resin, hardener and resultant mixture, respectively. Considering the size fractions used in our work (0ϕ to + 4ϕ) and the diameter of the ring form, 3 g of epoxy is optimal for each PEGM (~ 2 g of resin, ~ 1 g of hardener). To prepare the epoxy, place the mixture beaker on the scale, then set the scale to zero. Pour the resin and the hardener consecutively into the beaker in the required quantities considering the number of PEGMs being prepared. Blend the mixture slowly with the stick, keeping it vertical. Slow gentle stirring minimizes air bubbles in the epoxy, negating the need to cure the samples in a vacuum. Strings will appear in the mixture as the resin and hardener have different viscosities. Stir until no strings are visible and the solution appears fairly homogeneous.

Finally, place the mounted samples on the balance, set to zero, then pour 3 g of the epoxy mixture into each mold (Fig. 2.3d). Leave the samples to cure at room temperature and atmospheric pressure overnight (or in a vacuum if air bubbles are visible), and **place heavy weights on top of each ring form to avoid epoxy leakage from the base of the ring form.** This aspect is crucial, since otherwise the detachment of the ring form will generate a tilted PEGM. This means that the grains will not be exposed at the same level, making the PEGM unsuitable for analysis.

2.9.4 Manual grinding and polishing

Automated grinding and polishing machines are available in some labs, but here we present a manual method that only requires a simple grinding/polishing machine (Fig. 2.3e). The protocol developed in this work exposes the central portion of the smallest juvenile particles embedded in a PEGM. It consists of up to five steps (3 of grinding, 2 of polishing) using first abrasive papers, then abrasive powder-water mixtures. For 0ϕ and + 1ϕ size fractions, run steps 1 to 5; for + 2ϕ, start at step 2; for + 3ϕ and +4ϕ, start directly at step 3 (Fig. 2.16). Each step can be adjusted according to the machinery and conditions available at other institutions. Please refer to table 2.4 for the complete set of thicknesses to be eroded for each full phi size fraction.

If using half-ϕ size fractions in which the retaining sieve is a whole number, the relevant thicknesses to be removed are the same as for full-ϕ fractions: for example, for the + 0.5 to + 1ϕ fraction (0.71–0.5 mm), follow the instructions for the full + 1ϕ fraction (1–0.5 mm). I.e., in both cases, we remove a total of 0.25 mm of mold, resin and particles to expose the center of the smallest grains.

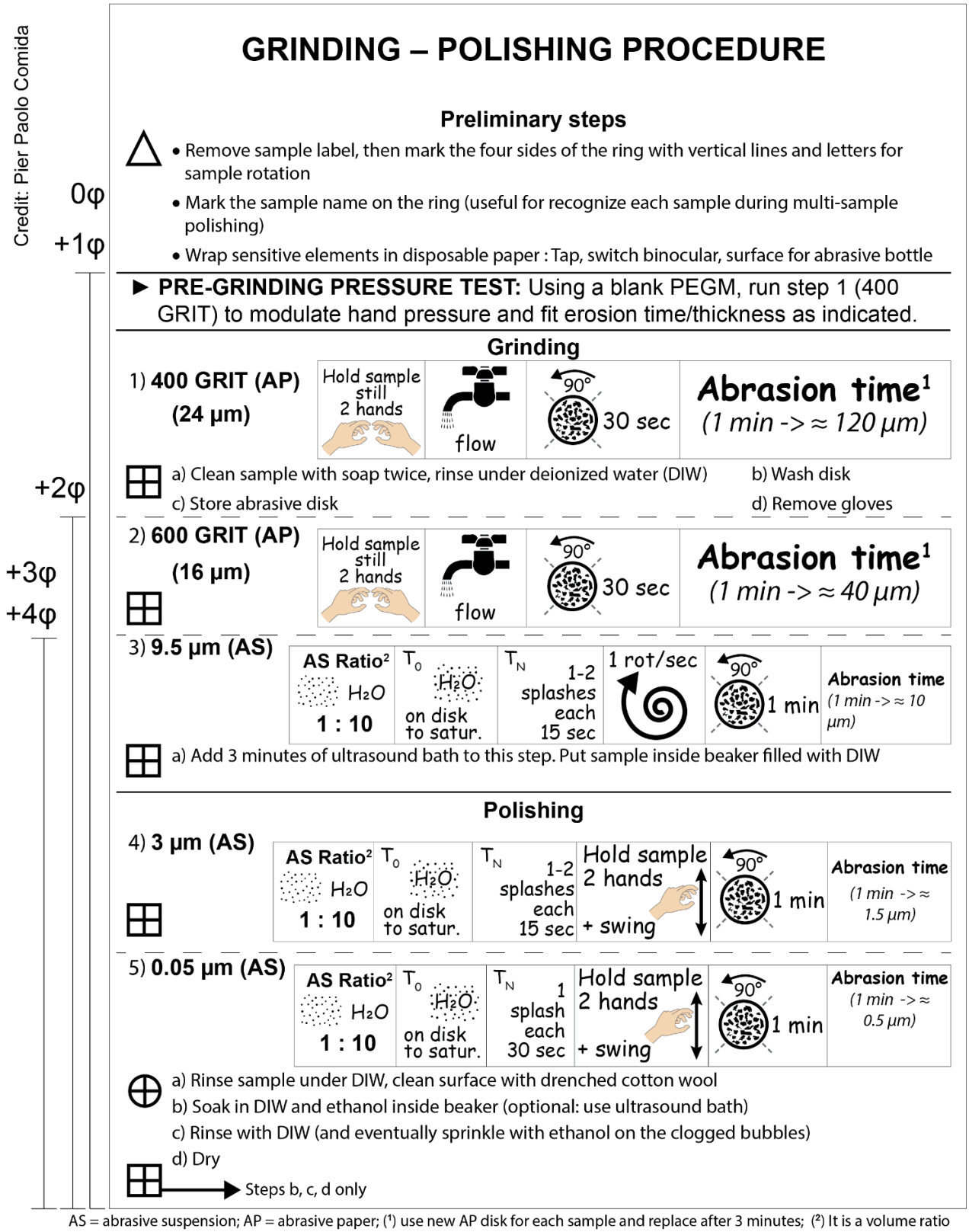

Figure 2.16: Printable directions for manual grinding and polishing of PEGMs.

Table 2.4: Thickness to erode during grinding/polishing, in order to reach the center of the smallest particle found on each size fraction

Steps	Size fraction ϕ (μm)				
	0 (2000–1000)	+ 1 (1000–500)*	+ 2 (500–250)	+ 3 (250–125)	+ 4 (125–63)*
Grinding	Thickness to erode (μm)				
1) 24 μm (400 GRIT)	375	150	-	-	-
2) 16 μm (600 GRIT)	100	75	90	-	-
3) 9.5 μm	15	15	25	50	18
Polishing					
4) 3 μm	8	8	8	10	10
5) 0.05 μm	2	2	2	3	3

* The instructions are the same whether using full phi sieves (example + 1ϕ = 1.0–0.5 mm) or half-phi sieves (example, narrow + 1ϕ = 0.71–0.5 mm) to create size fractions, since the aim is to grind and polish the mount down to the middle of the smallest particle.

2.9.4.1 Preliminary step

If there are any leaked epoxy or indentations, smooth the side of the PEGM surface to be grinded and polished using a coarse 400–600 grit (24–16 μm) SiC paper.

2.9.4.2 Grinding pressure test

In manual grinding, the pressure exerted on the sample placed on the rotating disk has a major influence on the thickness eroded within a specific amount of time. Applying too much pressure would result, for instance, in the irreversible loss of sample or the generation of fractures within the particles.

To minimize and control this issue, the user should run tests of grinding step 1 (see below) using a blank (juvenile particle-free) PEGM and adjust the hand pressure to fit the rates (~ 120 μm of abrasion per minute) provided in the printable directions (Fig. 2.16). Using that specific hand pressure, the abrasion times for each step will be correct.

2.9.4.3 Grinding steps

1) 24 µm (400 GRIT) SiC abrasive paper – With the grinder on and water flowing, hold the sample firmly with two hands, and press its surface onto the rotating abrasive paper disk. The sample is not continuously moved during this step, but is rotated counterclockwise by 90° every 30 seconds, in order to keep the surface horizontal. For the + 1ϕ size fraction, remove ~ 150 µm of material (corresponding to a grinding time of ~ 75 seconds).
2) 16 µm (600 GRIT) SiC abrasive paper – Same directions as step 1. For + 1ϕ, remove ~ 75 µm of material (corresponding to a grinding time of ~ 115 seconds).
3) 9.5 µm Al_2O_3 abrasive suspension – To grind with the abrasive suspension, fit the platen with the polishing pad of choice, and saturate it with the abrasive suspension (once the machine is on). Press the sample onto the pad and rotate in the opposite direction relative to the platen, at a pace of about one circle per second, drawing a spiral back and forth toward the center. Turn the sample counterclockwise by 90° every minute. In order to keep the surface of the platen constantly moistened, pour 1–2 splashes of suspension roughly each 15 seconds. For + 1ϕ, remove ~ 15 µm of material (corresponding to a grinding time of ~ 70 seconds).

After each grinding step, the sample is thoroughly cleaned with a detergent to avoid cross-contamination. At the end of step 3 the sample is additionally cleaned in the ultrasound bath.

2.9.4.4 Polishing steps

1) 3 µm Al_2O_3 abrasive suspension – Directions are the same as for step 3, but the sample is now shifted back and forth from the center of the platen. For + 1ϕ, remove ~ 8 µm of material (corresponding to a polishing time of ~ 320 s).
2) 0.05 µm Al_2O_3 abrasive suspension – Same directions as step 4, with splashes of suspension added every 30 seconds or less. For + 1ϕ, remove ~ 2 µm of material (corresponding to a polishing time of ~ 360 s).

The final cleaning of the sample surface involves the use of cotton wool and running water. A very short cycle in the ultrasound bath and ethanol can be used to remove abrasive powder stuck inside open vesicles, if necessary.

2.10 Online Resource 2.2: Measurement data spreadsheets

The morphometric and textural measurement data will be available in the final version of the journal manuscript.

2.11 Online Resource 2.3: Axial ratio versus pixel density plots

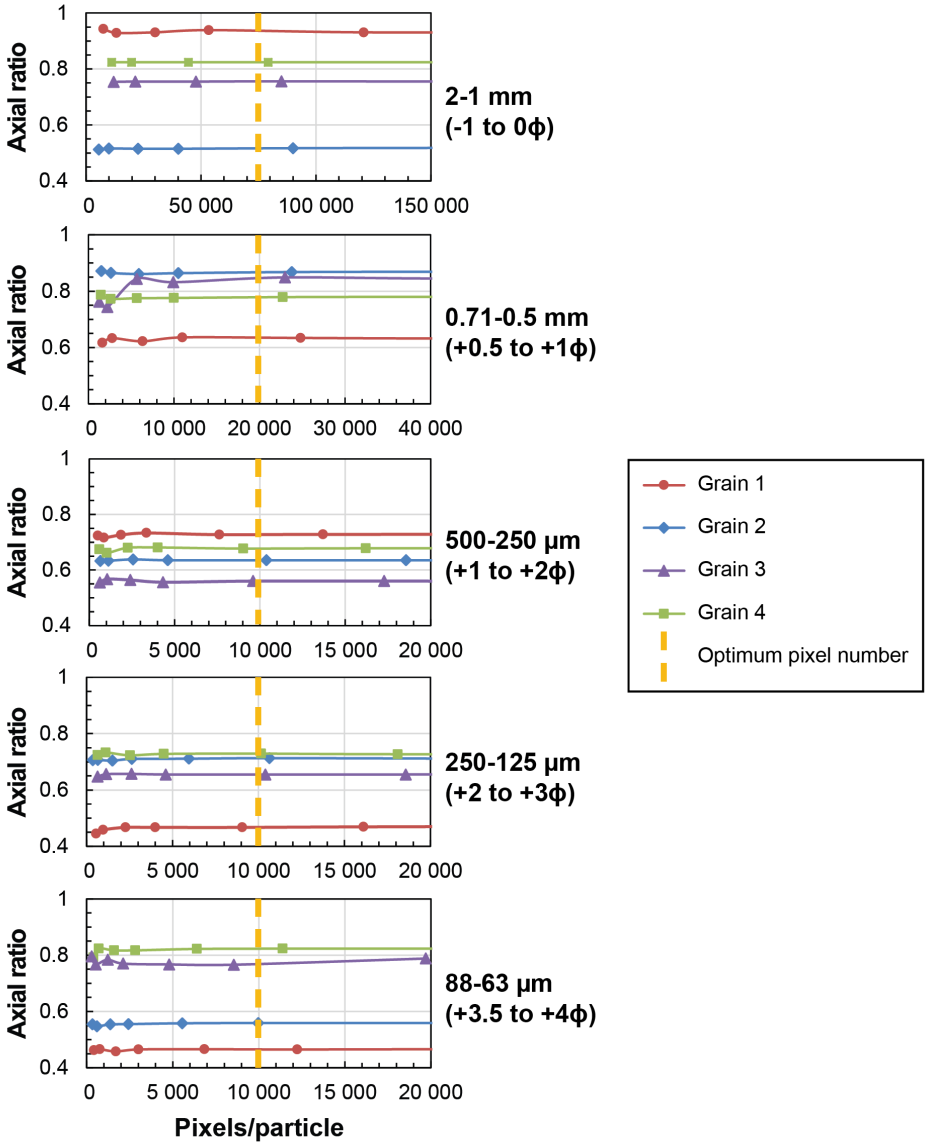

Pixel number test for axial ratio, using the Ukinrek strombolian sample. Four grains were tested for each size fraction, covering the highest and lowest axial ratio. Each trend line corresponds, within a single size fraction, to the same grain. The vertical dashed lines indicate the optimum pixel numbers for each size fraction (all parameters considered, see also Figs. 2.6 and 2.7).

3 SECOND ARTICLE: BREAKUP REGIMES IN LAVA FOUNTAINS

Liquid jet breakup regimes in lava fountains

Régimes de fragmentation des jets liquides dans les fontaines de lave

Authors:

Pier Paolo Comida[1], Pierre-Simon Ross[1], Bernd Zimanowski[2], Ralf Büttner[2], Ingo Sonder[3]

1. Institut national de la recherche scientifique, 490 rue de la Couronne, Québec (Qc), G1K 9A9, Canada

2. Physikalisch Vulkanologisches Labor, Universität Würzburg, Pleicherwall 1, 97070, Würzburg, Germany

3. Center for Geohazards Studies, University at Buffalo, 126 Cooke Hall, Buffalo, NY 14260, United States

Title of the journal:

Journal of Volcanology and Geothermal Research

Ready to submit

3.1 Abstract

Primary magma fragmentation in “fluid-dominated” (as opposed to “ash-dominated”) lava fountains involves the hydrodynamic breakup of a jet of magma. Lava fountains partly resemble industrial liquid jets issued from a nozzle into a quiescent atmosphere, on which there is a vast literature. Depending on the internal liquid properties, nozzle diameter and ejection velocity, liquid jet breakup in industrial applications occurs in four regimes: (I) coarse laminar breakup (Rayleigh regime); (II) transition region between laminar and turbulent breakup (first wind-induced regime); (III) turbulent breakup at the jet surface and unstable but intact liquid core (second wind-induced regime); (IV) fully turbulent fine spray (atomization regime).

Ductile magma breakup associated with regimes II, III and IV have been reproduced during the initial expansion of experimental magma fragmentation pulses as part of this study. Each experiment utilized 200–250 g of volcanic rock re-melted at 1200°C in a crucible. Using compressed argon injected within, or at the base of, the magma, ejection and fragmentation occurred within a few tens of milliseconds, as recorded by a high-speed camera. Three compositions were used: olivine-melilitite, alkali basalt, and basaltic trachy-andesite. Each composition was ejected at 3 and 10 MPa gas driving pressure, yielding exit velocities between 11–13 and 33–44 m/s, respectively. The ultramafic magma ejected at high speed developed quickly into a fully developed spray (regime IV), whereas the basaltic trachy-andesite ejected at low-speed initially expanded as a coherent magma mass before breaking into coarse domains (regime II). The observed variability among the experiments is linked to the relative balance among surface tension, viscosity, density, jet diameter and ejection velocity of the magma versus external aerodynamic effects acting on the jet surface. These factors, particularly viscosity and exit velocity, are also likely to control jet breakup regimes in natural lava fountains and some Strombolian pulses.

3.2 Introduction

Hawaiian style lava fountains are a common type of subaerial eruption (Parfitt and Wilson 2009; Taddeucci et al. 2015). These fountains typically involve volatile-rich mafic magmas, last several minutes to several days, and consist of jets that can rise from meters to several hundred meters into the atmosphere (Cashman and Scheu 2015; Taddeucci et al. 2015; Calvari et al. 2018; Mueller et al. 2018). Magma fragmentation is typically ductile (hydrodynamic) in the “fluid-

dominated" (as opposed to "ash-dominated") fountains with which we are concerned here (La Spina et al. 2021).

Lava fountains can be seen as a natural example of liquid jet breakup (Eggers and Villermaux 2008). There is a vast literature on the hydrodynamic breakup of liquid jets in industrial and commercial applications, such as ink jet printers or diesel engines. This shows that four jet breakup regimes exist, ranging up to full sprays; the controls on these regimes are well known (Reitz and Bracco 1986; Eggers and Villermaux 2008; Birouk and Lekic 2009; Lefebvre and McDonell 2017 and references therein). The four breakup regimes are often shown on the Ohnesorge diagram, which uses two dimensionless parameters (Reitz and Bracco 1986; Lefebvre and McDonell 2017).

This study aims to better understand controls on lava fountains by comparing them with jet breakup phenomena documented for industrial applications. We introduce a modified version of the Ohnesorge diagram and illustrate the effect of changing each of the important parameters. We then present ejection experiments involving fragmentation of remolten volcanic rocks (referred as to informally "magma" for simplicity). We changed only two parameters, magma composition and ejection velocity, between each run, but accessed three of the four regimes of jet breakup. Those same three regimes also seem present in examples of natural lava fountains.

The rest of this chapter is organized as follows. We start with a review of liquid jet breakup mechanisms and regimes in industrial and commercial applications (section 3.3). In the methods (section 3.4), the tested materials and experimental setup" are presented. Next comes the description of the physical properties of the magmas (section 3.5). In section 3.6, the results of the experiments are presented, using the high-speed video footage. Finally, section 3.7 discusses the similarities between industrial liquids jets and our magma jets, before drawing a comparison with natural lava fountains.

3.3 Review of liquid jet breakup in industrial and commercial applications

The disintegration of liquid jets ejected from a nozzle has been the object of scientific research for over 130 years, vastly exploited for several industrial and commercial applications (Eggers and Villermaux 2008; Birouk and Lekic 2009; Lefebvre and McDonell 2017). The studied fluids span different rheological behaviors (e.g. inviscid, Newtonian and non-Newtonian), viscosities over several orders of magnitude and varied ejection velocities (McCarthy and Molloy 1974; Reitz and Bracco 1986; Eggers and Villermaux 2008; Birouk and Lekic 2009; Clasen et al. 2012; Lefebvre and McDonell 2017). There are also different ejection configurations: classic studies

involved liquids issued vertically downward into a quiescent atmosphere, although other setups have also been used (Eggers and Villermaux 2008; Wang et al. 2012; Jones et al. 2019). The shape of the nozzle and the characteristics of the surrounding medium are the other main control factors dictating the disintegration of a liquid jet. The surrounding medium, when involving gasses, can be of three types: i) quiescent air/gas (Reitz and Bracco 1986; Chigier and Reitz 1996); ii) a coaxial flow issued from an annular orifice fixed around the liquid nozzle, ejecting gas in the same direction as the liquid jet (Chigier and Reitz 1996); iii) a crossflow which blows air/gas perpendicularly to the liquid jet ejection axis (Sallam et al. 2004; Cao et al. 2007).

3.3.1 Why liquid jets break up

Given the very large number of combinations of ejected liquids and surrounding medium configurations, a unified description of the breakup process is not possible. For the purpose of assessing the jet breakup mechanisms in our experiments and in nature, we consider in the rest of this section the basic downward ejection of a liquid at constant velocity into quiescent air at atmospheric pressure (Birouk and Lekic 2009; Lefebvre and McDonell 2017). As the jet moves away from the nozzle, the competition between forces within the liquid and external aerodynamic forces at the jet surface will generate wave-like disturbances. Once a critical wave amplitude is reached, the liquid jet breaks up into filaments and drops; this is known as primary breakup. Secondary breakup of the newly formed drops and threads into smaller fragments might occur if the primary drops are still large enough (Birouk and Lekic 2009; Lefebvre and McDonell 2017), and sufficient time and travel distance are given. In a state of equilibrium, the internal pressure distributed at the liquid surface is equal to the sum of external aerodynamic and surface tension pressures (Lefebvre and McDonell 2017). As the latter is inversely proportional to the drop size, aerodynamic effects acting on a relatively large liquid drop will be stronger than surface tension pressures, leading to deformation and breakup. As the newly formed drops become progressively smaller, surface tension pressure will increase relative to the aerodynamic pressures, until the critical drop size is reached. Beyond this size, surface tension pressures will be able to accommodate any destabilizing effect by aerodynamic forces, and no further breakup will occur (Lefebvre and McDonell 2017).

3.3.2 Jet breakup regimes

Several time and length scales are related in a complex manner during the breakup process of liquid jets. Time scales of early thinning and breakup of an initially coherent liquid volume into

threads or drops varies strongly depending on the liquid's material properties, the ejection velocity, and the surrounding medium. The disintegration may affect the whole mass at once, or it may be initially limited to the surface of the jet. Over the past four decades, the investigation into this variety of conditions has led to the identification of different breakup regimes. Several regime classifications have been used. Since each regime is generally defined by a similar set of conditions regardless of the classification method, we will briefly introduce the main two classifications before describing each regime.

3.3.2.1 Jet stability curve classification

On one side, the relationship between ejection velocity and the intact length of the liquid jet (distance from the nozzle exit to the point of primary breakup) constitutes the basis of the stability curve classification of jet breakup regimes (Fig. 3.1a). For the simplest case of a liquid issued downward into the atmosphere, a progressive shift in the expansion and fragmentation of the liquid is observed when increasing ejection velocity (Fig. 3.1b). At the lowest ejection velocity, the liquid jet is unable to form a coherent liquid jet and breaks up into drops upon exiting the nozzle because of liquid inertia and surface tension; this is known as the dripping region (not shown). For larger ejection velocities, a fully formed liquid jet is established and four main breakup regimes exist, as described below.

3.3.2.2 Ohnesorge classification

The velocity of the liquid influences its internal flow regime (i.e. laminar, transitional or turbulent) before it emerges from the nozzle, contributing to its final disintegration once in the air, along with aerodynamic forces. The development of internal disturbances within the liquid jet also depends on its internal properties; liquids with different densities (ρ), viscosities (η) and surface tensions (σ) issued with the same velocity (u) will break up differently from one another. These variables are typically combined into two dimensionless parameters, the Reynolds number for Newtonian viscosities $Re = \frac{\rho u d}{\eta}$ and the Weber number $We = \frac{\rho u^2 d}{\sigma}$, where d is a characteristic length usually represented by the nozzle diameter. Both *Re* and *We* quantify the relative importance of fluid's inertia, relative to its viscosity and surface tension, respectively.

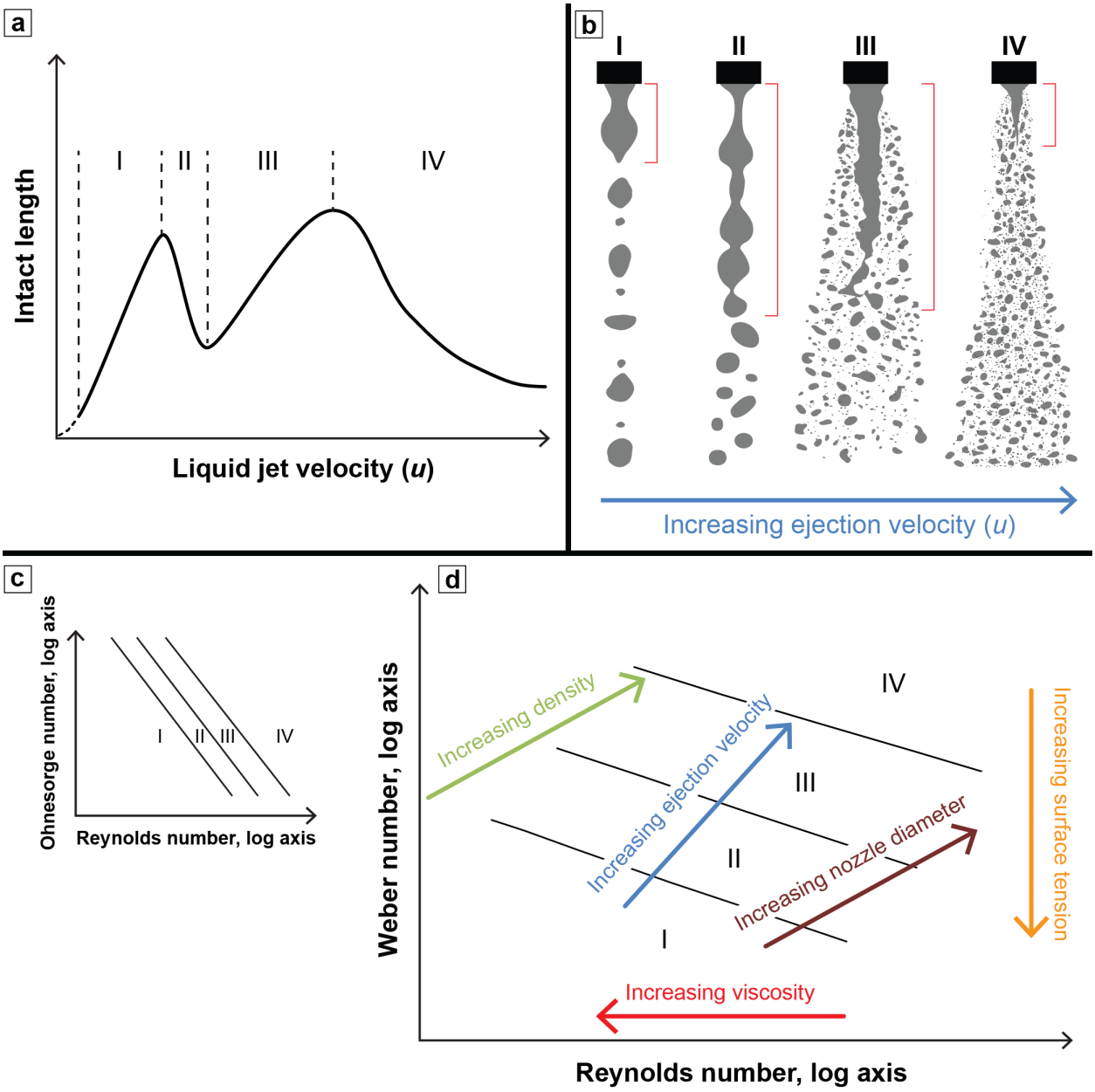

Figure 3.1: Four liquid jet breakup regimes occur in industrial applications: I – Rayleigh regime, II – First wind-induced regime, III – Second wind-induced regime, IV – Atomization regime. (a) Jet stability curve displaying the relationship between intact length before primary breakup and ejection velocity of the liquid jet; after Lefebvre and McDonell (2017). (b) Visual representation of the liquid jet within each regime, for a jet issued downward in a stagnant atmosphere. One way to transition from one regime to another is to change the ejection velocity, which corresponds to different intact length for primary breakup (vertical red bars); after Chigier and Reitz (1996) and Lefebvre and McDonell (2017). (c) Traditional Ohnesorge classification determined through the relationship between the Ohnesorge and Reynolds numbers; after Lefebvre and McDonell (2017). (d) Modified "Ohnesorge" diagram showing the Weber and Reynolds numbers. Colored arrows illustrate the effect of varying the main parameters. The power decay of the regime boundaries is ~ $Re^{-0.5}$.

A third dimensionless parameter widely used in jet breakup studies, the Ohnesorge number, is a ratio of the first two: $Oh = \frac{\sqrt{We}}{Re} = \frac{\eta}{\sqrt{\rho\sigma d}}$. The traditional *Ohnesorge* diagram plots *Oh* versus *Re* and shows the four breakup regimes (Fig. 3.1c).

On this diagram, viscosity has opposite effects on *Oh* versus *Re*, making it difficult to visualize the effect of viscosity on regime changes. Since viscosity is a very relevant parameter when dealing with magmas, we introduce an alternative way to assess regime transitions in liquid jet breakup, obtained by comparing *We* and *Re* (Fig. 3.1d). Now the viscosity appears only in the x axis, so increasing the viscosity produces a simple leftward trend on the diagram, progressively crossing regime boundaries. The regime boundaries in this new diagram decay with $We \sim Re^{-0.5}$.

3.3.2.3 The four jet breakup regimes

The four main jet breakup regimes are, for increasing ejection velocities:

I. Laminar flow region of the stability curve classification (Rayleigh's regime in the Ohnesorge classification) – At relatively low ejection velocity, the liquid jet is initially in a predominant laminar flow state. Surface tension and liquid inertia dominate the breakup process, with negligible aerodynamic effects, resulting in small surface disturbances that fragment the liquid jet into drops (regime I on Fig. 3.1). In this regime, there is a direct relationship between longer threads and ejection velocity. After breakup, the width of the drop might be generally larger than the nozzle diameter but within the same order of magnitude.

II. Transition region (first wind-induced regime) – At higher ejection velocity, the liquid jet develops internal turbulence that is transmitted towards the gas-liquid interface. Aerodynamic effects are no longer negligible, enhancing wave disturbances at the liquid surface that contribute to the ultimate breakup of the jet (regime II in Fig. 3.1). This regime is characterized by an inverse relationship between ejection velocity and intact length of the liquid jet. The size of the newly formed fragments is still within the same order of magnitude as the initial liquid jet, and breakup still occurs at a certain distance from the nozzle exit.

III. Turbulent flow region (second wind-induced regime) – In this regime, aerodynamic forces at the gas-liquid interface become important on the breakup process, relative to internal turbulence in the liquid jet. Surface wave disturbances cause the disintegration of the liquid jet relatively closer to the nozzle exit, although there is still an intact (unfragmented) portion

to the jet near the nozzle. The length of the drops tends to again increase with increasing velocity (regime III in Fig. 3.1a). The size of the newly formed drops is now much smaller than the nozzle diameter (Fig. 3.1b).

IV. Fully developed spray region (atomization regime) – At extremely high ejection velocities (up to, and beyond the speed of sound), the flow is fully turbulent. Also, strong aerodynamic forces at the jet front cause the violent disintegration of the liquid jet very close to the nozzle. The length of the newly formed drops progressively decreases with increasing ejection velocity (regime IV in Fig. 3.1), and their size will be up to several orders of magnitude smaller than the nozzle diameter (Fig. 3.1b).

Regime transitions can also be obtained by keeping the velocity constant but changing one of the other main parameters. Increasing either the liquid density or the nozzle diameter leads to both higher *We* and *Re*, promoting the fine disintegration of the liquid jet (Fig. 3.1d). Increasing surface tension leads to a lower *We*, shifting the jet towards the Rayleigh regime. Increasing viscosity reduces *Re*, again enabling the transition toward the Rayleigh regime (Fig. 3.1d).

3.4 Methods

Magma fragmentation experiments were carried out at the *Physikalisch Vulkanologisches Labor* (PVL) in the University of Würzburg (Germany). Discrete upward moving pulses of artificial 'magma' were produced and filmed. This allowed access to three breakup regimes (II, III and IV).

3.4.1 Tested materials

The experiments used three volcanic rock materials, ranging from ultramafic to intermediate compositions (Fig. 3.2a). They include: i) Hohenstoffeln lava lake, a dense olivine-melilitite with ~ 38 wt.% SiO_2 from the Tertiary Hegau volcanic field in Germany (Zimanowski et al. 1997; Hobiger et al. 2011); ii) Billstein, a thick and dense alkaline basalt lava flow with ~ 45 wt.% SiO_2 from the Rhön volcanic field, Germany (Zimanowski et al. 2004; Dürig et al. 2012); iii) Sommata, a basaltic trachyandesite lapilli-size scoria deposit with ~ 54 wt.% SiO_2 from the island of Vulcano in the Aeolian archipelago, Italy (Büttner et al. 2002; Hobiger et al. 2011; De Astis et al. 2013). Despite the Sommata material being scoriaceous, after remelting it also produced a dense (bubble-poor) magma, like the other two materials.

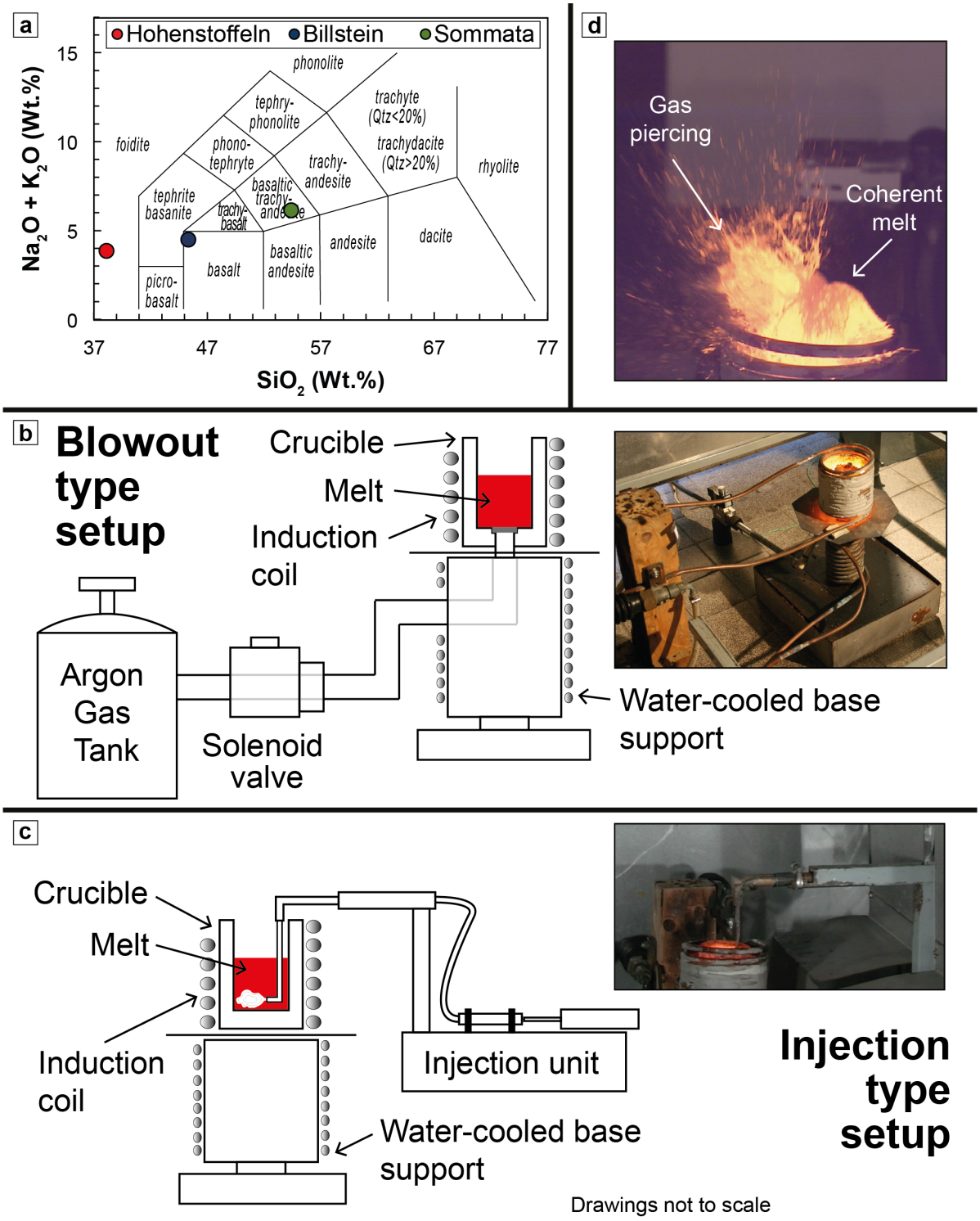

Figure 3.2: Magma compositions and experimental setups. (a) Total alkalis vs. silica diagram (Le Bas et al. 1986). Data for Hohenstoffeln and Sommata from Hobiger et al. (2011) and Billstein from Zimanowski et al. (2004). (b) Schematic drawing of the "high-speed" (10 MPa) blowout type experiment setup. (c) Schematic drawing of the "low-speed" (3 MPa) injection type experiment setup. Schemes modified from Austin-Erickson et al. (2008). (d) Frame of an experiment run (Billstein 10 MPa) at the beginning of the free air expansion, showing the portion of the melt affected by gas piercing (on the left) and the still coherent portion of the melt plug (on the right).

3.4.2 Experiment setup and timeline

The selected volcanic rocks were re-melted and then fragmented using two different experimental setups. The reason for using two different setups is that these experiments were part of a larger program, which also involved phreatomagmatic experiments. Out of this larger program, for this paper, we selected six successful gas-driven hydrodynamic fragmentation runs covering three magma compositions and two driving pressures.

Regardless of the experiment configuration (detailed below), preparation for each run involved placing a set amount of granulated rock inside a 5 cm (inner diameter) steel crucible. The granules were heated to 1200°C within one hour, using an induction furnace (Figs. 3.2b, c). Such rapid heating might leave some crystals in the magma.

The first experimental setup, informally known as the “blowout” (detailed in Büttner et al. 2006), was used for the “high speed” runs (Fig. 3.2b). About 200 g of granulated material was employed in each run. A fixed volume of compressed argon at 10 MPa (100 bars) was suddenly introduced through a hole at the base of the crucible by opening a valve. This rapidly pushed the magma upward as a plug, causing hydrodynamic fragmentation at the gas-magma plug interface within the crucible. In almost all the experiment runs, the arrival of the magma plug at the crucible opening coincided with the argon gas laterally piercing through the magma, leading to droplet generation (Fig. 3.2d). As will be seen below, this gas piercing phase is relatively minor in terms of volume of fragmented magma. Further and complete fragmentation of the perturbed magma plug occurred in the atmosphere, and this is the liquid jet breakup part that we are interested in for this paper.

The other setup ("injection type" configuration; e.g., Zimanowski et al. 1997), was used for the lower pressure experiments (Fig. 3.2c). Each run employed 255 g (± 10 g) of granulated volcanic rock. A discrete volume of compressed argon gas at 3 MPa (30 bars) was injected directly within the magma through a J-shaped steel pipe mounted on a servo drive. The injected gas pushed the magma upwards, again causing expansion and hydrodynamic fragmentation both within the crucible and in the atmosphere (Zimanowski et al. 1997).

For both setups, ejection from the crucible and associated fragmentation of the magma was completed within 50 and 80 ms, respectively.

3.4.3 Video footage analysis

The free air fragmentation phase of each run was recorded using high-speed cameras, as detailed in Zimanowski et al. (1997). We employed 2000 and 5000 frames per second to capture the 10 MPa and 3 MPa series, respectively. The experiments were also filmed from various angles using regular video cameras, and several parameters such as force, pressure, etc. were recorded.

Analysis of the high-speed video footage allowed to investigate thinning and breakup processes of the magma during each run. The average ejection velocity of the coherent magma plug was tracked at the crucible exit using a combination of Adobe Illustrator® and Phantom Camera Control (PCC) software®. The minor gas piercing phase had a much higher velocity but this is not relevant for studying liquid jet breakup regimes.

3.5 Experimental parameters and physical properties of the magmas

Similar to industrial liquids, jet breakup in magma is governed by its main internal properties, and the violent interaction of the magma with a quiescent atmosphere, influenced by ejection velocity.

3.5.1 Temperature

Magma temperature greatly influences viscosity, and to a lesser extent density and surface tension (Walker and Mullins 1981; Shimozuru 1994). All experiments were carried out at the same initial temperature of 1200°C. Since there was a slight temperature gradient in the crucible, and that in this paper we are primarily interested by what happens to the top part of the magma upon initial exit, we also consider some physical parameters for 1175°C below.

3.5.2 Ejection velocity

By using two driving pressures for each of the tested magmas, we anticipated that each driving pressure would correspond to a certain ejection velocity for all magmas. Indeed, the coherent portion of each magma plug considered in this study shows roughly similar exit velocities for a certain driving pressure (Table 3.1). The average exit velocity of the 10 MPa series is 38 m/s, which is 3.2 times faster than that of the 3 MPa series (~ 12 m/s).

Table 3.1: Physical parameters of the magma plug among different experiments, for the purpose of calculating the Weber and Reynolds numbers during the early stage of the jet phase, and observed breakup regime on high-speed videos.

Run	Crucible diameter (m)	Surface tension (N/m)	Density (kg/m^3)	Ejection velocity (m/s)[1]	Dynamic viscosity range (Pa*s)	Weber number	Reynolds number[3]	Observed regime
10 MPa series	-	-	-	-	-	-	-	-
Hohenstoffeln	0.05	~0.33	~3000	44	~20 – ~340	6.0 x 10^6	542 – 9220	IV
Billstein	0.05	~0.33	~2700[2]	33	~30 – ~1400	2.2 x 10^6	99 – 5691	IV-III
Sommata	0.05	~0.33	~2500	36	~45 – ~26 700	2.6 x 10^6	7 – 257	III
3 MPa series	-	-	-	-	-	-	-	-
Hohenstoffeln	0.05	~0.33	~3000	11	~20 – ~340	1.3 x 10^6	79 – 1350	IV-III
Billstein	0.05	~0.33	~2700[2]	11	~30 – ~1400	8.7 x 10^5	21 – 1174	III
Sommata	0.05	~0.33	~2500	13	~45 – ~26 700	7.4 x 10^4	2 – 83	II

([1]) Values of ejection velocity refer to the coherent portion of the magma plug upon exiting the crucible
([2]) Density of a similar magma composition within the 1175–1200°C temperature range (Galápagos alkali-olivine basalt, Murase and McBirney 1973)
([3]) For power-law fluids, calculated using Re_{pl} (from Madlener et al. 2009)

3.5.3 Surface tension

Available empirical σ values for Hohenstoffeln and Billstein (Koopmann 2004) along with another basalt and some more felsic compositions (Murase and McBirney 1973; Walker and Mullins 1981) are presented in Fig. 3.3a. Between 1175 and 1200°C, all of these magmas have surface tensions between ~ 280 and 350 mN/m, a very limited range. So differences in surface tension must not be the controlling factor in explaining the different fragmentation behavior of our three magmas.

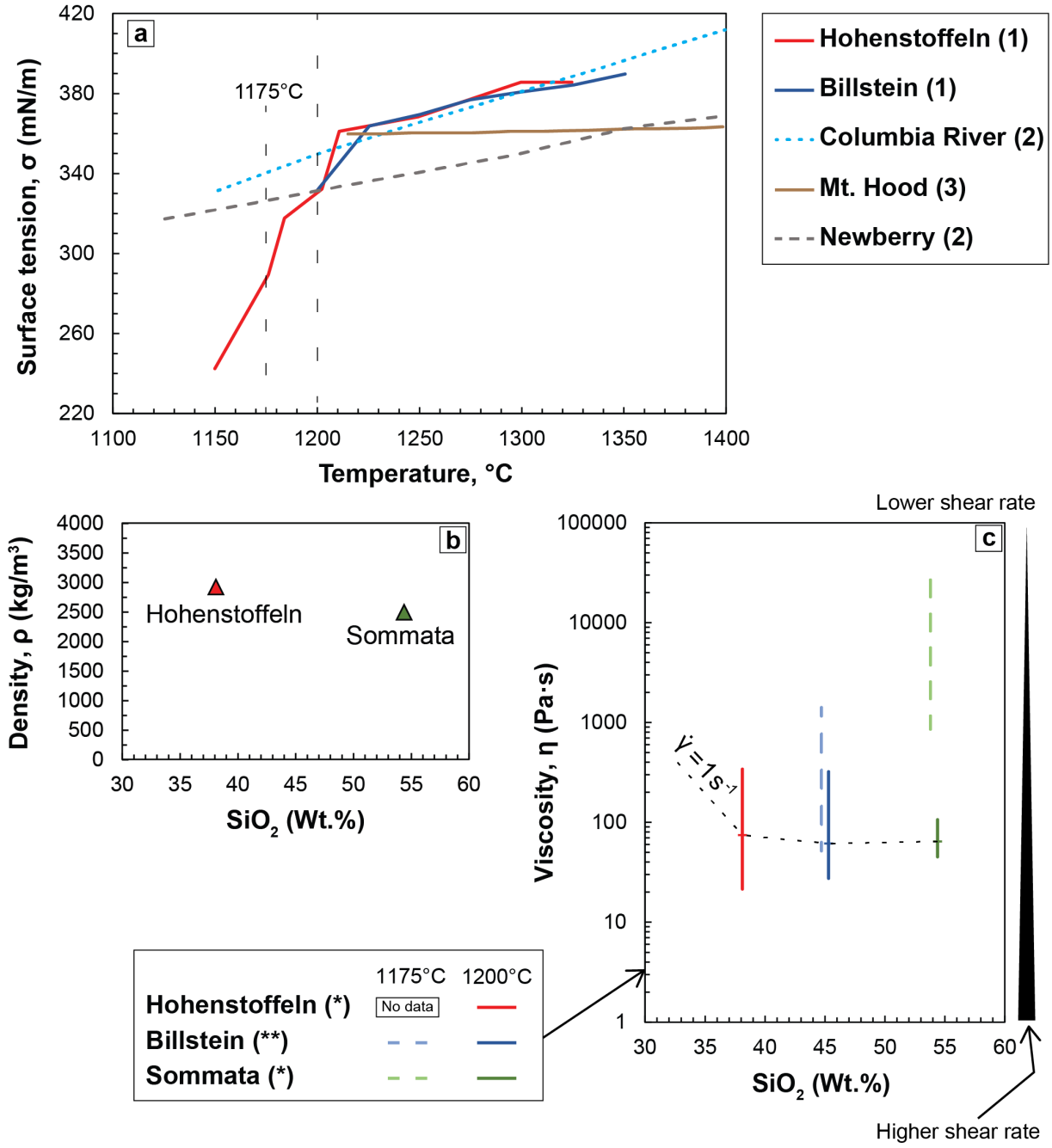

Figure 3.3: Physical properties of the tested magmas. (a) Temperature-dependent surface tensions of Hohenstoffeln (olivine-melilitite) and Billstein (alkaline basalt) magmas, along with other reference materials: i) Columbia River (basalt), ii) Mt. Hood (andesite), iii) Newberry (rhyolite). Surface tension for all material shows little variation within the 1175-1200°C temperature interval. Data sources: (1) Koopmann (2004); (2) Murase and McBirney (1973); (3) Walker and Mullins (1981). (b) Bubble-free density versus silica for Hohenstoffeln and Sommata, from Büttner et al. (1998, 2002). It can be assumed that Billstein has an intermediate density between these endmembers. (c) Viscosity versus silica trends for the tested magmas at 1175°C and 1200°C. Vertical lines show the effect of different shear rates on equilibrium viscosities in viscometry experiments. Hohenstoffeln and Sommata data from Hobiger et al. (2011), Billstein from Sonder et al. (2006).

3.5.4 Bubble-free density

The available bubble-free density (ρ) data for two of our tested magmas ranges between less than 3000 kg/m^3 (olivine-melilitite) and ~ 2500 kg/m^3 (basaltic-trachyandesite) at 1200°C (Büttner et al. 1998, 2002), and Billstein is assumed to have an intermediate density value (Fig. 3.3b). Again, this is a limited range. In our experimental magmas, the average vesicularities only account for few vol. %, therefore density does not explain the different fragmentation behavior.

3.5.5 Viscosity

Unlike the previous parameters, η can vary by several orders of magnitude between different magmas. Therefore, it has the potential to be one the main factors controlling jet breakup processes (Clasen et al. 2012; Lefebvre and McDonell 2017). Even for a specific magma composition, η depends on temperature. A dramatic example is Sommata, where η is in the 50–100 Pa.s range at 1200°C but extends to values larger than 26 000 Pa.s at 1175°C (Fig. 3.3c). Moreover, magmas behave as non-Newtonian (shear-thinning) fluids, where η is dependent of the shear rate ($\dot{\gamma}$) at a certain temperature. This non-linear dependency is expressed as $\tau = \eta_0 \dot{\gamma}^m$, where m is the power-law coefficient for a specific non-Newtonian material at a given temperature and η_0 is the consistency (which differs from viscosity by the power of m). For shear-thinning fluids, m is less than 1, approaching 1 at increasing temperatures (for reference, m = 1 in Newtonian fluids). All our magmas exhibit shear thinning behavior in viscometry experiments, i.e. equilibrium viscosity decreases with increasing rates of deformation (Sonder et al. 2006, Hobiger et al. 2011). At the shear rates experienced in viscometry experiments, the equilibrium viscosity of our three magmas is similar at 1200°C for a given shear rate (Fig. 3.3c, black dashed line). However, the shear rates during the free air expansion phase are believed to be much higher in the current blowout experiments than in viscometry experiments, as detailed in the next sections.

3.6 Magma breakup in experiments

Compared to jet breakup for industrial liquids, the disintegration of the magma plug in our experiments is more complex. First, the magma is ejected as a discrete batch by pressurized gas, whereas classic liquid jets are issued from a pipe at constant rates over a certain amount of time. Second, our magmas are non-Newtonian liquids. Third, a portion of the magma fragmentation takes place inside the crucible, before the magma even exits it (Caffier 1998). Fourth, gravity slows down the upward moving magma plug and drops, whereas industrial liquid jets are

classically issued downwards. Fifth, the jet breakup of the magma plug and especially the drops beyond the field of view of the high-speed camera will be cooled in the atmosphere, influencing their rheology. Nonetheless, the physics of jet breakup still applies, allowing a detailed description of the extra-crucible fragmentation process in our experiments. We first deal briefly with in-crucible fragmentation, then asses the free-air expansion.

3.6.1 In-crucible magma fragmentation

The first stage of magma fragmentation in the experiments is in-crucible fragmentation (Zimanowski et al. 1997). The steel crucible is of course opaque, so the video documentation does not cover in-crucible events. However, injection-type runs (Fig. 3.2c) are similar to molten-fuel coolants (MFCI) experiments, except for the initial fine fragmentation unique to MFCI. So the documentation of MFCI experiments with transparent crucibles (Zimanowski et al. 2015), plus analogue experiments (Zimanowski et al. 1991, 1995, 1997) and theoretical considerations (Reitz and Bracco 1986; Caffier 1998; Eggers and Villermaux 2008; Birouk and Lekic 2009), help reconstruct in-crucible events for gas-driven hydrodynamic magma fragmentation.

As the pressurized argon gas is injected either at the base of (10 MPa series) or within (3 MPa series) the magma, the latter is pushed upward and laterally against the crucible walls, starting the ejection process (Fig. 3.4a). Rayleigh-Taylor instabilities form at the interface between the magma and the gas (Fig. 3.4a) (Zimanowski et al. 1991). The wavelike motion of the unstable magma-gas interface, enhanced by the high density contrast between the two fluids, causes magma droplets to detach once the amplitude reaches a critical level; this is a type of hydrodynamic fragmentation (Caffier 1998; Eggers and Villermaux 2008) (Fig. 3.4b). This process continues either until the magma plug is completely fragmented, or exits the crucible. A certain degree of brittle fragmentation might occur within the crucible at very high driving pressures (Zimanowski et al. 1997). The virtual absence of primary brittle fragments in the ejecta from the current experiments indicates either i) experimental conditions below the critical stress required for brittle fragmentation (Jones et al. 2019), or ii) effective reannealing of small brittle fragments within the hydrodynamic field (Zimanowski et al. 1997).

The amount of fragmentation produced within this stage depends on ejection velocity and magma composition (Zimanowski et al. 1991; Caffier 1998). A larger velocity will enhance in-crucible fragmentation, as the higher acceleration is directly proportional to larger disturbances at the gas-magma interface (Caffier 1998; Sallam et al. 2004; Lefebvre and McDonell 2017). Lower viscosity magmas are also more prone to in-crucible fragmentation (Caffier 1998). This means that an

ultramafic magma pushed by gas at a high driving pressure can exit the crucible already fragmented to a large degree, whereas a more evolved magma pushed at low driving pressure might exit the crucible mostly as a coherent plug.

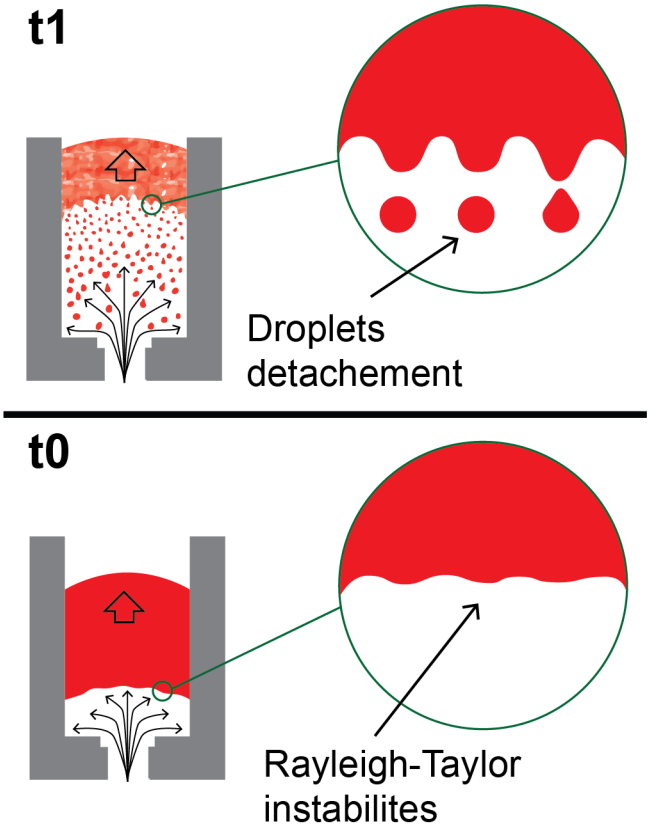

Figure 3.4: Initial movement of the magma plug and in-crucible fragmentation for the blowout-type setup. At t0, pressurized argon gas is injected at the base of the magma. Rayleigh-Taylor instabilities appear at the gas-magma interface. At t1, the wave disturbances reach a critical amplitude, and droplets are detached. This continues until the disturbed magma plug surpasses the crucible opening. In-crucible fragmentation depends on driving pressure and magma composition.

3.6.2 Free-air expansion and final fragmentation

3.6.2.1 Preamble

Figures 3.5 to 3.10 show the visible portion of the experiments. The initial conditions that cause the magma plug to expand in the atmosphere are acquired during acceleration within the crucible. The violent push exerted by the pressurized argon gas generates internal turbulence within the magma volume, initially partly damped by the confined geometry. Once the front of the magma plug surpasses the crucible opening, the sudden pressure release allows its full expansion. Ideally, the magma plug should expand upward and radially from the crucible opening.

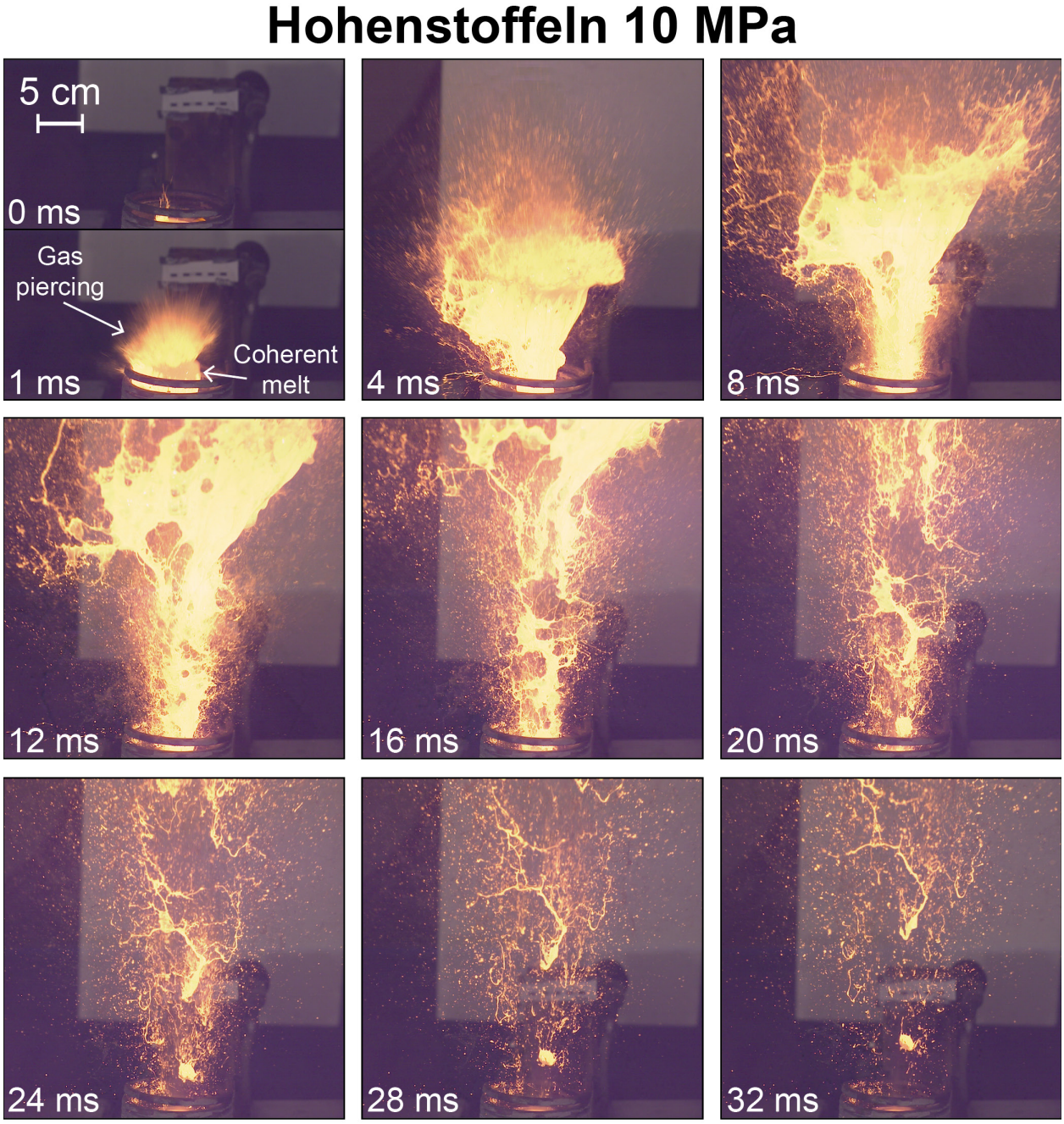

Figure 3.5: Time-lapse of the Hohenstoffeln 10 MPa run, emphasizing the entire free-air fragmentation and expansion of the magma. Time between each frame is 4 ms from the first appearance of the magma front at the crucible opening, plus a special frame at 1 ms to show the location of the gas piercing and coherent portions of the magma plug.

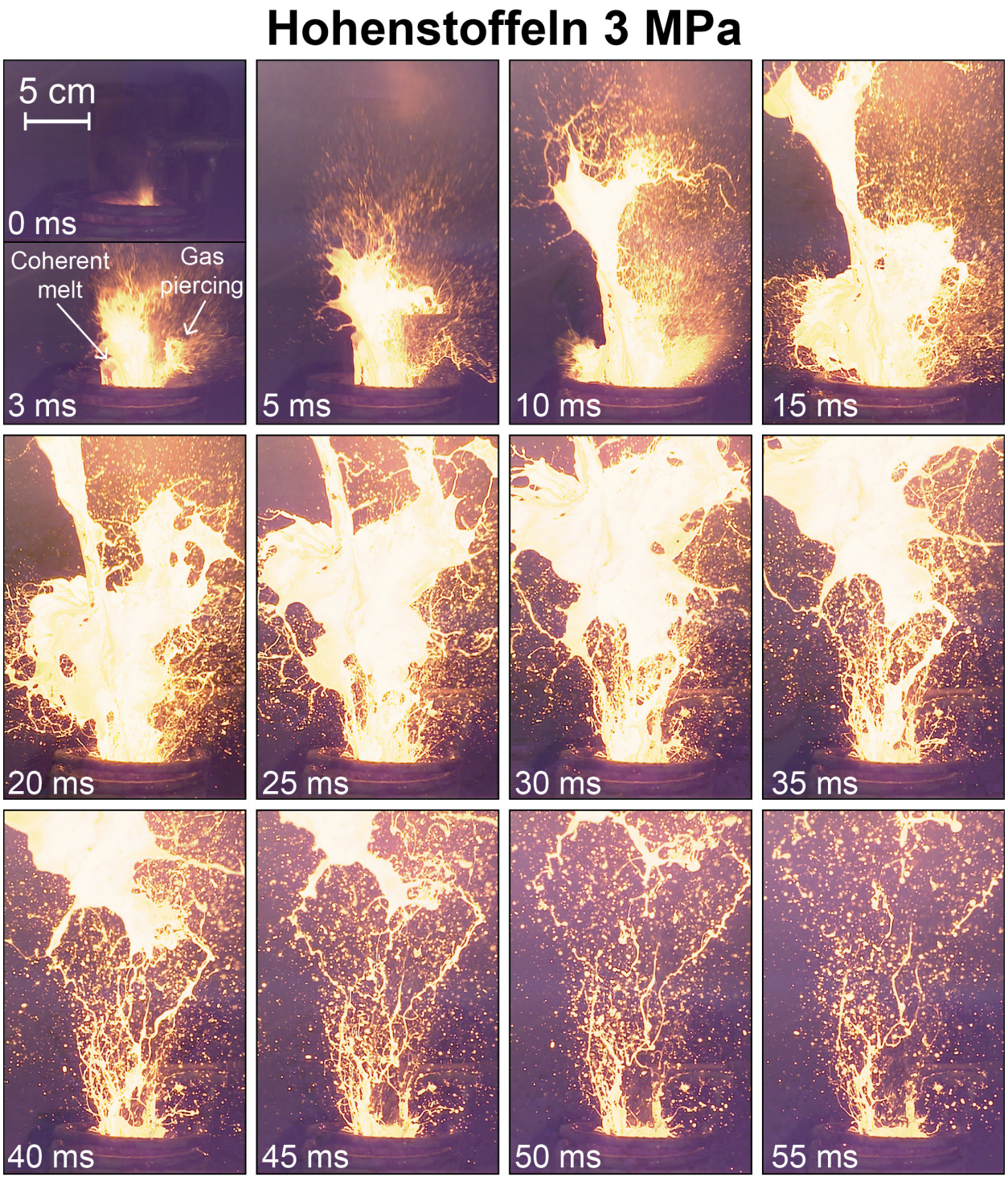

Figure 3.6: Time-lapse of the Hohenstoffeln 3 MPa run. Time between each frame is 5 ms, plus a special frame at 3 ms to show the location of the gas piercing and coherent portions of the magma plug.

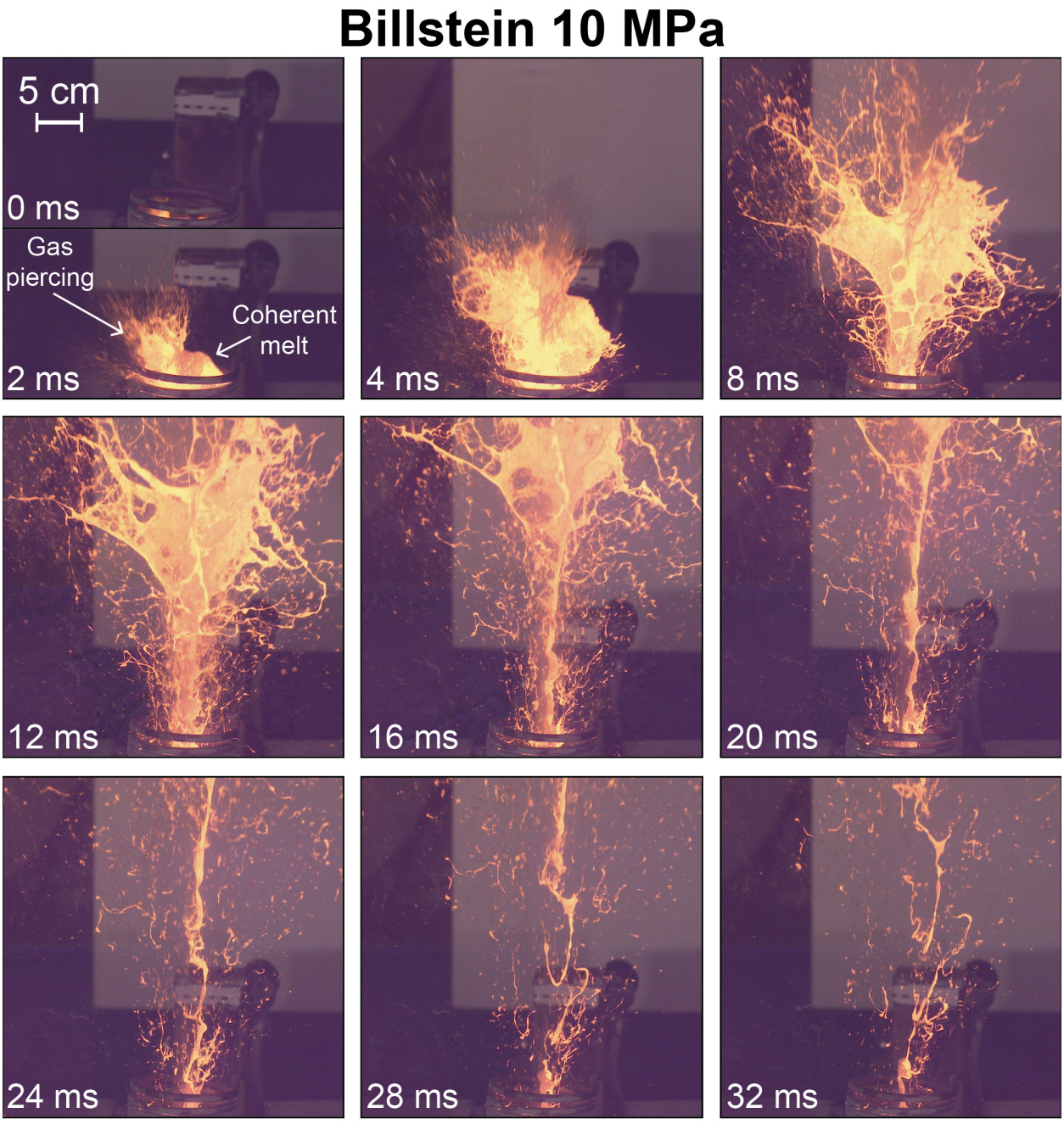

Figure 3.7: Time-lapse of the Billstein 10 MPa run. Time between each frame is 4 ms, plus a special frame at 2 ms to show the location of the gas piercing and coherent portions of the magma plug.

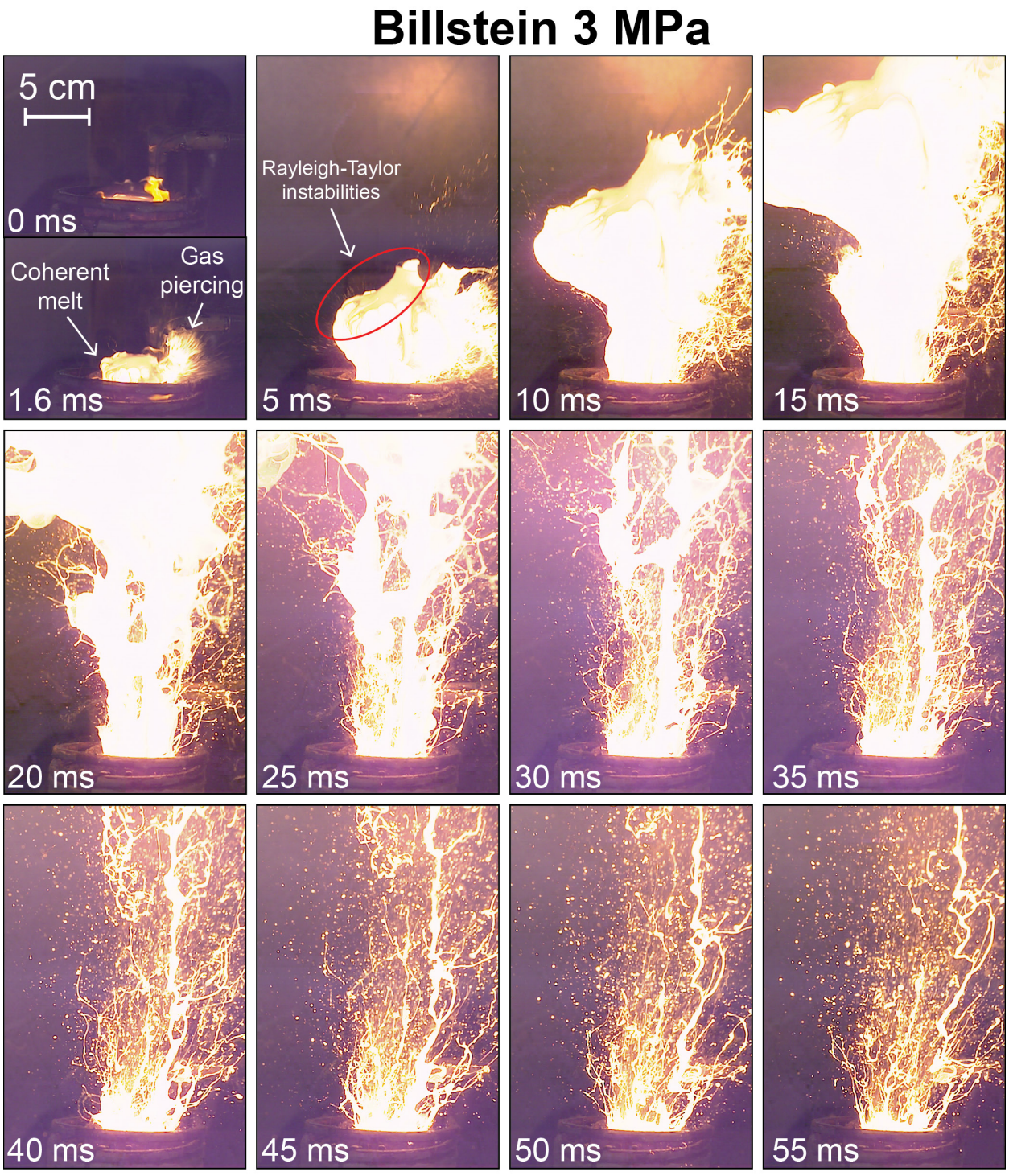

Figure 3.8: Time-lapse of the Billstein 3 MPa run. Time between each frame is 5 ms, plus a special frame at 1.6 ms to show the location of the gas piercing and coherent portions of the magma plug.

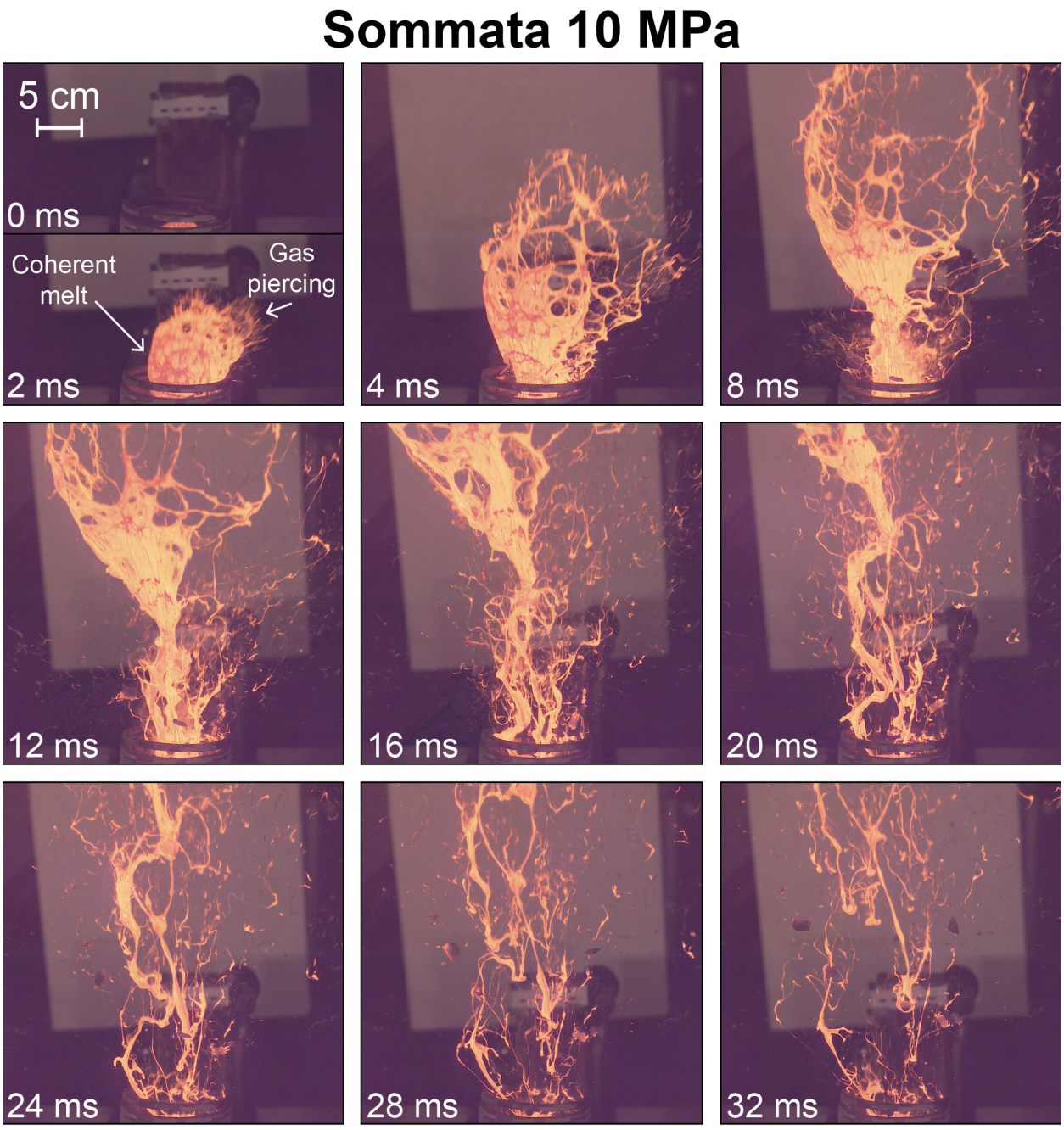

Figure 3.9: Time-lapse of the Sommata 10 MPa run. Time between each frame is 4 ms, plus a special frame at 2 ms to show the location of the gas piercing and coherent portions of the magma plug.

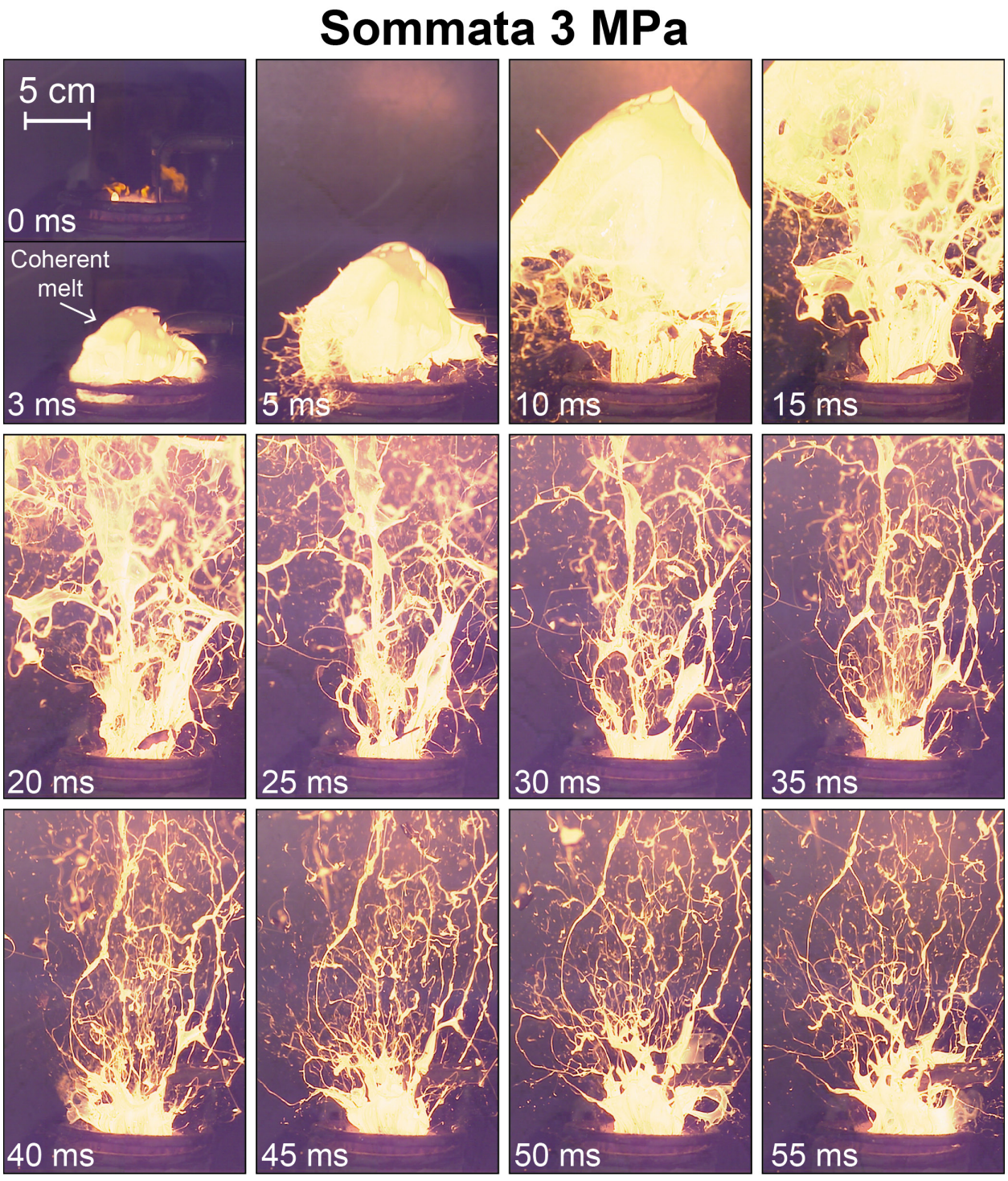

Figure 3.10: Time-lapse of the Sommata 3 MPa run. Time between each frame is 5 ms, plus a special frame at 3 ms, although for this run that was no visible gas piercing effect.

Nevertheless, an uneven spatial distribution of the pressurized argon at the gas-magma interface resulted in the asymmetric uncorking of the magma plug. This gas piercing phase can be observed in both 3 and 10 MPa experiment series (Figs. 3.5 to 3.9) except for the Sommata 3

MPa run (Fig. 3.10), where the more cohesive structure of the magma plug prevented this phenomenon. In the 10 MPa series, the gas piercing phase mostly occurred on the left (relative to the viewing direction of the camera) (see 1 and 2 ms frames in Figs. 3.5, 3.7 and 3.9), whereas in the 3 MPa series the “L” shape of the injection pipe resulted in the rebound and piercing of the gas to the right (see 3 and 1.6 ms frames in Figs. 3.6 and 3.8, respectively). In what follows, we ignore these asymmetric uncorking artefacts produced by the gas piercing effect in order to investigate the jet breakup phenomena.

3.6.2.2 Early stage of the jet

The initial interaction of the still coherent portion of the magma at the non-driven (top) surface is with the stagnant atmosphere. Because of its inertia, the atmosphere starts to impinge on the magma surface, creating Rayleigh-Taylor wave disturbances (Lefebvre and McDonell 2017). A good example of this process is captured during the Billstein 3 MPa at 5 ms (Fig. 3.8). Simultaneously, possible internal turbulence within the magma plug transmits to the surface, amplifying the disturbances (Lefebvre and McDonell 2017). Later on, small drops are finally detached from the magma surface and rapidly propelled in the atmosphere once the amplitude of the wave disturbances reaches a critical level (Eggers and Villermaux 2008; Birouk and Lekic 2009; Lefebvre and McDonell 2017). The amount of early-detached droplets from the plug surface is directly proportional to ejection velocity and inversely proportional to magma viscosity.

The vertical velocities of the magma plug in the early stage of the jet phase are presented in Table 3.1. The measurements were obtained by tracking the visible, coherent portion of the magma plug at the beginning of the free air expansion, over a time interval of 1.5 ms. The travelled distance corresponded to three and about seven frames, respectively for the 10 MPa and 3 MPa series. At one extreme, the Sommata 3 MPa magma plug exits the crucible as a coherent mass with an average velocity of 13 m/s. The plug expands in the air and beyond the field of view as a mushroom head shape with no relevant detachment of small fragments, except for some fragmentation induced by the magma flowing through the induction coil which extends slightly above the crucible (Fig. 3.10). On the other hand, the Hohenstoffeln 10 MPa magma plug exits at an average velocity of 44 m/s, and starts fragmenting immediately (Fig. 3.5).

The visual appearance of the initially coherent portion of the magma plug once it begins to expand in the atmosphere provides a unique opportunity to constrain its breakup regime. Starting with the Hohenstoffeln 10 MPa run, the magma appears to be within regime IV (spray/atomization) (Birouk and Lekic 2009; Lefebvre and McDonell 2017), because of the ease with which it breaks up into

abundant drops several orders of magnitude smaller than the crucible diameter (Fig. 3.5, 12–20 ms).

Both Billstein 10 MPa and Hohenstoffeln 3 MPa runs are likely to be somewhere around the IV-III (atomization – second wind-induced breakup) boundary, with the following observable characteristics: i) the size of the abundant detached droplets is still several orders of magnitudes smaller than the magma plug diameter; ii) the intact length is longer than what is observed for the Hohenstoffeln 10 MPa (Fig. 3.6, 15 ms; Fig. 3.7, 8 ms).

Compared to what is described above, Sommata 10 MPa and Billstein 3 MPa appear to be completely within regime III, because of the relatively smaller amount of detached drops and the length of coherent strips of magma observable in the video footage (Fig. 3.8, 5–15 ms; Fig. 3.9, 12–20 ms). Unlike industrial liquids or our two more mafic magmas, Sommata is much more viscous, and breaks up as threads instead of drops, but this will be discussed in more detail in Chapter 4.

Finally, Sommata 3 MPa is thought to be well within regime II (first wind-induced breakup), due to the early fully coherent appearance of the magma plug (Fig. 3.10, 3-10 ms). When that plug eventually starts to disintegrate, some of the initial separating domains are within the same order of magnitude than the crucible diameter (Fig. 3.10, 15 ms).

These different fragmentation regimes for different runs translate into different grain size distributions, with Hohenstoffeln runs producing finer-grained pyroclasts than Sommata runs (Chapter 4). This is due to a shorter time allowed for fragmentation in lower breakup regimes as well as prolonged thinning at higher silica compositions which delays final breakup.

3.6.2.3 Intermediate and final stages of the jet

In the intermediate stage, further upward and away from the crucible, the magma progressively decelerates due to gravity. Prolonged flow of argon from below continues to provide partial thrust to the yet unfragmented, but unstable, portion of the magma mass, which moves toward different directions as several lobes or even threads, each one with a different velocity.

The final upward stages of the experiments involve the thinning (stretching) and secondary breakup of the now several thousand newly formed drops and filaments, depending on the magma composition. For the front part of the magma jet, this portion of the fragmentation process occurred outside the field of view of the high-speed camera, but the process can be clearly observed in the tail of the jet (Figs. 3.5-3.7-3.9, 20–32 ms; Figs. 3.6-3.8-3.10, 30–55 ms).

3.7 Discussion

3.7.1 Jet breakup regimes in the experiments

In the previous section we visually associated a breakup regime to each of the experimental runs. Observed regimes during initial expansion beyond the crucible range from a spray (regime IV) for Hohenstoffeln at 10 MPa to the first wind-induced breakup regime (regime II) for Sommata at 3 MPa. Only gas driving pressure and melt material were changed between each run, not the crucible geometry. Therefore, the parameters left that change the Weber and Reynolds numbers, and are suspected to be responsible for the observed variety in breakup regimes, are ejection velocity and magma viscosity.

In order to take into account the non-Newtonian (shear-thinning) nature of our tested magmas, we calculated Reynolds numbers specifically for power-law fluids (from Madlener et al. 2009): $Re_{pl} = \frac{\rho \cdot u^{2-m} \cdot d^m}{\eta_0} f_m$, with $f_m = \frac{8^{1-m}}{\left(\frac{3 \cdot m+1}{4 \cdot m}\right)^m}$. Values of m for Hohenstoffeln and Sommata magmas are available from Hobiger et al. (2011), and for Billstein from Sonder et al. (2006).

For each run, the values of the physical parameters used to compute both *We* and Re_{pl} are presented in Table 3.1. We consider the early stage of the free air expansion of the coherent magma plug, so we assume that the relevant characteristic length (i.e., our "nozzle diameter") is the inner diameter of the crucible, 5 cm. We used the same surface tension value for all runs, for simplicity (recall that surface tensions vary very little between magmas, see Fig. 3.3). Density among the three magmas varies within a limited range. We calculated an overall ejection velocity for the coherent portion of the melt plug, focusing on the first 1.5 ms after a traceable part becomes visible. Magma viscosity is the major unknown, since:

(i) Magmas (especially Hohenstoffeln and Billstein) display non-Newtonian behavior, but there are no instantaneous viscosity measurements at the relevant, very high shear rates (which themselves are unknown).

(ii) A single value of viscosity cannot be assumed for an unstable mass of magma propelled at high speed into the atmosphere. For individual runs, viscosity may be changing over time and space.

For illustration purposes, we used all available rheology data for our magmas generated through viscometry experiments within the 1175–1200°C temperature range (Sonder et al. 2006; Hobiger et al. 2011). We hope that the correct instantaneous viscosity for each run is within the utilized

range, which is several orders of magnitude wide in some cases, providing a safety margin, but we cannot be certain of that.

The two dimensionless numbers are plotted in our modified Ohnesorge diagram (Fig. 3.11). Our experiments plot partly beyond the known regime boundaries, defined from data on diesel sprays used in internal combustion engines (Lefebvre and McDonell 2017). Specifically, our Weber numbers are higher, because of the larger density, surface tension and jet diameter relative to typical industrial applications. Our Reynolds numbers are also likely to be different (extending to lower ranges), because of magma viscosity values between four and seven orders of magnitude higher than diesel fuels or water.

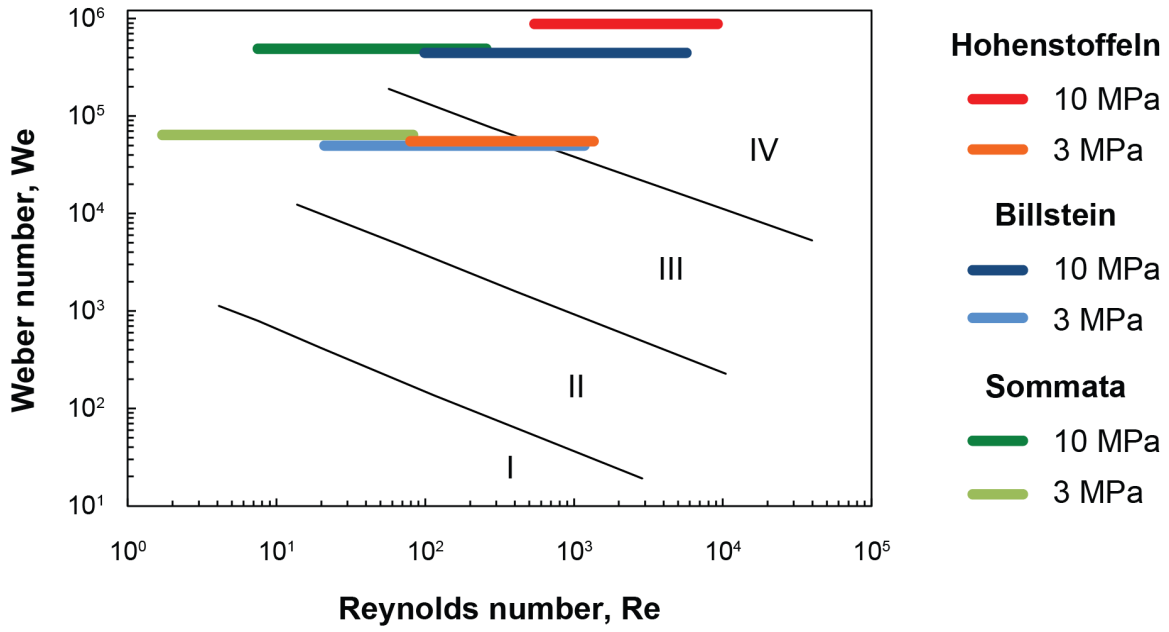

Figure 3.11: Modified "Ohnesorge" diagram showing the Weber and Reynolds numbers, applied to the early stage of the jet phase during free air expansion, for each experimental run. See text and Table 3.1 for how each experiment was positioned on this diagram.

Hohenstoffeln 10 MPa is visually (on the high-speed video) in regime IV (Table 3.1), and indeed plots there on the *We-Re* diagram (Fig. 3.11). Billstein 10 MPa and Sommata 10 MPa are qualitatively observed to be somewhere between regimes IV and III and within regime III, respectively, but plot mostly within regime IV. A better fit exists for Hohenstoffeln 3 MPa and Billstein 3 MPa, which both plot in the 'correct' regimes (Fig. 3.11). However, Sommata 3 MPa visually appears to be within regime II, but on the diagram it is rather inside regime III or its presumed extension.

The discrepancies that occur between the observed regimes on the high-speed videos and where the experiments plot on Fig. 3.11 could be from the use of incorrect viscosity values. Secondly, the diagram may not be fully applicable to magmas and/or our experimental design. Determination of jet breakup regime boundaries at higher *We* values and perhaps lower *Re* values should be the focus of future work. For example, analogue fluids with rheological behavior, viscosities, densities and surface tensions similar to our magmas, could be investigated in jet breakup experiments to verify and extend the regime boundaries.

3.7.2 Jet breakup regimes in Hawaiian eruptions

Rather than dense magma being pushed up and fragmented by suddenly injected pressurized argon gas as in our experiments, in natural lava fountains, a magma column is rapidly accelerated upward by exsolved volatile gases coupled to the magmatic melt (Parfitt 2004; La Spina et al. 2021). Our experimental transient magma jets last less than 1 s (Zimanowski et al. 1997), whereas natural lava fountains episodes can be sustained for several hours to a few days (Gonnermann and Manga 2013; Taddeucci et al. 2015). But despite the apparent “steady” appearance of some lava fountain phases, they are actually produced by the fast repetition of discrete pulses (Taddeucci et al. 2015). In this regard, our experiments might be regarded as comparable to a single pulse of a lava fountain, and to some extent to an instant in the emission of an industrial liquid jet breaking up within a certain regime.

Strong, high and narrow lava fountains partly resemble full sprays, hence liquid jets in regime IV. Viable examples from Hawaii include the Pu'u 'Ō'ō (Kīlauea) 1983 eruption episode 23 (Fig. 3.12a), or Kīlauea Iki 1959 episodes 1 and 3 (Fig. 3.12b, c).

Some weaker, stubbier, lower fountains might be in regime III, with many clasts forming but an intact (unfragmented) liquid core near the vent that is either observable or at least plausible (the external fragmented part of the fountain tends to hide the coherent internal part, if present). Examples include Bardarbunga-Holuhraun (Iceland) 2014 (Fig. 3.12d), or the Lower East Rift Zone (Kīlauea) 2018 fissure 22 (Fig. 3.12e).

Jet breakup characteristics similar to regime II might be seen where very weak fountains feed lava flows. Fragmentation is coarse, and the weak jet might be largely unfragmented when first exiting the vent. Most clasts probably coalesce back together upon landing. An example is the Lower East Rift Zone (Kīlauea) 2018 fissure 8 (Fig. 3.12f, g).

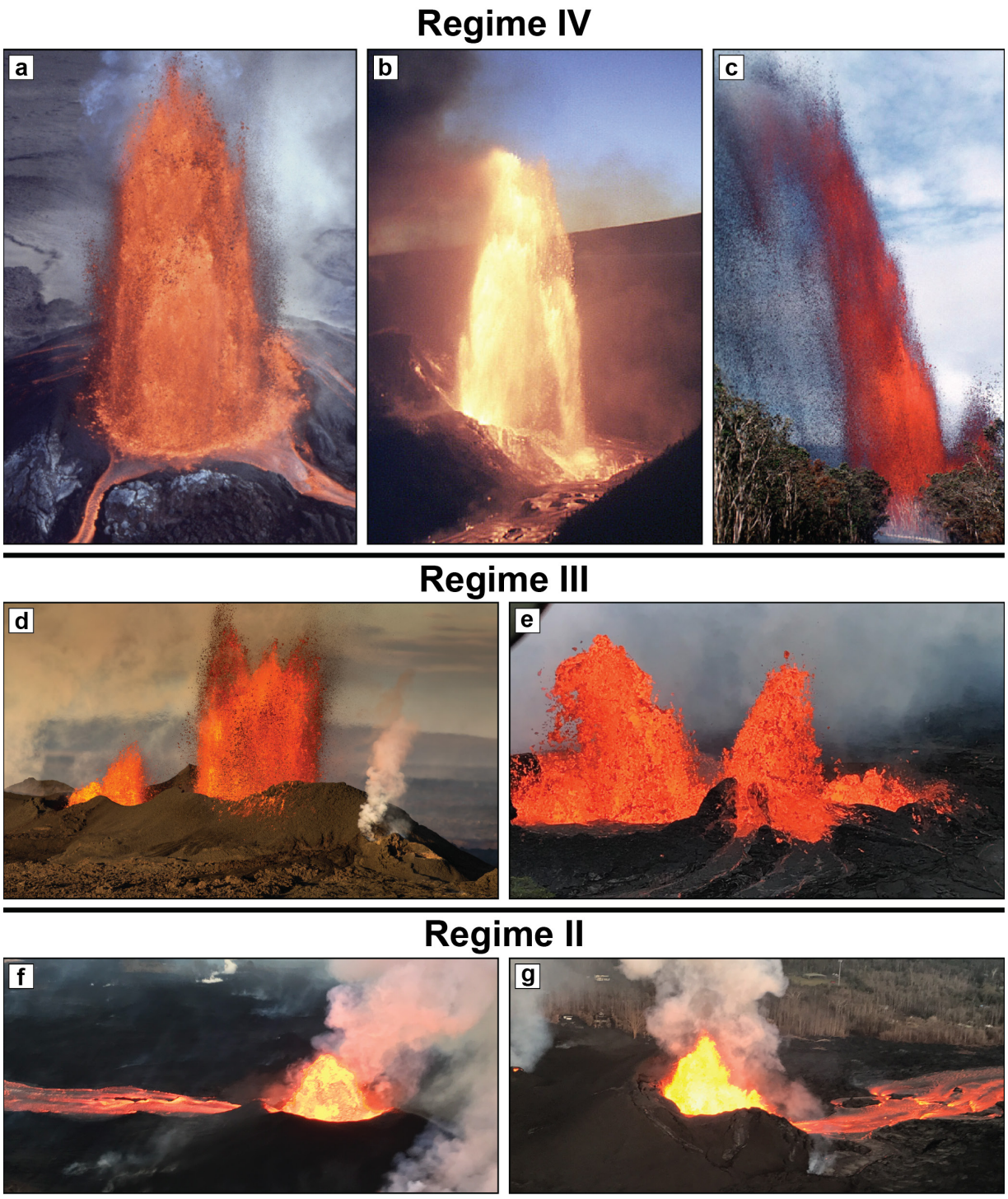

Figure 3.12: Potential examples of breakup regimes in lava fountains: (a)-(c), regime IV, (d)-(e) regime III, (f)-(g) regime II. (a) Episode 23, Pu'u 'Ō'ō eruption (Kīlauea), July 28, 1983 (Hawaii, U.S.A). Credit: U.S. Geological Survey/photo by J.D. Griggs. (b) Episode 1 of the Kīlauea Iki eruption, November 18, 1959 (Hawaii, U.S.A). Credit: U.S. Geological Survey. (c) Episode 3 of the same eruption, November 29, 1959. Credit: U.S. Geological Survey. (d) Bardarbunga-Holuhraun eruption, September 13, 2014 (Iceland). Credit: Tom Pfeiffer / www.volcanodiscovery.com (used with permission). (e) Fissure 22, Lower East Rift Zone (Kīlauea), May 21, 2018 (Hawaii, U.S.A). Credit: U.S. Geological Survey. (f) Fissure 8, Lower East Rift Zone (Kīlauea), (Left) June 7, 2018. (g) Same eruption, June 9, 2018. Credit: U.S. Geological Survey.

Regime I-type jets probably do not occur in Hawaiian eruptions because they would be largely dampened by gravity. So regime I and the even weaker dripping regime are likely replaced by lava oozing from the vent without fragmentation (Parfitt 2004; Gonnermann and Manga 2013).

3.7.3 Controls on natural lava fountains

Although La Spina et al. (2021) focus on high *Re* as leading to strong lava fountains in their simulations, our work suggests that high *We* values are also important to reach regime IV. This leads us back to figure 3.1d, which can be used to discuss the controls on natural lava fountains.

3.7.3.1 Ejection speed

In general, a certain mass discharge rate will be needed to reach and stay within the fountaining style. In the initial stage of a fountain pulse, assuming both conduit diameter and viscosity to be constant, increasing ejection velocity would result in a shift towards the atomization regime (regime IV).

3.7.3.2 Conduit size

All else being equal including the ejection speed, a larger conduit diameter (and therefore a high mass eruption rate) would favor development of internal turbulence within the flow, and would therefore promote the transition to higher regimes. However if the mass ejection rate is fixed, a smaller conduit favors a higher ejection velocity. This is why fissures that evolve to cylindrical conduits favor fountaining (Jones et al. 2017).

3.7.3.3 Viscosity

On the contrary, an increase in magma viscosity (e.g., a slightly more silicic chemical composition, or a slightly lower magma temperature) would cause a fountain pulse to begin in a lower regime, with less or no atomization. Alternatively, a magma with a higher viscosity would require a larger ejection velocity in order to produce and sustain a lava fountain, relative to an ultramafic or hot mafic magma.

During a fountaining episode, an overall decrease in magma temperature over time combined with increased crystallization and decrease in volatiles would impede late pulses to attain highest breakup regimes relative to the earlier pulses (Cashman and Scheu 2015; Taddeucci et al. 2015). Moreover, possible drainback of colder, crystallized and degassed lava into the vent would

decrease the overall magma temperature, contributing to the transition to lower regimes (Wallace et al. 1998).

3.7.3.4 Bubbles and density

In lava fountains, the abundance of gas bubbles introduces some contrasting phenomena. From a jet breakup perspective, a higher volume fraction of bubbles would decrease the bulk density of the magma, therefore theoretically promoting the transition towards the Rayleigh regime (Fig. 3.1d). However, this effect of gas bubbles on density is likely cancelled by magma acceleration in the conduit, so that the net effect of more bubbles is higher *We* and *Re*.

3.7.3.5 Surface tension

Like in industrial liquids, the hydrodynamic breakup of natural magmas in lava fountains is strongly influenced by surface tension, with which the other internal properties and aerodynamic effects compete. Although surface tension varies only within a limited range in magmas, other variables vary greatly and dictate whether the effects of surface tension will dominate or not. During the climax of large lava fountain episodes, surface tension is overwhelmed by ejection velocity and aerodynamic effects, typical for regime IV (atomization). By contrast, magma fragmentation in relatively low and weak fountaining episodes would be dominated by surface tension.

3.8 Conclusions and outlook

After reviewing the breakup of liquid jets in industrial and commercial applications, we ejected remolten volcanic rocks from a crucible using compressed gas, leading to the formation of transient ‘magma’ jets. Changing the gas driving pressure and the magma compositions in the experiments led to three different regimes of liquid jet breakup. Our modified Ohnesorge diagram plotting *We* versus *Re* and our experimental “fountain pulses” suggest how the relative competition among different internal melt properties and external aerodynamic effects might lead to various jet breakup regimes. Magma viscosity and ejection velocity seem to be the main factors controlling regime transitions, because these parameters can vary by several orders of magnitude. A higher ejection velocity will result in higher internal turbulence and strong external aerodynamic effects, leading to the fine primary breakup of the magma, within the atomization/spray regime. Lower ejection velocities allow surface tension to play a bigger role, dampening atomization. Magma viscosity has the reverse effect: a lower viscosity favors sprays.

A preliminary examination of natural lava fountains suggests that these three regimes might also occur in Hawaiian eruptions. Lava fountain pulses might be potentially regarded as discrete jets with breakup behaviors ranging from regime II (very weak fountains at the head of lava flows) to regime III (moderate fountains with a perturbed but intact liquid core) and regime IV (fully developed sprays in strong fountains).

This study represents only a first, preliminary attempt to characterize jet breakup mechanisms of discrete pulses such as those occurring in lava fountains and Strombolian eruptions. Significant future work is warranted. First, calculating *We* and *Re* requires correct input parameters. A key issue is the magma rheological response over milliseconds, at very high deformation rates. Instantaneous viscosity values needed for *Re* calculations of transient magma jets seem to be different from those obtained through chemical models or viscometer experiments. Then there is potential to further improve our *We*-*Re* diagram to better fit conditions in lava fountains. Regime transitions in various conditions including high *We* and/or low *Re* could be accessed through fragmentation experiments using analogue liquid materials able to mimic some aspects of magma behavior, minus the challenges involved in working with molten rock. Finally, high-speed video analysis of actual lava fountains could then be used to validate the diagram

3.9 Declaration of competing interest

The authors declare that they have no known competing financial interests or personal relationships that could have appeared to influence the work reported in this paper.

3.10 Acknowledgments

This project was funded by a NSERC Discovery Grant to PSR. We thank Jacopo Taddeucci and Lucy Porritt for reviewing a draft of the manuscript.

4 THIRD ARTICLE: PYROCLAST SHAPES IN LAVA FOUNTAINS

Controls on juvenile ash morphologies in lava fountains: insights from laboratory experiments

Contrôles sur la morphologie des cendres juvéniles dans les fontaines de lave: nouvelles idées provenant d'expériences en laboratoire

Authors:

Pier Paolo Comida[1], Pierre-Simon Ross[1], Bernd Zimanowski[2], Ralf Büttner[2], Tobias Dürig[3]

1. Institut national de la recherche scientifique, 490 rue de la Couronne, Québec (Qc), G1K 9A9, Canada

2. Physikalisch Vulkanologisches Labor, Universität Würzburg, Pleicherwall 1, 97070, Würzburg, Germany

3. Institute of Earth Sciences, University of Iceland, Sturlugata 7, 101 Reykjavík, Iceland

Title of the journal:

Bulletin of volcanology

Ready to submit

4.1 Abstract

Hawaiian lava fountains produce a wide variety of pyroclasts, including achneliths, i.e. fluidal juvenile fragments. These range from nearly perfect spheres to very elongate Pele's hairs, but the controls on such variations are not yet entirely clear. We therefore conduct laboratory-scale experiments using magmas of three different compositions (olivine-melilitite with 38 wt.% SiO_2, alkali basalt with 45 wt.% SiO_2, and basaltic trachyandesite with 54 wt.% SiO_2). These magmas are ejected from a crucible using two different gas driving pressures (3 and 10 MPa) which correspond to low and high exit velocities. All magmas are at the same initial temperature of 1200°C, and each run is somewhat comparable to a very short (< 1 s) lava fountain or strombolian pulse. We collect and sieve the artificial ejecta and focus on two ash fractions, 0.71–0.5 mm (narrow + 1ϕ) and 88–63 µm (narrow + 4ϕ). We measure the componentry, morphometric parameters and internal textures of these particles. We find two end-members in terms of fluidal ash morphologies: (1) olivine-melilitite ejected at low velocity mostly generates spheres and other compact shapes; (2) basaltic trachy-andesite ejected at high speed mostly generates Pele's hairs and other elongate shapes. Natural achneliths from the 1959 Kīlauea Iki eruption (Hawaii, USA) are most similar in shape to the artificial ones generated with the alkali basalt ejected at high speed, and mostly consist of fluidal elongate grains and Pele's tears.

We analyze shape-controlling processes using high-speed video recordings of the experiments, and filament thinning theory. When hydrodynamic fragmentation occurs, surface tension acts to reshape clasts towards a sphere. Opposing factors can extend filament thinning timescales, and the two most relevant ones here are magma viscosity and ejection speed. This, along with the effects of rapid cooling, largely explains the observed morphological variety in artificial and natural fluidal-shaped juvenile ash.

4.2 Introduction

Hawaiian lava fountains are a spectacular and relatively frequent style of subaerial explosive activity (Richter et al. 1970; Taddeucci et al. 2015; Houghton et al. 2016). They can occur for example on intraplate shield volcanoes (e.g., 1959 Kīlauea Iki eruption, USA; Richter et al. 1970; Mueller et al. 2018), on stratovolcanoes (e.g., 2015 summit eruption of Mount Etna, Italy; Andronico et al. 2008; Corsaro et al. 2017) and in monogenetic fields (e.g., Hopi buttes volcanic field, USA; Latutrie and Ross 2020). A fountain episode is the sum of multiple closely spaced fragmentation pulses of low-silica magma (Cashman and Scheu 2015). Lava fountains display

large fluctuations in mass flux rates, and fountain heights range from near zero to over 1500 m (Calvari et al. 2018). Fountain durations range between several hours and a few days (Taddeucci et al. 2015; Mueller et al. 2018). Convective ash plumes rising above lava fountains can reach up to several kilometers high (Richter and Murata 1966; Andronico et al. 2015; Corsaro et al. 2017), representing an important source of hazard (Andronico et al. 2015; Mueller et al. 2018; Neal et al. 2018).

The study of juvenile pyroclasts remains essential to understand primary magma fragmentation. In lava fountains, coarse lapilli and bombs (see White and Houghton 2006 for definition of grain size terms) are deposited close to the vent following ballistic trajectories (Fig. 4.1a) (Walker and Croasdale 1971; Stovall et al. 2011). Smaller juvenile pyroclasts lofted within the fountain and ash plume are deposited at progressive distances from the vent as fallout deposits (Taddeucci et al. 2015). This forms a fallout blanket of lapilli and mostly coarse ash (Richter et al. 1970; Andronico et al. 2008; Taddeucci et al. 2015; Calvari et al. 2018). The shapes of juvenile pyroclasts in the blanket range from fluidal achneliths with smooth surfaces, such as Pele's spheres, tears and hairs (Walker and Croasdale 1971), to vesicle-dominated morphologies (Stovall et al. 2011). Scoria, transitional fragments and golden pumices are recognized by the progressive shift from a closed to open vesicular network, up to the extreme ≥ 95% open-cell froth observed in reticulite (Heiken 1972; Mangan and Cashman 1996; Porritt et al. 2012).

Ash-sized fluidal juvenile grains are the particles most likely to preserve original morphologies and internal textures acquired upon, or shortly after, magma fragmentation (Porritt et al. 2012). Their relatively small size implies rapid cooling, only moderate vesiculation overall, and limited post-fragmentation vesiculation in particular (Stovall et al. 2011; Porritt et al. 2012). Ash-sized juvenile grains in general are also of interest for comparative studies of primary magma fragmentation (Dellino and La Volpe 1995; Andronico et al. 2009; Dürig et al. 2012a; Jordan et al. 2014; White and Valentine 2016; Dürig et al. 2020a, 2020b; Chapter 2; Appendix I). In lava fountain deposits, but also weak Hawaiian and Strombolian styles, a wide variety of fluidal morphologies are observed (Walker and Croasdale 1971; Heiken 1972; Stovall et al. 2011; Villermaux 2012; Cannata et al. 2019). Insights from industrial jets involving other fluids provide a general base to understand the formation of spherical droplets versus long threads (Reitz and Bracco 1986; Shimozuru 1994; Jones et al. 2019). However, lava fountains are much more complex than industrial jets, due to factors such as the multiphase nature of magmas, the variable exit velocities over time, and the effect of rapid cooling of pyroclasts from magmatic temperature.

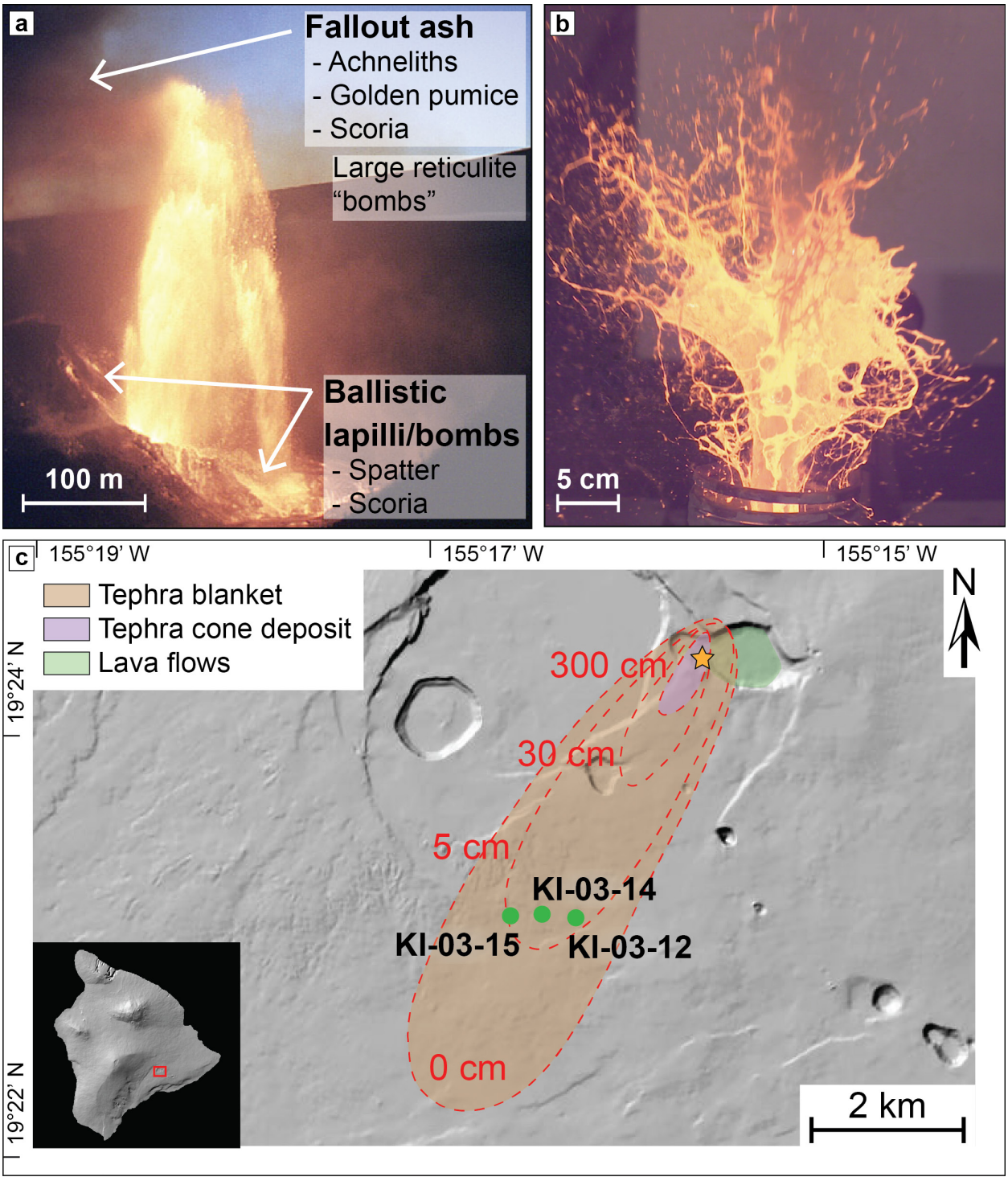

Figure 4.1: Lava fountains and melt ejection experiments. (a) 18 November fountain from episode 1 of the 1959 Kīlauea Iki eruption. The bulk of the ejected, coarse-grained mass tend to be dispersed locally, while gas and finer fragments rise buoyantly, creating an ash (and lapilli) plume, to be deposited further from the vent as a fallout blanket (image credit: U.S. Geological Survey). (b) Alkaline basalt jet from the "high speed" (10 MPa) experimental series. (c) Schematic isopach map of the tephra deposit from the summit portion of the 1959 Kīlauea Iki eruption, with location of the three samples used in this study (green dots). Zero and 5 cm isopachs from Mueller et al. (2019); 30 and 300 cm isopachs from Richter et al. (1970). DTM base source: USGS.

So what controls the morphologies of fluidal juvenile particles in lava fountains? To address this question, we use fragmentation experiments involving remolten volcanic rocks (informally called “magma” henceforth) to explore different sources of morphological variation. The magma is expelled from a crucible using compressed gas, and this forms a transient fragmenting liquid jet in the atmosphere. The artificial pyroclasts are collected and analyzed, based largely on the workflow of Appendix I. We focus on a coarse ash fraction and a very fine ash fraction. The componentry and morphometric data on the artificial pyroclasts is then compared with that obtained on distal deposits from the 1959 Kīlauea Iki eruption. Finally, we combine insights from the high-speed video footage of the experiments and filament thinning theory to assess i) the role of internal magma properties and external factors such as exit velocity in producing the observed morphological variety; and ii) how cooling might interfere with the reshaping process. We also highlight the limits of the very fine ash fraction in comparative studies of primary magma fragmentation for relatively low-intensity explosive styles.

4.3 Methods

A detailed description of the methodology is presented in Online Resource 4.1[3], and a summary is provided here.

4.3.1 Experiments and samples

Artificial juvenile pyroclasts are produced through hydrodynamic (ductile) magma fragmentation experiments at the *Physikalisch Vulkanologisches Labor* (University of Würzburg, Germany). Olivine-melilitite (Hohenstoffeln, ~ 38 wt.% SiO_2), alkaline basalt (Billstein, ~ 45 wt.% SiO_2) and basaltic trachyandesite (Sommata, ~ 54 wt.% SiO_2) are prepared in granulated form and re-melted in a steel crucible up to 1200°C within 1 hour. Magma is then pushed out and fragmented through the injection of pressurized argon gas at 3 or 10 MPa. The combination of three compositions and two driving pressures led to six different successful experiments, recorded with high-speed and regular cameras (Online Resource 4.2). Ejection velocity measurements of (i) clouds of droplets from the gas-piercing effect (explained below), (ii) the coherent magma plug upon crucible exit, and (iii) single drops were performed through the video footage of the experiments. Hydrodynamic fragmentation of each magma mimics a single lava fountain pulse (Fig. 4.1b), producing mainly vesicle-poor, achnelith-type juvenile pyroclasts. The discrete nature

[3] Online Resource 4.1 appears at the end of this chapter.

of the fragmentation pulse also resembles a Strombolian pulse, where subordinate achneliths might also be present (Andronico et al. 2014; Cannata et al. 2019).

Natural juvenile fragments are selected from distal tephra deposits (3.5–4 km from the vent) of the 1959 Kīlauea Iki summit eruption (Fig. 4.1c), produced by sustained fountaining episodes (Richter et al. 1970; Mueller et al. 2018). These basaltic (~ 49 wt.% SiO_2; Murata and Richter 1966) juvenile fragments range from achneliths to pumice.

4.3.2 Analysis of samples

Experimental and natural samples are characterized at INRS, broadly following the workflow of Appendix I. Samples are first gently hand-sieved, providing a full-ϕ grain-size distribution (Fig. 4.2). Extra sieves are used to narrow down the two ash fractions of interest for this study, 710–500 µm (narrow + 1ϕ) which is in the coarse ash range, and 88–63 µm (narrow + 4ϕ), which is part of the very fine ash range. These fractions are cleaned ultrasonically.

For the narrow + 1ϕ fraction, juvenile particles are extracted under the binocular. Images are obtained to carry out componentry measurements of these juvenile grains. Componentry relies on a hierarchical classification that distinguishes fluidal, transitional, vesicle-dominated and angular particles, based on luster, overall morphology, surface characteristics and internal texture (Fig. 4.3 and Online Resource 4.1). A number of juvenile particles are then mounted as a polished epoxy grain mount (PEGM) for each sample.

For the narrow + 4ϕ fraction, a carbon tape grain mount (CTGM) is prepared using the bulk size fraction. The juvenile particles are then distinguished from non-juvenile ones under the scanning electron microscope (SEM). A morphological classification of the juvenile particles is done based on SEM images using the already mentioned hierarchical scheme; this is the equivalent of componentry but relying only on particle shape.

SEM images of both particle cross-sections (narrow + 1ϕ fraction) and silhouettes (narrow + 4ϕ fraction) are processed in order to obtain morphometric and textural data using both the PASTA (Chapter 2) and PARTISAN (Dürig et al. 2018) softwares. All measurements on the particles used in this study are available in Online Resource 4.3. All raw SEM images are available online from the Zenodo.org data repository (Comida et al. 2021c).

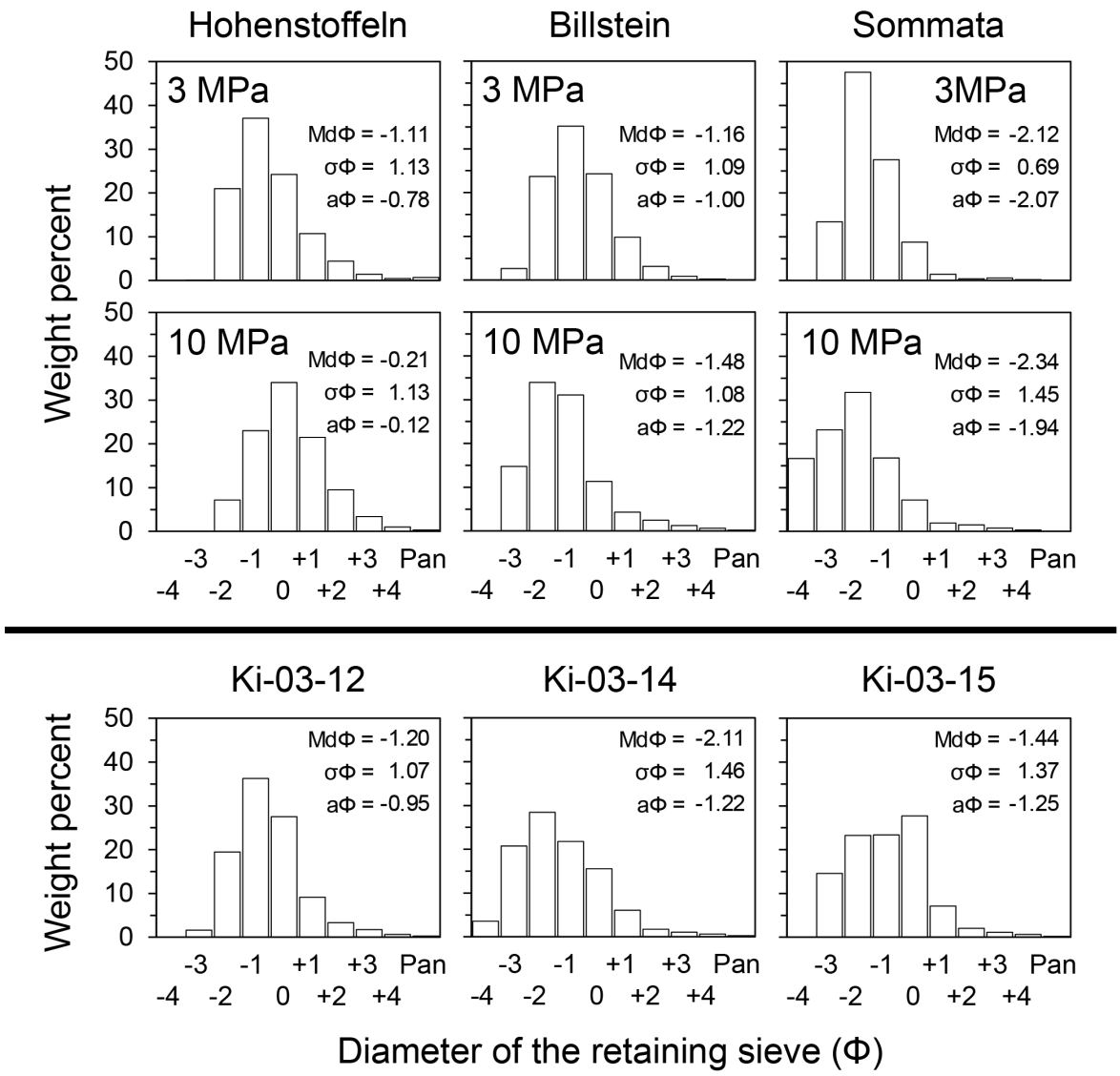

Figure 4.2: Grain size distributions of the nine tested samples, based on manual dry sieving with full-phi sieves. Top two rows, artificial samples. Bottom row, natural samples.

4.4 Results

4.4.1 Grainsize distribution

The natural and experimental samples tested in this work are generally well sorted, characterized by a unimodal grainsize distribution of variable symmetry (Fig. 4.2). For the 3 MPa experimental series, median (Mdϕ, Folk and Ward 1957) values are within the fine lapilli range (following White and Houghton 2006), from about - 2ϕ to - 1ϕ. The distribution is positively skewed (aϕ, Walker and Croasdale 1971), with an abrupt upper limit, then a gently sloped tail.

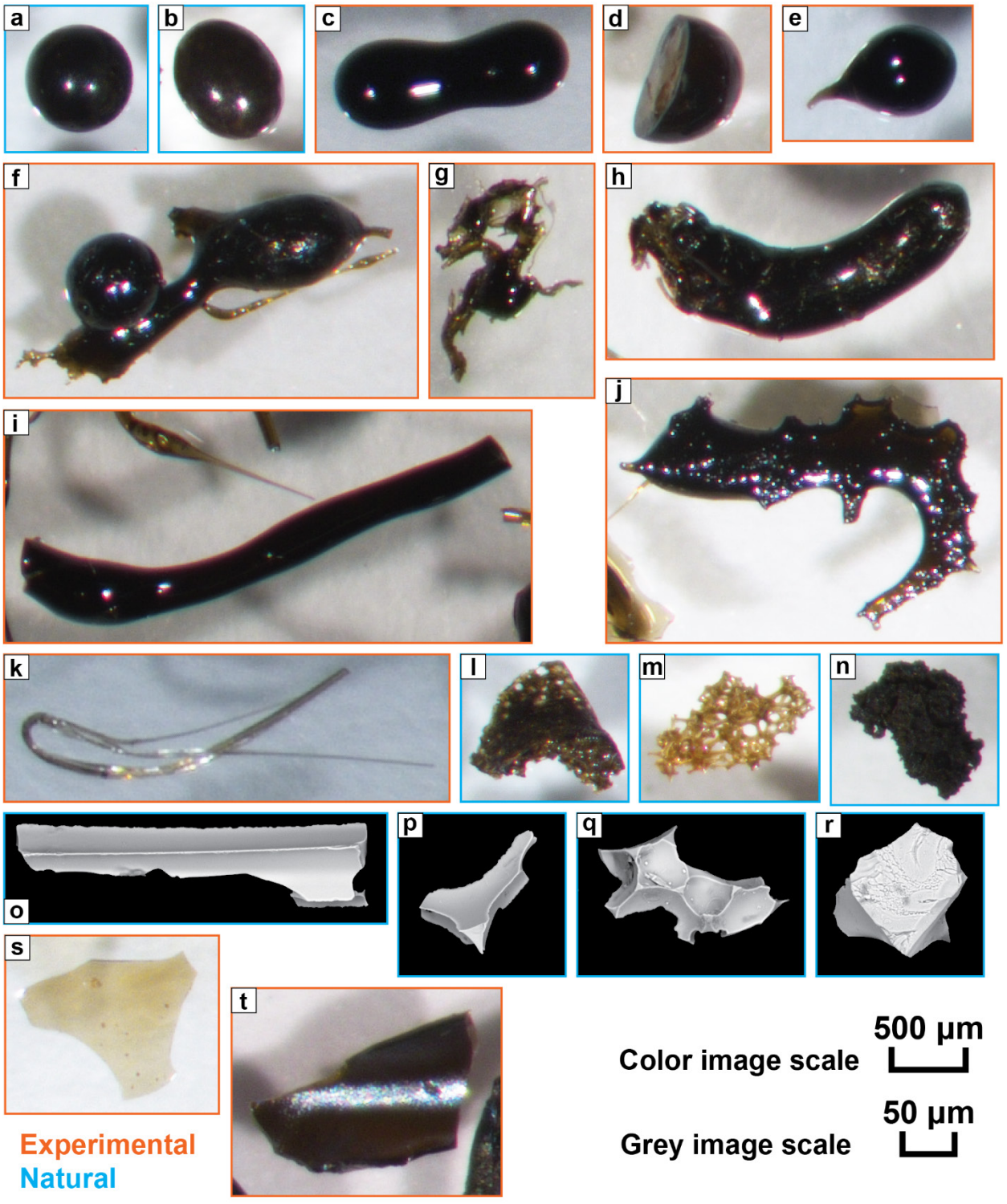

Figure 4.3: Binocular microscope (color) and SEM-BSE (greyscale) images of both natural (blue box frame) and experimental (orange box frame) juvenile pyroclasts, representing each class of the hierarchical classification: (a) spherical; (b) ovoid; (c) lobate; (d) equant broken; (e) Pele's tear; (f) welded; (g) irregular; (h) sub-elongate; (i) thick Pele's hair; (j) ragged elongate; (k) thin Pele's hair; (l) transitional; (m) golden pumice; (n) scoria; (o) VD_elongate; (p) vesicle wall; (q) vesicular-irregular; (r) blocky; (s) glass film; (t) platy.

The Sommata sample shows the coarsest median values. Moving to the 10 MPa series, Mdϕ values range from about - 2ϕ to 0ϕ. Lower skewness values imply a positively skewed to nearly symmetrical distribution. Again, coarser median values set Sommata apart from the more mafic samples. As discussed by Chapter 3, the varying median grain sizes between experiments might be related to different regimes of liquid jet breakup.

The Kīlauea Iki samples are characterized by Mdϕ values between about - 2ϕ to - 1ϕ and are positively skewed to nearly symmetrical. Both the experimental Billstein samples and the natural Kilauea samples are basaltic and have similar grain size distributions. Of course, our Kīlauea samples are relatively distal (near the 5 cm isopach, Fig. 4.1c), and proximal samples from the same eruption would be much coarser than those studied, and much coarser than the experimental samples.

4.4.2 Detailed juvenile componentry of the coarse ash fraction

In experimental samples, juvenile particles in the narrow + 1ϕ (710–500 μm) size range are almost entirely represented by fluidal grains, with subordinate angular fragments (Fig. 4.4). Natural counterparts are instead characterized by a more varied distribution among fluidal, transitional and vesicle-dominated grains, with rare angular fragments.

In more detail, in the “low-speed” (3 MPa) experimental series (Fig. 4.4, top), spheres (Fig. 4.3a) make about half of the ultramafic (Hohenstoffeln) grains, followed by ovoid particles (Fig. 4.3b) and Pele’s tears (Fig. 4.3e). Lobate (Fig. 4.3c) and fluidal elongate grains are less important. Angular grains are mostly represented by glass films (Fig. 4.3s). Moving to the alkaline basalt (Billstein), spherical grains decrease to about one-third, compensated by the increase in Pele’s tears. A sharp increase in glass films is observed. Pele’s tears become the dominant type in the basaltic trachyandesite (Sommata), making over half of the population, whereas spherical grains sharply decrease. In summary, shifting from Hohenstoffeln to Sommata sees a decrease in spherical and related shapes (lobate and ovoid), counteracted by an increase in tears.

Within the “high-speed” (10 MPa) series (Fig. 4.4, center), Hohenstoffeln has over one third Pele’s tears. Spheres, lobate grains and fluidal irregular grains (Fig. 4.3g) are also well represented. Thick Pele’s hairs are the main type within the fluidal elongate group. Moving to Billstein, Pele’s tears account to nearly half, followed by fluidal elongate grains, dominated by thick Pele’s hairs. Spheres and ovoid grains are rare. The Sommata sample is largely represented by fluidal elongate grains, equally divided into thick and thin Pele’s hairs. Pele’s tears are subordinate. Glass films in the sample account to about 18%, while blocky particles (Fig. 4.3r) are rare.

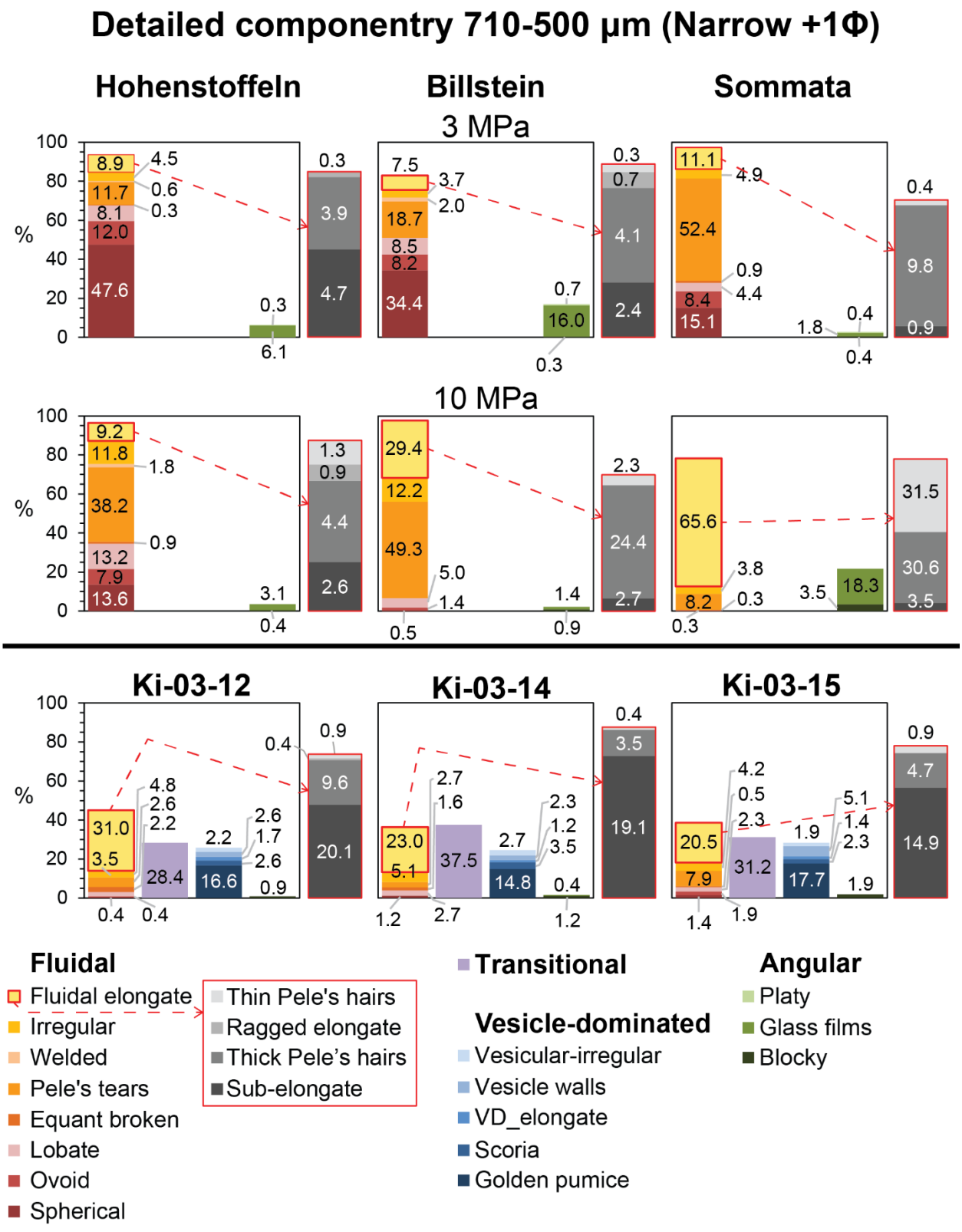

Figure 4.4: Detailed juvenile componentry proportions for the narrow + 1ϕ (710–500 µm) fraction. Top two rows, experimental samples. Bottom row, natural samples.

In summary, for the 10 MPa series, a sharp decrease in compact grains is observed from Hohenstoffeln to Sommata, counteracted by the six-fold increase in elongate grains. Pele's tears increase from Hohenstoffeln to Billstein, but then decrease dramatically within Sommata. These experimental juvenile fragments have remarkable shiny surfaces, sometimes iridescent. Shapes are rather simple in Hohenstoffeln and Billstein, and more complex in Sommata.

The three Kīlauea Iki samples represent several fountaining episodes mixed together (S. Mueller, pers. comm., 2019). They show roughly the same class proportions among themselves (Fig. 4.4, bottom). Therefore, they will be described together. Within the fluidal group, elongate grains are consistently the major type, ranging from about 20 to 30%. Pele's tears are the second most abundant type within fluidal grains. Transitional grains (Fig. 4.3l) are the second major group among the samples, accounting from 28 to 38% of the total sample. Lastly, vesicle-dominated particles account for 24% to 28% of the entire juvenile population. Within this group, golden pumices (Fig. 4.3m) are the major class. Scoria (Fig. 4.3n), vesicle walls (Fig. 4.3p) and other complex vesicle-dominated fragments are subordinate. Blocky grains dominate the angular group. In comparison to the experimental samples, natural fluidal grains have mainly dull surfaces, with Pele's tears and lobate grains showing often rather complex shapes that differ from the classic "smooth" tear commonly portrayed.

4.4.3 3D morphology of juvenile particles from the very fine ash fraction

Juvenile grains from the very fine ash fraction are morphologically different between experimental and natural samples, more so than in the studied coarse ash fraction. Experimental particles lack transitional and vesicle-dominated classes, which dominate the Kīlauea Iki juvenile assemblage (Fig. 4.5).

Within the 3 MPa series (Fig. 4.5, top), Hohenstoffeln fluidal grains consist mainly of spherical grains, followed by Pele's tears, and ovoid particles. Angular grains are mainly represented by glass films, with subordinate blocky grains. Billstein is also dominated by spheres, with subordinate Pele's tears and ovoids, whereas angular grains are absent. The Sommata very fine ash within this series was not characterized, due to very low total weight. In summary, the amount of compact juvenile particles decreases passing from the ultramafic to the mafic composition, with a relative counter-increase in fluidal elongate particles.

Within the 10 MPa series (Fig. 4.5, center), Hohenstoffeln consists mainly of Pele's tears, followed by fluidal elongate grains mainly represented by thick Pele's hairs. Spheres and ovoid grains are subordinate. Billstein is dominated by fluidal elongate particles, mainly represented by thick Pele's

hairs. Less abundant classes are Pele's tears and fluidal irregular particles. Sommata is also prominently constituted by fluidal elongate grains, with thick Pele's hairs more abundant than thin Pele's hairs. Pele's tears and fluidal irregular grains are subordinate, whereas glass films and vesicle walls are rare. In summary, the shift from the ultramafic to the basaltic trachyandesite magma is characterized by an over fivefold increase in fluidal elongate particles, and the total disappearance of the "compact" classes (i.e., spherical, ovoid and lobate). Among fluidal elongate particles, thick and thin Pele's hairs increase dramatically towards Sommata.

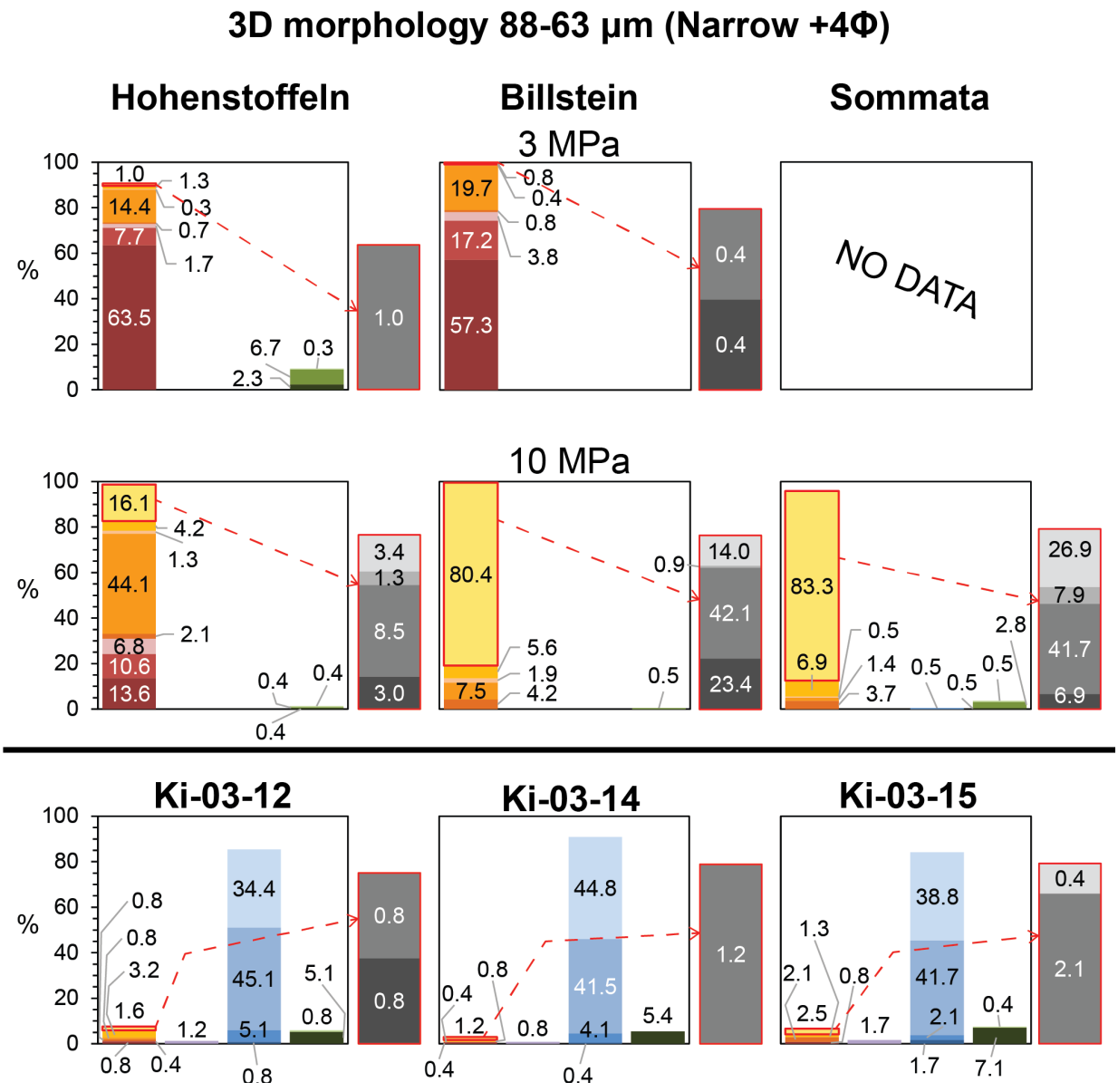

Figure 4.5: 3D morphology proportions for juvenile particles from the + 4ϕ (88–63 µm) fraction. Top two rows, experimental samples. Bottom row, natural samples. See legend in Fig. 4.4.

As for the natural counterpart (Fig. 4.5, bottom), vesicle-dominated juvenile grains are the major group. Classes are equally shared between vesicle walls and vesicular irregular (Fig. 4.3q) grains. VD_elongate particles (Fig. 4.3o) are minor. Cumulatively, the fluidal group is well below 10%, mainly represented by elongate and irregular fragments. Blocky grains are among the most relevant subordinate classes.

4.4.4 Internal textures and morphometry of the coarse ash fraction

4.4.4.1 Experimental juvenile particles

The fluidal character of the experimental juvenile fragments in the coarse ash size range is well reflected in the 2D cross-sectional slices (Fig. 4.6). Particles from both the 3 MPa and the 10 MPa series range from non-vesicular to incipiently vesicular (Houghton and Wilson 1989), with vesicles that rarely intersect the particle edge. Bulk crystallinity is also generally low, with partially resorbed phenocrysts of olivine for Hohenstoffeln (Fig. 4.6, top) and Billstein (Fig. 4.6, center), and clinopyroxene plus plagioclase for Sommata (Fig. 4.6, bottom). The groundmass of the artificial juvenile particles is represented by microlite-free sideromelane (glass).

Within the 3 MPa series, the Axial ratio (AxlR) versus Solidity (SLD) plot emphasizes very high median values for the three melt compositions (Fig. 4.7, top). Median AxlR ranges between 0.7 and 0.85, with the lowest single-grain values for Sommata down to 0.4. Median SLD is consistently higher than 0.95 for all samples (Fig. 4.7, top left), with Sommata showing again the lowest single-grain values, down to 0.45. Median 2D vesicularity (VES) is also very low, ranging between 0.2% for Hohenstoffeln and Billstein, up to 8.5% for Sommata (Fig. 4.7, top right). Sommata has a few vesicular grains, reaching up to 67% vesicles. 2D Crystallinity (XLS, not shown) reaches a maximum of ~ 37% in single grains from Billstein, but median values for all samples are about 0%, indicating virtually crystal-free juvenile particles (Fig. 4.6).

Moving to the 10 MPa series (Fig. 4.7, center), the three experimental samples show distinct values. Hohenstoffeln displays the highest median values for AxlR and SLD, respectively at 0.8 and 1.0 (Fig. 4.7, center left). Minimum single-grain values reach as low as 0.35 and ~ 0.40 for AxlR and SLD, respectively. On the other hand, Sommata has the lowest median AxlR and SLD values, respectively at ~ 0.4 and 0.7. Minimum single-grain values for both parameters go down to 0.15 and 0.3, respectively. Median VES values for Hohenstoffeln and Sommata are about 1% and 16%, respectively (Fig. 4.7, center right).

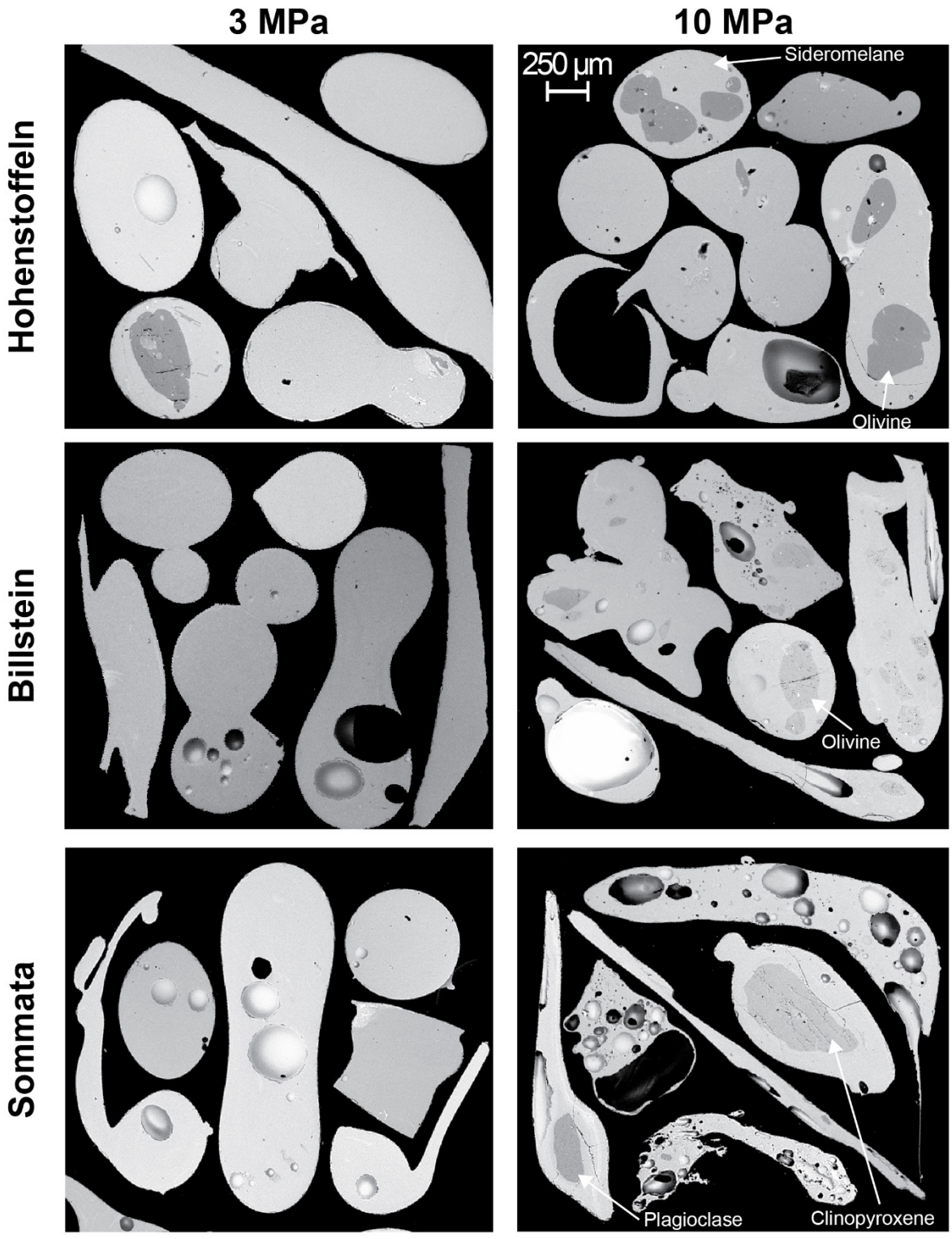

Figure 4.6: SEM-BSE images of cross-sections of experimental juvenile pyroclasts, for the narrow + 1ϕ (710–500 µm) fraction. Each composite image shown combines representative particles from several images, to illustrate the diversity of particle shapes and internal textures. Image acquisition settings are 68X magnification, 2048x1536 resolution and high-quality scan (about 160 sec).

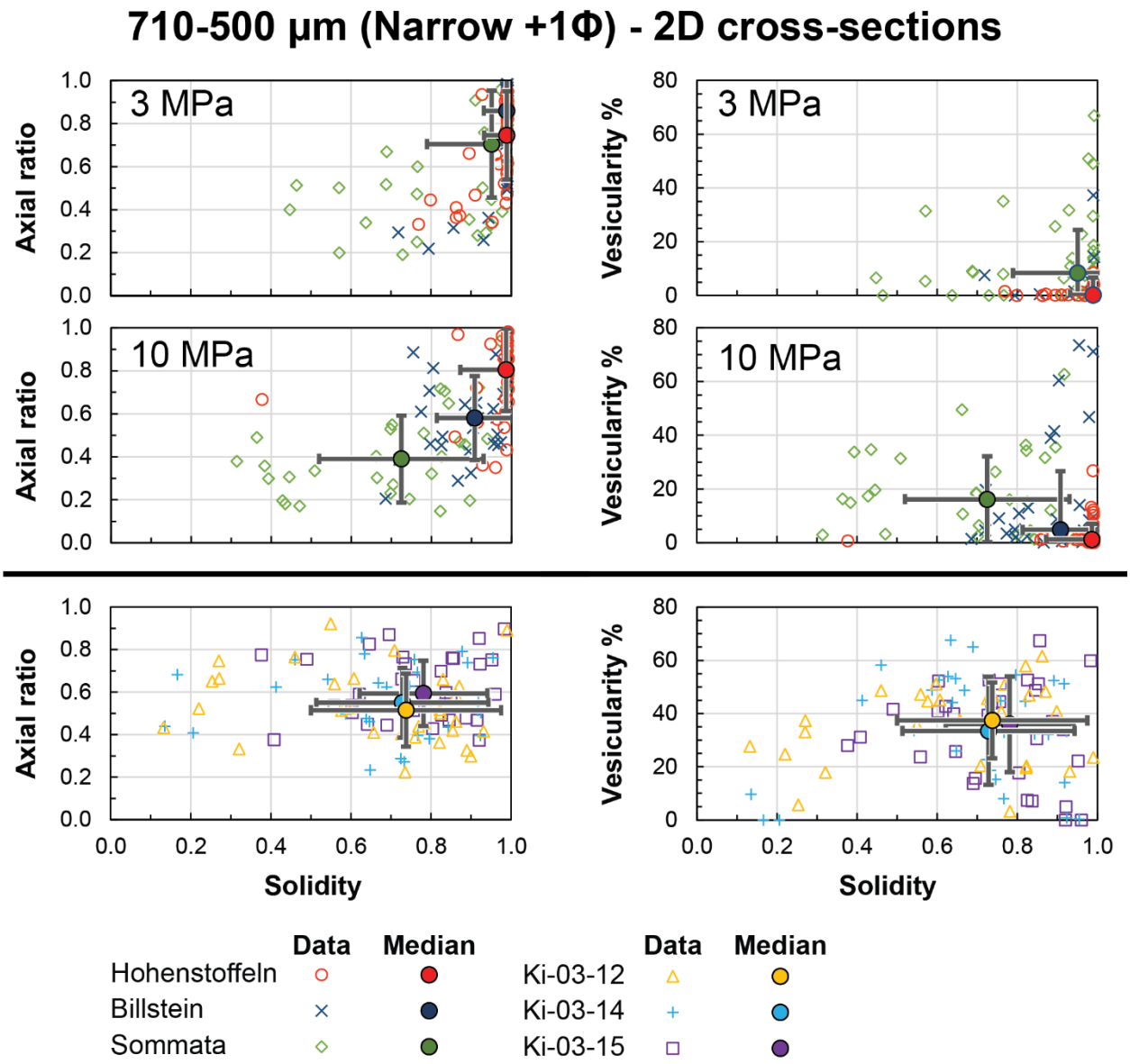

Figure 4.7: Axial ratio (left) and vesicularity (right) versus solidity for both experimental and Kīlauea Iki samples, for the narrow + 1ϕ (710–500 µm) 2D cross-sections.

Hohenstoffeln, with nearly 38%, displays the highest value for XLS (not shown but see Fig. 4.6), with median values over 9% for Billstein. The latter shows intermediate median AxlR, SLD, and VES values between Hohenstoffeln and Sommata.

4.4.4.2 Natural juvenile particles

Kīlauea Iki juvenile pyroclasts in the coarse ash fraction have a higher vesicularity (Fig. 4.8) relative to their experimental counterparts. The bulk groundmass is completely glassy, with only rare grains showing lathy feldspar microlites, as observed by Richter and Murata (1966).

The sparse phenocryst population is mainly represented by Mg-rich olivine (Fig. 4.8), with subordinate clinopyroxene and plagioclase (not shown).

Median AxlR is about 0.5–0.6, while median SLD is consistently around 0.75 (Fig. 4.7, bottom left). Minimum single-grain values for both parameters reach ~ 0.2–0.4 and ~ 0.1–0.4, respectively. Internally, the particles are mostly poorly vesicular (Houghton and Wilson 1989), with median VES values around 35% (Fig. 4.7, bottom right), and maximum single-grain values over 65%.

4.4.5 Morphometry of the very fine ash fraction

4.4.5.1 Experimental juvenile particles

In the 3 MPa series, medians of AxlR, SLD and Convexity (CVX) for both Hohenstoffeln and Billstein are consistently over 0.95, reflecting the major presence of compact grains such as spheres (Fig. 4.9, top). Hohenstoffeln displays the lowest AxlR values at about 0.15 (for individual grains) due to the presence of glass films, while the presence of long-tailed Pele's tears in Billstein set the minimum single grain SLD and CVX values to 0.35 and 0.6, respectively.

In the 10 MPa series, AxlR provides a good distinction among the three samples. Hohenstoffeln has the highest median values for AxlR and SLD, respectively at 0.6 and 0.9, due to the high presence of equant grains (Fig. 4.9, center left). Long tails for both parameters show minimum single-grain values as low as 0.1 and ~ 0.25, respectively, due to the presence of elongate fragments, either Pele's tears or thick Pele's hairs. Sommata has the lowest median AxlR and SLD values, respectively at ~ 0.2 and ~ 0.8. Minimum single-grain values for both parameters go as low as ~ 0.05 and ~ 0.2, respectively, due to the conspicuous presence of thick and thin Pele's hairs. CVX has the same median values for all three compositions, just over 0.90 (Fig. 4.9, center right). Minimum single-grain CVX values for Hohenstoffeln go as low as 0.45, due to the presence of bent Pele's tears and fluidal irregular fragments.

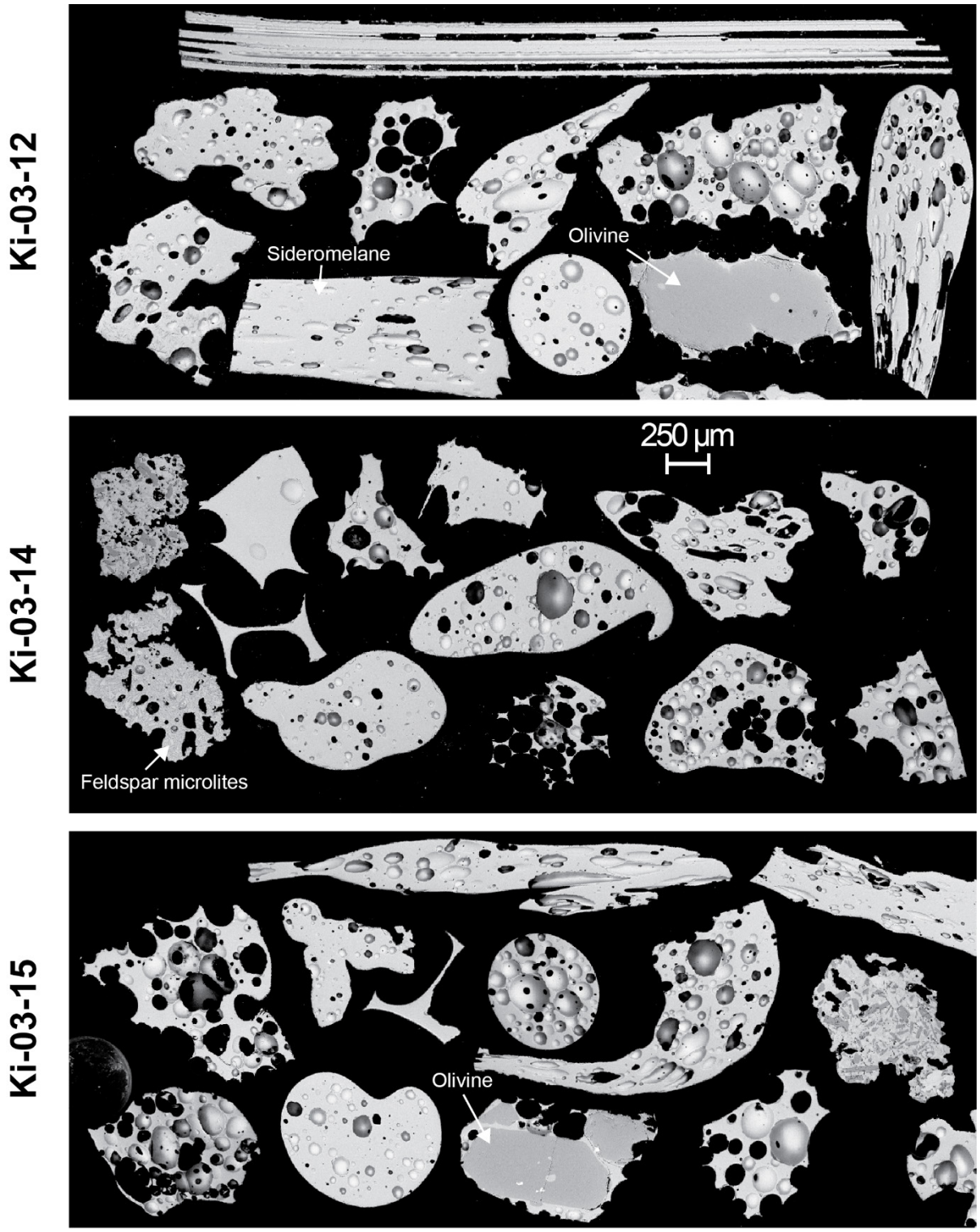

Figure 4.8: SEM-BSE images of particle cross-sections of the Kīlauea Iki juvenile pyroclasts, for the narrow + 1ϕ (710–500 µm) fraction. Each composite image shown combines representative particles from several images, to illustrate the diversity of particle shapes and internal textures. Image acquisition settings are the same as in Fig. 4.6.

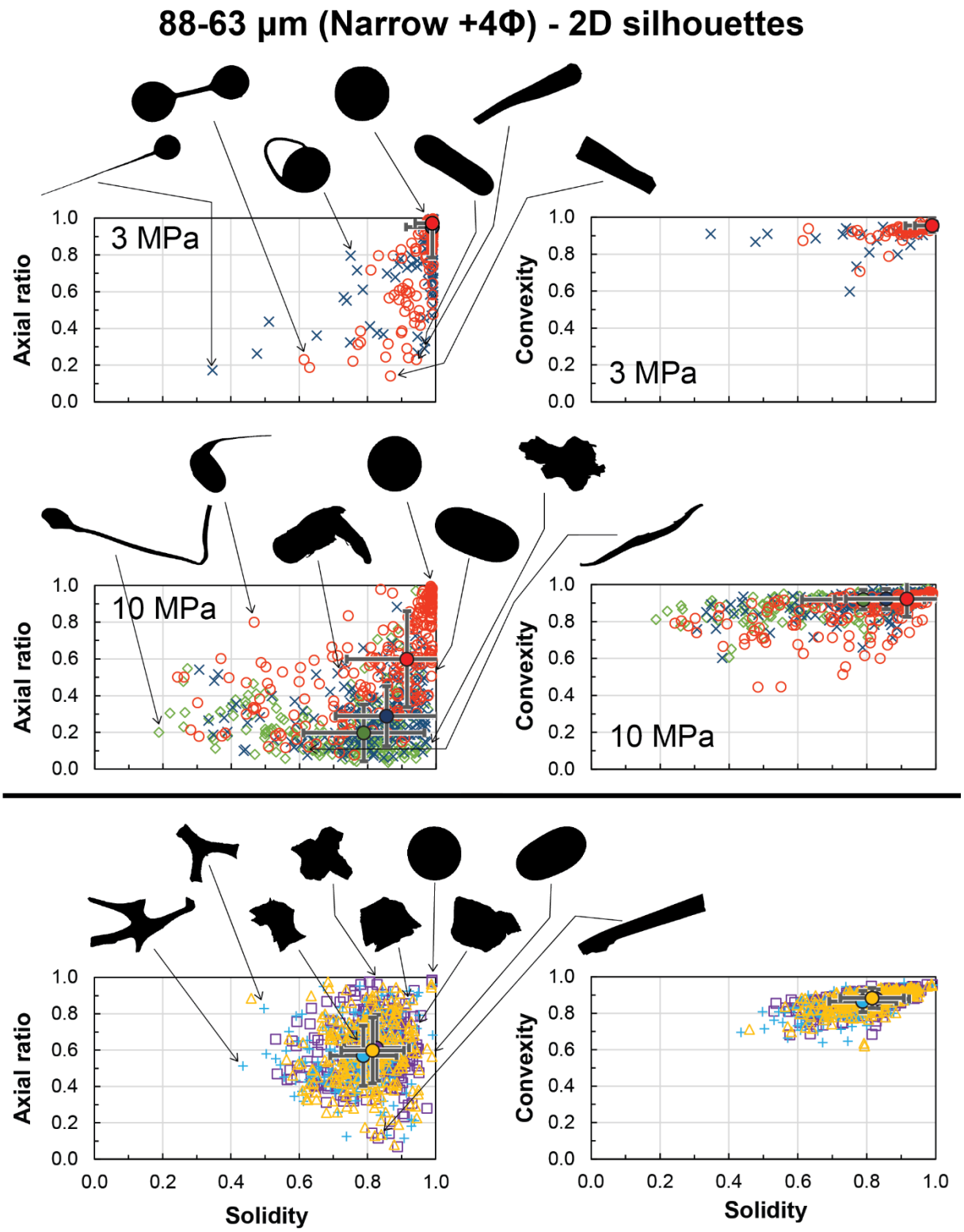

Figure 4.9: Axial ratio (left) and convexity (right) versus solidity for both experimental and Kīlauea Iki samples, for the narrow + 4ϕ (88–63 µm) silhouettes. Binary silhouette images of several clasts illustrate different positions on the axial ratio versus solidity plots. Size of the binary images was homogenized to the same particle height for display purposes. See Fig. 4.7 for the legend.

4.4.5.2 Natural juvenile particles

The very fine ash fraction for the Kīlauea Iki samples show consistently similar morphometric median values (Fig. 4.9, bottom). Median AxIR for all three samples is around 0.6, with minimum single-grain values as low as 0.08 due to the abundant presence of VD_elongate particles. Median SLD is around 0.8, but minimum single-grain values reach as low as 0.45, due to the high presence of vesicle walls. Median CVX is over 0.85, with lowest values down to ~ 0.6.

4.5 Discussion

The experimental and distal Kilauea Iki samples have similar grain size distributions, and all contain abundant fluidal juvenile particles in the coarse ash fraction. This highlights the ability of the experiments to replicate, to some extent, the fragmentation processes characterizing Hawaiian lava fountains. This section starts with a generalized account of our fragmentation experiments, focusing on where and when fragmentation takes place, and where and when the final pyroclast shapes may be acquired.

Later, we address what parameters control the varying pyroclast morphologies, and compare our experimental juvenile fragments with those deposited by natural lava fountains. Finally, we emphasize the limits of the very fine ash fraction in studies of primary magma fragmentation for low-intensity mafic eruptions.

4.5.1 Summary of magma fragmentation during a typical experimental run

Our transient magma jet experiments are described and interpreted in detail Chapter 3, but here we summarize the main steps, in preparation for the next subsections on pyroclast shapes.

4.5.1.1 In-crucible fragmentation

Following the sudden injection of argon gas either within (3 MPa series) or at the base of (10 MPa series) the magma in the crucible, Rayleigh-Taylor instabilities form at the magma-gas interface. While the magma plug is violently propelled upward, droplets detach from the wavy magma-gas interface (Zimanowski et al. 1991; Caffier 1998; Chapter 3) (shown below the magma plug at t_a in Fig. 4.10). The base of the magma plug is progressively consumed until the crucible opening is surpassed. Spherical droplets in the range between 90–500 μm are most likely to form during this stage (Zimanowski et al. 1991, 1997; Caffier 1998).

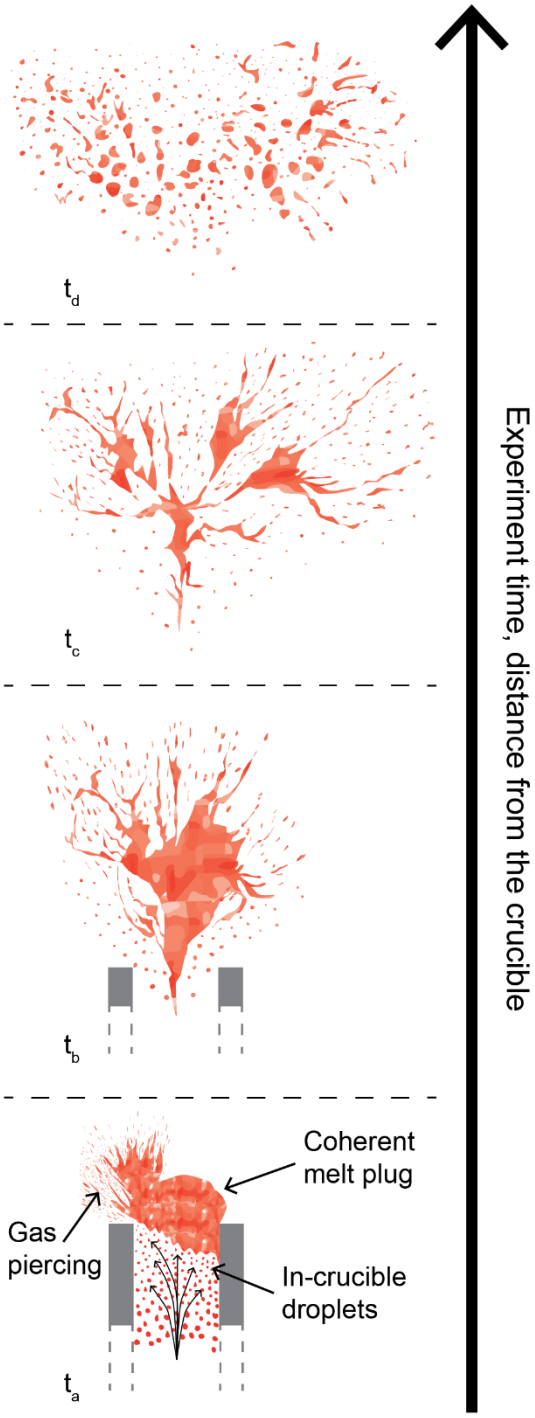

Figure 4.10: Schematic drawing of magma fragmentation in the experiments. (t_a) Magma is pushed up by compressed gas (arrow), leading to in-crucible fragmentation at the base of the plug. At the crucible opening, a gas piercing effect causes early detachment and fast propulsion of droplets ahead of the coherent portion of the magma plug. (t_b) Once the bulk of the magma plug has left the crucible, the top surface interacts with the stagnant atmosphere. Several lobes start expanding in different directions, accompanied by fast stretching and detachment of what will become thin Pele's hairs and teared droplets. (t_c) Further upward and later, the core of the magma plug is completely broken into several large lobes. (t_d) Further thinning and breakup of the large lobes into smaller drops and threads. Particles then fall back down to the lab floor (not shown).

The extent of in-crucible fragmentation depends on ejection velocity and magma composition; a larger velocity will enhance it (Caffier 1998; Lefebvre and McDonell 2017). Both parameters will also set the range of viscosities experienced by the fragmenting magma at the tested temperature, as described in the next section. A lower viscosity ultramafic magma plug will fragment more readily than an intermediate composition one, for which in-crucible fragmentation may be very minor.

4.5.1.2 Magma fragmentation in the atmosphere

Upon reaching the crucible opening, the magma plug was expected to exit symmetrically, pushed by the argon gas. In reality, in all runs but the Sommata 3 MPa, the argon gas pierced laterally between the magma plug and the inner wall of the crucible (t_b, Fig. 4.10). This gas piercing effect caused some drops and threads to be peeled off from the side of magma plug and quickly propelled in the atmosphere ahead of the still coherent portion of the magma plug, possibly along with more droplets formed during in-crucible fragmentation.

Regardless of the gas piercing effect, the coherent magma plug forms a transient liquid jet (t_b, Fig. 4.10).

How this jet will initially behave and fragment in the atmosphere depends on which breakup regime the jet is in (Chapter 3, and references therein): i) in the Rayleigh's regime, surface tension and liquid inertia dominate the breakup process, and the liquid jet is in a laminar flow state; ii) in the first wind-induced regime, a higher ejection velocity of the liquid jet leads to more internal turbulence and aerodynamic effects, promoting larger wave disturbances at the liquid surface (i.e. more intense breakup than the previous regime); iii) in the second wind-induced regime, aerodynamic forces at the liquid jet surface control breakup process relative to internal turbulence; iv) in the atomization regime, the very high ejection velocities and strong aerodynamic forces result in the violent breakup of the liquid jet into a spray.

In regimes IV (atomization) and III (second wind-induced breakup), there will be early detachment and fast propulsion of droplets from the top of the plug. This is due to internal turbulence, and Rayleigh-Taylor wave disturbances at the front of the plug as it hits against the quiescent atmosphere (Eggers and Villermaux 2008; Lefebvre and McDonell 2017). An example of this is the Hohenstoffeln 10 MPa run (high-speed video available in Online Resource 4.2). Lower velocities and higher magma viscosities tend to shift the initial breakup regime towards regime II (first wind-induced breakup regime), where fragmentation of the flow front is delayed, and

produces coarser size fragments. An example of this is Sommata 3 MPa run, where the coherent magma plug exits the crucible with a mushroom shape with no initial wave disturbances (Online Resource 4.2).

At a slightly farther distance from the crucible opening, the perturbed yet roughly intact core of the magma plug begins to expand toward different directions (t_b, Fig. 4.10). Each of the lobes (e.g. Billstein 3 MPa) or threads (for Billstein 10 MPa) stretches at a different velocity, leading to breakup into smaller fragments (t_c, Fig. 4.10). This is also the stage where extremely thin Pele's hairs and long tailed Pele's tears form, due to the prolonged linear stretching of magma lobes, along with Kelvin-Helmholtz instabilities. The latter form as wave disturbances on the drop's surface during motion, causing films of magma to be stripped off from a drop's surface if the the velocity is high enough (Caffier 1998). Furthermore, balloon-like inflation of other lobes will result in the formation of glass films.

During the late ascent, several thousand drops and threads further fragment, still in a liquid state, at relatively low velocity, resulting in small spheres, lobate particles, Pele's tears and thick Pele's hairs (t_d, Fig. 4.10). This final particle shape is acquired in variable places depending on where the particle is created during the experiment (in-crucible phase, t_a, t_b, t_c or t_d of the free air expansion). Cooling rates must also vary across time and space.

4.5.2 What controls juvenile particle morphologies in experiments?

Regardless of where juvenile clasts form – within the crucible, during the initial expansion stage in the atmosphere or as a result of secondary breakup later on – the morphological fate of each drop or thread is dictated by two consecutive events: i) thinning and clast formation; ii) cooling and morphology preservation.

4.5.2.1 Thinning and clast formation

Each juvenile pyroclast that is eventually collected begins as a molten magma lobe parting and breaking up from its parent mass for the last time. Any prior event that occurred to that drop or thread will be overwritten by subsequent deformation and aerodynamic reshaping, leaving no trace. The last thinning and breakup process is therefore the most appropriate moment to discuss what influences the final particle morphology.

In general, the separation of a magma drop from its parental mass occurs because of their relative difference in speed and direction (Clasen et al. 2012; Jones et al. 2019; Chapter 3). Thinning at the necking point and ultimate breakup between two parting magma masses is governed by surface tension, counterbalanced by inertial, viscous and elastic forces (Clasen et al. 2012; Lefebvre and McDonell 2017; Chapter 3, and references therein). The balance among these main forces varies over time. In the following discussion, we are considering the entire juvenile population of each experiment, which consists of particles formed at different moments, as discussed above. Since we are considering the fate of several thousand particles rather than a single one, it makes sense to constrain what properties might have varied (or not) among the experiments in order to explain the different shape class proportions and morphometric parameters.

The **internal diameter** of the crucible (5 cm) was the same for all experiments. The gas driving pressure (3 or 10 MPa) influences **ejection speed**, which partly controls the jet breakup regime of the magma (Chapter 3). The ejection velocity of the magma plug, but also the differential velocity between each detaching lobe or newly formed droplet/thread and the surrounding gaseous medium (both argon gas and the atmosphere in the experiments), also influence stretching and the overall shaping process. In general, a relatively high ejection velocity will favor filament extension (Clasen et al. 2012). In contrast, a too high or too low ejection velocity will lead to early breakup. In the experiments, each magma composition reacted differently to the same applied driving pressure, but also a same composition ejected at low and high driving pressures experienced a different fragmentation history. The minor gas piercing effect present in all but the Sommata 3 MPa run allowed a cloud of droplets to move faster than the trailing magma plug (Table 4.1). Droplets entrained in the gas piercing phase were the fastest for Hohenstoffeln between 50 and 115 m/s, respectively for the 3 and 10 MPa series. In contrast, the coherent magma plugs had similar ejection velocities of about 11 and 36–44 m/s, respectively for the 3 and 10 MPa series.

The effect of the internal magma parameters can be isolated by comparing runs with the same driving pressure but a different composition. The initial magma temperature was set at 1200°C for all runs. Temperature mainly affects viscosity, but also density and surface tension. Due to a possible gradient from bottom to top of the crucible, we consider a 25°C temperature interval down to 1175°C.

Table 4.1: Relevant physical parameters of the magmas in the experiments and the Kīlauea Iki fountains, expressed either as single values or ranges in the temperature interval 1175–1200°C.

Sample	Crucible diameter (m)	Driving pressure (MPa)	Density (kg/m^3)	Surface tension (N/m)	Viscosity (Pa*s)	Initial ejection velocity (m/s)	
-	-	-	-	-	-	Gas piercing	Coherent plug
Hohenstoffeln	0.05	3/10	3000 (1)	~0.29 – ~0.33	~21 – ~340 (2)	~50/115	11/44 (3)
Billstein	0.05	3/10	N/A	~0.33	~28 – ~1410	~45/~75	11/33 (3)
Sommata	0.05	3/10	2500 (4)	N/A	~45 – ~26 700	n.a./~85	13/36 (3)
Kīlauea Iki 1959	N/A	N/A	900 – 2800 (5)	N/A	~55 (6)	110 (7)	

(1) Bubble-free densities from Büttner et al. (1998).
(2) For Hohenstoffeln, data available only at 1200°C.
(3) Initial ejection velocities of the coherent portion of magma plug in the 3 and 10 MPa series, from Chapter 3.
(4) Bubble-free densities from Büttner et al. (2002).
(5) Vesicularity-derived densities for the 1959 Kīlauea Iki juveniles from the narrow + 1ϕ size fraction.
(6) Melt viscosity calculated from Giordano et al. (2008), using a temperature of 1150°C (Porritt et al. 2012) and the average geochemical composition of several spatter and pumice fragments from Murata and Richter (1966). Since crystal content is very low, we did not adjust the viscosity for crystal cargo.
(7) Derived exit velocity required to feed the highest lava fountain, from Porritt et al. (2012).

The **density** of the magma influences the inertia of a separating magma drop during breakup. In extremely low viscosity conditions relevant for many industrial liquids, inertia opposes breakup by promoting filament extension (Clasen et al. 2012). Our lowest magma viscosities are comparable to the highest ones encountered in most industrial applications. Moreover, for our three poorly vesiculated magmas, the bubble-free density spans between ~ 2500–3000 kg/m^3 at 1200°C (Büttner et al. 1998, 2002). Therefore, inertia is not likely to be a major factor in our experiments, and the relatively narrow density interval does not justify the observed morphological diversity.

Surface tension is one of the major parameters influencing fragment shapes (Shimozuru 1994; Clasen et al. 2012; Porritt et al. 2012). It acts to contract the magma masses at both ends of the neck toward a minimum energy configuration (i.e. a sphere; Li 2008), therefore promoting breakup and spherical shapes. Yet, empirical surface tension values for the two more mafic compositions (Table 4.1) in the considered temperature interval only vary between ~ 0.29 and 0.33 N/m (Koopmann 2004). Therefore, surface tension is likely not responsible, in absolute terms, for the

different pyroclast morphologies. Its relevance during thinning will be instead controlled by other parameters, which may counterbalance the surface tension, or not.

Viscosity and elasticity will work to delay breakup by promoting filament extension (Clasen et al. 2012). Within the range of compositions and applied shear rates at initial eruption temperatures, elastic effects are thought to be minor (Wadsworth et al. 2019), leaving viscosity as the main parameter opposing surface tension during thinning and breakup. Viscosity values for our three magmas in viscometry experiments span several orders of magnitude, as a function of temperature and applied shear rate (Sonder et al. 2006; Hobiger et al. 2011; Dürig et al. 2012b) (Table 4.1). The actual instantaneous viscosities (and associated shear rates) during the fragmentation experiments are not known, but observed jet breakup regimes (Chapter 3) and final pyroclast shapes (this chapter) suggest that Hohenstoffeln had the smallest instantaneous viscosity and Sommata the greatest, leading to markedly different thinning histories.

The control of magma viscosity and ejection velocity in the experiments is evident in the overall proportion between elongate and compact fluidal juvenile particles between the ultramafic and the intermediate composition endmembers. At low ejection velocities and low viscosities, for example in the Hohenstoffeln 3 MPa run, the breakup process is dominated by surface tension. The thinning velocity at the necking point is larger than the overall jet velocity. Local instantaneous viscosities at the necking point upon droplet detachment might be large enough to occur within the brittle regime, promptly followed by fast viscous healing (Taddeucci et al. 2021). Pinched edges and tails are rapidly suppressed due to effective relaxation, often with the conversion into smaller satellite droplets (Fig. 4.11a). As an example of this behavior, we show a thread ~ 15 mm long located 10 cm above the crucible, and moving with an upward velocity of 3.2 m/s during the late stages of the Hohenstoffeln 3 MPa run (Fig. 4.12a). First a top lobe starts to expand upward from the main mass (Fig. 4.12a, 7 ms after, dark blue arrow); over the next 6.6 ms, the process of thinning and breakup is completed, resulting in the partition of the original thread into four droplets 2.9, 3.7, 1.1 and 3.3 mm in diameter, respectively (Fig. 4.12a, 13.6 ms after). The overall abundance of compact grains such as spheres, ovoid and lobate particles in the Hohenstoffeln 3 MPa sample (Figs. 4.4, 4.5), as well as the high values for both axial ratio and solidity (Figs. 4.7, 4.9, 4.11c), are a direct result of the surface tension-controlled thinning and breakup. Billstein 3 MPa also has a large proportion of such particles, compared to more elongate particles (Figs. 4.4, 4.7, 4.11c).

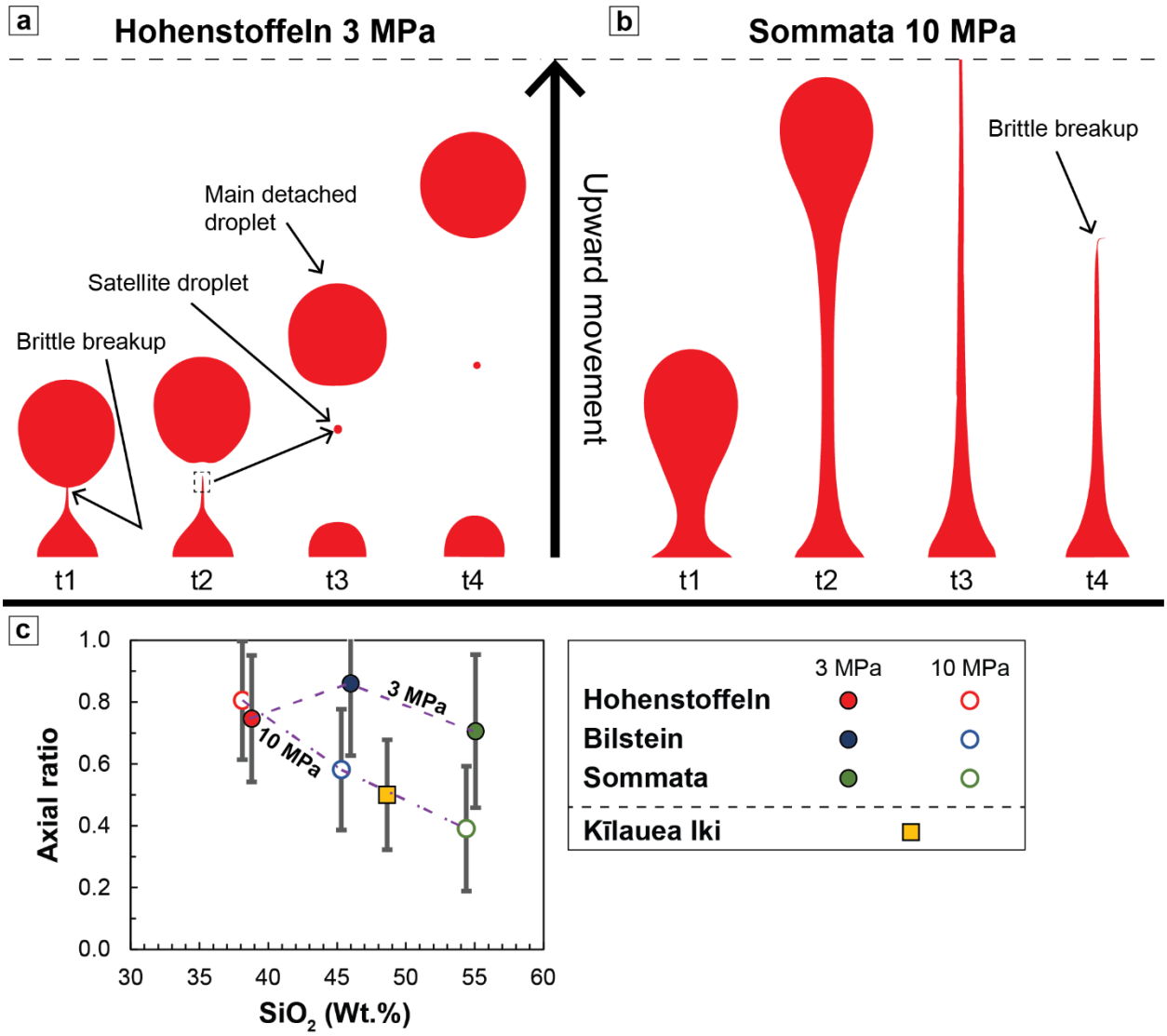

Figure 4.11: Endmember behaviors for the thinning and breakup of magma: (a) For low silica magmas and/or low ejection velocity, surface tension dominates the process, causing early pinching and relaxation effects which result in droplet formation; (b) for magmas with higher silica contents, viscosity greatly opposes surface tension. Thinning timescales are larger and breakup is delayed, resulting in filament formation. (c) Comparison of median axial ratio versus silica of the narrow + 1ϕ size fraction for experimental and natural samples. Median axial ratio data for Kīlauea Iki represents the average of fluidal grains only. Note: Silica contents of the 3 MPa medians are arbitrarily shifted by 0.6 wt.% for easier visualization.

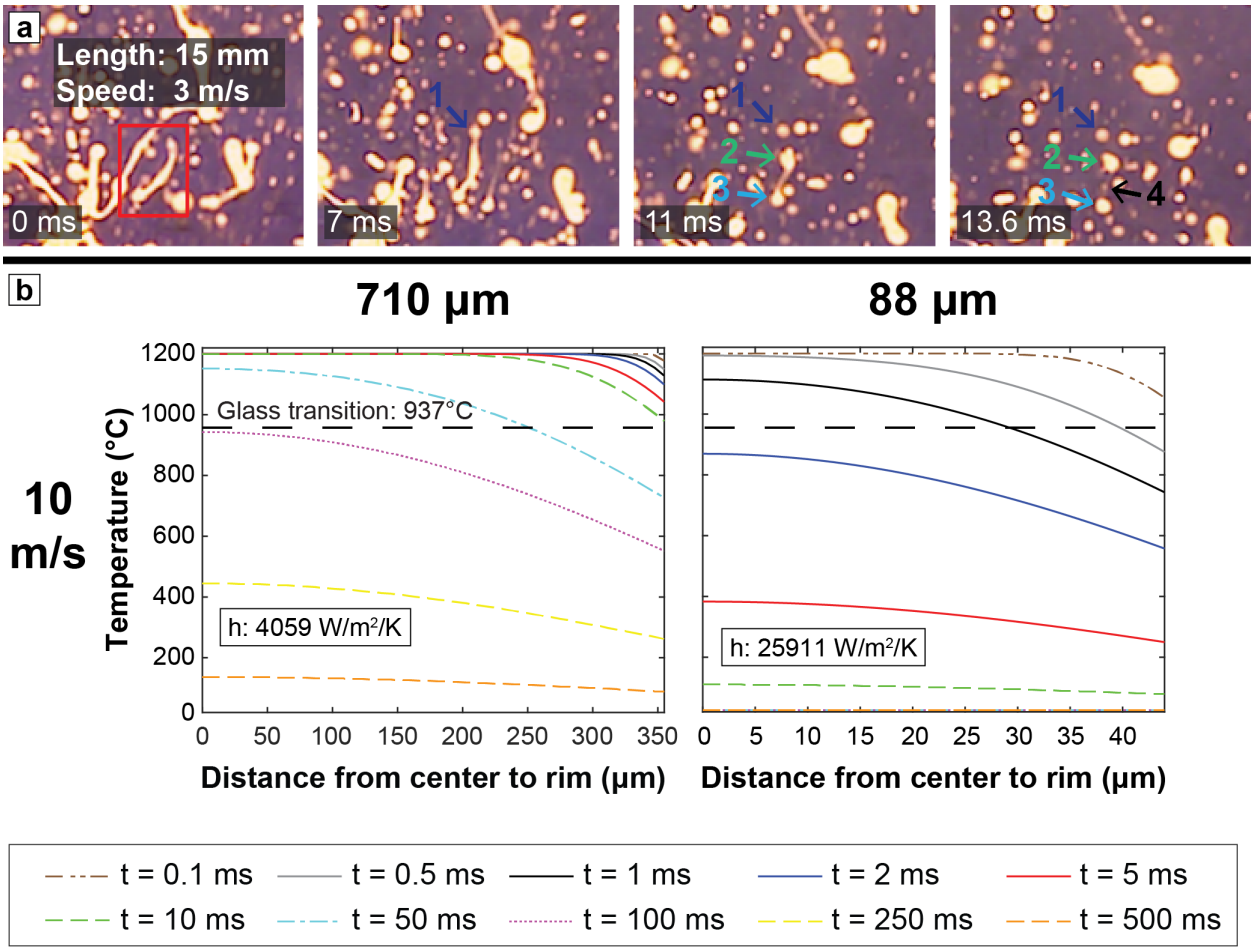

Figure 4.12: (a) Time lapse of liquid thinning and breakup of a thread into four droplets observed during the late stage of the 3 MPa Hohenstoffeln run: 0 ms) Initial thread, 15 mm long, moving upward and to the right at ~ 3 m/s; 7 ms after) Drop 1 starts separating from the main mass; 11 ms after) The remaining thread starts separating in the middle, leading to the formation of drops 2 and 3, while drop 1 is fully detached; 13.6 ms after) Drops 2 and 3 are finally detached, with production of a satellite drop in between (drop 4). (b) Modeled cooling of the largest droplets in the 710–500 µm (narrow + 1ϕ) and 88–63 µm (narrow + 4ϕ) size fractions, for the Hohenstoffeln magma, using the 1-D transient heat conduction model of Recktenwald (2006). Droplet speed is 10 m/s but the results are similar for 1 or 100 m/s (not shown). Glass transition temperature from Büttner et al. (1998).

The opposite endmember is Sommata 10 MPa, with a high ejection velocity and the highest instantaneous viscosity among the experiments. Here, viscosity better competes with surface tension, extending filament-thinning timescales, which delays breakup (Fig. 4.11b). Even after breakup has occurred, the pinched edge of the elongate fragment undergoes only a partial retraction driven by surface tension. Consequently, the median axial ratio of juvenile particles is much lower (i.e., fragments are more elongate; Fig. 4.11c), and the + 1ϕ fraction is dominated by fluidal elongate particles, mostly thick and thin Pele's hairs (Fig. 4.4).

In summary, the most important variables dictating the overall morphology of fluidal juvenile particles and their proportions in our experiments are the ejection velocity, the differential velocity between magma and gas, and the instantaneous viscosity of the magma.

4.5.2.2 Cooling and morphology preservation

The reshaping discussed above is only possible if the particle is still liquid; reshaping may be stopped by cooling the particle below the glass transition. It is likely unnecessary to cool the whole particle for its shape to be frozen, but what glass thickness is required to do this is not known. If we consider drop 1 from Fig. 4.12a, full contraction was observed to occur within 1 ms, faster than any significant cooling for a particle several mm across. Yet the deposits yield a conspicuous number of spheres of this size, indicating that such particles will cool before landing; otherwise they would flatten on one side.

For the analyzed ash fractions (narrow + 1ϕ and narrow + 4ϕ), which are significantly smaller than "drop 1", the shape of the fragments also suggests that they did not deform upon landing. But how long will it take to cool + 1ϕ or + 4ϕ droplets in order to preserve their final shape? To answer this, we determined the cooling timescale of a spherical droplet using the Nusselt-Reynolds relationship developed by Moitra et al. (2018). We use the Hohenstoffeln magma since we have all physical parameters required. For simplicity, we focus on the cooling rate of spherical droplets generated during the free air expansion stage, assuming an initial droplet core temperature of 1200°C and a surrounding ambient air temperature of 25°C (Fig. 4.12b).

We use particle diameters (*d*) of 710 and 88 µm, respectively for narrow + 1ϕ and narrow + 4ϕ, i.e. the maximum diameter of the respective fractions; any smaller particle will only cool faster. Since the ejection velocity (*u*) of the drops propelled in the atmosphere varies from start to finish and among experiments, we model the cooling rate at 100, 10 and 1 m/s, broadly encompassing the measured velocities at various stages of the experiments, including the gas piercing phase. For each pair, we first calculate the dimensionless Nusselt number, which quantifies the total heat transfer from the droplet to the surrounding air:

$$Nu = a + b\, Re^{1/2}\, Pr^{1/3}$$

where *Re* is the Reynolds number ($Re = \frac{u\, d}{\nu_{air}}$; where ν_{air} is the kinematic viscosity of air), *Pr* is the Prandtl number ($Pr = \frac{\nu_{air}}{\alpha_{air}} = 0.71$), where α_{air} is the thermal diffusivity of air), and *a* and

b are the fitting parameters in high temperature conditions (Moitra et al. 2018). Next, we use *Nu* and the thermal conductivity of air (k_{air}) to compute the heat transfer coefficient ($h = \frac{Nu\ k_{air}}{d}$) of the droplets, which ranges between 6888–3165 and 33 945–23 370 W/m^2·K, respectively for the large and small grain diameter in the considered *u* interval (Moitra et al. 2018). Finally, we determine the cooling rate of each droplet size from the initial temperature of 1200°C down to ambient temperature (25°C), using the transient 1-D spherical heat conduction model of Recktenwald (2006) implemented in MatlabTM. Input parameters are *h*, *d*, plus the melt thermal conductivity (k_m) and diffusivity (α_m) for Hohenstoffeln, which at 1200°C are 1.1 W/m·K and 2.19 x 10^7 m^2/s, respectively (Büttner et al. 1998). Since the derived *h* variations produce only a slight difference with ejection velocity, we only show the 10 m/s plots (Fig. 4.12b). We assume the magma had not started to cool yet up to this point, for simplicity, meaning that calculated cooling times are maxima.

For the 710 µm droplet diameter, the surface of the grain reaches ~ 979°C after 10 ms (Fig. 4.12b, left), just above the glass transition temperature (Tg) (937°C, Büttner et al. 1998). Since we observed plenty of spherical juvenile grains within this size fraction in Hohenstoffeln 3 MPa, it is reasonable to affirm that viscous relaxation occurred well within 10 ms, similarly to what was directly observed for drop 1, and that the spherical shape was then preserved by cooling.

For a 88 µm droplet, the surface of the particle is below the glass transition after only 0.5 ms, forming a cooled rim ~ 5 µm-thick (Fig. 4.12b, right). The preponderant amount of perfect spheres observed in the very fine ash for both Hohenstoffeln and Billstein at 3 MPa (Fig. 4.5) indicates that viscous relaxation after breakup occurred within this time window, taking less than 0.5 ms.

Although non-spherical particles have a greater surface area for a given volume, and therefore cool even faster, the calculations for spheres give a rough estimate of cooling timescales for all the studied juvenile ash particles. If surface tension is to reshape a liquid droplet, there is only a few ms or even less time (depending on grain size) to do so before the particle becomes solid and the non-spherical shape gets frozen. Any factor extending filament thinning timescales, such as an increased viscosity, will allow elongate shapes and tears to be preserved by extremely rapid cooling. An increased ejection speed also favors non-spherical grains.

4.5.3 Kīlauea Iki 1959 versus experiments

The natural juvenile particles from the 1959 Kīlauea Iki eruption fall within the range of magma compositions tested in our experiments, with Billstein as the closest geochemical analogue (Fig.

4.13a in Online Resource 4.1). Both Kīlauea Iki and Billstein are expected to have comparable values of surface tension, at eruption temperatures. In contrast, densities of Kīlauea Iki juvenile grains, across all size fractions, are much broader than their artificial counterparts, ranging from 600 to 2700 kg/m^3 (Mueller et al. 2018), although reticulite can go as low as 50 kg/m^3 (Stovall et al. 2011). For the studied size fractions of narrow + 1ϕ and narrow + 4ϕ, we measured 2D vesicularities between 0 and 68% in the pyroclasts, which translates as densities from about 2800 to 900 kg/m^3 (derived using the dense rock equivalent value of 2800 kg/m^3 reported in Stovall et al. 2011).

The median axial ratio of Kīlauea Iki pyroclasts for the narrow + 1ϕ fraction is most similar to that of the Billstein 10 MPa run (Fig. 4.11c). It is worth noting, however, that the estimated peak ejection velocity of Kīlauea Iki (~ 110 m/s, Porritt et al. 2012) is much higher than the coherent portion of the magma plugs in the experiments (Table 4.1). The gas piercing phase of the 10 MPa experiments, however, generated velocities comparable to the estimated peak ejection velocity of Kīlauea Iki (115 m/s for Hohenstoffeln and ~ 75 m/s for Billstein; Table 4.1). Nonetheless, the observed similarities between natural and experimental fluidal pyroclasts highlight the role played by composition and rheological properties of the magmas in controlling the final morphology of juvenile particles. The experiments well mimicked the discrete nature of fountain pulses but also other weak styles involving mafic and ultramafic magmas, generating similar fluidal morphologies such as Pele's tears and Pele's hairs, the latter also found in Strombolian pulses (Cannata et al. 2019).

Beyond the similarities, the experiments remain a rather simplified version of a lava fountain. In nature, a single eruptive pulse is part of a large, fast-paced sequence making up entire episodes (Taddeucci et al. 2015). The virtually sustained ejection of gas-rich magma over several hours allows the development a central hot zone within the fountain (Stovall et al. 2011). The longer the time spent by a fragment within this zone, the more bubble growth and expansion will occur, until the initial fluidal appearance is replaced by a vesicle-dominated morphology (Porritt et al. 2012). In the experiments, the ejection of bubble-poor magma as a discrete burst does not ultimately generate the highly vesicular pyroclasts observed in the Kīlauea Iki samples (Fig. 4.4).

4.5.4 Limits of very fine juvenile ash in studies of primary magma fragmentation for lava fountains

In general, for comparative studies of primary magma fragmentation, the very fine ash is crucial to constrain the intensity of the fragmentation mechanisms, along with identifying possible

magma-water interaction signatures (Büttner et al. 1999, 2002; Dellino et al. 2012; Dürig et al. 2020a, 2020b; Appendix I). However, in weakly explosive styles such as lava fountains or Strombolian activity, the primary production of very fine particles tends to be comparatively low (D. Andronico, personal comm., 2020), so the fine ash is rarely studied. Our distal Kīlauea Iki 1959 samples contain only 0.8–0.9 wt.% particles in the full + 4ϕ fraction (125–63 μm) plus the pan (< 63 μm) combined. In the analyzed narrow + 4ϕ (88–63 μm) interval, these particles are mostly characterized by vesicle wall fragments, with less than 10% fluidal pyroclasts (Fig. 4.5, bottom). In contrast, in the narrow + 1ϕ fraction of the same samples (Fig. 4.4, bottom), fluidal particles make up over one third of the population and the amount of vesicle walls is very low. We consider the large proportion of vesicle walls in the narrow + 4ϕ fraction from Kīlauea Iki to be result of secondary brittle breakage of scoria, golden pumice and other vesicular fragments. In the narrow + 4ϕ fraction, only the achneliths are thought to result from primary magma fragmentation. So if fine ash from weakly explosive magmatic styles is to be integrated in comparative studies of primary fragmentation, care will be needed to exclude the products of secondary breakage.

4.6 Conclusions

Lava fountains, in Hawaii and elsewhere, produce fluidal juvenile pyroclasts (“achneliths”) due to hydrodynamic magma fragmentation. The morphology of these fluidal particles ranges from spherical to extremely elongate (Pele’s hairs). We have conducted liquid jet breakup experiments at laboratory scale, using three magma compositions and two driving pressures, that shed light on the controls on fragmentation and pyroclast shapes in lava fountains.

We have established that:

(1) The interplay between magma composition, ejection velocity and cooling history is ultimately responsible for the diversity in fluidal clast shapes;
(2) For ultramafic magmas, surface tension governs breakup at low ejection velocities, promoting the generation of spherical and other compact juvenile morphologies such as ovoids, lobate particles and short-tailed Pele’s tears. For this magma composition at high ejection velocities, enhanced stretching leads to a larger production of Pele’s tears and other elongate fragments, although spheres are still present;
(3) With increasing silica content, viscosity becomes the main factor opposing surface tension, resulting in longer times for liquid thinning. For the intermediate composition

magmas in the experiments, this leads to a preponderance of long-tailed Pele's tears and Pele's hairs, respectively at low and high ejection velocities;

(4) The cooling history of an incandescent magma drop will determine its ability to retain or lose the initial shape generated upon breakup. For the studied ash size fractions, cooling to below the glass transition proceeds within a few ms or less. These short timescales allow low-silica droplets to reshape intro spheres, but higher viscosity particles cannot do that. Moreover, for a same composition, reshaping to a minimum energy configuration is easier when magmas are expelled at lower velocities, as limited elongation requires less time to contract;

(5) Some of our experimental fluidal juvenile particles have shapes that strongly resemble those of natural achneliths from distal deposits of the 1959 Kīlauea Iki eruption. The best morphological fit is with our high-velocity basaltic experiment. The marked morphological similarities between artificial and natural juvenile particles suggest that comparable clast-forming and clast-shaping processes apply to natural lava fountains. Nonetheless, the combination of gas-rich magma with growing bubbles and the closely spaced repetition of several pulses within a natural lava fountain episode leads to a broader range of morphologies, which includes highly vesicular pyroclasts;

(6) The presence of these very fragile scoriaceous to pumiceous juvenile particles leads to an overrepresentation of broken vesicle walls in the very fine ash size fractions. These are formed by secondary breakage, so the information retrievable for investigating primary magma fragmentation mechanisms might be limited in very fine ash from low intensity magmatic eruptions such as Hawaiian and Strombolian ones.

We recommend additional work on pyroclast shapes in lava fountains. Comparisons could be made with achneliths from other natural lava fountain deposits, representing a range of ejection velocities, magma compositions, and eruption temperatures. Follow-up laboratory experiments could explore jets of magmas with different vesicularities, or even heterogeneous vesicularities. Such hydrodynamic fragmentation experiments should ideally be filmed with high-speed cameras that allow the study of sub-mm droplets separating and cooling in the atmosphere within very short timescales. Other experiments might try to access not only hydrodynamic fragmentation of the classic achnelith-forming fountains seen in Hawaii for example, but also the additional brittle fragmentation related to high strain rates, that results in "ash-rich" fountains typical of the Etna paroxysms (La Spina et al. 2021). Finally, instantaneous viscosity in 'explosive' magma fragmentation remains a major unknown and this topic should be studied.

4.7 Acknowledgements

This study was funded by a Discovery Grant to PSR from the Natural Sciences and Engineering Research Council of Canada (NSERC) (RGPIN-2015-06782). We thank Sebastian Mueller, Bruce Houghton and Wendy Cockshell for providing the Kīlauea Iki 1959 samples. We thank Jacopo Taddeucci and Lucy Porritt for their comments on a draft for this paper.

4.8 Online Resource 4.1: Detailed methodology

4.8.1 Tested materials

Two kinds of juvenile pyroclasts were utilized in this study: experimental and natural.

4.8.1.1 Experimental samples

Artificial juvenile pyroclasts were produced during magma fragmentation experiments at the *Physikalisch Vulkanologisches Labor* (PVL) in the University of Würzburg (Germany). The three rock materials remelted for the experiments span from ultramafic to intermediate compositions, covering a wide range of land volcano types and eruptive styles (Fig. 4.13a). They include:

1) Hohenstoffeln, a dense olivine-melilitite lava with ~ 38 wt.% SiO_2 sourced from a Tertiary lava lake in the Hegau volcanic field in Germany (Zimanowski et al. 1997; Hobiger et al. 2011);
2) Billstein, a thick and dense alkaline basalt lava flow with ~ 45 wt.% SiO_2 from the Rhön volcanic field, Germany (Zimanowski et al. 2004);
3) Sommata, a basaltic trachyandesite lapilli-size scoria deposit with ~ 54 wt.% SiO_2 from the island of Vulcano in the Aeolian archipelago, Italy (Büttner et al. 2002; Hobiger et al. 2011; De Astis et al. 2013).

4.8.1.2 Natural samples

Natural juvenile pyroclasts come from the summit portion of the 1959 Kīlauea Iki eruption (Hawaii, USA). The event consisted of 17 eruptive episodes, the first 16 of which were characterized by major lava fountaining (Richter et al. 1970). Based on the accounts of Richter et al. (1970) and the more recent summaries of Stovall et al. (2011) and Mueller et al. (2018), the summit eruption started in the evening of November 14, 1959, from a discontinuous, > 750 m-long fissure located at mid-height on the SW side of the Kīlauea Iki pit crater and lasted for 36 days.

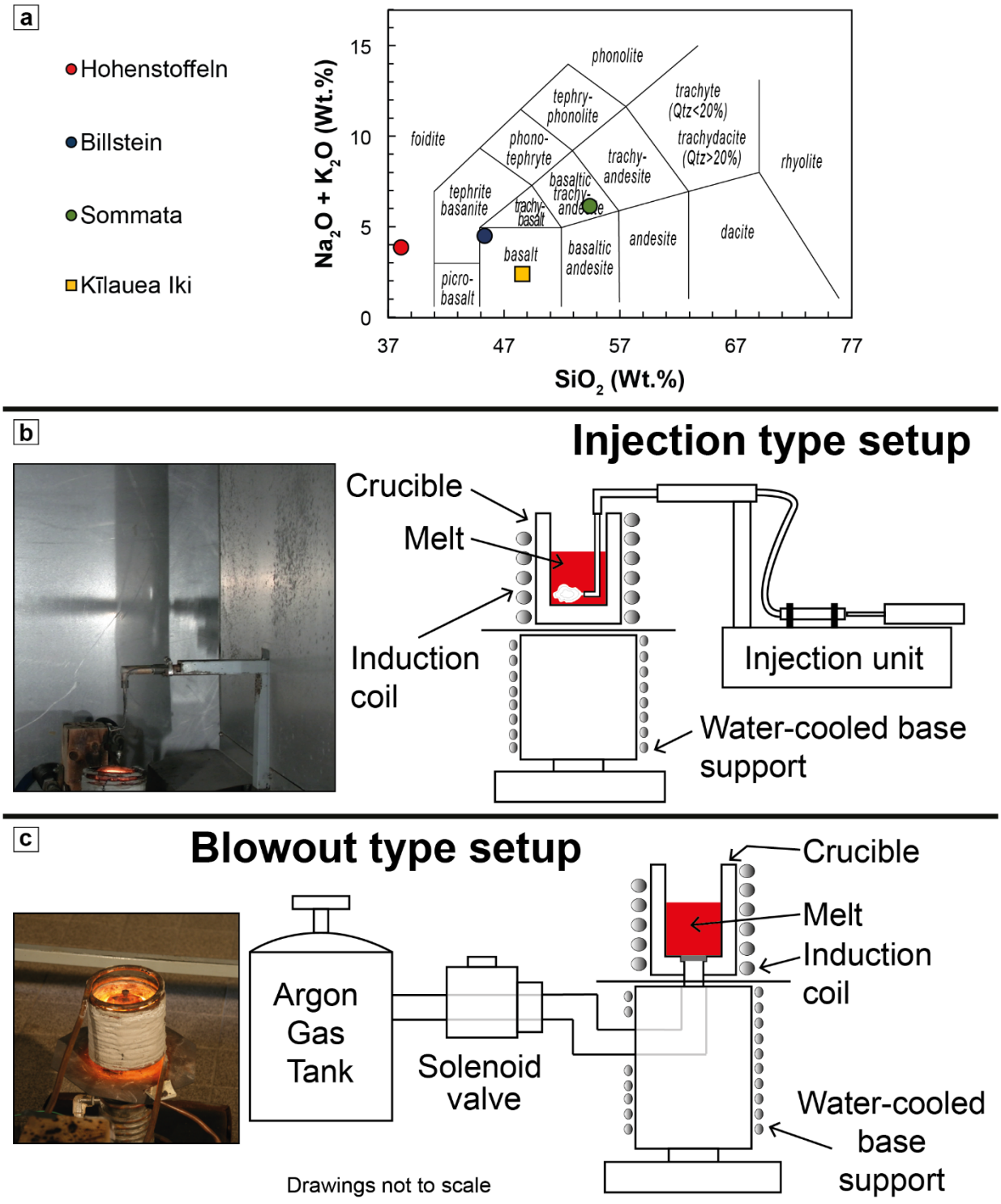

Figure 4.13: (a) Total alkalis vs. silica diagram of the four studied materials (modified from Le Bas et al. 1986). Data for Hohenstoffeln and Sommata from Hobiger et al. (2011). Data for Billstein from Zimanowski et al. (2004). Average composition from spatter and pumice fragments for Kīlauea Iki from Murata and Richter (1966). (b) Scheme of the injection-type experiment setup used to produce the "low-speed" (3 MPa) artificial pyroclasts. (c) Scheme of the blowout-type experiment setup used to produce the "high-speed" (10 MPa) artificial pyroclasts. Modified from Austin-Erickson et al. (2008).

Ten vents (A to J) were active during the first two days of the eruption, with a mix of lava effusion, low fountains and spattering. From the night of November 15 onwards, activity focalized on vent A with the buildup of a > 60 m-high agglutinated cone. Fountain phases up to 580 m high (Stovall et al. 2011) characterized the first 16 episodes, with durations between 2 hours and > 6 days, and repose times between 7 hours and 4 days (Mueller et al. 2018). Throughout the whole summit eruption, primary and clastogenic lava flows fed a vast lava lake within the pre-existing pit crater (Fig. 4.1c). With the exception of episode 1, each fountain phase was followed by incipient lava drainback from the lava lake into the vent, causing the drop in fountain height or its ultimate cessation. The pyroclastic products in the ash size range (and some lapilli) generated during the summit eruption were dispersed SW by the prevailing winds over about 15 km from the active vents (Fig. 4.1c). Importantly, due to the location of the vents halfway inside the SW slope of the pre-existing Kīlauea Iki pit crater, only the pyroclastic products from fountains higher than the crater edge are preserved in the tephra sheet (Mueller et al. 2018).

The three samples selected for this study are located in the tephra fallout sheet between 3.5 and 4 km from the vent area (Fig. 4.1c). Thickness of the deposits was 4–5 cm (S. Mueller, personal communication, 2019), and about 40 wt.% of each sample falls in the ash size fraction (< 2 mm). Despite the difficulty to link each tephra unit to a specific eruptive episode, the samples likely include pyroclastic material from episode 1 (marked by the presence of Pele's hairs) as well as episode 3, 15 and 16 (S. Mueller, personal communication, 2019). Chemical composition of all Kīlauea Iki samples is fairly narrow, falling within the sub-alkaline basalt field (Fig. 4.13a). SiO_2 is ~ 49 wt.%, with a modal composition (in volume %) dominated by volcanic glass or fine groundmass at ~ 84%.

4.8.2 Experiment setup and timeline

In order to generate the artificial juvenile pyroclasts, the selected materials were re-melted and then fragmented using two different experimental setups. The two different experimental configurations were part of a larger program, which also involved phreatomagmatic experiments. For this paper, we selected three magma compositions and two driving pressures, resulting in six successful gas-driven hydrodynamic fragmentation runs.

The first step for each run involved placing a set amount of granulated rock inside a 5 cm (inner diameter) steel crucible, regardless of the experiment configuration (detailed below). The coarsely ground material was heated to 1200°C within one hour, inside an induction furnace (Figs. 4.13b,

c). It worth noting that some crystals originally present in the rock might have been present in the magma, due to the rapidity of the heating process.

The “low-speed” artificial pyroclasts were generated using the injection-type configuration (Fig. 4.13b) and 255 g (± 10 g) of granulated volcanic rock (see Zimanowski et al. 1997 for a complete description). A discrete volume of compressed argon gas at 3 MPa (30 bars) was injected within the magma through a J-shaped steel pipe mounted on a servo drive. This led to the violent upward expansion and hydrodynamic fragmentation of the ejected magma within the crucible and in the atmosphere (Zimanowski et al. 1997). The vertical velocity of the magma plug upon exiting the crucible was about 44 m/s for Hohenstoffeln, 33 m/s for Billstein and 36 m/s for Sommata. This setup can also be employed to inject water into the melt, but the experiments reported on here relied exclusively on compressed argon to fragment and eject the melt.

The second experimental setup is informally known as the “blowout” configuration (see Büttner et al. 2006 for details). It was used to generate the “high speed” artificial pyroclasts (Fig. 4.13c), employing about 200 g of granulated material in each run. Unlike to the previous setup, the compressed argon at 10 MPa (100 bars) required for fragmentation was introduced through a hole at the base of the crucible, regulated by a solenoid valve. Like in the low speed series, upward magma ejection was accompanied by expansion and hydrodynamic fragmentation both within the crucible and in the atmosphere. The vertical velocity of the magma plug upon surpassing the crucible was about 11 m/s for Hohenstoffeln, 11 m/s for Billstein and 13 m/s for Sommata.

The bulk ejection and fragmentation of the magma plug in the 3 MPa and 10 MPa series took about 80 and 50 ms, respectively. Each run was mainly recorded by use of a high-speed camera at 5000 (3 MPa series) and 2000 (10 MPa series) frames per second (details in Chapter 3; see Online resource 4.2 for the videos). For each run we measured (i) the average ejection velocity of the first cloud of drops generated by the gas piercing phase, (ii) the speed of the intact portion of the magma plug at the crucible exist, and (iii) specific drops, from the high-speed video footage. Measurements were performed using both Adobe Illustrator® and Phantom Camera Control (PCC) software®. A time interval of 1.5 ms was considered, corresponding to seven and three frames for the 3 and 10 MPa series, respectively. Other video cameras filmed the experiments from various angles, and several parameters such as force, pressure, etc. were recorded.

4.8.2.1 Collection of the experimental pyroclasts

Between each run, most of the experimental room (including the containment roof) was vacuum cleaned, then the portion of the floor used for collecting samples was very thoroughly washed and dried. Poorly accessible areas, which were not used for sampling, were nevertheless vacuumed and cleaned in order to minimize cross-contamination from previous experiments.

After each experimental run, the particles were carefully collected from two main designated areas. (1) The floor area between the crucible and the control room was covered with large paper sheets for the collection of very fine ash, in order to minimize cross-contamination. Sheets were weighted, then carefully folded and bagged. (2) Particles having landed in the front of the experiment room were vacuumed from the floor using pre-weighted filter bags, to be used for the analysis of the bulk sample and coarse fractions, upon addition of the net weight from the paper sheets.

Fragile elements, such as glass films and “rock wool” (Pele’s hairs clusters), were handpicked and bagged separately prior to collection of the main samples, in order to avoid post-fragmentation breakage and sieving issues. These fragile elements were weighted but excluded from grainsize analysis.

4.8.3 Particle characterization

4.8.3.1 Overview of the work done at INRS

To investigate shape and textural variations in our samples, we largely followed the “standard and recommended steps” workflow proposed in Appendix I (2021, see Fig. A1.2). Preliminary steps on the full samples involved i) hand sieving, and ii) short, low intensity ultrasonic cleaning of 0.71–0.5 mm (narrow + 1ϕ) and 88–63 µm (narrow + 4ϕ) size fractions. The justification for working on these specific coarse ash and very fine ash fractions was provided in Appendix I and Chapter 2.

The following stages varied according to the size fraction considered. For the 0.71–0.5 mm (narrow + 1ϕ) fraction, given the virtually “lithic-free” nature of both natural and experimental samples, “basic componentry” (see Appendix I, Fig. A1.2) was replaced with juvenile particle selection at the binocular microscope. Selected + 1ϕ juvenile grains were then subjected to the following steps: i) Detailed componentry on loose grains, at the binocular microscope; ii) 2D shapes and internal texture analysis of particle cross-sections prepared as polished epoxy grain mounts (PEGMs), and imaged at the scanning electron microscope (SEM).

For the 88–63 μm (narrow + 4ϕ) fraction, a random portion from each bulk fraction was mounted as a carbon tape grain mount (CTGM) and imaged at the SEM. Unwanted foreign debris and lithics were filtered out using a combination of visual distinction and chemistry comparison by the use of energy-dispersive x-ray spectroscopy (EDS). Analysis of + 4ϕ juvenile grains entailed i) a 3D morphology study and ii) 2D shape measurements on juvenile particle silhouette images acquired at SEM.

4.8.3.2 Pre-cleaning, dry hand sieving and ultrasonic treatment

Prior to sieving, artificial samples were examined in order to remove most of the undesired material, such as coarse steel shards from the crucible and pieces of the ceramic floor from the experiment room. Very fragile material such as rock wool (i.e., an agglomerate of Pele's hairs), if present, were also extracted to avoid further breakage during sieving, which would have resulted in i) clogging of the sieve mesh, ii) overrepresentation of such population in the investigated size fractions and iii) particles' overcrowding during mounting and observation.

Pre-cleaned artificial samples were gently hand sieved using full ϕ intervals, providing a grain size distribution. The size fractions of interest, + 1ϕ and + 4ϕ, were further processed with half ϕ sieves, yielding 710–500 μm (narrow + 1ϕ) and 88–63 μm (narrow + 4ϕ) fractions, respectively.

Natural samples arrived pre-sieved down to + 0.5ϕ, whereas the finer material was not yet sieved. We dry sieved the material between + 1ϕ and + 4ϕ as previously described for the experimental samples, and extracted the same two fractions.

The narrow + 1ϕ and narrow + 4ϕ fractions of each sample were finally "washed" in distilled water using an ultrasound bath up to 3 minutes (depending on sample conditions), in order to remove adhering fine dust present on the grains. Once treated, samples were dried at 60°C for 6–8 hours.

4.8.3.3 Selection of juvenile particles

The 710–500 μm (narrow + 1ϕ) fractions were examined under the binocular microscope and found to consist overwhelmingly of glassy juvenile material. For the experimental samples, foreign debris from the experiment room and very rare grains from previous runs (with different compositions) that escaped the pre-sieving cleaning process were set aside. Rare lithic fragments in the Kīlauea Iki material, most likely associated to the opening stage of the eruption, were set aside, along with very rare free crystals (mostly olivine). This left a glassy juvenile concentrate.

For the 88–63 μm (narrow + 4ϕ) fraction, juvenile particles are very difficult to isolate at the binocular, due to their extremely small size. Therefore, a random portion of the bulk fraction was mounted on ~ 12 mm aluminum stubs as a CTGM. Au/Ir-Pd coated CTGMs were imaged using a Zeiss EVO 50 SEM in backscatter mode (BSE). A mix of greyscale contrast difference and EDS chemistry was used to distinguish glassy juvenile particles of the expected composition from unwanted material.

4.8.3.4 Detailed componentry and 3D morphology study of juvenile particles

Detailed componentry (for the + 1ϕ fraction) and 3D morphology study (for the + 4ϕ fraction) were carried out on multi-particle images. For the + 1ϕ fraction, images of loose grains were acquired during juvenile selection at the binocular microscope, equipped with a high-resolution camera. An average of 12 images, each containing an average of 23 juvenile grains, were needed to acquire over 200 juvenile particles per sample. For the SEM-BSE imaging of + 4ϕ juvenile pyroclasts, enough grains were mounted to cover the whole area of the carbon tape, with the goal to have over 200 juvenile grains after filtering out foreign debris and other undesired grains. Both + 1ϕ and + 4ϕ images were subsequently loaded into the free software JMicrovision (Roduit 2007; https://jmicrovision.github.io/). Juvenile particles were separated into different classes through manual point counting to obtain the relative proportions.

A three-level hierarchical classification was developed, which applies to both studied size fractions and to both natural and artificial samples (Fig. 4.14, Table 4.2). It uses a comprehensive set of criteria, such as: i) luster (only applicable to + 1ϕ binocular images), ii) surface characteristics, iii) overall morphology (e.g., degree of elongation, angularity and flattening; mass distribution of the particle from its center, etc.) and iv) visually-observed complexity of inter-vesicle networks (for vesicular grains). In summary, four main classes define the top level: i) fluidal; ii) transitional; iii) vesicle-dominated; iv) angular. Fluidal juvenile pyroclasts encompass the broad variety of achneliths (Walker and Croasdale 1971) observed in natural deposits, such as Pele's tears and Pele's hairs. The latter displayed a sharp thickness bimodality, prompting for a further distinction between thin and thick Pele's hairs. While the former are up to few microns in diameter, the latter have average thicknesses within the same order of magnitude as the size fraction in which they are observed. The thickness range of all examined hairs is in line with that reported in the literature (Duffield et al. 1977; Cannata et al. 2019), ranging from 1 μm up to 900 μm.

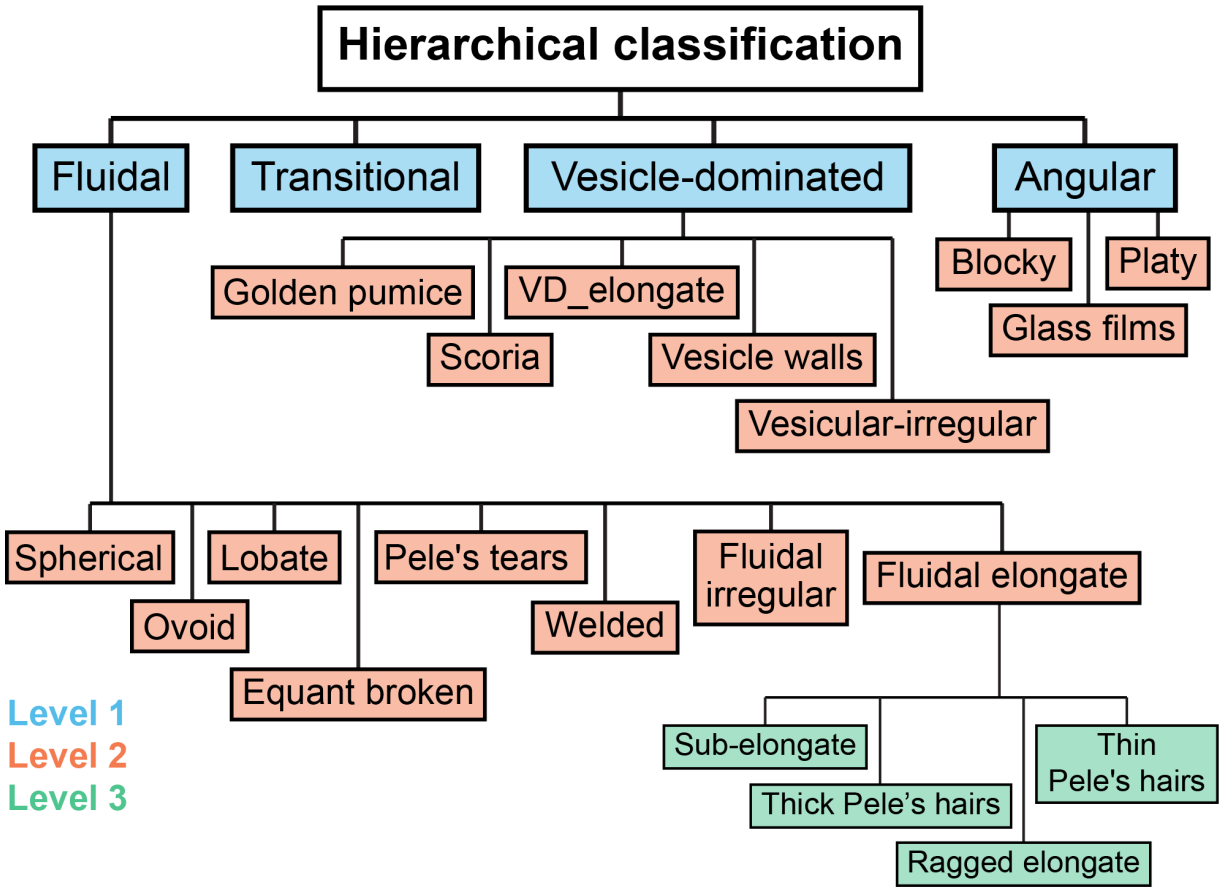

Figure 4.14: Hierarchical classification used for detailed componentry (+ 1ϕ) and 3D morphology (+ 4ϕ) of the juvenile particles from the tested samples.

Vesicle-dominated grains include golden pumice, scoria and vesicle walls. In a lava fountain context, transitional juvenile pyroclasts show intermediate characteristics between fluidal and vesicle-dominated clasts (Stovall et al. 2011). Scoria, transitional clasts and golden pumice are mainly differentiated by an increasing abundance and interconnection of the internal vesicle lattice and decreasing thickness of the walls separating adjacent vesicles.

4.8.3.5 2D morphometric and internal texture measurements

For the 710–500 μm (narrow + 1ϕ) fraction, the two-dimensional measurement of several morphometric parameters, 2D bulk crystallinity and 2D bulk vesicularity was carried out by following the steps detailed in Chapter 2, for which a summary is provided here.

Table 4.2: Breakdown of the hierarchical classification for detailed componentry and 3D morphology study

Level 1	Level 2	Level 3	Class description
Fluidal	Spherical (Fig. 4.3a) (1)	-	Spherical to nearly spherical shapes. Either shiny or dull in luster (for binocular images)
	Ovoid (Fig. 4.3b) (1)	-	Egg-shaped to ellipsoidal grains
	Lobate (Fig. 4.3c) (1)	-	Two or three lobes are visible. Includes dumbbells. Usually characterized by smooth, round sides
	Equant broken (Fig. 4.3d) (1)	-	Broken fluidal grains, equant to sub-equant in shape, with at least one sharp side that indicates secondary brittle breakage
	Pele's tears (Fig. 4.3e) (1)	-	Tear shaped grains characterized by one or more tails. The main center of mass might varies from spherical to lobate. Includes spindle-shaped tears, and those whose tail is largely missing
	Welded (Fig. 4.3f) (1)	-	Multiple fluidal juvenile grains joined together
	Fluidal irregular (Fig. 4.3g) (1)	-	Complex shapes difficult to associate to one of the previous fluidal classes
	Fluidal elongate	Sub-elongate (Fig. 4.3h) (1)	Rod-type grains characterized by a smooth simple rim. Width/length ratio can be up to 1:5 or more compact. Some particles may show pinched edges reminiscent of a spindle shape, or a broken side as part of a longer fragment
		Thick Pele's hairs (Fig. 4.3i) (1)	Long, smooth rods with a width/length ratio of at least 1:5. Might be characterized by decreasing thickness from one end to the opposite end.
		Ragged elongate (Fig. 4.3j) (1)	Elongate particle characterized by a ragged, complex perimeter
		Thin Pele's hairs (Fig. 4.3k) (1)	Very thin glass strands with a diameter of few microns. When present together, thin hairs will be clearly much thinner than thick Pele's hairs. Thin hairs might be intertwined
Transitional (Fig. 4.3l) (1)	-	-	Span the textural range between fluidal achneliths and golden pumices. Characterized by moderate vesicularity, often showing both a smooth, fluidal side and a ragged, vesicle-dominated rim. Close-cell, vesicle lattice texture characterized by dark brown thick walls, although local open-cell foam might be also present
Vesicles-dominated (VD)	Golden pumice (Fig. 4.3m) (1)	-	Spongy, light golden color (under the binocular), open-cell type foam with ≥ 85% vesicles. Includes reticulite herein to simplify scheme
	Scoria (Fig. 4.3n) (1)	-	Ragged grains with dull tone, characterized by a close-cell foam with ≤ 85% vesicles. Vesicles have thicker walls than in pumice.
	VD_elongate (Fig. 4.3o) (1)	-	Long rods with a width/length ratio of 1:5 or more, characterized by lengthwise concave vesicle walls that dominate the entire shape

Table 4.2, continued.

Level 1	Level 2	Level 3	Class description
Angular	Vesicle walls (Fig. 4.3p) (1)	-	Glass remnant between broken, large vesicles. Characterized by one to four vertices. Includes cuspate grains
	Vesicular-irregular (Fig. 4.3q) (1)	-	Complex shapes, difficult to associate to one of the previous VD classes. Includes complication of vesicle walls where a portion of glass has vesicles nested inside
	Blocky (Fig. 4.3r) (1)	-	Angular, typically dense to poorly vesicular grains characterized by sharp edges, equant to sub-equant shapes. “Fluidal” surfaces are absent
	Glass films (Fig. 4.3s) (1)	-	Very thin (4 to 20 microns) membranes of sideromelane (volcanic glass). Equant to elongate in shape, with angular corners. Often flat (sometimes curved), might show corrugations or wilting
	Platy (Fig. 4.3t) (1)	-	Same main features than blocky, but with the longest side much larger than the others. If present together, platy grains will be always much thicker than glass films

([1]) See figure 4.3.

For each sample, 50 juvenile grains were embedded in epoxy resin, then ground and polished to remove 250 µm, i.e. half the mesh size of the retaining sieve. Au/Ir-Pd coated PEGMs were imaged using a SEM in BSE mode. Image acquisition settings, such as magnification and resolution, were optimized to yield over 20 000 pixels per particle (Chapter 2). Brightness and contrast were set to provide a satisfactory distinction (expressed as grayscale intensity) both between the resin and the particle edge, and among the particle groundmass, crystals and vesicles within each grain. Image preparation in Adobe Photoshop© was necessary to refine the proper particle outline and to clean the epoxy area between the grains, which was converted to a uniform color background. Additional refinements involved blackening internal vesicles, enhancing the contrast of crystals relative to the groundmass, and filling cracks.

For the 88–63 µm (narrow + 4ϕ) fraction, measurement of morphometric parameters was carried out on the SEM-BSE silhouette images of the CTGMs already used in the 3D morphology study.

Image processing of either particle cross-sections or silhouette images was then carried out using the PASTA package (Comida and Ross 2021), plus the script PARTISAN (Dürig et al. 2018) for the measurement of additional shape parameters.

4.9 Online Resource 4.2: High-speed video recordings

The high-speed video recordings of the experiments will be available in the final version of the journal manuscript.

4.10 Online Resource 4.3: Measurement data spreadsheets

The morphometric and textural measurement data will be available in the final version of the journal manuscript.

5 GENERAL CONCLUSIONS

5.1 Summary of the main outcomes

This dissertation explored primary magma fragmentation processes and juvenile pyroclast shapes in lava fountains, through the use of laboratory experiments. These transient magma jet experiments were compared with industrial liquid jets and with lava fountain pulses. A standardized methodology was developed to study juvenile pyroclasts for comparative studies of primary magma fragmentation; this methodology was applied here to the experimental and natural lava fountaining products, but it can be utilized on any pyroclastic deposit. While developing the standardized methodology, insights were also gained about the products of Strombolian pulses and phreatomagmatic explosions at a maar-diatreme volcano.

5.1.1 Standardized methodology for comparative studies of primary magma fragmentation using juvenile pyroclasts

Juvenile pyroclasts are crucial in the investigation of primary magma fragmentation mechanisms (Dellino and La Volpe 1996; Büttner et al. 1999, 2006; Liu et al. 2015, 2017; Polacci et al. 2019; Liu 2021; Namiki et al. 2021; Taddeucci et al. 2007; 2021). Both external morphology and internal textures retain essential information on the state of magma upon fragmentation, as well as on fragmentation processes and eruptive styles (Heiken 1972; Cioni et al. 1992; Büttner et al. 1999; Stovall et al. 2011; Dellino et al. 2012; Porritt et al. 2012; Jordan et al. 2014; Leibrandt and Le Pennec 2015; Liu et al. 2015, 2017; Avery et al. 2017; Dioguardi et al. 2017). However, the absence of a standard methodology to study juvenile pyroclasts makes it difficult to produce comparable data from different volcanoes and different laboratories. This existing gap led to the development – by an international group of workers including the author – of a first complete standardized workflow, spanning from sample collection in the field, to the ultimate measurement of specific parameters on juvenile pyroclasts (Appendix I and Chapter 2).

Specifically, steps of the workflow directly developed by the author during this PhD project include the manufacture of high-quality polished epoxy grain mounts (PEGMs) at INRS (Chapter 2), and the double mounting procedure for the carbon tape grain mount (CTGM)-PEGM conversion (Appendix I). All subsequent steps developed by the author relate to cross-section analysis of juvenile particles using backscattered electron scanning electron microscope (SEM) imaging (Chapter 2):

- The assessment of the minimum SEM magnification and resolution – which together control number of pixels per particle – required to obtain statistically reliable average values of morphometric parameters, 2D crystallinity and 2D vesicularity; compared to previous studies that analyzed only shapes, it was found that a higher number of pixels per particle is required to also measure textural parameters;
- The definition of the minimum number of juvenile particles needed for the statistically robust measurements of the morphometric and textural parameters; this investigation showed that for a specific size fraction and using high-quality images, a much lower number of grains is needed to stabilize average values, compared to suggestions from most previous studies;
- The choice of the 0.71–0.5 mm (+ 0.5 to + 1ϕ) coarse ash interval as the ideal size fraction to measure morphometric and textural parameters on PEGMs, based on theoretical considerations (grain size commonly found in most deposits, large enough clasts size to contain representative proportions of crystals and vesicles, versatile fraction to study particle- and groundmass-scale details) and practical experience (ease of cleaning, juvenile selection, PEGM mounting, SEM image acquisition and processing);
- The development of the free open source Particle Shapes & Textures Analyzer (PASTA) (Comida and Ross 2021) package for the preparation, processing and measurement of morphometric parameters, 2D crystallinity and 2D vesicularity of juvenile pyroclasts acquired as SEM images.

The natural pyroclasts from the 1977 Ukinrek maars eruption (Alaska) (Kienle et al. 1980; Ort et al. 2018) functioned both as test material during the development of each step and as the first samples to be investigated. Chapter 2 shows that Strombolian and phreatomagmatic juvenile grains from Ukinrek can be distinguished based on morphometric and bulk textural analysis of 2D cross sectional slices; for example using a plot of solidity versus 2D crystallinity or convexity.

5.1.2 Hydrodynamic breakup regimes in lava fountains

Chapter 3 focused on primary magma fragmentation in lava fountains, specifically on the hydrodynamic (ductile) breakup of a coherent magma mass into liquid drops (Porritt et al. 2012; Jones et al. 2019). This mode of fragmentation is still incompletely understood, due to the complexity of the involved magmas and the difficulty to access active volcanic vents. The fragmentation experiments performed at *Physikalisch Vulkanologisches Labor* (PVL) provided a direct view on hydrodynamic magma breakup through the use of high speed cameras. Using three

magma compositions – spanning from ultramafic to intermediate – and two driving pressures allowed an exploration of how silica content and ejection velocity influence hydrodynamic breakup. The existing comprehensive literature on industrial and commercial liquid jets (Eggers and Villermaux 2008; Birouk and Lekic 2009; Lefebvre and McDonell 2017) was used to analyze high speed video imagery from the experiments. This literature distinguishes four breakup regimes for liquid jets: (I) Rayleigh, (II) first wind-induced, (III) second wind-induced, (IV) atomization or spray. These regimes are often depicted on the traditional Ohnesorge diagram (Reitz and Bracco 1986; Lefebvre and McDonell 2017), which relates two dimensionless numbers (Fig. 1.3). The effect of viscosity, an important parameter in the current experiments, is not straightforward on this traditional diagram, so a new one plotting Weber number versus Reynolds number was prepared to better illustrate which parameter among internal properties and external aerodynamic effects dominated magma breakup (Fig. 5.1).

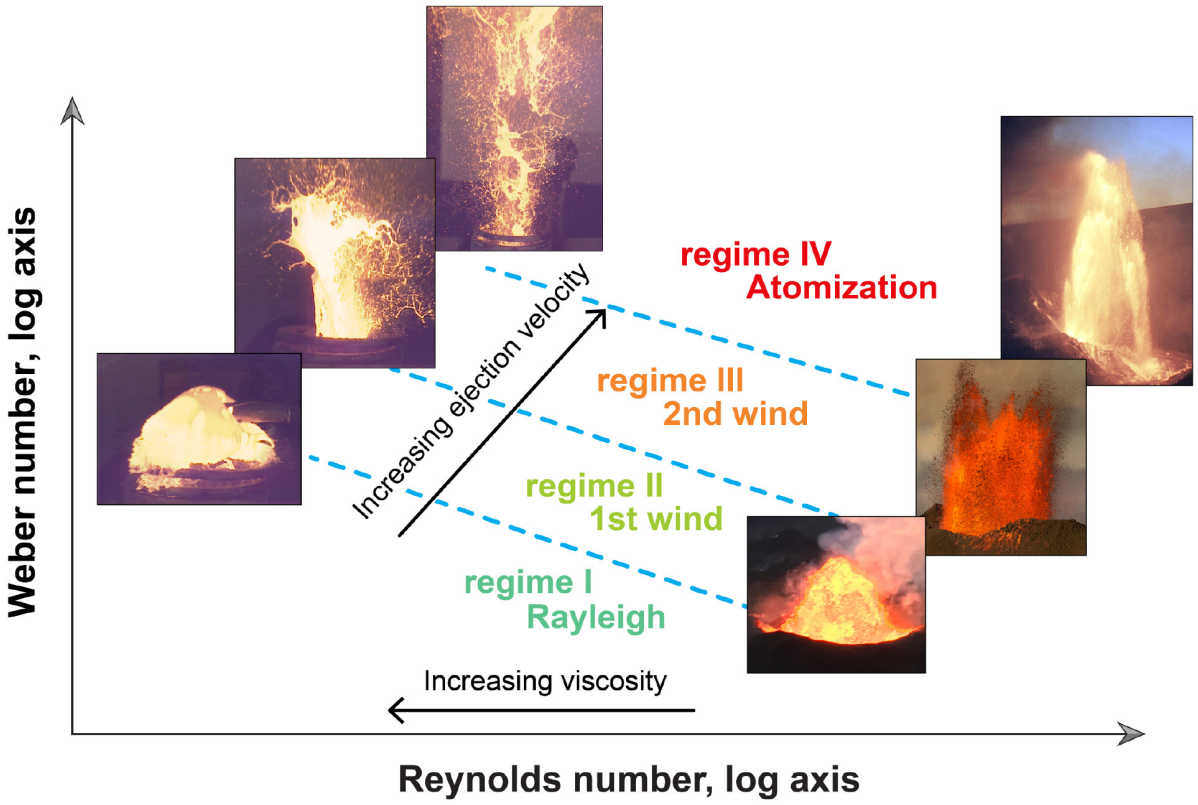

Figure 5.1: Modified Ohnesorge diagram for the identification of the breakup regimes. The images represent a visualization of the regimes II to IV in the experiments (left) and natural lava fountains (right). Image credit for natural lava fountains: U.S. Geological Survey and Tom Pfeiffer / www.volcanodiscovery.com (used with permission).

Finally, the findings were linked to hydrodynamic breakup in natural lava fountain pulses. The main outcomes are:

- Identification of magma viscosity and ejection velocity as the main factors dictating the breakup regime of a fragmenting magma mass, in the experiments and lava fountain pulses alike. These factors span several orders of magnitude, whereas others like surface tension and magma density have much narrower ranges. A high ejection velocity promotes atomization, whereas a high viscosity inhibits it, leading to lower jet breakup regimes (Fig. 5.1);
- Two end-member behaviors are observed on first exiting the crucible: the ultramafic magma at high velocity is in regime IV, whereas the intermediate composition magma at low velocity is in regime II, with all other experiments falling in between these end-members;
- Similarly to the experiments, different breakup regimes might also characterize lava fountain pulses, ranging between weak fountaining (regime II) to a fully atomized jet (regime IV) observed in the strongest fountain episodes (Fig. 5.1).

5.1.3 What achneliths can tell about primary magma fragmentation

In *Chapter 4*, the fragmentation experiments were used to explore what pyroclast shapes can tell on the hydrodynamic breakup mechanisms (Zimanowski et al. 1991, 1997; Caffier 1998; Büttner et al. 1999), and what happens to still liquid pyroclasts immediately after breakup. The use of ultramafic to intermediate bubble-poor magmas and two driving pressures generated a diverse panoply of artificial achneliths (fluidal juvenile pyroclasts). Their study using the standardized protocol and comparison to natural achneliths from the 1959 Kīlauea Iki eruption (Hawaii) (Ritcher et al. 1970; Stovall et al. 2011; Porritt et al. 2012; Mueller et al. 2018) provided a way to better understand fragmentation dynamics in lava fountains.

The main findings are:

- The final morphology of a fluidal juvenile particle is governed by magma composition, ejection velocity and differential velocity between magma and the surrounding gas, but also by particle size and cooling;
- Surface tension dominates breakup for ultramafic magmas, leading to the preponderant generation of compact droplets such as spheres and Pele's tears. For ash-size particles, viscous relaxation proceeds within very short time frames (ms or less), before the outer portion of the grain cools below the glass transition;
- A higher viscosity, related to an increasing silica content, leads to prolonged stretching between two parting masses before any breakup can take place. Associated achneliths

are Pele's hairs and long-tailed Pele's tears, as observed in the intermediate magma fragmented at high velocity. The limited contraction and the retention of the elongate shape is a combination of rapid cooling and high viscosity opposing surface tension;

- The morphological similarity between the Kīlauea Iki achneliths and the high-velocity basalt experiment indicates that similar breakup mechanisms occur in lava fountain pulses. Differences include the variable, but typically higher, bubble content of actual magmas and the fast repetition of multiple pulses at the subsecond-second scale in natural fountains. This leads to sustained fountain episodes and the production of a conspicuous amount of vesicle-dominated pyroclast morphologies;
- The post-fragmentation breakage of these vesicular pyroclasts leads to an overrepresentation of broken vesicle walls and shards in the very fine ash fraction, which limits its use for studies of primary magma fragmentation for low-intensity basaltic magmatic explosive styles such as classic Strombolian and Hawaiian.

5.2 Linking the main outcomes: juvenile pyroclasts and primary magma fragmentation in basaltic eruptions

5.2.1 Importance of the standardized methodology

One challenge to the advancement of our understanding of primary magma fragmentation is the lack of a detailed, standardized, reproducible approach for the analysis of juvenile pyroclasts, for comparative studies. The diverse morphological and textural features of juvenile pyroclasts provide a unique window on primary magma fragmentation, allowing to discern eruption style(s), in order to better model hazard scenarios based on past eruptions. Unfortunately, without a shared, flexible and relatively low-cost approach of investigation, similar pyroclastic deposits from distinct volcanoes analyzed in different ways will generate incompatible datasets. Different techniques employed to perform the same task will end up being equipment-, resources- and budget-dependent, curbing data sharing and collaboration.

The first international effort to develop such a standardized methodology resulted in a comprehensive workflow to guide the volcanologist from sample collection in the field to laboratory analysis of juvenile pyroclasts. In the standard guidelines, each step was designed to be as time-and-cost effective as possible, and to be performed with accessible and common techniques available at most research centers and universities. These are not trivial aspects, as they will facilitate the application of the methodology while leading to the increase of compatible datasets. The hope is that in the next five to ten years, a uniform juvenile pyroclast database from different

eruption styles and magma compositions will emerge, allowing volcanologists to retrieve information on primary magma fragmentation from the pyroclastic deposits of unwitnessed eruptions, perhaps by using new “fragmentation diagrams”. This will allow reconstruction of past eruptions and development of more accurate hazard plans for future events. Data generated during this PhD can be integrated in the uniform juvenile pyroclast database and new fragmentation diagrams, and relates specifically to relatively mild basaltic eruptive explosive styles, including phreatomagmatic, Strombolian and Hawaiian, as will be discussed below.

Finally, the standardized methology developed in this project constitutes a base to test the accuracy of newly defined morphometric and textural methods and parameters in the future. By integrating as many steps of the methodology as possible in the analysis of juvenile pyroclasts for a specific eruption, volcano scientists could compare the results obtained through the use of new methods with those proposed in the workflow. In this regard, the standardized methodology could function as a first “standard” for juvenile pyroclast morphometry and textural analysis, allowing researchers to validate their approach against the standard, as done in other scientific disciplines.

5.2.2 An improved understanding of lava fountains

Primary magma fragmentation in lava fountains remain, like in others eruption styles, a poorly accessible and complex phenomenon to investigate. Spectacular fountain episodes are a dangerous and not completely understood. The laboratory scale “fountain pulses” generated in the experiments and the study of their artificial achneliths detailed in this dissertation clarified crucial aspects of hydrodynamic magma breakup, and how this results in the observed morphological variety. This has broad implications for volcanological research and hazard assessment, as well as for industrial usages of materials behaving similarly to magmas.

Lava fountain pulses can be regarded as transient jets of magma. As such, they might break up within three regimes similarly to industrial liquid jets, increasing in fragmentation intensity from regime II to regime IV, the fully developed spray. Understanding what controls these regimes in lava fountains is crucial for establishing what kind of main activity will characterize a particular fountaining event, and therefore what kind of risk it might pose to surrounding areas. As example, a repetition of pulses in regime IV will be more likely to grow into a fully developed sustained fountain, above which an ash plume will rise, requiring an assessment of the effects posed by ash fallout and dispersion. Regime II fountain pulses might instead lead to the early generation of

clastogenic lava flows capable to reach distances of several tens of kilometers (depending on feeding rate and favorable topography), requiring a different type of risk assessment.

Breakup regimes at past Hawaiian style eruptions can be inferred from the pyroclastic deposits. The fallout sheet is of particular interest; its dispersion, grain size distribution, and componentry (e.g., achneliths versus vesicles-dominated juvenile grains) can be used to reconstruct the eruptions. For example, the presence of fines-rich fallout deposits dispersed over a wide area will be indicative of an efficient atomization (i.e., regime IV) during the eruption. Moreover, the abundance of vesicles-dominated juveniles in the same deposit will indicate prolonged vesiculation of gas-rich magma, which is promoted by the presence of a sustained fountain plume (Stovall et al. 2011, 2012). By contrast, a relative absence of distal fallout deposits and/or the presence of loose proximal coarse deposits composed by achneliths will indicate weaker fountaining (i.e., regime III) either from a central or fissural vent, as observed at Kīlauea volcano and elsewhere (Ritcher et al. 1970; Carracedo-Sánchez et al. 2016).

Achnelith morphologies (and their relative proportions) are related to specific ejection velocities, magma viscosities, and cooling rates. One end-member achnelith shape is the sphere, which requires a low magma viscosity, and enough time before cooling for surface tension to reshape the particle. In the experiments, a low ejection velocity of ultramafic and mafic magmas produced the largest amount of spherical juvenile pyroclasts. For natural fountains implying basalt, abundant spheres therefore indicate a relatively low viscosity (probably due to a high magma temperature), and a low ejection velocity. This allows surface tension to dominate over viscosity, and newly formed drops quickly relax back into a sphere. At even lower viscosities such as in carbonatite magmas, the control of surface tension during the breakup and reshaping process would be even more pronounced, allowing production of spheres even at high ejection velocities (Kurszlaukis and Lorenz 1997; Bosshard-Stadlin et al. 2014).

Another end-member achnelith shape is the Pele hair. In silicate melts, these shapes form when magmas are ejected at relatively high ejection velocities (Zimanowski et al. 1997). The experiments presented here also show a viscosity control, with thick Pele's hairs increasing sharply when magma composition becomes more silica-rich. These factors promote stretching at the necking point between two parting masses. When breakup occurs, the now elongate threads with very fine diameter will be able to undergo only limited contraction (if at all), before being "frozen" by cooling below the glass transition.

The contemporaneous presence in a deposit of both achneliths and vesicle-dominated pyroclasts in lava fountains is thought to be related to the different journey of the pyroclasts from the vent to

the ground (Stovall et al. 2011; Porritt et al. 2012). Vertical changes in the proportions of achneliths versus vesicle-dominated clasts in pyroclastic deposits may indicate intensity variations in the fountain and/or changes in magma composition over time. Changes in achnelith shapes also indicate changing conditions. All together, these characteristics retrieved from past deposits of lava fountains might help to predict future behaviors.

In industry, the use of silicate melts ranges from glass manufacturing to the production of insulation, filtration, soundproofing and hydroponic materials (Sirok et al. 2008). Basaltic melts are commonly used to create mineral wool (Jamshaid and Mishra 2016), but the experiments presented here have shown than even magmas with lower and higher silica contents are able to generate rock wool, given the right mix of temperature, viscosity and ejection velocity. Insights on magma breakup dynamics can be therefore shared with other disciplines beyond volcanology.

5.2.3 Building a fragmentation diagram for mild basaltic eruptions

An improvement in the understanding of primary fragmentation processes from the study of juvenile pyroclasts is inextricably linked to the existence of a standardized methodology of analysis. The availability of comparable data from different volcanoes will eventually allow to discern different fragmentation mechanisms and eruption styles based on different values for morphometric and textural parameters among the compared samples.

In this dissertation, the characterization of two volcanoes and three different eruption styles (Hawaiian, Strombolian and phreatomagmatic) already provides a hint of what hopefully could be achieved in the future, once a larger dataset will exist. Future fragmentation diagrams for the distinction of different eruption styles may have to combine more than two parameters, but initially the simplest way to plot the data is cross-plots of morphometric and textural parameters (e.g., Fig. 5.2). For example, diagrams of 2D vesicularity or axial ratio versus solidity are shown for the 0.71–0.5 mm size fraction. Although there is some overlap between the fields (represented by the 80% confidence ellipses in Fig. 5.2), the medians are distinct between the Kilauea Iki 1959 products, the Strombolian deposits from Ukinrek, and the phreatomagmatic ones from the same volcano. Ukinrek Strombolian is exclusively composed by scoria, in which vesicles control the outer pyroclast morphology. In contrast, the closed-cell, fine vesicularity of the Ukinrek phreatomagmatic juvenile pyroclasts does not control their outer morphology, leading to a higher solidity value relative to the Strombolian counterpart, despite the similar values of axial ratio and vesicularity. The Kīlauea Iki samples, representing lava fountaining, contain several types of juvenile pyroclasts, mainly falling into achneliths (smooth fluidal particles) and vesicle-dominated

morphologies (scoria, golden pumice, transitional). Both types are distinct from the Ukinrek particles, and can be distinguished from each other by the solidity values (Fig. 5.2). Experimental magmas had low bubble contents, and pyroclasts were generated by hydrodynamic fragmentation, leading to a very low median vesicularity, solidity values up to 1, and variable axial ratios.

In summary, this first attempt clearly shows the potential of juvenile pyroclasts for comparative studies of primary fragmentation, and therefore the relevance to implement a standardized methodology for the generation of a vast database, perhaps hosted in a centralized repository, to make this comparison easier.

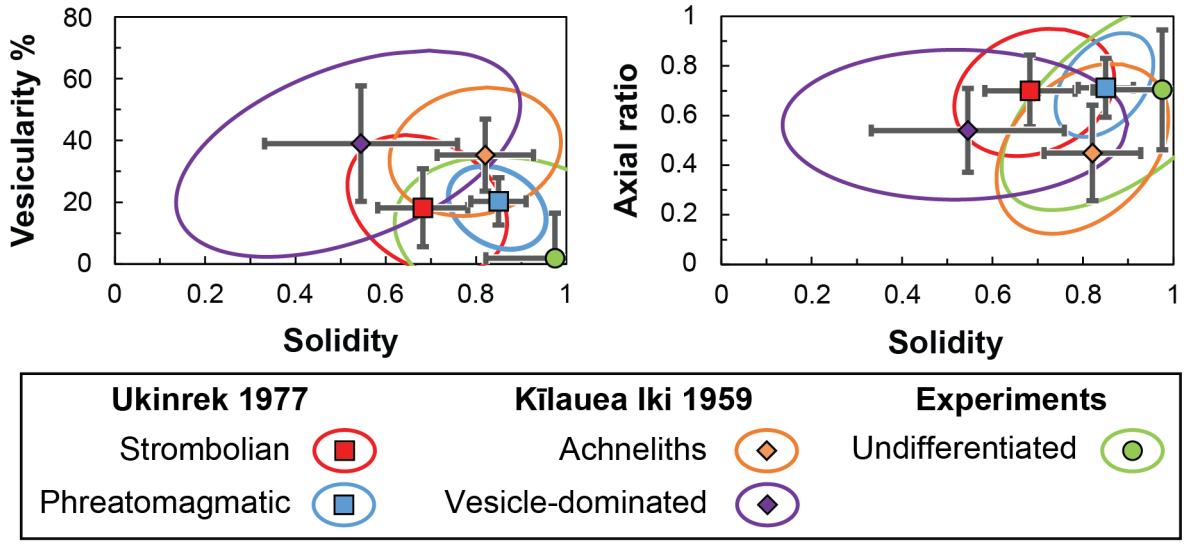

Figure 5.2: Sketch of potential basalt fragmentation diagrams able to distinguish different mild explosive eruption styles and/or experimental conditions through the comparative study of juvenile pyroclasts (0.71–0.5 mm or narrow + 1 phi fraction). Each data point represents the median and standard deviations of a certain population of pyroclasts. The ellipses enclose the 80% of the morphological population.

5.3 Future directions

5.3.1 Distinguishing magmatic from phreatomagmatic fragmentation through the analysis of juvenile pyroclasts

Reconstructing eruptive styles and fragmentation mechanisms from the pyroclastic deposits of past eruptions has been one of the goals of volcanology since the 1970s, but this is still not a straightforward task. This must be done by combining as many parameters as possible, including outcrop scale features such as bedding, grain size, componentry, and the details of juvenile particles, on which this thesis has focused, and for which further work is envisaged. The future accumulation of comparable quantitative data on juvenile primary pyroclasts will serve as a basis

to design novel fragmentation diagrams. The recommended cohort of morphometric and textural parameters should be further investigated in detail, potentially with the use of multivariate statistics, in order to operate a clear distinction of different eruption styles by using several parameters at the same time. More specifically, the combination of more than two morphometric and textural parameters is recommended for discriminating between high solidity fluidal and angular juvenile pyroclasts, as existing diagrams operate only a limited separation (Büttner et al. 2002). In this regard, the addition of novel morphometric and textural parameters (e.g., fragmentation-related broken crystals linked to viscous healing of magmas, Taddeucci et al. 2021) to the existing library is envisaged to improve discriminations among different eruption styles, etc. This distinction is extremely important in mafic eruptions to identify signatures of magma-water interaction. Still on the evidence of phreatomagmatism, a more in-depth investigation is advised on in the topic of interactive particles and their surface features. Stepped features, for example, are the product of high-stress brittle fragmentation (Dürig et al. 2012a), including in phreatomagmatism, but are they also found in the products of other eruptive styles, and in which proportions? It would be useful to characterize unambiguously each feature both quantitatively and qualitatively. It is important to understand the origin of each surface feature and the relative abundance in phreatomagmatic versus magmatic deposits, and laboratory experiments using real magmas and different systems for water interaction are extremely promising in this regard (Büttner et al. 1999; Austin-Erickson et al. 2008).

5.3.2 Understanding magma breakup at high deformation rates

The characterization of hydrodynamic fragmentation in lava fountains through the analogy with industrial liquid jets and associated breakup regimes was shown to have important implications for understanding eruption style dynamics. The new Ohnesorge-type diagram proposed in Chapter 3 needs to be further improved by addressing how regime boundaries behave at low Reynolds numbers and high Weber numbers, in order to become directly applicable to natural fountains. Accessing such regimes could initially be done through jetting experiments involving analogue liquids with high viscosities but Newtonian behavior. Eventually though the problem of the instantaneous viscosity of magma in jetting experiments and natural lava fountains will need to be addressed. Instantaneous viscosities experienced by magmas in both jetting experiments and lava fountains seem to be different than those measured by viscometers and/or derived from chemical models.

In understanding hydrodynamic magma breakup, the fragmentation experiments carried out for this project confirmed to be an exceptional tool of investigation, because almost all of the relevant parameters are known (with instantaneous viscosity the vexing exception) and high-speed video can be readily obtained. The current experiments were limited to bubble- and crystal-poor ultramafic to intermediate magmas and resulted mainly in the main generation of fluidal particles (achneliths). Future fragmentation experiments could therefore involve runs using variably vesicular and crystalline magmas. These experiments could enable to observe the transition from hydrodynamic breakup to brittle fragmentation within a same run. For the purpose of hazard assessment of currently active volcanoes displaying lava fountain activity, the presence of a certain proportion and variety of achneliths observed in past deposits might help to predict future behaviors. In this regard, the use of high-resolution, high-speed cameras to investigate different zones of magma fragmentation during both experiments and ongoing lava fountains could help in further deepening the knowledge on the link between fragmentation mechanisms and associated primary juvenile morphologies (Edwards et al. 2020).

5.3.3 From volcanology to industry: future work on Pele's hairs

The complexity involved in the hydrodynamic breakup of magma goes beyond the volcanology realm, with implications that could benefit certain industrial applications such as the mineral fiber production. Currently, in fact, the emphasis has been given to promote the atomization of liquids (Eggers and Villermaux 2008; Lefebvre and McDonell 2017). A less explored field is instead the inhibition of atomization and the promotion of long thinning timescales for the production of thin but continuous threads. From the experiments, we directly confirmed that by using the right combination of silicate melt composition and ejection velocity, thinning processes can be enhanced to create masses of Pele's hairs commonly referred to as "rock wool". Rock wool is commonly produced from basaltic rocks (Sirok et al. 2008; Dhand et al. 2015; Jamshaid and Mishra 2016), but Pele's hairs in the experiments were generated for all tested compositions, from ultramafic to intermediate. In this regard, future fragmentation experiments focused on generating long threads by using different compositions and ejection velocities could benefit the whole industry.

6 REFERENCES

Agustín-Flores J, Németh K, Cronin SJ, Lindsay JM, Kereszturi G (2015) Construction of the North Head (Maungauika) tuff cone: a product of Surtseyan volcanism, rare in the Auckland Volcanic Field, New Zealand. Bull Volc 77:11

Andronico D, Del Carlo P (2016) PM10 measurements in urban settlements after lava fountain episodes at Mt. Etna, Italy: pilot test to assess volcanic ash hazard to human health. Nat Hazards Earth Syst Sci 16:29-40

Andronico D, Cristaldi A, Scollo S (2008) The 4–5 September 2007 lava fountain at South-East Crater of Mt Etna, Italy. J Volcanol Geotherm Res 173:325–328

Andronico D, Cristaldi A, Del Carlo P, Taddeucci J (2009) Shifting styles of basaltic explosive activity during the 2002–03 eruption of Mt. Etna, Italy. J Volcanol Geotherm Res 180:110–122

Andronico D, Scollo S, Lo Castro MD, Cristaldi A, Lodato L, Taddeucci J (2014) Eruption dynamics and tephra dispersal from the 24 November 2006 paroxysm at South-East Crater, Mt Etna, Italy. J Volcanol Geotherm Res 274:78–91

Andronico D, Scollo S, Cristaldi A (2015) Unexpected hazards from tephra fallouts at Mt Etna: The 23 November 2013 lava fountain. J Volcanol Geotherm Res 304:118–125

Austin-Erickson A, Büttner R, Dellino P, Ort MH, Zimanowski B (2008) Phreatomagmatic explosions of rhyolitic magma: Experimental and field evidence. J Geophys Res Solid Earth 113, https://doi.org/10.1029/2008JB005731

Avery MR, Panter KS, Gorsevski PV (2017) Distinguishing styles of explosive eruptions at Erebus, Redoubt and Taupo volcanoes using multivariate analysis of ash morphometrics. J Volcanol Geotherm Res 332:1–13

Bagheri GH, Bonadonna C, Manzella I, Vonlanthen P (2015) On the characterization of size and shape of irregular particles. Powder Technol 270:141–153

Birouk M, Lekic N (2009) Liquid jet breakup in quiescent atmosphere: A review. Atomization and Sprays, 19:501–528

Blackburn E, Wilson L, Sparks RSJ (1976) Mechanisms and dynamics of strombolian activity. J Geol Soc London 132:429–440

Bosshard-Stadlin SA, Mattsson HB, Keller J (2014) Magma mixing and forced exsolution of CO_2 during the explosive 2007–2008 eruption of Oldoinyo Lengai (Tanzania). J Volcanol Geotherm Res 285:229–246

Büttner R, Zimanowski B (1998) Physics of thermohydraulic explosions. Physical Review E - Statistical Physics, Plasmas, Fluids, and Related Interdisciplinary Topics 57:5726-5729

Büttner R, Zimanowski B, Blumm J, Hagemann L (1998) Thermal conductivity of a volcanic rock material (olivine-melilitite) in the temperature range between 288 and 1470 K. J Volcanol Geotherm Res 80:293–302

Büttner R, Dellino P, Zimanowski B (1999) Identifying magma-water interaction from the surface features of ash particles. Nature 401:688–690

Büttner R, Dellino P, La Volpe L, Lorenz V, Zimanowski B (2002) Thermohydraulic explosions in phreatomagmatic eruptions as evidenced by the comparison between pyroclasts and products from Molten Fuel Coolant Interaction experiments. J Geophys Res Solid Earth 107:ECV 5-1 – 5–14

Büttner R, Dellino P, Raue H, Sonder I, Zimanowski B (2006) Stress-induced brittle fragmentation of magmatic melts: Theory and experiments. J Geophys Res Solid Earth 111, https://doi.org/10.1029/2005JB003958

Caffier I (1998) Investigations on the fragmentation of magmatic melt by expanding gas (Unpublished master's dissertation). Physikalisch-Vulkanologisches Labor, Institut für Geologie & Physikalisches Institut, Julius-Maximilians-Universität, Würzburg, Germany

Calvari S, Cannavò F, Bonaccorso A, Spampinato L, Pellegrino AG (2018) Paroxysmal Explosions, Lava Fountains and Ash Plumes at Etna Volcano: Eruptive Processes and Hazard Implications. Front Earth Sci 6, https://doi.org/10.3389/feart.2018.00107

Cannata CB, De Rosa R, Donato P, Donato S, Lanzafame G, Mancini L, Houghton BF (2019) First 3D imaging characterization of Pele's hair from Kilauea volcano (Hawaii). Sci Rep 9:1711

Cappello A, Ganci G, Calvari S, Pérez NM, Hernández PA, Silva SV, Cabral J, Del Negro C (2016) Lava flow hazard modeling during the 2014–2015 Fogo eruption, Cape Verde. J Geophys Res Solid Earth 121:2290–2303

Cao X-K, Sun Z-G, Li W-F, Liu H-F, Yu Z-H (2007) A new breakup regime of liquid drops identified in a continuous and uniform air jet flow. Phys Fluids 19:057103

Carracedo-Sánchez M, Sarrionandia F, Arostegui J, Errandonea-Martin J, Gil-Ibarguchi JI (2016) Petrography and geochemistry of achnelithic tephra from Las Herrerías Volcano (Calatrava volcanic field, Spain): Formation of nephelinitic achneliths and post-depositional glass alteration. J Volcanol Geotherm Res 327:484–502

Cas RAF, Wright JV (1987) Volcanic successions, modern and ancient. Allen & Unwin, London, 528 p.

Cashman KV (2004) Volatile Controls on Magma Ascent and Eruption. In: The State of the Planet: Frontiers and Challenges in Geophysics pp 109–124

Cashman KV, Scheu B (2015) Chapter 25 - Magmatic Fragmentation - *In*: Sigurdsson H, Houghton B, McNutt SR, Rymer H, Stix J (eds) The Encyclopedia of Volcanoes (Second Edition). Academic Press, Amsterdam, pp 459–471

Chigier N, Reitz RD (1996) Regimes of jet breakup and breakup mechanisms (physical aspects). Prog. Astronaut. Aeronaut 166:109

Cassidy M, Manga M, Cashman K, Bachmann O (2018) Controls on explosive-effusive volcanic eruption styles. Nat Commun 9:2839

Cioni R, Sbrana A, Vecci R (1992) Morphologic features of juvenile pyroclasts from magmatic and phreatomagmatic deposits of Vesuvius. J Volcanol Geotherm Res 51:61–78

Cioni R, D'Oriano C, Bertagnini A (2008) Fingerprinting ash deposits of small scale eruptions by their physical and textural features. J Volcanol Geotherm Res 177:277–287

Cioni R, Pistolesi M, Bertagnini A, Bonadonna C, Hoskuldsson A, Scateni B (2014) Insights into the dynamics and evolution of the 2010 Eyjafjallajökull summit eruption (Iceland) provided by volcanic ash textures. Earth Planet Sci Lett 394:111–123

Cioni R, Pistolesi M, Rosi M (2015) Chapter 29 - Plinian and Subplinian Eruptions - *In*: Sigurdsson H, Houghton B, McNutt SR, Rymer H, Stix J (eds) The Encyclopedia of Volcanoes (Second Edition). Academic Press, Amsterdam, pp 519–535

Clasen C, Phillips PM, Palangetic L, Vermant, J (2012) Dispensing of rheologically complex fluids: The map of misery. AIChE Journal 58:3242–3255

Cole PD, Guest JE, Duncan AM, Pacheco JM (2001) Capelinhos 1957–1958, Faial, Azores: deposits formed by an emergent surtseyan eruption. Bull Volc 63:204

Colombier M, Scheu B, Kueppers U, Cronin SJ, Mueller SB, Hess K-U, Wadsworth FB, Tost M, Dobson KJ, Ruthensteiner B, Dingwell DB (2019) In situ granulation by thermal stress during subaqueous volcanic eruptions. Geology 47:179-182

Comida PP, Ross P-S (2021) PierCVolc/PASTA: PASTA project (Version 3.7, February 22, 2021), http://doi.org/10.5281/zenodo.3336335

Comida PP, Ross P-S, Dürig T, White JDL, Lefebvre N (2021a) Standardized analysis of juvenile pyroclasts in comparative studies of primary magma fragmentation; 2. Choice of size fractions and method optimization. Bull Volc https://doi.org/10.1007/s00445-021-01517-5

Comida PP, Ross P-S, Dürig T, White JDL, Lefebvre NS (2021b) SEM_raw_images_Comida_et_al_2021 (Version 1, March 26, 2021), http://doi.org/10.5281/zenodo.4639399

Comida PP, Ross P-S, Zimanowski B, Büttner R, Dürig T (2021c) Raw_SEM_images_Juvenile_pyroclasts_lava_fountains_Comida_et_al_2021 (Version 1, August 2, 2021), https://doi.org/10.5281/zenodo.5153404

Corsaro RA, Andronico D, Behncke B, Branca S, Caltabiano T, Ciancitto F, Cristaldi A, De Beni E, La Spina A, Lodato L, Miraglia L, Neri M, Salerno G, Scollo S, Spata G (2017) Monitoring the December 2015 summit eruptions of Mt. Etna (Italy): Implications on eruptive dynamics. J Volcanol Geotherm Res 341:53–69

De Astis G, Lucchi F, Dellino P, La Volpe L, Tranne CA, Frezzotti ML, Peccerillo A (2013) Geology, volcanic history and petrology of vulcano (central aeolian archipelago). In: Geo Soc Mem, pp 281–349

Del Bello E, Lane SJ, James MR, Llewellin EW, Taddeucci J, Scarlato P, Capponi A (2015) Viscous plugging can enhance and modulate explosivity of strombolian eruptions. Earth Planet Sci Lett 423:210–218

Dellino P, La Volpe L (1995) Fragmentation versus transportation mechanisms in the pyroclastic sequence of Monte Pilato-Rocche Rosse (Lipari, Italy). J Volcanol Geotherm Res 64:211–231

Dellino P, La Volpe L (1996) Image processing analysis in reconstructing fragmentation and transportation mechanisms of pyroclastic deposits. The case of Monte Pilato-Rocche Rosse eruptions, Lipari (Aeolian islands, Italy). J Volcanol Geotherm Res 71:13–29

Dellino P, Gudmundsson MT, Larsen G, Mele D, Stevenson JA, Thordarson T, Zimanowski B (2012) Ash from the Eyjafjallajökull eruption (Iceland): Fragmentation processes and aerodynamic behavior. J Geophys Res Solid Earth 117, https://doi.org/10.1029/2011JB008726

Dhand V, Mittal G, Rhee KY, Park S-J, Hui D (2015) A short review on basalt fiber reinforced polymer composites. Composites Part B: Engineering 73:166–180

D'Oriano C, Bertagnini A, Cioni R, Pompilio M (2014) Identifying recycled ash in basaltic eruptions. Sci Rep 4:5851

Dioguardi F, Mele D, Dellino P, Dürig T (2017) The terminal velocity of volcanic particles with shape obtained from 3D X-ray microtomography. J Volcanol Geotherm Res 329:41–53

Duffield W, Gibson E, Heiken G (1977) Some characteristics of Pele's hair. J Res US Geol Surv 5:93–101

Durant AJ, Rose WI, Sarna-Wojcicki AM, Carey S, Volentik ACM (2009) Hydrometeor-enhanced tephra sedimentation: constraints from the 18 May 1980 eruption of Mount St. Helens. J Geophys Res 114:B03204

Dürig T, Zimanowski B (2012) ‘‘Breaking news’’ on the formation of volcanic ash: Fracture dynamics in silicate glass. Earth Planet Sci Lett 335-336:1–8

Dürig T, Mele D, Dellino P, Zimanowski B (2012a) Comparative analyses of glass fragments from brittle fracture experiments and volcanic ash particles. Bull Volc 74:691–704

Dürig T, Sonder I, Zimanowski B, Beyrichen H, Büttner R (2012b) Generation of volcanic ash by basaltic volcanism. J Geophys Res Solid Earth 117, https://doi.org/10.1029/2011JB008628

Dürig T, Bowman MH, White JD, Murch A, Mele D, Verolino A, Dellino P (2018) PARTIcle Shape ANalyzer PARTISAN–an open source tool for multi-standard two-dimensional particle morphometry analysis. Ann Geophys-Italy 61:31

Dürig T, Schmidt LS, White JDL, Bowman MH (2020a) DendroScan: an open source tool to conduct comparative statistical tests and dendrogrammatic analyses on particle morphometry. Sci Rep 10: article 21682

Dürig T, White JDL, Murch AP, Zimanowski B, Büttner R, Mele D, Dellino P, Carey RJ, Schmidt LS, Spitznagel N (2020b) Deep-sea eruptions boosted by induced fuel–coolant explosions. Nat Geosci 13:498–503

Dürig T, White JDL, Zimanowski B, Büttner R, Murch A, Carey RJ (2020c) Deep-sea fragmentation style of Havre revealed by dendrogrammatic analyses of particle morphometry. Bull Volc 82:article 67

Dürig T, Bowman HM (2021) lsschmidt/PARTISAN (Version 2.0, March 10, 2021), https://doi.org/10.5281/zenodo.4593833

Dürig T, Ross P-S, Dellino P, White JDL, Mele D, Comida PP (2021) A review of statistical tools for morphometric analysis of juvenile pyroclasts. Bull Volc 83:79

Edwards MJ, Pioli L, Harris AJL, Gurioli L, Thivet S (2020). Magma fragmentation and particle size distributions in low intensity mafic explosions: the July/August 2015 Piton de la Fournaise eruption. Sci Rep, 10: 13953.

Eggers J, Villermaux E (2008) Physics of liquid jets. Rep Prog Phys 71:036601

Fisher RV, Schmincke H-U (1984) Pyroclastic rocks. Springer-Verlag, Berlin, 472 p.

Folk RL, Ward WC (1957) Brazos River bar: a study in the significance of grain size parameters. J Sediment Res 27:3–26

Freundt A, Rosi M (1998) From magma to tephra. Elsevier, New York, 336 p.

Giordano D, Russell JK, Dingwell DB (2008) Viscosity of magmatic liquids: a model. Earth Planet Sci Lett 271:123–134

Gonnermann HM (2015) Magma Fragmentation. Annu Rev Earth Pl Sc 43:431–458

Gonnermann HM, Manga M (2013) Dynamics of magma ascent in the volcanic conduit. *In*: Lopes RMC, Fagents SA, Gregg TKP (eds) Modeling Volcanic Processes: The Physics and Mathematics of Volcanism. Cambridge University Press, Cambridge, pp 55–84

Gottsmann J, Komorowski J-C, Barclay J (2019) Volcanic Unrest and Pre-eruptive Processes: A Hazard and Risk Perspective. *In*: Gottsmann J, Neuberg J, Scheu B (eds) Volcanic Unrest : From Science to Society. Springer International Publishing, Cham, pp 1–21

Heggie TW (2009) Geotourism and volcanoes: Health hazards facing tourists at volcanic and geothermal destinations. Travel Med Infect Di 7:257–261

Heiken G (1972) Morphology and petrography of volcanic ashes. Geol Soc Am Bull 83:1961–1988

Heiken G (1974) An atlas of volcanic ash. Smithsonian Contributions to the Earth Sciences 12, 101 p.

Heiken G, Wohletz K (1985) Volcanic ash. University of California Press, Berkeley, 246 p.

Heiken G, Wohletz K (1991) Fragmentation processes in explosive volcanic eruptions. *In*: Fisher RV, Smith GA (eds) Sedimentation in volcanic settings. Society of Economic Paleontologists and Mineralogists, Special Publication 45, pp 19–26

Hobiger M, Sonder I, Büttner R, Zimanowski B (2011) Viscosity characteristics of selected volcanic rock melts. J Volcanol Geotherm Res 200:27–34

Hornby AJ (2018) IPC shape macro (Version 1.0.2, September 28, 2018), http://doi.org/10.5281/zenodo.1438445

Houghton BF, Wilson CJN (1989) A vesicularity index for pyroclastic deposits. Bull Volc 51:451–462

Houghton B, White JDL, Van Eaton AR (2015) Chapter 30 - Phreatomagmatic and Related Eruption Styles - *In*: Sigurdsson H, Houghton B, McNutt SR, Rymer H, Stix J (eds) The Encyclopedia of Volcanoes (Second Edition). Academic Press, Amsterdam, pp 537-552

Houghton BF, Taddeucci J, Andronico D, Gonnermann H, Pistolesi M, Patrick MR, Orr TR, Swanson D, Edmonds M, Gaudin D (2016) Stronger or longer: Discriminating between Hawaiian and Strombolian eruption styles. Geology 44:163–166

Jamshaid H, Mishra R (2016) A green material from rock: basalt fiber – a review. The Journal of The Textile Institute 107:923–937

Jones TJ, Llewellin EW, Houghton BF, Brown RJ, Vye-Brown C (2017) Proximal lava drainage controls on basaltic fissure eruption dynamics. Bull Volc 79:81

Jones TJ, Reynolds CD, Boothroyd SC (2019) Fluid dynamic induced break-up during volcanic eruptions. Nat Commun 10:3828

Jordan S, Dürig T, Cas RAF, Zimanowski B (2014) Processes controlling the shape of ash particles: results of statistical IPA. J Volcanol Geotherm Res 288:19–27

Kameda M, Kuribara H, Ichihara M (2008) Dominant time scale for brittle fragmentation of vesicular magma by decompression. Geophys Res Lett 35: L14302, doi:10.1029/2008GL034530

Kienle J, Kyle PR, Self S, Motyka RJ, Lorenz V (1980) Ukinrek Maars, Alaska, I. April 1977 eruption sequence, petrology and tectonic setting. J Volcanol Geotherm Res 7:11–37

Koopmann A (2004) Magma mingling: die hydrodynamische Genese magmatischer Dispersionen. Dissertation zur Erlangung des naturwissenschaftlichen Doktorgrades der Bayerischen Julius- Maximilans- Universität Würzburg. 148pp

Krumbein WC, Sloss LL (1963) Stratigraphy and sedimentation. 2nd edn. Freeman, San Francisco.

Kurszlaukis S, Lorenz V (1997) Volcanological features of a low-viscosity melt: the carbonatitic Gross Brukkaros Volcanic Field, Namibia. Bull Volc 58:421–431

La Spina G, Arzilli F, Llewellin EW, Burton MR, Clarke AB, de' Michieli Vitturi M, Polacci M, Hartley ME, Di Genova D, Mader HM (2021) Explosivity of basaltic lava fountains is controlled by magma rheology, ascent rate and outgassing. Earth Planet Sc Lett 553:116658

Latutrie B, Ross P-S (2019) Transition zone between the upper diatreme and lower diatreme: origin and significance at Round Butte, Hopi Buttes volcanic field, Navajo Nation, Arizona. Bull Volc 81:26

Latutrie B, Ross P-S (2020) Phreatomagmatic vs magmatic eruptive styles in maar-diatremes: a case study at Twin Peaks, Hopi Buttes volcanic field, Navajo Nation, Arizona. Bull Volc 82:28

Lautze NC, Houghton BF (2007) Linking variable explosion style and magma textures during 2002 at Stromboli volcano, Italy. Bull Volc 69:445–460

Le Bas MJ, Le Maitre RW, Streckeisen A, Zanettin B (1986) A Chemical Classification of Volcanic Rocks Based on the Total Alkali-Silica Diagram. J Petrol 27:745–750

Lefebvre AH, McDonell VG (2017) Atomization and sprays. CRC press, Boca Raton, 300 p. https://doi.org/10.1201/9781315120911

Leibrandt S, Le Pennec J-L (2015) Towards fast and routine analyses of volcanic ash morphometry for eruption surveillance applications. J Volcanol Geotherm Res 297:11–27

Li D (2008) Encyclopedia of microfluidics and nanofluidics. Springer Science & Business Media, New York, 3535 p.

Liu EJ (2021) Magma behaving brittly. Nat Geosci 14:180–181

Liu EJ, Cashman KV, Rust AC (2015) Optimising shape analysis to quantify volcanic ash morphology. GeoResJ 8:14–30

Liu EJ, Cashman KV, Rust AC, Höskuldsson A (2017) Contrasting mechanisms of magma fragmentation during coeval magmatic and hydromagmatic activity: the Hverfjall Fires fissure eruption, Iceland. Bull Volc 79:68

Mader HM, Llewellin EW, Mueller SP (2013) The rheology of two-phase magmas: A review and analysis. J Volcanol Geotherm Res 257:135–158

Madlener K, Frey B, Ciezki HK (2009) Generalized Reynolds number for non-newtonian fluids. EUCASS Proceedings Series – Advances in AeroSpace Sciences 1:237–250

Mangan MT, Cashman KV (1996) The structure of basaltic scoria and reticulite and inferences for vesiculation, foam formation, and fragmentation in lava fountains. J Volcanol Geotherm Res 73:1–18

McCarthy MJ, Molloy NA (1974) Review of stability of liquid jets and the influence of nozzle design. The Chemical Engineering Journal 7:1–20

Mele D, Dellino P, Sulpizio R, Braia G (2011) A systematic investigation on the aerodynamics of ash particles. J Volcanol Geotherm Res 203:1–11

Mele D, Dioguardi F (2018) The grain size dependency of vesicular particle shapes strongly affects the drag of particles. First results from microtomography investigations of Campi Flegrei fallout deposits. J Volcanol Geotherm Res 353:18–24

Mele D, Dioguardi F, Dellino P (2018) A study on the influence of internal structures on the shape of pyroclastic particles by X-ray microtomography investigations. Ann Geophys-Italy 61:AC27

Moitra P, Sonder I, Valentine GA (2018) Effects of size and temperature-dependent thermal conductivity on the cooling of pyroclasts in air. Geochem Geophy Geosy 19:3623–3636

Moore JG, Nakamura K, Alcaraz A (1966) The 1965 Eruption of Taal Volcano. Science 151:955–960

Mueller SB, Houghton BF, Swanson DA, Fagents SA, Klawonn M (2018) Intricate episodic growth of a Hawaiian tephra deposit: case study of the 1959 Kīlauea Iki eruption. Bull Volc 80:73

Mueller SB, Houghton BF, Swanson DA, Poret M, Fagents SA (2019) Total grain size distribution of an intense Hawaiian fountaining event: case study of the 1959 Kīlauea Iki eruption. Bull Volc 81:43

Murase T, McBirney AR (1973) Properties of some common igneous rocks and their melts at high temperatures. Geol Soc Am Bull 84:3563–3592

Murata KJ, Richter DH (1966) Chemistry of the lavas of the 1959–60 eruption of Kīlauea Volcano, Hawai‘i. In: The 1959–60 eruption ofKīlauea volcano, Hawai‘i. US Geol Surv Prof Pap, 537-A:A1– A26

Murtagh RM, White JDL (2013) Pyroclast characteristics of a subaqueous to emergent Surtseyan eruption, Black Point volcano, California. J Volcanol Geotherm Res 267:75–91

Namiki A, Patrick MR, Manga M, Houghton BF (2021) Brittle fragmentation by rapid gas separation in a Hawaiian fountain. Nat Geosci 14:242–247

Neal CA, Brantley SR, Antolik L, et al. (2019) The 2018 rift eruption and summit collapse of Kīlauea Volcano. Science 363:367–374

Ort MH, Lefebvre NS, Neal CA, McConnell VS, Wohletz KH (2018) Linking the Ukinrek 1977 maar-eruption observations to the tephra deposits: New insights into maar depositional processes. J Volcanol Geotherm Res 360:36–60

Parfitt EA (2004) A discussion of the mechanisms of explosive basaltic eruptions. J Volcanol Geotherm Res 134:77–107

Parfitt EA, Wilson L (2009) Fundamentals of physical volcanology. John Wiley & Sons, 252 p.

Pering T, Tamburello G, McGonigle A, Aiuppa A, James M, Lane SJ, Sciotto M, Cannata A, Patanè D (2015) Dynamics of mild strombolian activity on Mt. Etna. J Volcanol Geotherm Res 300:103–111

Pioli L, Erlund E, Johnson E, Cashman K, Wallace P, Rosi M, Delgado Granados H (2008) Explosive dynamics of violent Strombolian eruptions: The eruption of Parícutin Volcano 1943–1952 (Mexico). Earth Planet Sci Lett 271:359–368

Polacci M, Corsaro RA, Andronico D (2006) Coupled textural and compositional characterization of basaltic scoria: Insights into the transition from Strombolian to fire fountain activity at Mount Etna, Italy. Geology 34:201–204

Polacci M, Andronico D, de’ Michieli Vitturi M, Taddeucci J, Cristaldi A (2019) Mechanisms of Ash Generation at Basaltic Volcanoes: The Case of Mount Etna, Italy. Front Earth Sci 7, https://doi.org/10.3389/feart.2019.00193

Porritt L, Russell J, Quane S (2012) Pele's tears and spheres: Examples from Kilauea Iki. Earth Planet Sci Lett 333:171–180

Rausch J, Grobéty B, Vonlanthen P (2015) Eifel maars: Quantitative shape characterization of juvenile ash particles (Eifel Volcanic Field, Germany). J Volcanol Geotherm Res 291:86–100

Recktenwald G (2006) Transient, one-Dimensional heat conduction in a convectively cooled sphere. MATLAB Code /http://www.webcitation.org/60nDyv3YyS

Reitz RD, Bracco VF (1986) Chapter 10 - Mechanism of breakup of round liquid jets – *In*: Lin S, Wang C (1986) Encyclopedia of fluid mechanics. Ed. Cheremisioff, Gulf. Houston, pp 223–249

Richter DH, Murata KJ (1966) Petrography of the lavas of the 1959-60 eruption of Kilauea Volcano, Hawaii. *In*: The 1959–60 eruption of Kīlauea volcano, Hawai'i. US Geol Surv Prof Pap, 537-D:D1–D12

Richter DH, Eaton JP, Murata KJ, Ault WU, Krivoy HL (1970) Chronological narrative of the 1959–60 eruption of Kīlauea volcano, Hawai'i. *In*: The 1959–60 eruption of Kīlauea volcano, Hawai'i. US Geol Surv Prof Pap, 537-E:E1–E73

Ripepe M, Delle Donne D, Harris A, Marchetti E, Ulivieri G (2008) Stromboli volcano: an integrated study of the 2002–2003 eruption. Dynamics of Strombolian Activity. Geophysical Monograph Series 182:39–48

Rosi M, Pistolesi M, Bertagnini A, Landi P, Pompilio M, Di Roberto A (2013) Stromboli volcano, Aeolian Islands (Italy): present eruptive activity and hazards. Geo Soc Mem 37:473–490

Roduit N (2007) JMicroVision : un logiciel d'analyse d'images pétrographiques polyvalent. PhD thesis, Université de Genève

Ross PS, White JDL, Zimanowski B, Büttner R (2008) Rapid injection of particles and gas into non-fluidized granular material, and some volcanological implications. Bull Volc 70:1151–1168

Ross P-S, Dürig T, Comida PP, Lefebvre NS, White JDL, Andronico D, Thivet S, Eychenne J, Gurioli L (2021) Standardized analysis of juvenile pyroclasts in comparative studies of primary magma fragmentation; 1. Overview and workflow. Bull Volc https://doi.org/10.1007/s00445-021-01516-6

Rust AC, Cashman KV (2011) Permeability controls on expansion and size distributions of pyroclasts. J Geophys Res Solid Earth 116, https://doi.org/10.1029/2011JB008494

Sallam KA, Aalburg C, Faeth GM (2004) Breakup of Round Nonturbulent Liquid Jets in Gaseous Crossflow. AIAA Journal 42:2529–2540

Schindelin J, Arganda-Carreras I, Frise E, Kaynig V, Longair M, Pietzsch T, Preibisch S, Rueden C, Saalfeld S, Schmid B, Tinevez J-Y, White DJ, Hartenstein V, Eliceiri K, Tomancak P, Cardona A (2012) Fiji: an open-source platform for biological-image analysis. Nat Methods 9:676

Schipper CI, Castro JM, Tuffen H, James MR, How P (2013) Shallow vent architecture during hybrid explosive-effusive activity at Cordón Caulle (Chile, 2011–12): evidence from direct observations and pyroclast textures. J Volcanol Geotherm Res 262:25–37

Schipper CI, Jakobsson SP, White JDL, Palin JM, Bush-Marcinowski T (2015) The Surtsey Magma Series. Sci Rep 5:11498

Schmith J, Höskuldsson Á, Holm PM (2017) Grain shape of basaltic ash populations: implications for fragmentation. Bull Volc 79:14

Self S, Kienle J, Huot J-P (1980) Ukinrek Maars, Alaska, II. Deposits and formation of the 1977 craters. J Volcanol Geotherm Res 7:39–65

Schneider CA, Rasband WS, Eliceiri KW (2012) NIH Image to ImageJ: 25 years of image analysis. Nat Methods 9:671–675

Shea T, Houghton BF, Gurioli L, Cashman KV, Hammer JE, Hobden BJ (2010a) Textural studies of vesicles in volcanic rocks: An integrated methodology. J Volcanol Geotherm Res 190:271–289

Shea T, Houghton B, Gurioli L, Cashman K, Hammer J, Hobden B, Stovall W, Carey R (2010b) SEM image processing with Photoshop. University of Hawaii and University of Oregon, USA, http://www.soest.hawaii.edu/GG/FACULTY/tshea/foams/methodsimrec.html

Shimozuru D (1994) Physical parameters governing the formation of Pele's hair and tears. Bull Volc 56:217–219

Sigurdsson H (2015) Introduction. *In*: Sigurdsson H, Houghton B, McNutt SR, Rymer H, Stix J (eds) The Encyclopedia of Volcanoes (Second Edition). Academic Press, Amsterdam, pp 1–12

Sirok B, Blagojevic B, Bullen P (2008) Mineral wool: production and properties. Elsevier, 192 p.

Sohn YK (1996) Hydrovolcanic processes forming basaltic tuff rings and cones on Cheju Island, Korea. Geol Soc Am Bull 108:1199–1211

Sonder I, Zimanowski B, Büttner R (2006) Non-Newtonian viscosity of basaltic magma. Geophys Res Lett 33, https://doi.org/10.1029/2005GL024240

Stovall WK, Houghton BF, Gonnermann H, Fagents SA, Swanson DA (2011) Eruption dynamics of Hawaiian-style fountains: the case study of episode 1 of the Kīlauea Iki 1959 eruption. Bull Volc 73:511–529

Stovall WK, Houghton BF, Hammer JE, Fagents SA, Swanson DA (2012) Vesiculation of high fountaining Hawaiian eruptions: episodes 15 and 16 of 1959 Kīlauea Iki. Bull Volc 74:441–455

Sumner JM (1998) Formation of clastogenic lava flows during fissure eruption and scoria cone collapse: the 1986 eruption of Izu-Oshima Volcano, eastern Japan. Bull Volc 60:195–212

Taddeucci J, Scarlato P, Andronico D, Cristaldi A, Büttner R, Zimanowski B, Küppers U (2007) Advances in the study of volcanic ash. Eos Trans AGU, 88:253–256, doi:10.1029/2007EO240001

Taddeucci J, Edmonds M, Houghton B, James MR, Vergniolle S (2015) Chapter 27 - Hawaiian and Strombolian Eruptions - *In*: Sigurdsson H, Houghton B, McNutt SR, Rymer H, Stix J (eds) The Encyclopedia of Volcanoes (Second Edition). Academic Press, Amsterdam, pp 485–503

Taddeucci J, Cimarelli C, Alatorre-Ibargüengoitia MA, Delgado-Granados H, Andronico D, Del Bello E, Scarlato P, Di Stefano F (2021) Fracturing and healing of basaltic magmas during explosive volcanic eruptions. Nat Geosci 14:248–254

Thorarinsson S (1967) The Surtsey eruption and related scientific work. Polar Record 13:571-578

Valentine GA, Gregg TKP (2008) Continental basaltic volcanoes – Processes and problems. J Volcanol Geotherm Res 177:857–873

Verolino A, White JDL, Dürig T, Cappuccio F (2019) Black Point – Pyroclasts of a Surtseyan eruption show no change during edifice growth to the surface from 100 m water depth. J Volcanol Geotherm Res 384:85–102

Villermaux E (2012) The formation of filamentary structures from molten silicates: Pele's hair, angel hair, and blown clinker. Comptes Rendus Mécanique 340:555-564

Vonlanthen P, Rausch J, Ketcham RA, Putlitz B, Baumgartner LP, Grobéty B (2015) High-resolution 3D analyses of the shape and internal constituents of small volcanic ash particles: the contribution of SEM micro-computed tomography (SEM micro-CT). J Volcanol Geotherm Res 293:1–12

Wadsworth FB, Witcher T, Vasseur J, Dingwell DB, Scheu B (2019) When Does Magma Break? *In*: Gottsmann J, Neuberg J, Scheu B (eds) Volcanic Unrest: From Science to Society. Springer International Publishing, pp 171–184

Walker D, Mullins O (1981) Surface tension of natural silicate melts from 1,200°–1,500° C and implications for melt structure. Contrib Mineral Petr 76:455–462

Walker GPL (1973) Explosive volcanic eruptions – a new classification scheme. Geologische Rundschau 62:431–446

Walker GPL, Croasdale R (1971) Characteristics of some basaltic pyroclastics. Bull Volc 35:303–317

Wallace PJ, Anderson Jr. AT (1998) Effects of eruption and lava drainback on the H_2O contents of basaltic magmas at Kilauea Volcano. Bull Volc 59:327–344

Wallace PJ, Plank T, Edmonds M, Hauri EH (2015) Chapter 7 - Volatiles in Magmas. *In*: Sigurdsson H, Houghton B, McNutt SR, Rymer H, Stix J (eds) The Encyclopedia of Volcanoes (Second Edition). Academic Press, Amsterdam, pp 163–183

Wang X-h, Huang Y, Wang S-l, Liu Z-l (2012) Bag Breakup of Turbulent Liquid Jets in Crossflows. AIAA Journal 50:1360–1366

White JDL (1989) Basic Elements of Maar-Crater Deposits in the Hopi Buttes Volcanic Field, Northeastern Arizona, USA. The Journal of Geology 97:117–125

White JDL, Houghton B (2000) Surtseyan and related phreatomagmatic eruptions. Encyclopedia of volcanoes. Academic, San Diego:495–513

White JDL, Houghton B (2006) Primary volcaniclastic rocks. Geology 34:677–680

White JDL, Ross PS (2011) Maar-diatreme volcanoes: A review. J Volcanol Geotherm Res 201:1–29

White JDL, Valentine GA (2016) Magmatic versus phreatomagmatic fragmentation: absence of evidence is not evidence of absence. Geosphere 12:1478–1488

White JDL, Fisher RV, Smith GA (1991) The Depositional Record of Small, Monogenetic Volcanoes with in Terrestrial Basins. In: Sedimentation in Volcanic Settings. SEPM Society for Sedimentary Geology, 1 p.

Wohletz KH, McQueen RG (1984) Experimental studies of hydromagmatic volcanism. In: Explosive Volcanism: Inception, Evolution, and Hazards, Studies in Geophysics, National Academy Press, Washington, D.C. pp 158–169

Wohletz K, Zimanowski B, Büttner R (2013) Magma-water interactions – *In*: Lopes R, Fagents S, Gregg T.K.P., Modeling Volcanic Processes: The Physics and Mathematics of Volcanism. Cambridge University Press, pp 230–256

Zimanowski B, Fröhlich G, Lorenz V (1991) Quantitative experiments on phreatomagmatic explosions. J Volcanol Geotherm Res 48:341–358

Zimanowski B, Fröhlich G, Lorenz V (1995) Experiments on steam explosion by interaction of water with silicate melts. Nucl Eng Des 155:335–343

Zimanowski B, Büttner R, Lorenz V, Häfele HG (1997) Fragmentation of basaltic melt in the course of explosive volcanism. J Geophys Res Solid Earth 102:803–814

Zimanowski B, Wohletz K, Dellino P, Büttner R (2003) The volcanic ash problem. J Volcanol Geotherm Res 122:1–5

Zimanowski B, Büttner R, Koopmann A (2004) Experiments on magma mixing. Geophys Res Lett 31:L09612 09611–09613

Zimanowski B, Büttner R, Dellino P, White JDL, Wohletz KH (2015) Chapter 26 - Magma–Water Interaction and Phreatomagmatic Fragmentation - *In*: Sigurdsson H, Houghton B, McNutt SR, Rymer H, Stix J (eds) The Encyclopedia of Volcanoes (Second Edition). Academic Press, Amsterdam, pp 473–484

APPENDIX I: STANDARDIZED METHODOLOGY

Standardized analysis of juvenile pyroclasts in comparative studies of primary magma fragmentation; 1. Overview and workflow

Pierre-Simon Ross[1], Tobias Dürig[2,3], Pier Paolo Comida[1], Nathalie Lefebvre[4], James D.L. White[2], Daniele Andronico[5], Simon Thivet[6,7], Julia Eychenne[6], Lucia Gurioli[6]

[1]Institut national de la recherche scientifique, 490 rue de la Couronne, Québec (Qc), G1K 9A9, Canada

[2]Department of Geology, University of Otago, 360 Leith Street, Dunedin 9016, New Zealand

[3]Now at Institute of Earth Sciences, University of Iceland, Sturlugata 7, 101 Reykjavík, Iceland

[4] ETH Zurich, Institute of Geochemistry and Petrology, Clausiusstrasse 25, 8092 Zurich, Switzerland

[5]Istituto Nazionale di Geofisica e Vulcanologia, Osservatorio Etneo - Sezione di Catania, Piazza Roma, 2, 95125 Catania, Italy

[6]Laboratoire Magmas et Volcans, Université Clermont Auvergne - CNRS - IRD, OPGC, 6 Avenue Blaise Pascal, 63170 – Aubière, France

[7]Now at Section for Mineralogy, Petrology & Geochemistry, Department of Earth and Environmental Sciences, Ludwig-Maximilians-University Munich, Theresienstrasse 41, 80333 München, Germany

Title of the journal:

Bulletin of Volcanology

Accepted: 16 November 2021

DOI: 10.1007/s00445-021-01516-6

This appendix is the accepted version of the research article:

Ross P-S, Dürig T, Comida PP, Lefebvre NS, White JDL, Andronico D, Thivet S, Eychenne J, Gurioli L (2021) Standardized analysis of juvenile pyroclasts in comparative studies of primary magma fragmentation; 1. Overview and workflow. Bull Volc.

Abstract

Juvenile pyroclasts, especially in the ash size range, provide important information on primary fragmentation processes, i.e. initial explosive magma fragmentation, and on the state of the magma both prior to and at the point of fragmentation and quenching. There exists an extensive body of literature focusing on the quantification of juvenile particle morphology (shape), internal textures and surface features spanning several decades, however a standardized method has yet to emerge for comparative studies. No community-wide consensus currently exists (i) regarding the most representative size fraction(s) to be examined, (ii) on sample preparation procedures (such as whether to use whole particle silhouettes or 2D cross-sections), (iii) on imaging techniques and image acquisition parameters, or (iv) on the optimal morphometric parameters to measure. Lack of a standardized method precludes robust comparison between different studies and laboratories. We propose here a preliminary “best practices” and workflow for characterization of juvenile pyroclasts, for comparative studies of primary fragmentation. If the community follows such a standardized method, it will become possible to accumulate a large volume of consistent data on juvenile pyroclasts from a range of eruption styles, fragmentation mechanisms, and magma compositions. This will ultimately allow deeper insights into the full panoply of magma-to-pyroclast processes that drive particle-producing volcanic eruptions. One or more “fragmentation diagrams” may eventually be developed to allow different types of magmatic and phreatomagmatic explosive eruptions to be distinguished based on their products.

Keyword: standardized methodology, juvenile pyroclasts, magma fragmentation, shapes, internal textures, surface features, fieldwork, laboratory analysis, componentry, grain size distribution

Introduction

For unwitnessed explosive eruptions, volcanologists rely on pyroclastic deposits to reconstruct eruptive styles, modes of transport/deposition, dispersal and fragmentation processes within various volcanic contexts (e.g., Campi Flegrei caldera, Italy: Wohletz et al. 1995; Pistolesi et al. 2017; Vesuvius stratovolcano, Italy: Barberi et al. 1989; Cioni et al. 2003; Gurioli et al. 2010; Sulpizio et al. 2010; various monogenetic volcanoes: White 1991; Jordan et al. 2014, 2016; Agustín-Flores et al. 2015; Graettinger and Valentine 2017; Fitch and Fagents 2020). Even for witnessed eruptions, some aspects of eruption dynamics, such as magma ascent, vesiculation and primary fragmentation can only be reconstructed from pyroclastic deposits, with a particular

focus on juvenile fragments (e.g., Dellino and La Volpe 1995; Andronico et al. 2009; Pardo et al. 2014a; Gurioli et al. 2015, 2018; Liu et al. 2017; Polacci et al. 2019; Thivet et al. 2020a, b, c). Juvenile particles are “clasts derived from the newly erupted magma” (White and Houghton 2006). Most juvenile clasts are glassy, although some are nearly glassy, such as tachylitic clasts formed by some basaltic eruptions (Fisher and Schmincke 1984). Juvenile clasts can be further divided into primary and recycled (Houghton and Smith 1993; White and Houghton 2006; D'Oriano et al. 2014). Recycled clasts have fallen back into the crater and have then been ejected again (D'Oriano et al. 2014). Non-juvenile fragments, often called lithics (White and Houghton 2006), are fragments “derived from rock or sediment that predates the eruption”. A final type of fragment consists of ‘composite’ clasts which combine juvenile and non-juvenile material (White and Houghton 2006).

Here, “primary” fragmentation is used for initial explosive magma fragmentation, as opposed to “secondary” fragmentation that can occur during transport of pyroclasts (Cashman and Scheu 2015). The focus of this paper being explosive magma fragmentation, we are not concerned with phreatic eruptions (which don’t directly fragment magma), hyaloclastite formation (which is not explosive), and so on. Identifying the mechanisms of primary fragmentation (magmatic or phreatomagmatic) can be particularly contentious (e.g., Wohletz 1983a; Rausch et al. 2015; White and Valentine 2016; Schmith et al. 2017). Magmatic fragmentation has been described as “driven solely by gasses originally dissolved in the magma” and as occurring “(1) when magma ascends rapidly during explosive eruptions, (2) after rapid decompression caused by plug pressurization or collapse of volcanic edifices and lava domes, (3) by shearing of magma at the conduit walls, or (4) by impact-induced explosion of hot solid blocks during dome collapse” (Cashman and Scheu 2015). Phreatomagmatic fragmentation is a consequence of thermohydraulic fuel-coolant interaction processes between the magmatic melt and external water, which results in shockwave-generated fine ash particles and rapid melt quenching (Wohletz 1986; Büttner and Zimanowski 1998; White and Valentine 2016; Dürig et al. 2020b). Elucidating primary magma fragmentation mechanisms has important implications for understanding the hazards posed by active volcanoes, since different eruptive styles pose different ranges of hazards (e.g., Beget et al. 2005; Cioni et al. 2008a; Nemeth et al. 2012; Brand et al. 2014).

Interpretation of primary magma fragmentation mechanisms, and the state of magma at the time of fragmentation, is traditionally based on grain-size distribution, componentry, as well as the morphologies, surface features and textural characteristics of juvenile pyroclasts. The ash fraction

(≤ 2 mm; see White and Houghton 2006 and Table A1.1 for definition of grain size terms) has often been preferred, since ash particles are rapidly quenched in air or water.

Table A1.1: Correspondence between the ϕ scale and mm, for half-ϕ sieving columns.

Passing through (ϕ)	Retaining sieve (ϕ)	Size range (mm)	Grain size term*
		> 64	Block/bomb
- 6	- 5.5	64 – 45.3	Coarse lapilli
- 5.5	- 5	45.3 – 32	Coarse lapilli
- 5	- 4.5	32 – 22.6	Coarse lapilli
- 4.5	- 4	22.6 – 16	Coarse lapilli
- 4	- 3.5	16 – 11.3	Medium lapilli
- 3.5	- 3	11.3 – 8	Medium lapilli
- 3	- 2.5	8 – 5.7	Medium lapilli
- 2.5	**- 2**	**5.7 – 4**	**Medium lapilli**
- 2	- 1.5	4 – 2.8	Fine lapilli
- 1.5	- 1	2.8 – 2	Fine lapilli
- 1	- 0.5	2 – 1.4	Very coarse ash
- 0.5	0	1.4 – 1	Very coarse ash
0	+ 0.5	1 – 0.71	Coarse ash
+ 0.5	**+ 1**	**0.71 – 0.5**	**Coarse ash**
+ 1	+ 1.5	0.5 – 0.35	Medium ash
+ 1.5	+ 2	0.35 – 0.25	Medium ash
+ 2	+ 2.5	0.25 – 0.18	Fine ash
+ 2.5	+ 3	0.18 – 0.125	Fine ash
+ 3	+ 3.5	0.125 – 0.088	Very fine ash
+ 3.5	**+ 4**	**0.088 – 0.063**	**Very fine ash**
		< 0.063	Extremely fine ash

* White and Houghton (2006)

Such characteristics have been studied for several decades (e.g., Heiken 1972, 1974; Heiken and Wohletz 1985; Cioni et al., 1992, 2008b, 2014; Dellino and La Volpe 1995; Büttner et al. 1999; Dellino et al. 2001, 2012; Taddeucci et al. 2002; Dürig et al., 2012b, 2020a, 2020b, 2020c; Ross and White 2012; Lautze et al. 2012, 2013; Jordan et al. 2014; Bagheri et al. 2015; Leibrandt and Le Pennec 2015; Liu et al. 2015a, 2015b, 2017; Avery et al. 2017; Dioguardi et al. 2017). Many different methods have been used by different workers, with variations in terms of the size fraction(s) to be analyzed, on sample preparation including whether to use whole-particle silhouettes or 2D cross-sections, on imaging techniques and image acquisition parameters, on

the optimal morphometric parameters to measure, etc. This makes comparisons between different studies and laboratories challenging, since these decisions influence the measurements. Furthermore, many studies were done on unwitnessed eruptions, rather than to document juvenile pyroclast characteristics from an unambiguously known style or fragmentation mechanism. Thus, it is not yet entirely clear how to specifically link juvenile ash characteristics (particle size, morphology, internal features such as crystals and vesicles, surface features, geochemical composition) with specific eruptive styles (Bonadonna et al. 2016) or fragmentation processes (Thivet et al. 2020c).

In order to build our understanding of primary fragmentation processes, it is essential to be able to directly compare juvenile pyroclasts from different eruptions and volcanic systems. The volcanology community must therefore converge on a standardized method for analysis of juvenile pyroclasts in comparative studies of primary magma fragmentation. This paper and its companion (Chapter 2) propose a standardized workflow, and we hope that it is either adopted widely, or at least forms a basis for discussions in international workshops. When a broad community consensus has been reached, we shall rigorously sample fresh natural pyroclastic deposits from observed eruptions, and compare them with artificial pyroclasts resulting from experiments where “eruption” parameters are well constrained. Then we can measure juvenile ash characteristics with the standardized method. The community should aim to cover the whole spectrum of magma compositions, eruptive styles, and magnitudes. This would allow generation of a large database of juvenile ash characteristics, and deepen our understanding of "what juvenile pyroclasts can tell us". This could also hopefully permit the creation of diagrams that can discriminate primary fragmentation processes or eruption styles based on particle characteristics, a.k.a. “fragmentation diagrams”.

Overview of the workflow and target users

The workflow proposed here prescribes steps within the stages of sample selection and preparation, and then data acquisition and analysis. The workflow has standard, recommended and optional steps.

- The *standard* steps are those minimally required to obtain uniform data on the grain size, basic componentry, as well as the morphologies, surface features and internal textures of juvenile pyroclasts, for comparative studies. Determining the geochemical composition of the juvenile component is also standard.

- The *recommended* steps yield a better understanding of each sample and produce additional information that can help discriminate between eruptive styles or fragmentation mechanisms.
- The *optional* steps produce information that complements other data from the standard and recommended steps.

Two flowcharts are presented: one with the standard steps only (Fig. A1.1) and one with standard and recommended steps (Fig. A1.2). Optional steps are not shown to avoid overcrowding the diagrams.

Who should use standardized analysis of juvenile pyroclasts?

Scientists interested by comparative studies of primary magma fragmentation should follow at least Fig. A1.1 (standard steps), and as much as possible of Fig. A1.2 (standard and recommended steps). Community adoption of common particle analysis protocols will result in a large database of standardized, directly comparable data to better understand magma fragmentation.

Workers studying specific eruptive events in detail are of course free to utilize whatever methods they think are best suited to comprehensively understand those events. But if they *also* follow at least the flowchart with the standard steps (and if possible, some of the recommended steps), then their data can be used in comparative studies as well, extending the relevance of their work.

Researchers from volcano observatories and civil defense agencies are under pressure to get data on current or recent eruptions out quickly, and may not be realistically able to completely follow even the Fig. A1.1 flowchart. However, if they have the standardized methodology in mind when they collect their samples and carry out their measurements, they can more easily make pyroclastic material available to their collaborators, who can then complete the standardized analysis.

Overview of standard outputs

The standard outputs were chosen to capture a range of relatively easily measured parameters covering magma composition, particle size, componentry, and the overall morphology, internal textures (crystals and vesicles), and surface features of juvenile particles.

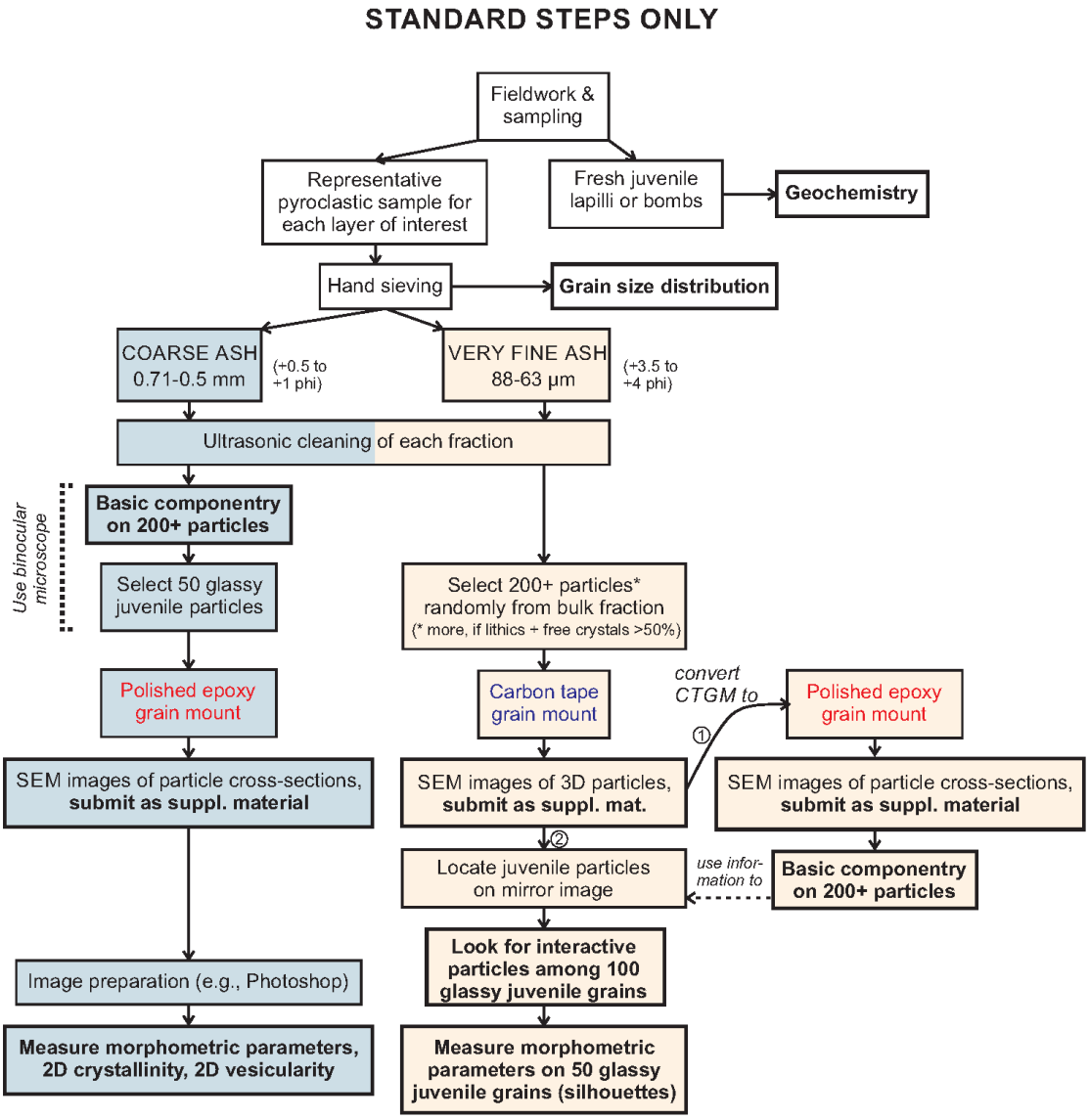

Figure A1.1: Flowchart of the steps needed to analyze juvenile pyroclasts for comparative fragmentation studies, showing standard steps only. Bold items are outputs. A separate sample of "fresh juvenile lapilli or bombs" may not be needed, if geochemistry is done through micro-analysis on the coarse ash fraction (see text for a full explanation).

It is important to always use the same size fractions in future comparative studies, because particle morphologies vary as a function of grain size (e.g., Wohletz 1983a; Porritt et al. 2012; Mele et al. 2011; Leibrandt and Le Pennec 2015; Liu et al. 2015a; Avery et al. 2017; Fitch et al. 2017; Mele and Dioguardi 2018; Comida et al. 2018, Chapter 2), and so does vesicularity (e.g., Walker 1981; Houghton and Wilson 1989; Mele et al. 2011; Eychenne and Le Pennec 2012; Gurioli et al. 2015; Liu et al. 2017; Chapter 2) and componentry (e.g., Eychenne and Le Pennec 2012; Murtagh and White 2013; Eychenne et al. 2015; Liu et al. 2015b, 2017). So the standardized method must be applied to juvenile pyroclasts from specific particle size fractions.

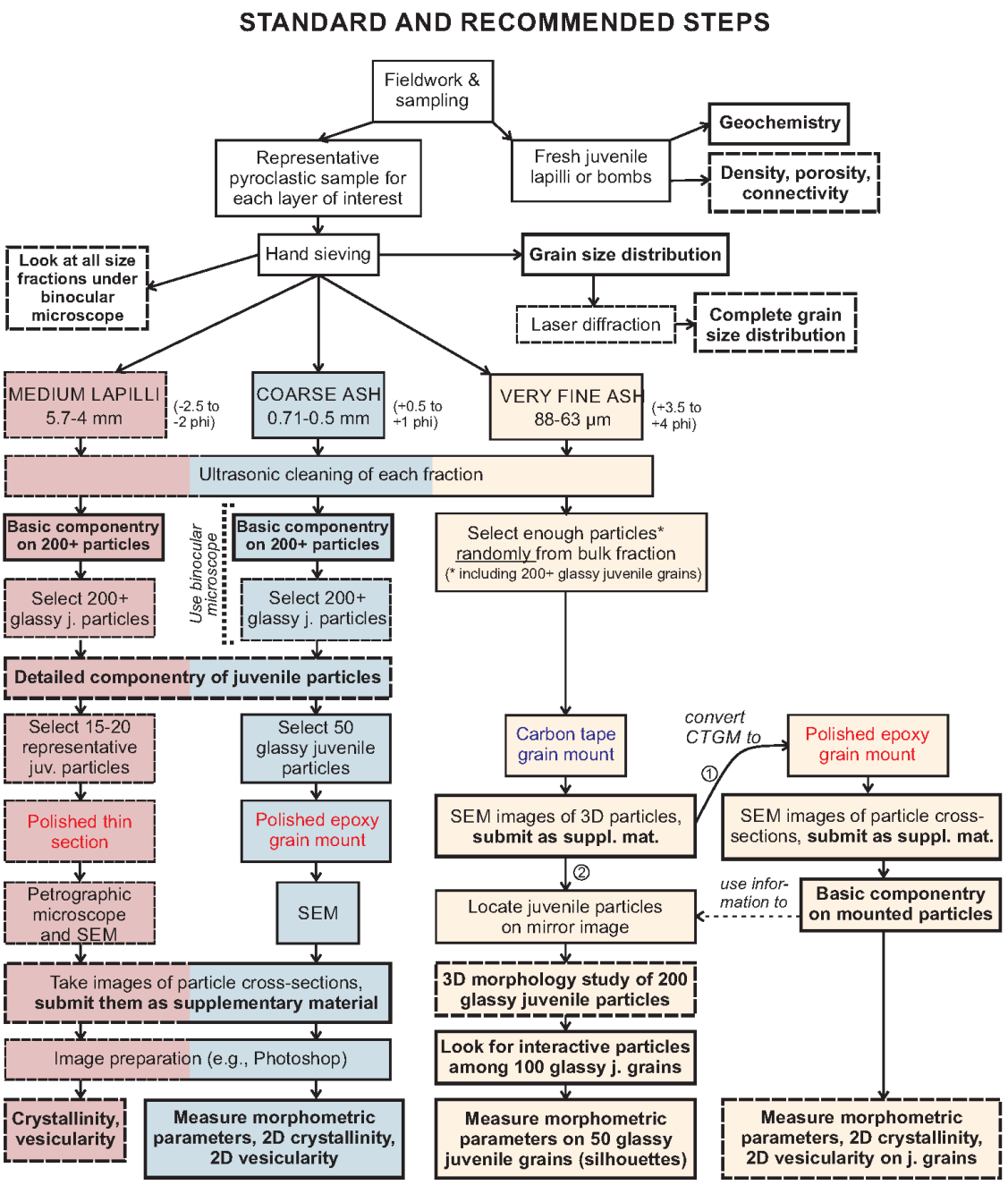

Figure A1.2: Flowchart of the steps needed to analyze juvenile pyroclasts for comparative fragmentation studies, showing standard steps (continuous lines) and recommended steps (dashed lines). Bold items are outputs.

We propose to work on three evenly spaced half-ϕ size fractions separated from a bulk pyroclastic sample: 5.7–4 mm (- 2.5 to - 2ϕ), 0.71–0.5 mm (+ 0.5 to + 1ϕ) and 88–63 µm (+ 3.5 to + 4ϕ) (ϕ = $-\log_2 D$, where D is the diameter in mm of the particle; Krumbein 1934; Table A1.1). The two ash fractions are included in the standard outputs, whereas the lapilli fraction is recommended. The Fig. A1.1 workflow starts with fieldwork and ends with the following standard outputs:

- Characterization of the geochemistry of the juvenile component of the eruption (based either on whole rock geochemistry of selected large juvenile pyroclasts, or micro-analysis of the groundmass from coarse ash, see details below);
- A grain-size distribution for each sample based on sieving;
- Basic componentry (the proportion of juvenile versus non-juvenile clasts) for both ash fractions studied;
- Scanning electron microscope (SEM) images of cross-sections (polished epoxy grain mounts) for both ash fractions;
- Measurements of morphometric parameters (i.e., non-dimensional shape descriptors), 2D crystallinity and 2D vesicularity, on the 0.71–0.5 mm (+ 0.5 to + 1ϕ) cross-section images;
- SEM images of 3D juvenile grains, to visualize their surface features and count "interactive particles" (explained below), or lack thereof, in the 88–63 μm (+ 3.5 to + 4ϕ) fraction;
- Measurements of morphometric parameters on silhouettes (binarized images) from the 88–63 μm (+ 3.5 to + 4ϕ) fraction.

Overview of recommended outputs

The version of the workflow with standard and recommended steps adds some or all of the following outputs (Fig. A1.2):

- A range of density, porosity and connectivity measurements;
- A "complete" grain-size distribution for studied samples, including the fine tail where appropriate, based on a combination of methods;
- Qualitative descriptions of all whole ϕ size fractions under the binocular microscope;
- Basic componentry for the 5.7–4 mm (- 2.5 to - 2ϕ) fraction;
- Detailed componentry on juvenile particles, for the 5.7–4 mm (- 2.5 to - 2ϕ) and the 0.71–0.5 mm (+ 0.5 to + 1ϕ) fractions;
- 2D crystallinity and 2D vesicularity data on juvenile particles from the 5.7–4 mm (- 2.5 to - 2ϕ) fraction;
- 3D morphology study on juvenile particles from the 88–63 μm (+ 3.5 to + 4ϕ) fraction
- 2D morphology and textural parameters on juvenile particles from the 88–63 μm (+ 3.5 to + 4ϕ) fraction, based on cross-sections.

Organization of the paper

To keep the manuscript length manageable, the following sections describe only the standard steps of the methodology, i.e. those included in the Fig. A1.1 flowchart. The presentation broadly follows the order of the steps on the flowchart. The recommended and optional steps are presented in Online Resource A1.1. Excel templates of the typical outputs are presented in Online Resource A1.2.

Fieldwork and pyroclastic sampling

Fieldwork (standard)

Fieldwork or experiments are the first step to collect natural or obtain artificial juvenile particles, respectively. Detailed advice on fieldwork is beyond the scope of this paper, but we stress that a detailed geological framework is needed in order to collect representative samples (Gurioli et al. 2015). Building such a framework often means studying the pyroclastic deposits from a specific eruption at several sites. It is important to know the mode of transport (pyroclastic fall versus pyroclastic density currents, PDCs). In some cases, specific eruptive units might be targeted, perhaps to represent distinct eruptive styles. Without this field-based knowledge, any data on juvenile pyroclasts is without proper context.

Sampling pyroclastic deposits for particle size, morphologies, surface features and internal textures (standard)

All types of unconsolidated pyroclastic deposits can be sampled, with caveats. If there is a choice between fallout and PDC deposits, fallout is strongly preferred, for reasons explained below. However there is no *a priori* reason to expect identical fragmentation processes for different eruptive phases that lead to different transport regimes.

Fall deposits from plumes, with no secondary transport, will probably best reflect the primary fragmentation signature of the plume-forming eruption or phase, although abrasion can also take place in vents (Jones and Russell 2017). Grain morphology in fall deposits is known to change as a function of distance from vent (Saxby et al. 2020), even within the same size fraction (J. Eychenne, work in progress). Therefore, samples should ideally be taken at different distances from the vent along the dispersal axis.

It is preferable to collect samples along the dispersal axis to avoid crosswind fractionation (Carey and Sparks 1986). Depending on eruptive styles and intensities, fall-deposit fields can range

widely in size (Figs. A1.3a to A1.3d). Proximal, medial and distal areas can be identified (Fig. A1.3e) where significant variations in thickness, lithology, grain size, density, grain morphology and emplacement mechanisms are observed or inferred (Fig. A1.3f).

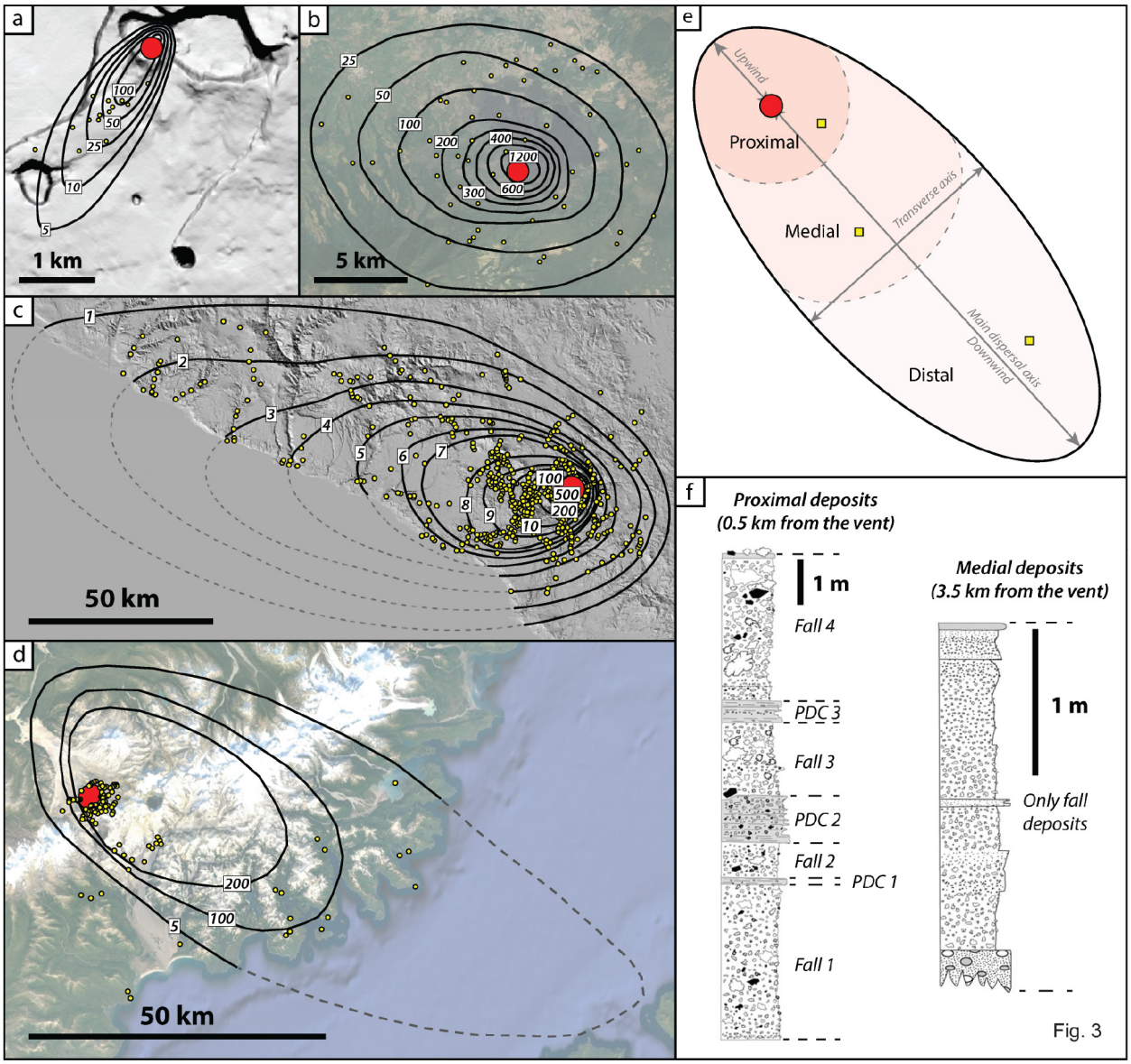

Figure A1.3: Characteristics of fallout deposits from different eruptive styles. (a)-(b)-(c)-(d) Isopach maps from (a) Hawaiian fountaining activity, episode 4–8 of the 1959 Kīlauea Iki eruption, Hawaii, USA (modified from Mueller et al. 2018); (b) violent Strombolian monogenic activity, 1952 Paracutín eruption, Mexico (modified from Pioli et al. 2008); (c) Plinian activity, 1600 CE Huaynaputina eruption, Peru (modified from Prival et al. 2019). (d) Plinan activity, 1912 Novarupta eruption, Alaska, USA (modified from Houghton et al. 2004). Contours are in cm, eruptive vents and thickness measurements are represented by the large red and small yellow circles, respectively. (e) Sketch of the different spatial zones that can be identified in a fallout field. The proximal, medial and distal zone positions vary depending on the intensity of the eruptions: the proximal zone reaches around 0.5 km from the vent for the 1959 Kīlauea Iki eruption but around 50 km for the 1600 CE Huaynaputina eruption. Yellow squares are hypothetical sampling sites. (f) Complex stratigraphic logs of the 1912 Novarupta Plinian deposits showing the potential spatial and temporal variations of the deposit characteristics (modified from Houghton et al. 2004).

Samples from a targeted eruption or phase should ideally contain the three size fractions that are being targeted, but not all need to be present at single sites. Temporal variations can also affect the deposit of a single explosive event when changes in eruptive style interact with variations in wind direction and intensity. These variations can cause stratigraphic changes through each sampling site (Fig. A1.3f). Houghton and Wilson (1989) and Gurioli et al. (2015) recommend that narrow stratigraphic intervals should be sampled to best represent a specific fragmentation moment. If sampling is performed along the dispersal axis at multiple sites, it is important at each site to collect from the same level in the deposit (if dealing with thick deposits/long sustained eruptions).

Deposit sampling (after the eruptive activity) is usually performed in order to collect the entire sequence of a studied eruption (Gurioli et al. 2018). Gurioli et al. (2015) also summarize advice on sampling fallout during eruptions, which can be performed when field, safety and weather conditions permit. This way of sampling is usually performed in order to collect time-resolved samples, focused on a specific eruptive phase and/or single explosion. Sampling devices can be placed inside the fallout field, at different distance from the vent. Plastic sheets (e.g. Harris et al. 2013; Colo' et al. 2020), pre-existing cleaned surfaces (e.g., Andronico et al. 2009; Eychenne et al. 2012; Houghton et al. 2013) or buckets (e.g. Yoshimoto et al. 2005; Swanson et al. 2009; Bustillos et al. 2016), have been used to collect sufficient material (within known surface areas) to estimate the magnitude of the event through the mass load per unit area and to obtain a sufficient number of clasts for chemical and textural characterization. More sophisticated devises, designed especially for ash, have been used for collecting ash, but also to measure its load (Bernard 2013; Shimano et al. 2013), its grain size and terminal velocity (Freret-Lorgeril et al. 2019; Thivet et al. 2021).

PDC deposits are less suitable for studying primary fragmentation, for two reasons. First, primary juvenile fragments in PDCs are comminuted and smoothed during transport, as is well known for cm-sized pumice (Manga et al. 2011; Bernard and Le Pennec 2016) and in basaltic lapilli from a PDC at Etna (Andronico et al. 2018). The same effect has been documented in 0.5 mm clasts from Vesuvius (Mele et al. 2011). Milling experiments show that even 0.5-0.25 mm grains are progressively rounded during transport (Jones et al. 2016). However, in general, ash is less susceptible to shape modification than lapilli (Buckland et al. 2018). The fine to extremely fine ash (Table A1.1) preferentially travels as suspended load and among target particles is least susceptible to abrasion (Kuenen 1960; Jerolmack et al. 2011). The second issue with PDCs is that a portion of the fine to extremely fine ash will be generated within the current, rather than

from primary magma fragmentation (Wohletz et al. 1989; Büttner et al. 2002; White and Valentine 2016), requiring the separation of 'primary' from 'secondary' particles in the sample. If eruption phases producing PDCs are under investigation, or sampling sites are limited and PDC deposits are the only option, then vent-proximal samples from dilute PDCs are preferable, because they presumably undergo less secondary fragmentation.

How much material to sample depends on the grainsize distribution of the pyroclastic deposit and the type of eruption (e.g., Strombolian/transient versus Plinian/long lasting; see Appendix in Houghton and Carey 2015) and more specifically on the abundances of the targeted size fractions within the deposit. For example, in the figure A1.1 flowchart, 100 juvenile grains are needed for the very fine ash fraction (explained below). If the deposit is lithic-poor, relatively fine-grained and well sorted, these grains can generally be extracted from much less than 100 g of material. On the other hand, for poorly sorted deposits, many kilograms of material might be needed to both obtain a representative grainsize distribution and to extract a sufficient amount of the three size fractions. Mosley and Tindale DS (1985) and Fitch and Fagents (2020) suggest that no individual clast should weigh > 5% of the total sample weight. For each sample, the information to be noted is listed in Online Resource A1.2.

Contamination from adjacent layers should be minimized during sampling. In relatively fine-grained deposits, a spade or Japanese gardening tool (Fig. A1.4a) can be used for cleaning the face and a knife or trowel are useful for sampling. Additional information is available from the “Checklist for tephra collection” document produced by the “Tephra 2014” workshop (Bursik et al. 2015).

Geochemical analysis (standard)

Why geochemistry is needed

Whether magma fails in a brittle or in a ductile way is determined by its rheological properties in conjunction with the deformation rate it is confronted with, i.e. the increase of stress over a certain time period (Dürig and Zimanowski 2012). Since the rheological properties are affected by magma composition, particle morphologies and textures are moderately to strongly influenced by magma geochemistry (e.g., Heiken 1972; Heiken and Wohletz 1991; Pardo et al. 2014a; Comida et al. 2017; Mele et al. 2018).

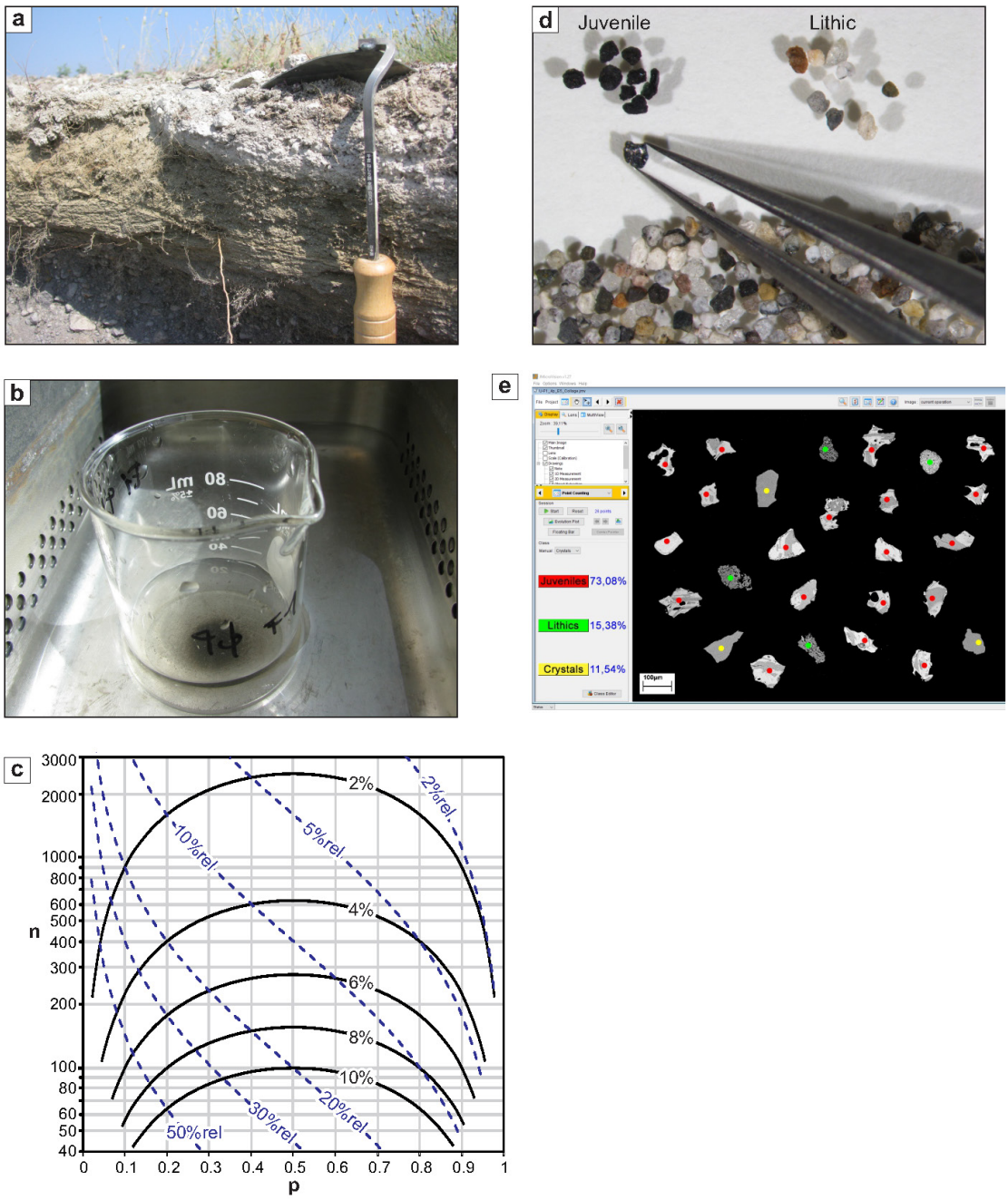

Figure A1.4: Field work, ultrasonic cleaning, and basic componentry. (a) The Japanese garden tool often used for cleaning the face during field work. The brown and grey pyroclastic deposits are products of the May 18, 1980 lateral blast at Mont St. Helens, USA. (b) Ultrasonic cleaning of a size fraction in distilled water. (c) Simplified version of the error chart developed by van der Plas and Tobi (1965) for petrographic point counting. 'p' is the abundance of a component and n is the number of points to be counted. The black continuous curves represent two standard deviations (2σ). For example, the 4% absolute error curve intersects the p = 0.2 vertical line at n = 400. This means that a component with a real abundance of 20% in the sample will be measured between 16% (p-2σ) and 24% (p+2σ) abundance, 95% of the time, if 400 points are counted. The blue dashed curves are relative errors (2σ/p). For example, if a 20% relative error is acceptable, and p = 0.2, then n must equal 400. (d) Componentry of the coarse ash fraction with tweezers under the binocular microscope. (e) Componentry of the very fine ash fraction using a polished epoxy grain mount, SEM images and manual point counting in JMicrovision. The colored dots have been enlarged for better visibility.

Thus, in basalts for example, magmatic fragmentation is typically a ductile process in Hawaiian eruptions (Porritt et al. 2012; Thivet et al. 2020c), whereas phreatomagmatic fragmentation of the molten fuel-coolant interaction (MFCI) type produces both brittle and ductile particles (Büttner et al. 2002; Zimanowski et al. 2015). In contrast, both magmatic and phreatomagmatic fragmentation of rhyolite is typically, though not always (Murch et al. 2019a), a brittle process (Austin-Erickson et al. 2008; Cashman and Scheu 2015; Dürig et al. 2020b). Therefore, the composition of the magma (including the crystals) and/or the melt (now preserved as the groundmass i.e. glass and microlites) needs to be determined before fragmentation rates can be assessed. There are two geochemical strategies, not mutually exclusive, to do this: whole-rock analysis of juvenile pyroclasts, or groundmass analysis by electron microprobe.

Whole-rock analysis of juvenile pyroclasts

Whole-rock geochemistry is typically reported in petrological studies, and is based on analysis of large juvenile fragments (Cashman and Rust 2016). Fresh, unweathered juvenile bombs or large lapilli should be sampled, and cracked open to make sure that no non-juvenile (lithic) inclusions are present. At least a fist-sized volume of material is needed for each geochemical analysis (e.g., Webster et al. 1996; Suda et al. 2018). If necessary to obtain sufficient material, several lapilli can be combined into one sample (e.g., Pardo Villaveces 2012) with the assumption of compositional homogeneity. If several juvenile populations appear to be present in the field, based on color, mineralogy or textures, one can either sample the dominant composition, or better, sample each juvenile component.

When performing the analysis, typical quality assurance/quality control procedures should be followed (e.g., Piercey 2014), including the use of certified reference materials. The minimum information to be obtained is major oxides plus loss on ignition (LOI). Major oxides are typically determined by wavelength-dispersive X-ray fluorescence (WD-XRF) (e.g., Austin-Erickson et al. 2011; Pardo et al. 2014a; Chamberlain et al. 2016), or inductively coupled plasma atomic emission spectroscopy (ICP-AES), also known as ICP-optical emission spectrometry (ICP-OES) (e.g., Kapelanczyk et al. 2012; Gurioli et al. 2018).

Groundmass geochemistry

Microprobe analyses of the groundmass (glass and microlites) can be done on the polished epoxy grain mounts of juvenile clasts already required for other purposes (see below) and in that case, no additional sampling is necessary. If reported together with phenocryst percentages, species

and compositions, this can provide adequate information about magma composition. It has the advantage that it reports information from the particles analyzed, rather than making the assumption that ash compositions match those of large particles, particularly if they cannot be sampled at the same site.

The composition of the groundmass (glass and microlites) represents the melt portion of the magma, without the larger crystals. The composition of the groundmass is typically different from that of the bulk rock (e.g., Pardo et al. 2014a; Cashman and Rust 2016; Suda et al. 2018), unless of course the material is entirely glassy. So the groundmass composition cannot typically be used to name the whole rock. However, since it represents the liquid, the composition of the groundmass is more directly relevant to magma rheology (e.g., viscosity) in a magma fragmentation context (Giordano et al. 2008).

Groundmass composition can be obtained quickly with an electron microprobe, and the focus is typically on analyzing the glass (Andronico et al. 2009). The pyroclasts are mounted in epoxy, polished to get a flat surface, the mount is coated with carbon, and then each grain is analyzed (Hunt and Hill 1993). Attention must be paid to sodium loss, with mitigation strategies including use of a defocused beam (at least 10–20 μm across), low beam current (≤ 10 nA), analysis of Na first, or time-dependent analysis of Na (Hunt and Hill 1993; Devine et al. 1995; Morgan and London 1996; Gurioli et al. 2008; Hayward 2011; Gaunt et al. 2016). The percentages, types and compositions of phenocrysts should also be reported if they are present in significant abundance. This allows assessment of whether melt and crystals were in equilibrium, as well as offering additional information useful in rock classification.

As an alternative to an electron microprobe, energy dispersive X-ray spectroscopy (EDS) analysis with an SEM may also provide adequate information on groundmass compositions (Taddeucci et al. 2004). We recommend that a set of reference standards be analyzed before each session (Caracciolo et al. 2021).

Sieving (standard)

There are two reasons why sieving is standard in the workflows: to determine particle size distributions and to extract specific size fractions. Both polished epoxy grain mounts (described and justified below) and carbon tape grain mounts (described and justified below) are also best prepared using individual size fractions.

Particle-size distributions

Grainsize distribution is traditionally one of the criteria used to help distinguish fragmentation styles (e.g., Walker 1973; Wohletz 1983a, 1986; Houghton and Hackett 1984; Barberi et al. 1989; Rust and Cashman 2011; Liu et al. 2015b; White and Valentine 2016; Liu et al. 2017). The classic Walker (1973) diagram for fallout deposits uses the proportion of < 1 mm particles at 0.1 T_{max} (with T_{max} the maximum thickness of the deposit) to distinguish phreatomagmatic eruptions from the suite of magmatic fields (Hawaiian to ultraplinian; e.g., Houghton and Gonnermann 2008). There are also sorting versus median size diagrams in the literature where different fields are shown for magmatic versus phreatomagmatic fragmentation (e.g., Houghton and Carey 2015) and also fields for pyroclastic flow, surge and fall (e.g., Walker 1971). Grainsize parameters can also be plotted as a function of distance from the vent (Sparks et al. 1981; Osman et al. 2020). For most cone-like and sheet-like fall deposits, grainsize distributions taken at representative sampling locations (to account for fractionation effects during transport) will provide essential insights into the fragmentation mechanisms that will then be refined by the subsequent analyses suggested here. Note that only the total grain-size distribution estimated over the whole deposit for the eruption or phase investigated is capable of supporting statements about fragmentation separate from transport effects (e.g. Mueller et al 2019).

In general, even total grain-size distribution on its own will not unambiguously reveal primary fragmentation mechanisms, due in part to secondary fragmentation processes such as breakage during transport, especially in PDCs (Wohletz et al. 1989; Büttner et al. 2002; White and Valentine 2016). Taking maar-diatreme volcanoes as an extreme example, beyond the fragmentation mechanism and transport, there are other influences on grain size such as the scaled depth of explosions, topographic effects on jet behavior, country rock mechanical properties and recycling processes (White 1996a; Valentine et al. 2017).

Is 'complete' grainsize distribution needed?

We present gentle manual dry sieving to 63 μm as the standard grainsize technique (Fig. A1.1), and complementary methods to obtain a complete grainsize distribution are recommended (Fig. A1.2). The term "complete" is used here to designate a full grainsize characterization for a specific sample, including the fine tail if applicable, with the fine tail analysis based on methods other than sieving (Online Resource A1.1). If sieving results for a certain sample show a large proportion of fine ash, or a bimodal distribution with a fine mode, then workers are urged to obtain the complete grainsize distribution. Bimodal distributions can have a number of different origins, but might

indicate, for example, contemporaneous deposition from a primary plume and a co-PDC plume (Engwell and Eychenne 2016), in which case some or all of the fine constituents in the deposit may not be from primary fragmentation.

Sieving techniques

Sieving techniques for pyroclastic deposits are described in Online Resource A1.3.

Our choice of size fractions

Previous studies on juvenile particles have used a wide range of size fractions (for an overview see Dürig et al. 2019). This is one of the several factors that make data from different volcanoes, eruptions and research groups difficult to compare. In future comparative work, we propose to focus on three representative size fractions for morphological and textural characterization: a medium lapilli fraction (recommended, see Online Resource A1.1), a coarse ash fraction (standard), and a very fine ash fraction (standard). The fine ash fraction is also used to study the surface features of particles.

Why use three size fractions for comparative studies? A single size fraction is unlikely to be present in all natural pyroclastic deposits, and no single size fraction will capture the entire size range of possible crystals and vesicles. Also, if particles have been affected by several consecutive fragmentation events, this should be easier to recognize if several size fractions are used (Wohletz et al. 1989; Graettinger et al. 2013). We do not recommend studying all possible size fractions for comparative studies since time and resources are limited.

Many existing studies select grain size(s) for detailed morphological and textural studies based on the subpopulations determined from sample grainsize distributions (e.g., Dellino and La Volpe 1995, 1996; Cioni et al. 2008b; Andronico et al. 2013; Bagheri et al. 2015). While work on the modal size fraction(s) is logical and important for studying a specific eruption, it does not produce generalizable data.

Coarse ash fraction (standard)

The 0.71–0.5 mm (+ 0.5 to + 1ϕ) fraction is our chosen coarse ash fraction, as it is suitable for both morphological and textural characterization using particle cross-sections (see Chapter 2 for details of this choice). It was previously examined by Cioni et al. (2008b), D'Oriano et al. (2011, 2014) and Pompilio et al. (2017). Other workers have used fractions close to this in ϕ terms:

- Cioni et al. (2014) and Fitch et al. (2017) used 1.4–1.0 mm (- 0.5 to 0ϕ);
- Miwa and Toramaru (2013) and Mele et al. (2018) selected a 0.5–0.35 mm (+ 1 to + 1.5ϕ) fraction;
- Fitch et al. (2017) used 0.35–0.25 mm (+ 1.5 to + 2ϕ).

The 0.71–0.5 mm (+ 0.5 to + 1ϕ) fraction is likely in many cases to represent the majority of vesicles and crystals, and "capture the internal heterogeneity of the magma" (D'Oriano et al. 2014). Ash-sized particles cool from magmatic temperatures to below the glass transition within seconds within air or water, i.e. much more quickly than the interiors of lapilli (e.g., Porritt et al. 2012; Moitra et al. 2018). Therefore, ash particles are small enough to minimize or avoid post-fragmentation effects in terms of phenocryst and microlite growth (D'Oriano et al. 2014; Thivet et al. 2020a) as well as vesicularity (Genareau et al. 2013; Gurioli et al. 2015; Thivet et al. 2020a).

For mafic pyroclasts from Hawaiian or Strombolian eruptions, however, bubble shape at the time of fragmentation may not be fully preserved even in very coarse to coarse ash, due to rapid bubble relaxation (Moitra et al. 2013). The overall morphologies of the 0.71–0.5 mm (+ 0.5 to + 1ϕ) particles might not be fully representative of fragmentation mechanisms, because of several factors, including whole-pyroclast relaxation, especially for ultramafic-mafic magmas (Lindoo et al. 2016). In some other cases, these post-fragmentation processes appear to be negligible, given the almost Gaussian vesicle size distributions and preservation of a large amount of isolated vesicles (Gurioli et al. 2018).

Very fine ash fraction (standard)

Fine to extremely fine ash allows particle surface features and particle morphologies to be determined on the same carbon tape grain mount. Grains with certain surface features are inferred to have been formed by contact with external water during explosive magma-water interaction, and are called "interactive" particles, based on a comparison between magma fragmentation experiments and nature (Dellino et al. 2001, 2012; Austin-Erickson et al. 2008; Jordan et al. 2014; Murtagh and White 2013; Zimanowski et al. 2015; Valentine and White 2017; Dürig et al. 2020a, 2020b, 2020c).

The overall morphologies of these grains are also highly relevant, since different magma fragmentation mechanisms can produce different morphologies in the fine ash to extremely fine ash range. Unless vesicles are very abundant, these particle morphologies are likely to carry a record of the primary fragmentation process (Wohletz 1983a; Heiken and Wohletz 1985; Dellino et al. 2012; Dürig et al. 2012b), and since they cool extremely quickly, they preserve their

diagnostic morphologies, even in ultramafic to mafic magmas. For example, in basalts, magmatic fragmentation can produce fluidal-shaped particles, especially for lava fountains (Heiken 1972; Heiken and Wohletz 1991), whereas phreatomagmatic fragmentation can produce a range of particle morphologies, but includes the products of brittle fragmentation (Wohletz 1983a; Zimanowski et al. 1997; Büttner et al. 1999, 2002). These particles are also sufficiently small that few remain in the bedload during transport, so abrasion effects are minimal.

Both the 250–125 μm (+ 2 to + 3ϕ) and the 125–63 μm (+ 3 to + 4ϕ) fractions are popular in the literature (e.g., Dellino et al. 2012; Colucci et al. 2013; Murtagh and White 2013; Cioni et al. 2014; Pardo et al. 2014b; Liu et al. 2015b; Alvarado et al. 2016; Fitch et al. 2017; Schmith et al. 2017, 2018; Dürig et al. 2020a, 2020b, 2020c). Some workers have also used particles smaller than 63 μm (e.g., Wohletz 1983a; Dellino and La Volpe 1995, 1996; Graettinger et al. 2013; Liu et al. 2015b).

We chose the 88–63 μm (+ 3.5 to + 4ϕ) fraction, which is part of the “very fine ash” range (Table A1.1), as the optimum fraction because it is the finest that can readily be obtained by sieving, and it maintains the 3 ϕ spacing between our three fractions. If not enough of these particles are available in a certain sample, the full 125–63 μm range could also be used.

The 88–63 μm (+ 3.5 to + 4ϕ) fraction particles are, however, too small to be representative for the magma vesicularity and crystallinity at fragmentation because larger crystals and vesicles are often larger than the particles (Gurioli et al. 2015; Chapter 2). This is why a coarse ash fraction and, preferably, a medium lapilli fraction, are also studied. Another potential caveat is that certain mildly explosive eruptive styles produce very few fine to extremely fine ash particles so some particles actually found in the 88–63 μm (+3.5 to + 4ϕ) fraction may represent breakage of larger clasts rather than primary magma fragmentation (Thivet al. 2020c).

Ultrasonic cleaning (standard)

Natural pyroclasts may have adhering finer particles, which hides their true morphologies and surface features. This coating can sometimes make discrimination of juvenile from non-juvenile, and selection of juvenile particles, difficult (e.g., Colucci et al. 2013; Pardo et al. 2014b; Gaunt et al. 2016). A cleaning step is therefore required. This involves short (a few minutes), low intensity ultrasonic cleaning in distilled water, only for the size fractions of interest (Miwa and Toramaru 2013; Alvarado et al. 2016; Liu et al. 2015a, 2017; Gaunt et al. 2016; Mele and Dioguardi 2018; Ort et al. 2018) (Fig. A1.4d). Using a solution of ~ 30 ml sodium hexametaphosphate (a dispersing/deflocculating agent) in 1 liter hot water may be useful for older eruptive products (e.g.,

Casalbore et al. 2010), to facilitate disaggregation. The particles are then dried in an oven, typically at 40–80°C (e.g., Miwa and Toramaru 2013; Liu et al. 2015a; Gaunt et al. 2016; Ort et al. 2018). Prolonged, high intensity ultrasonic treatment might damage particles (Cioni et al. 1992), so it should be avoided.

Basic componentry (standard)

Componentry is the quantification of different types of particles from a volcaniclastic deposit into different categories (bins). The two basic categories are juvenile and non-juvenile (lithic) (White and Houghton 2006). Although juvenile particles are typically glassy, there are some exceptions, like tachylitic grains in some basaltic pyroclastic deposits (Fisher and Schmincke 1984; Taddeucci et al. 2014). Free crystals can be assigned to the juvenile or lithic categories, depending on their inferred provenance. For example, in a basaltic deposit, free pyroxenes might be derived from the magma but loose quartz grains are probably from the country rocks. Free crystals of juvenile origin can often be recognized based on thin rims. If the assignation of free crystals is problematic, they can be kept as a distinct category. A final type of fragment consists of “composite” clasts which combine juvenile and lithic material (White and Houghton 2006).

Basic componentry can help separate different eruption types. Phreatic eruptions, by definition, do not produce juvenile particles (e.g., Barberi et al. 1992; Pardo et al. 2014b; Alvarado et al. 2016). Magmatic eruption products can have low to extremely low lithic contents (e.g., Heiken and Wohletz 1987; Valentine and Groves 1996; Allen and McPhie 2000; Valentine 2012). High lithic contents are commonly associated with phreatomagmatic eruptions that excavate deep craters into the country rocks (Doubik and Hill 1999; White and Ross 2011; White and Valentine 2016). However, other processes – such as caldera collapse, vent widening during Plinian eruptions, lithic lag breccias within pyroclastic flows, or flank eruptions during the first days on basaltic volcanoes – may also lead to high lithic contents (Taddeucci et al. 2002; White and Valentine 2016 and references therein). In contrast, phreatomagmatic eruptions involving surface water can produce lithic-poor pyroclastic deposits (e.g., White 1996b; Murtagh and White 2013; Agustín-Flores et al. 2015).

Basic componentry involves counting only the basic categories (juvenile, lithic, ± free crystals, ±composite) and is a standard step for the coarse ash and very fine ash fractions (Fig. A1.1). The result of the counting, for each investigated size fraction, is the number of particles from each component versus the total number of particles counted. This approximately corresponds to

volumetric proportions, since we are dealing with specific size fractions[4]. A more complete componentry exercise, where juvenile grains are subdivided into types, lithics are separated by stratigraphy, etc., can be very informative, and is recommended (Online Resource A1.1) but not standard. If full componentry is performed, the results should also be regrouped into the basic categories for ease of comparison with other studies.

The number of grains to be counted depends on the aims of the componentry study. For basic componentry, assuming that the major components have abundances greater than 10–20%, then 200+ particles are required. This was empirically defined by a sensitivity analysis for samples from the 1977 Ukinrek maar eruption, using low and high lithic abundance samples (Ort et al. 2018). Also, based on the theoretical error chart developed by van der Plas and Tobi (1965) for petrographic point counting, for a component that has a 10% abundance, counting a total of 200 points will yield an error range for this component slightly larger than 4% absolute (40% relative), within a 95% confidence interval (Fig. A1.4c). Still at 200 points, for a component with 40% abundance, the error is about 7% absolute, or ~ 18% relative (Fig. A1.4c). Ross et al. (2021) have updated the van der Plas and Tobi (1965) charts.

For the 0.71–0.5 mm (+ 0.5 to + 1ϕ) fraction, the user places the grains under the binocular microscope (Suzuki et al. 2013; Gaunt et al. 2016; Murch et al. 2019b), perhaps in a flat petri dish, and counts 200+ grains manually, with tweezers or a dissection probe, sorting them into basic componentry bins (Fig. A1.4d). Juvenile clasts should be kept apart to be reused later.

For the 88–63 μm (+ 3.5 to + 4ϕ) fraction, counting grains under the binocular microscope is tricky to handle with tweezers or a dissection probe, and juvenile identification may be difficult. So componentry is instead performed on a polished epoxy grain mount with SEM imaging, as the internal textures of each grain can then be identified (e.g., Barberi et al. 1989; Pardo et al. 2014b; Jones et al. 2016; Liu et al. 2017). Componentry with an SEM is based largely on internal textures of fragments, but can be aided, or partly automated, by adding chemical/mineralogical mapping with the EDS detector (Hornby et al. 2019; Pardo et al. 2020). To perform basic componentry based on SEM images, software such as the freeware JMicrovision (Roduit 2007; https://jmicrovision.github.io/) can be used on single images or image mosaics. If just enough grains have been mounted, than the “manual point counting” feature of JMicrovision allows the

[4] An alternative to counting the individual grains in each componentry bin is to weigh the entire bins using a precise analytical balance (Cas and Wright 1987; Barberi et al. 1989), although if different components have different densities, weighing the bins will not produce data equivalent to volumetric proportions.

user to count all grains (Fig. A1.4e). If more than 200 grains have been mounted, then grains can be selected on a square grid, by using the “recursive grid” option, until enough points have been classified.

Juvenile particle selection (standard)

The 0.71–0.5 mm (+ 0.5 to + 1ϕ) and 88–63 μm (+ 3.5 to + 4ϕ) fractions might each contain many more juvenile particles than the number needed for characterization of textures, morphologies and surface features. The fractions are also likely to contain non-juvenile clasts and free crystals, which are not wanted in subsequent steps: all morphological and textural measurements described here are to be done exclusively on glassy (or similar) juvenile particles, not on free crystals or lithics. A step of juvenile particle selection is therefore needed.

Coarse ash fraction (standard)

For the 0.71–0.5 mm (+ 0.5 to + 1ϕ) fraction, juvenile grains are manually set aside, under the binocular microscope, during basic componentry. Among those, 50 juvenile particles are randomly selected, which is more than should be actually needed (Chapter 2). These 50 juvenile particles are then made into a polished epoxy grain mount (Fig. A1.1).

Very fine ash fraction (standard)

For the 88–63 μm (+ 3.5 to + 4ϕ) fraction, juvenile particles are identified on SEM images of particle cross-sections during basic componentry. The same particles can be retrospectively located on SEM images of a carbon-tape grain mount, as part of a dual-mounting procedure. When preparing the carbon tape grain mount, mount enough grains to ensure that (1) the carbon tape grain mount retrospectively contains at least 100 juvenile particles and (2) the polished epoxy grain mount contains at least 200 grains in total, for basic componentry (Fig. A1.1).

Sample preparation for quantitative 2D morphological and internal texture analysis (coarse ash fraction) (standard)

For the 0.71–0.5 mm (+ 0.5 to + 1ϕ) fraction, the 2D morphological and internal texture measurements require either a polished epoxy grain mount (or ‘briquette’) (e.g., Maria and Carey 2002; Liu et al. 2015a, 2015b, 2017), or a polished thin section. Chapter 2 present detailed instructions for preparing polished epoxy grain mounts, which are easier to manufacture than polished thin sections. The 50 selected juvenile particles are mounted.

A photo of the whole polished grain mount or polished thin section can be obtained with a high-resolution handheld camera, a binocular microscope or a high-resolution flatbed scanner. This photo is then printed, and brought to the SEM for easier navigation.

Dual mounting of the very fine ash fraction (standard)

For the 88–63 μm (+ 3.5 to + 4ϕ) fraction, we established a dual mounting procedure, where 200+ particles from the bulk fraction (including at least 100 juvenile ones) are first mounted on a carbon tape, imaged with the SEM, and then converted to a polished epoxy grain mount and imaged again. The latter SEM images are used for basic componentry (standard), during which juvenile particles are identified. The same juvenile particles can then be retrospectively found on mirror SEM images of the carbon tape grain mount, to be used for identifying surface features and to make morphology measurements on silhouettes (both standard; Fig. A1.1). Detailed instructions for the dual mounting procedure are provided in Online Resource A1.4 and a brief summary is given here.

Carbon tape grain mount

The procedure starts with a circular double-sided carbon tape being stuck onto an aluminum disk (Fig. A1.5a). The top will be covered by a non-stick paper circle, on which a smaller circle is drawn, corresponding to the internal diameter of the ring form to be used later for the polished epoxy grain mount (Fig. A1.5b). The non-stick paper circle is then peeled off from the carbon tape (Fig. A1.5c). We offer four particle transfer methods. In the first quick method, particles are spread on the marked non-stick paper circle, and the sticky (carbon tape) side of the aluminum disc is very gently pressed on the sample (Fig. A1.5d). In the second quick method, a moistened glove-covered thumb is used to transfer the particles from the non-stick circle to the sticky side of the carbon tape, making sure to press down very gently to avoid crushing fragile grains (Fig. A1.5e). In the third quick method, a fine-tipped paintbrush is used. For the slow method, particles are transferred and deposited one by one onto the carbon tape, under the binocular microscope. This last method is ideal to get good particle separation but still mount the particles in a restricted area. With all mounting methods, a linear object with a thickness of ~ 50 μm or more is added, to be used as a “horizontal” reference later, during imaging (Fig. A1.5e). After coating the grain mount with a very thin layer of carbon or gold, it is ready to take to the SEM to image particles (Fig. A1.5f).

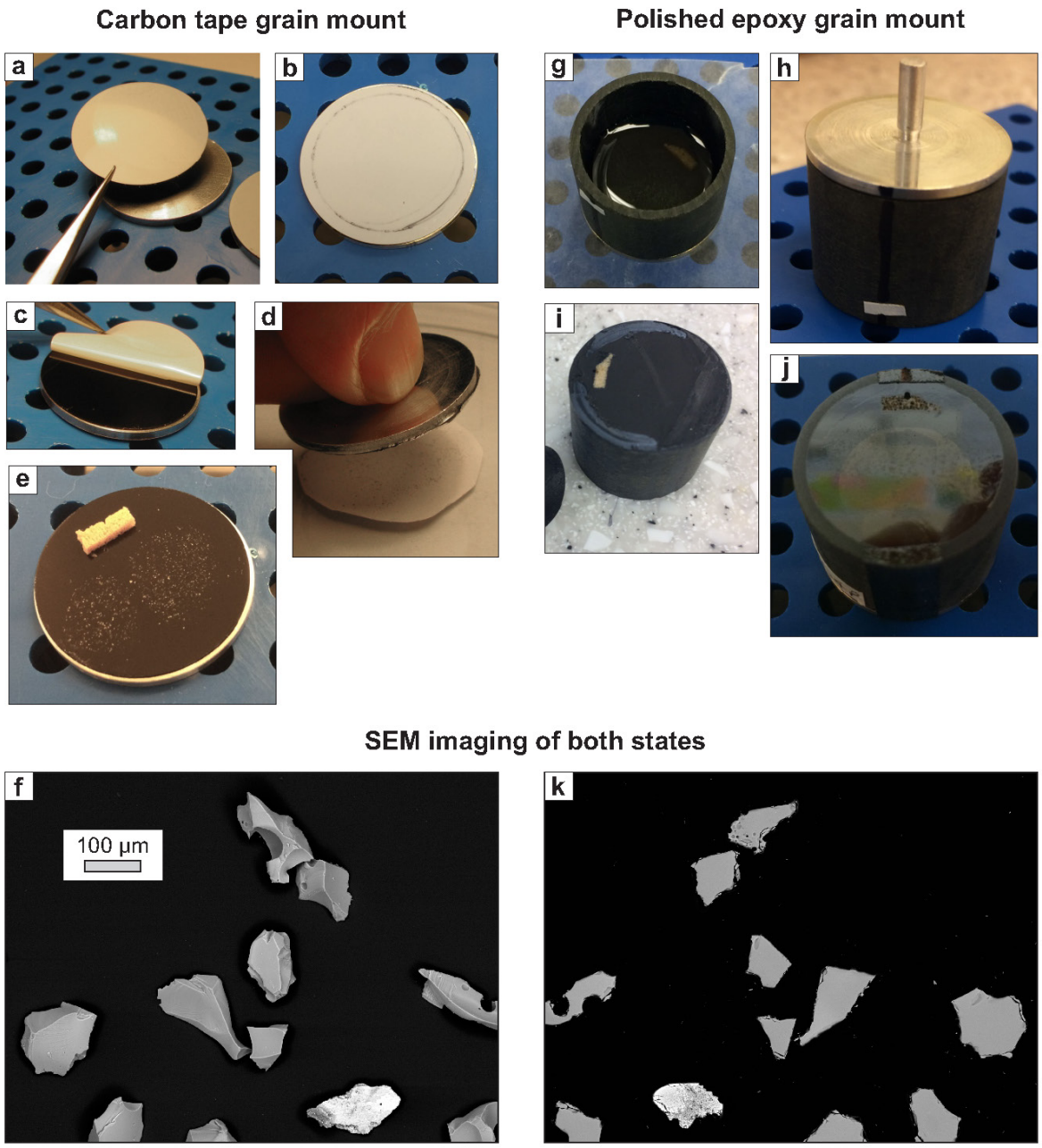

Figure A1.5: Dual mounting procedure for the very fine ash fraction, i.e. 88–63 µm (+ 3.5 to + 4ϕ): (a)-(e) carbon tape grain mount; (g)-(j) polished epoxy grain mount; (f)&(k) SEM images in each state. (a) Placing the carbon tape on the aluminum stub. (b) Drawing a smaller circle on the non-stick paper. (c) Peeling off the non-stick paper. (d) Spreading ash grains on the non-stick paper and very gently picking them up with the upside-down aluminum stub covered in carbon tape. (e) A finished carbon tape grain mount where particles have been transferred with the thumb method instead, with two side-by-side applications. A piece of cork is used for a horizontal line reference. The only step left is depositing a thin film or carbon before imaging. (f) SEM-BSE image of the 3D particles, to be used for measuring morphometric parameters and inspecting particle surface features (to search for interactive ones). (g) After the ring form is applied, epoxy resin is poured. (h) The resin is cured and the cured assembly can be turned upside down. This becomes the new 'up' direction'. (i) Removing the aluminum stub and carbon tape, before cleaning, grinding and polishing. (j) The finished polished epoxy grain mount after covering with a thin film of carbon. (k) SEM-BSE image of the particle cross-sections, to be used for basic componentry. This is the mirror image from (f). The grinding and polishing has been done quickly for demonstration purposes, so this image is only usable for basic componentry.

Polished epoxy grain mount

After SEM imaging, the carbon tape grain mount can be transformed into a polished epoxy grain mount. First, the plastic ring form is glued on the side where particles are present. Then the epoxy is poured (Fig. A1.5g). After curing, the assembly can be turned upside down (Fig. A1.5h). The aluminum stub and carbon tape are detached (Fig. A1.5i). The epoxy mount is then ready for grinding and polishing, the aim being to expose the center of the smallest particle. This leaves a finished polished epoxy grain mount, which can be coated with carbon (Fig. A1.5j) and taken back to the SEM for imaging (Fig. A1.5k). The raw SEM images of the polished grain mount should constitute mirror images of the carbon tape grain mount.

Quantitative morphology analysis

Overview of possible imaging methods

In previous studies, juvenile particle morphologies have been measured in 2D or in 3D. The 2D morphologies have often been based on silhouettes (projections) of 3D particles, acquired by SEM (e.g., Dellino and La Volpe 1996; Dürig et al. 2012b; Jordan et al. 2014; Avery et al. 2017) or on optical methods in various particle-sizing and imaging devices, also known as automated particle analyzers (e.g., Leibrandt and Le Pennec 2015; Schmith et al. 2017; Nurfiani and Bouvet de Maisonneuve 2018; Freret-Lorgeril et al. 2019; Thivet et al. 2020a). Alternatively, 2D morphologies can be based on particle cross-sections imaged with a petrographic microscope or an SEM, as long as very careful polishing is performed to preserve the original edge of the grain (e.g., Liu et al. 2015a, 2015b; Rausch et al. 2015; Jones et al. 2016; Buckland et al. 2018; Comida et al. 2018; Verolino et al. 2019). Emerging 3D techniques include micro-CT, for which improvements in voxel resolution are enabling increasingly small-scale morphological features to be resolved (e.g., Schipper et al. 2013; Vonlanthen et al. 2015; Dioguardi et al. 2017; Mele and Dioguardi 2018; Mele et al. 2018).

Unfortunately, morphometric parameters measured by the different 2D methods cannot be directly compared (Liu et al. 2015a; Buckland et al. 2018; Nurfiani and Bouvet de Maisonneuve 2018), and tomography cannot yet capture tiny but significant microlites or vesicles visible in SEM. Therefore, we had to make choices here on standard methods for the protocol. Our criteria were equipment accessibility, image acquisition costs (financial and temporal), and versatility. By versatility we mean the possibility of measuring not only morphometric parameters, but other

aspects such as componentry, groundmass chemical composition, internal textures and surface features.

Micro-CT provides true 3D information on particle morphologies, surface areas, vesicle sizes, and vesicle number density. Micro-CT is very useful for a number of applications, including study of aerodynamic drag, as shown by the papers cited above. However, in the context of the present standardized method for comparative studies, crystals are not always easily distinguishable from glass under X-ray (e.g., Mele et al. 2018), and imaging a sufficiently large number of particles at a high spatial resolution (~ 0.5 μm) involves a large temporal effort, plus computer power. In contrast, SEM methods are currently much more accessible worldwide, are easier to use than micro-CT devices, and also allow chemical (EDS) and crystallographic (e.g. electron backscatter diffraction) analysis if needed.

Automated particle analyzers based on optical methods are fast and are gaining popularity. Internal textures (vesicles and crystals) cannot, however, be assessed with these devices, and it can be difficult to determine whether a certain particle is a juvenile fragment, a non-juvenile (lithic) fragment, or a crystal. Replicability of measured shape populations across the increasing number of different analyzers remains to be established. In the context of comparative fragmentation studies such as those proposed here, we prefer SEM imagery for the standard parameters. Online Resource A1.1 describes how micro-CT devices and automated particle analyzers can be integrated to perform additional measurements.

We now further consider the two types of SEM imaging for shape analysis in more detail: 2D particle cross-sections (using a polished epoxy grain mount) or 2D particle silhouettes (using a carbon tape grain mount), each with its pros and cons (Table A1.2). Our proposed strategy is to use a polished epoxy grain mount (particle cross-sections) for the 0.71–0.5 mm (+ 0.5 to + 1ϕ) fraction and a dual mounting procedure for the 88–63 μm (+ 3.5 to + 4ϕ) fraction (Figs. A1.1, A1.2). This maximizes the information output while minimizing the sample preparation and imaging steps. The images should be stored in a lossless format (e.g., TIFF).

Imaging strategy for the coarse ash fraction

For the 0.71–0.5 mm (+ 0.5 to + 1ϕ) fraction, using a polished epoxy grain of the juvenile fragments (particle cross-sections) allows morphometric parameters, internal textures and groundmass composition to be studied on a single mount. Quantifying internal textures, as well as particle morphologies, is of fundamental importance. For example, vesicles have a strong influence on particle morphologies: the presence of vesicles affects the material properties and

stress distribution within glass, and therefore the geometry of brittle breakage (Liu et al. 2015a, 2015b; Mele et al. 2018). Therefore, knowing the vesicularity of the melt or glass at the time of fragmentation should help to interpret morphometric parameters and tease apart information about the magma's ascent versus the signatures of different fragmentation mechanisms.

Table A1.2: Comparison of three particle mounting methods for SEM imaging.

	2D particle cross-section (polished epoxy grain mount)	**2D projected silhouette (carbon tape grain mount)**	**Dual mounting**
Pros	• Provides information about particle morphology and internal textures • Can also be used to determine groundmass and phenocryst chemistry	• Silhouettes can be used in various morphological parameter systems and compared to published studies, if the same size fraction is used • Particle morphology can be directly linked with particle surface features, using the same grains • Full particle diameter and particle complexity captured	• Full suite of parameters can be determined (basic componentry, morphology, internal textures, surface features) • Assurance that only glassy (or similar) juvenile particles are actually used for morphological parameters and surface features
Cons	• Possible particle edge modification due to sample preparation (grinding and polishing must be done very carefully) • No direct information of original particle size (due to sectioning) • User must screen out particle cross-sections that are too small to be representative • Highly inequant particles (plates, hairs) may be systematically underrepresented	• No quantification of crystals and bubbles • Avoiding lithics and free crystals may be difficult (no view of the grain interior) • Depending on the depth of field of the imaging system used, care has to be taken to get the silhouette into sharp focus (possible for the + 4ϕ fraction, but can be a problem for coarser grains)	• More work than a single mounting technique used alone
Adopted for	0.71–0.5 mm (+ 0.5 to + 1ϕ)	88–63 µm (+ 3.5 to + 4ϕ), as part of dual mounting	88–63 µm (+ 3.5 to + 4ϕ)

Grain morphologies (and vesicle shapes) are also influenced by crystals (Thivet et al. 2020c). For example, Schmith et al. (2017) noted that their fragmentation diagram could “only be directly applied to phenocryst- and microlite-poor tephras of basaltic composition”, because they built their

diagrams using such particles. Therefore, we need to document geochemistry, particle morphologies, and internal textures together. The 0.71–0.5 mm (+ 0.5 to + 1ϕ) fraction is ideal for this since the particles are large enough to capture most crystals and bubbles in the magma, yet are small enough to avoid strong post-fragmentation effects.

Imaging strategy for the very fine ash fraction

For the 88–63 μm (+ 3.5 to + 4ϕ) fraction, we have developed a dual mounting procedure which involves converting a carbon tape grain mount to a polished epoxy grain mount. SEM images are acquired from both the carbon-tape and epoxy grain mounts using the same magnification, so that mirror images are obtained (Fig. A1.5). The images from the carbon tape grain mount are used for two purposes: (1) quantifying morphological parameters on silhouettes, and (2) studying surface features, which are diagnostic of some fragmentation processes, for fine to extremely fine ash. The morphology measurements on silhouettes facilitate comparisons with the existing body of literature (see Table 3 in Dürig et al. 2019). Results based on this method were used, for example, to compare tephra grains from different eruptions or products of different eruptive phases (e.g., Dellino and La Volpe 1996a; Cioni et al. 2008b; Dellino et al. 2012; Murtagh and White 2013; Jordan et al. 2014; Iverson et al. 2014; Alvarado et al. 2016) and on products of laboratory fragmentation to infer processes that generated the analyzed tephra particles (e.g., Büttner et al. 2002; Dürig et al. 2012b, 2020b; Schipper et al. 2013; Jordan et al. 2014). Note, however, that previous studies involving morphologies acquired from silhouettes have used a range of size fractions, so care should be taken to compare only particles of the same sizes.

Images from the polished epoxy grain mount are used for basic componentry (described above). Glassy or similar juvenile clasts are identified, their numbers noted, and then the same grains are flagged on the mirror images from the carbon tape grain mount. The dual mounting ensures that only convincing juvenile particles (not lithics or free crystals) are ultimately used to measure morphometric parameters and study surface features (Table A1.2).

Choice of morphometric parameters

A wide array of morphometric parameters have been reported by previous workers, as reviewed by Liu et al. (2015a), Leibrandt and Le Pennec (2015), Schmith et al. (2017) and Dürig et al. (2019). As a standard minimum parameter set for a quantitative description of the grains' morphologies, we propose a combination of two systems, the Image Particle Analysis (IPA) parameters of Dellino and La Volpe (1996) and the parameters suggested by Liu et al. (2015a).

We chose these two systems because they are well established in the literature and both contain parameters that capture different aspects of shape, as described in the original references. The IPA parameters are often combined in a diagram which aims to distinguish brittle from ductile fragmentation (Büttner et al. 2002). The definitions to be used for these parameters (circularity, compactness, rectangularity, elongation, convexity, solidity and aspect ratio) are provided in Figure A1.6. Numerous other parameters can also be measured (see Online resource A1.1).

Imaging details for the coarse ash fraction

For the polished epoxy grain mount of the 0.71–0.5 mm (+ 0.5 to + 1ϕ) fraction, the SEM is used in BSE mode (e.g., Liu et al. 2015a; Jones et al. 2016; Buckland et al. 2018), and images are acquired for 50 juvenile particles (see Chapter 2). Several images will be needed to cover each sample.

The magnification and resolution of these images is important, since low quality images do not produce reliable data. Particle perimeters and internal textures depend on image resolution (Dellino and La Volpe 1996; Maria and Carey 2002; Liu et al 2015a; Schmith et al. 2017; Chapter 2). The key metric is the total number of pixels per particle (a.k.a. pixel density), which is a function of both magnification and image resolution. Morphometric parameters are only comparable if the same pixel density is used between different studies. Previous studies, which focused only on particle morphologies, have recommended anywhere from 750 to 5000 pixels per particle (Mele et al. 2011; Dürig et al. 2012b; Liu et al. 2015a; Schmith et al. 2017). However, because internal textures will also be studied on the same images, the required pixel numbers are actually larger for the 0.71–0.5 mm (+ 0.5 to + 1ϕ) fraction, about 20 000 pixels to get stable convexity, vesicularity and crystallinity in a range of fragments from the Ukinrek maars (Chapter 2). With attention to particle spacing, image resolution, and magnification, single images can capture 10–20 particles suitable for analysis. Examples of suitable magnification and resolution settings, and advice on imaging details, are provided in Online resource A1.5.

Studies aiming to obtain a reliable vesicle-size distribution or crystal-size distribution have recommended a nested imaging procedure, where each particle is imaged at different magnifications (Shea et al. 2010). Here, because we are aiming only for bulk vesicularity and crystallinity as standard parameters, and we are measuring 50 particles per sample, we use only a single image per particle, to save time. We acknowledge that additional imaging may be needed for full microlite quantification.

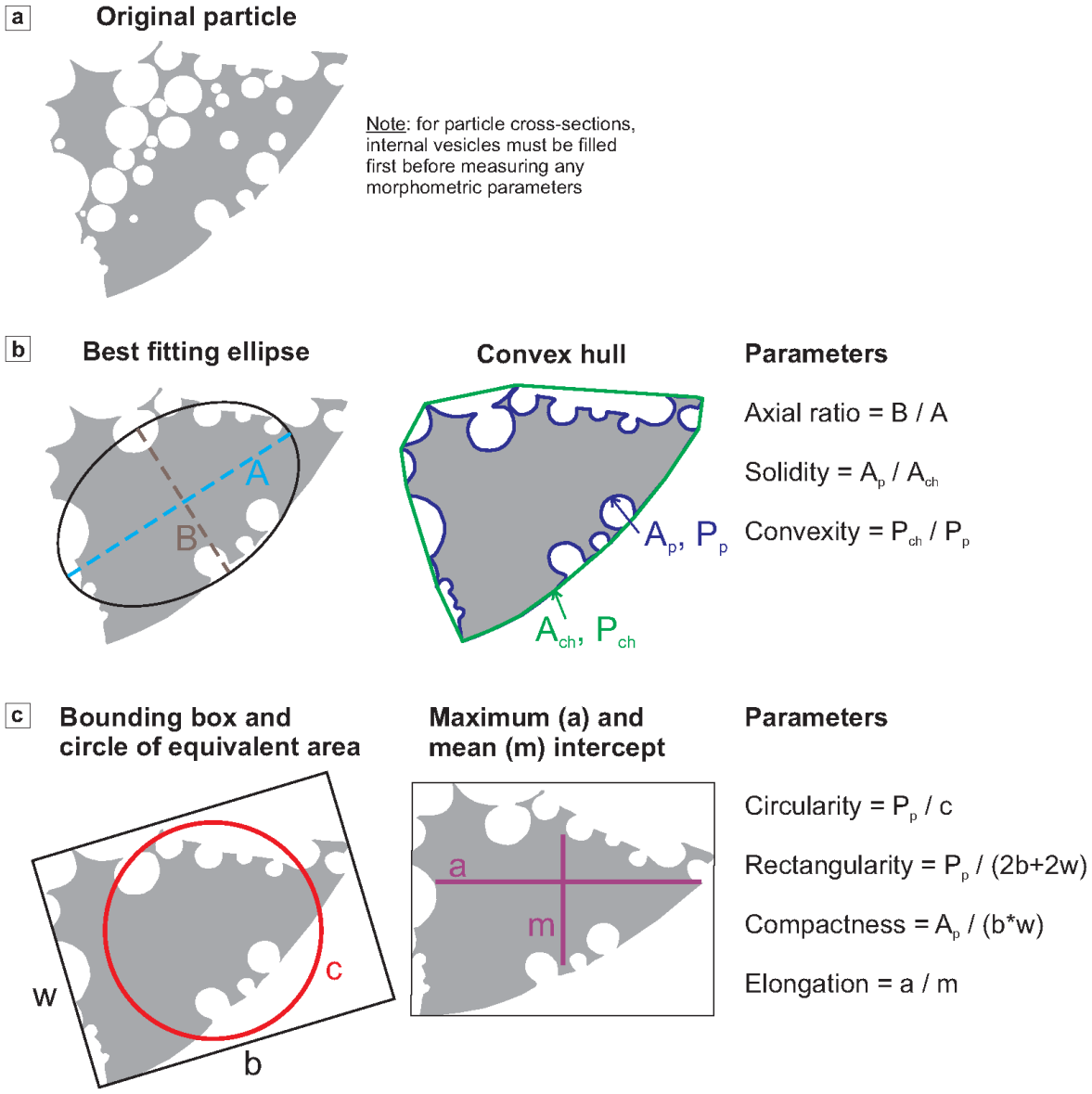

Figure A1.6: Definitions of the standard morphometric parameters, modified from Liu et al. (2015a) and Dürig et al. (2019). (a) The original particle, before infilling the *internal* vesicles. Note that for particle cross-sections, internal vesicles must be infilled before morphometric parameters are measured. (b) The three main parameters suggested by Liu et al. (2015a): axial ratio (sensitive to particle elongation), solidity (a measure of morphological roughness, sensitive to large-scale concavities) and convexity (a measure of textural roughness, sensitive to small-scale concavities or protrusions). A and B are the major and minor axes of the best-fitting ellipse, which has the same area, orientation and centroid as the original particle. A_p and P_p are the area and perimeter of the particle. A_{ch} and P_{ch} are the area and perimeter of the convex hull, which is like a rubber band enveloping the particle (ImageJ User Guide version 1.46r). (c) The IPA parameters of Dellino and La Volpe (1996): circularity, rectangularity, compactness and elongation. 'c' is the perimeter of a circle with area A_p. w and b are the width and breadth of the minimum area bounding box. Note that this box is not necessarily parallel to the sides of the original image. a is the maximum intercept, i.e. the longest segment inside a particle, parallel to the long side of the bounding rectangle. Finally m is the mean intercept, perpendicular to a. Parameters a and m are measured after the particle is rotated to the long axis of the minimum bounding box.

Imaging details for the very fine ash fraction

For the carbon tape grain mount of the 88–63 μm (+ 3.5 to + 4ϕ) fraction, the SEM is used in back-scatter mode and/or secondary electron mode (Goldstein et al. 2017). In our experience, the back-scatter mode produces images that are easier to use for morphological analysis (strong contrast between particle and the background), whereas the secondary electron provides better images for studying surface features. An acceptable compromise might to use only the back-scatter mode, but employ a high enough magnification and resolution to allow surface features to be clearly discernable. Examples of suitable settings are provided in Online resource A1.5. Again, we stress that it is important to always use the same pixel number so results from different studies are comparable.

For surface features, 100 glassy (or similar) juvenile grains should be classified. Of the 100 grains, a minimum of 50 should be measured for morphological parameters. This minimum number has been set based on previous studies and a stability test using 125–63 μm (+ 3 to + 4ϕ) ash from the silicic submarine Havre volcano, 2012 eruption (Dürig et al. 2020b). The sample used (HVR159) contained a mixture of particles from four different morphology classes (Murch et al. 2019a, 2019b), including blocky, highly vesicular, fluidal and elongate-tubular grains. Using 145 particles, we calculated the averages of four morphometric parameters, progressively adding particles in random order. We calculated the relative difference in percent between the overall average and the average for a specific number of particles (Fig. A1.7). In this test, the relative difference became less than 5% relative at 30 particles or less, and the averages for the different morphometric parameters looked very stable beyond 50 grains.

In routine measurements, to verify that enough particles have been measured, we suggest calculating the relative difference in cumulative average morphometric parameters for the 45^{th}, 46^{th}, 47^{th}, 48^{th}, and 49^{th} grains. If the relative difference is more than 5%, more grains should be imaged and analyzed.

For the polished epoxy grain mount of the 88–63 μm (+ 3.5 to + 4ϕ) fraction, the SEM is used again in back-scatter mode, and 200+ grains from the bulk fraction are imaged. Because the only aim is basic componentry (and juvenile identification) in the standard flowchart (Fig. A1.1), a lower resolution can be employed than for the carbon tape grain mount, significantly reducing imaging time. However, the same SEM magnification should be used, so that the same particles are placed in the field of view both on carbon tape and in the polished epoxy grain mount, for each frame. Examples of suitable SEM settings are provided in Online resource A1.5.

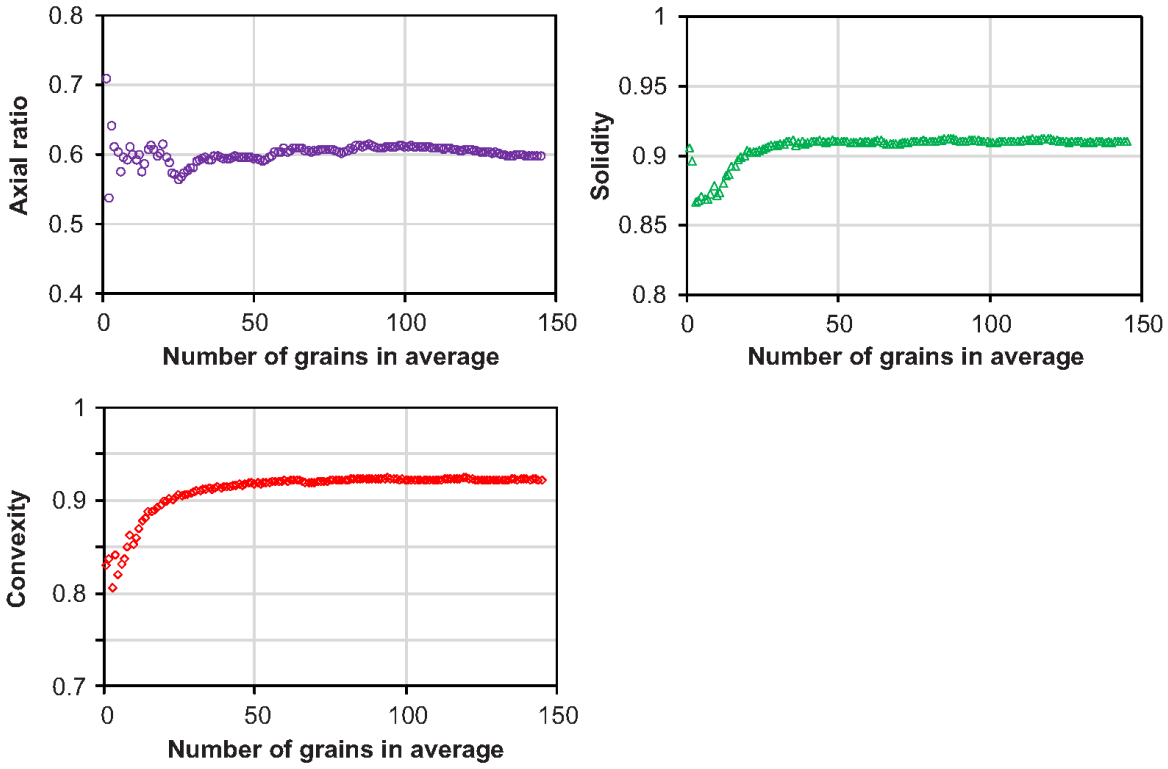

Figure A1.7: Stability test for morphology measurements of particle silhouettes, using an ash sample (HVR159, 125–63 µm or + 3 to + 4ϕ) from the 2012 eruption of Havre volcano (Kermadec Arc).

Measuring the morphometric parameters

Chapter 2 present a new Fiji code called Particle Shapes & Textures Analyzer) (PASTA, available on GitHub: http://doi.org/10.5281/zenodo.3336335) which allows separation of multi-particle images into single-particle images, and binarization. Once the single-particle binary images are available, they can be further analyzed within PASTA as batches, to yield the Liu et al. (2015a) parameters.

In addition, the single-particle binary images obtained with PASTA can be analyzed with the open source Matlab batch processing script PARTISAN (PARTIcle Shape Analyzer) developed by Dürig et al. (2019). The latest version (Dürig and Bowman 2021) provides 19 basic morphological metrics and 23 non-dimensional morphometric parameters from five different morphometric systems, including those of Dellino and La Volpe (1996), Cioni et al. (2014), Leibrandt and Le Pennec (2015), Liu et al. (2015) and Schmith et al. (2017). The provided results are independent of particle orientation.

Excluding grains that are too small (post-processing)

Juvenile grains that are obviously too small should be excluded from the images. But we also suggest a post-processing filter to remove grains that may only be slightly below the threshold size. The width of the particle bounding box measured in PARTISAN can be used: the width should be at least equal to the retaining sieve mesh (Chapter 2). Any grains smaller than this threshold are deleted.

Internal textures (coarse ash fraction)

Standard textural parameters

Juvenile pyroclasts comprise glass, and commonly also internal crystals (phenocrysts, microlites) and vesicles. The simplest textural parameters to measure on a routine basis are 2D vesicularity and 2D crystallinity (Polacci et al. 2006). For each particle, these parameters are simply taken as the area occupied by vesicles or crystals, respectively, divided by the total area of the particle. Note that these numbers are different from the 3D vesicularities and 3D crystallinities, which need tomography or stereological corrections and a knowledge of 3D vesicle and crystal shapes (e.g., Sahagian and Proussevitch 1998; Higgins 2000; Shea et al. 2010). Other possible textural measurements are described in Online Resource A1.1.

Preparing the SEM images

To measure the internal textures, the first step is to prepare the 0.71–0.5 mm (+ 0.5 to + 1ϕ) SEM images of particle cross-sections, typically using photo-processing software (Shea et al. 2009). This is discussed in detail by Chapter 2, who also present an “Action Pack” for Adobe Photoshop to facilitate and partly automate this step, as part of the PASTA package.

Textural measurements

PASTA transforms prepared greyscale images into segmented images, where the different features such as crystals, glass and vesicles are recolored. From those segmented images, PASTA calculates the 2D vesicularity and 2D crystallinity for each particle (Chapter 2).

Ash surface features (very fine ash fraction) (standard)

The surface features of juvenile fine to extremely fine ash particles can provide information on the energy involved in fragmenting the material (Dürig et al. 2012a, 2012b; Zimanowski et al. 2015).

They also record secondary processes such as transport and alteration (Wohletz and Krinsley 1978; Wohletz 1983b; Heiken and Wohletz 1985).

Interactive particles

As explained before, “interactive” particles are formed during phreatomagmatic fragmentation of the fuel-coolant interaction (FCI) type, when very high stress rates are applied where liquid water comes into direct contact with hot magma, allowing very rapid heat transfer and brittle fragmentation (Zimanowski et al. 1997, 2015 and references therein; Austin-Erickson et al. 2008; Dürig et al. 2020b). These interactive particles have generally angular shapes with particular fracture surface patterns, are glassy, and are typically of fine to extremely fine ash size, with specific surface features (Büttner et al. 1999; 2002). A distinction can be made between two types of FCI, depending on the magma composition. Molten fuel coolant interaction (MFCI) works well for ultramafic to mafic magmas and the laboratory version typically involves the engulfment of a liquid water domain into the magma (Zimanowski et al. 1997, 2015). Induced fuel coolant interaction (IFCI) applies to more felsic magmas and involves liquid water flowing into cracks in the magma (Austin-Erickson et al. 2008; Dürig et al. 2020b). Both processes produce the same types of interactive particles.

Laboratory MFCI experiments generate < 5 to 25% interactive particles. Interactive particles may be even rarer in nature because of the presence of crystals and lithic clasts in the deposits, and because interactive particles are concentrated in the fine size fractions. In contrast, magma fragmentation experiments where no water is involved do not commonly generate these interactive particles (Zimanowski et al. 1997). Miwa et al. (2009) have described particles displaying possible stepped features from vulcanian explosions. So the proportion of interactive particles must be quantified for many experiments and natural deposits to better understand what proportions are typical of different fragmentation mechanisms.

In MFCI experiments, the rest of the ejected pyroclasts are passive particles (Lorenz et al. 1994; Zimanowski et al. 2015). The morphologies and surface features of passive particles are not diagnostic of the fragmentation process, since passive particles can be generated by a range of fragmentation mechanisms (Zimanowski et al. 1997).

Interactive particles are recognized from their surface features, using the carbon tape grain mount of the 88–63 μm (+ 3.5 to + 4ϕ) fraction, under the SEM. Interactive particles include those displaying stepped features, branching quench cracks, and also moss-like particles (e.g., Wohletz 1983; Heiken and Wohletz 1985; Büttner et al. 1999, 2002; Dürig et al. 2012b; Zimanowski et al.

2015; Alvarado et al. 2016; Fitch and Fagents 2020). Because interactive particles make up a small percentage of the total ejected mass, at least 100 particles should be examined, to be confident that all particle types present in the sample are found in the selection. Interactive particles can be counted into classes (stepped fractures, branching quench cracks, and moss-like). All non-interactive particles can simply be labelled “other” for this exercise (see Excel templates in Online Resource A1.2), although it may also be interesting to count particles with hackle lines separately, as explained below.

Stepped features yield irregular particles with an “uneven surface made up of three-dimensional polyhedral elements” (Zimanowski et al. 2015). They are illustrated in Figs. A1.8a, A1.8b, A1.8e and A1.8f (see also Fig. 26.7c in Zimanowski et al. 2015). Stepped features are not to be confused with hackle lines (Quinn 2020), which are not diagnostic of phreatomagmatism. “Hackle” in glass fractography means “steps or lines on the fracture surface running parallel to the direction of crack propagation” (Quinn 2020). In other words, hackles can look like steps, but the true “stepped features” of interactive particles are more complex, and the steps occur “one step over the other (in 3D)” as opposed to “one behind the other (in 2D)” (P. Dellino, written commun., 2021). Hackle lines can form during slow or fast cracking (Quinn 2020), so finding one particle with these features is not diagnostic of FCI. However, there are many examples of particles that display both stepped features and hackle lines (Figs. A1.8e, A1.8f). Also, some IFCI experiments produce increased proportions of particles with hackle lines relative to similar experiments without water (T. Dürig, unpublished data), so more research seems warranted. In the meantime, counting hackle lines in a separate category could yield interesting data.

Branching quench cracks are fracture networks within fresh (unaltered) glass (Figs. A1.9a, A1.9b, and Figs. 26.7a-b in Zimanowski et al. 2015). If in doubt, an EDS analysis (e.g., Alvarado et al. 2016) may be needed to ensure that the glass is indeed fresh, since these fracture networks are not be confused with hydration cracks (Zimanowski et al. 2015). The branching quench cracks are a few microns wide (Büttner et al. 2002) and “form directly after fragmentation due to the sudden quenching and subsequent contraction of still-hot particles (…) due to the fast passage (a few ms) of newly fragmented particles through a domain of liquid water” (Zimanowski et al. 2015).

Moss-like particles are “elements bonded together to form complex irregularly shaped grains” (Büttner et al. 2002) (Fig. A1.9c). These "elements" are tiny fragments and can be angular (Büttner et al. 2002) to globular (Wohletz 1983) (see also Figs. 26.7e-f in Zimanowski et al. 2015).

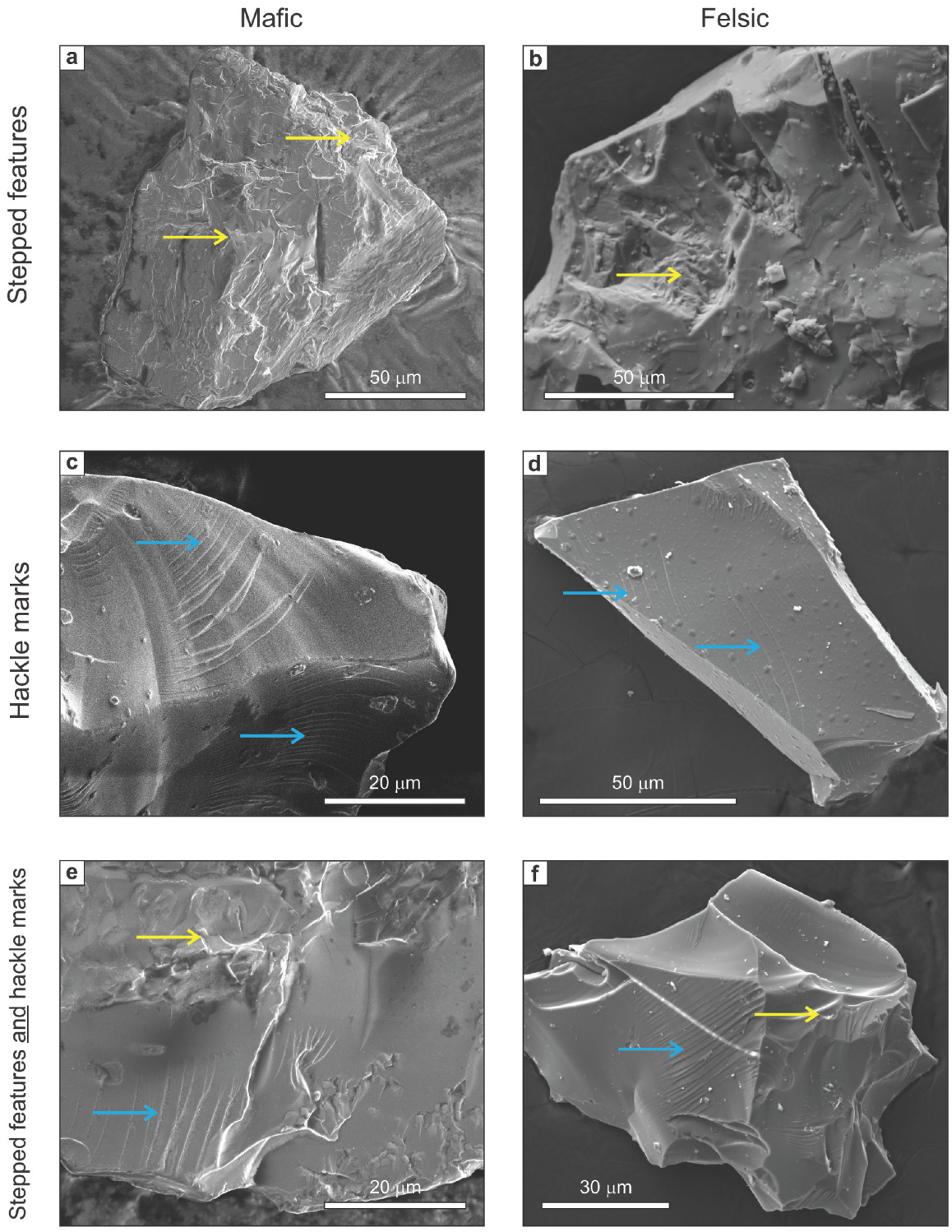

Figure A1.8: Secondary electron SEM images of stepped features and hackle marks. (a)-(c)-(e) are for mafic magma and (b)-(d)-(f) are for felsic magma. (a)-(b) Stepped features (yellow arrows). (c)-(d) Hackle marks (blue arrows). (e)-(f) Stepped features (yellow arrows) and hackle marks (blue arrows). All particles were created by fuel coolant interaction during experiments at the University of Würzburg, except (b) which is natural ash from the Havre 2012 eruption.

Moss-like particles are “interpreted in terms of annealing that occurs immediately after brittle fragmentation of very fine particles before effective cooling could act” (Büttner et al. 2002). A better name for these particles might be “welded microaggregates” but the term “moss-like” is entrenched in the literature.

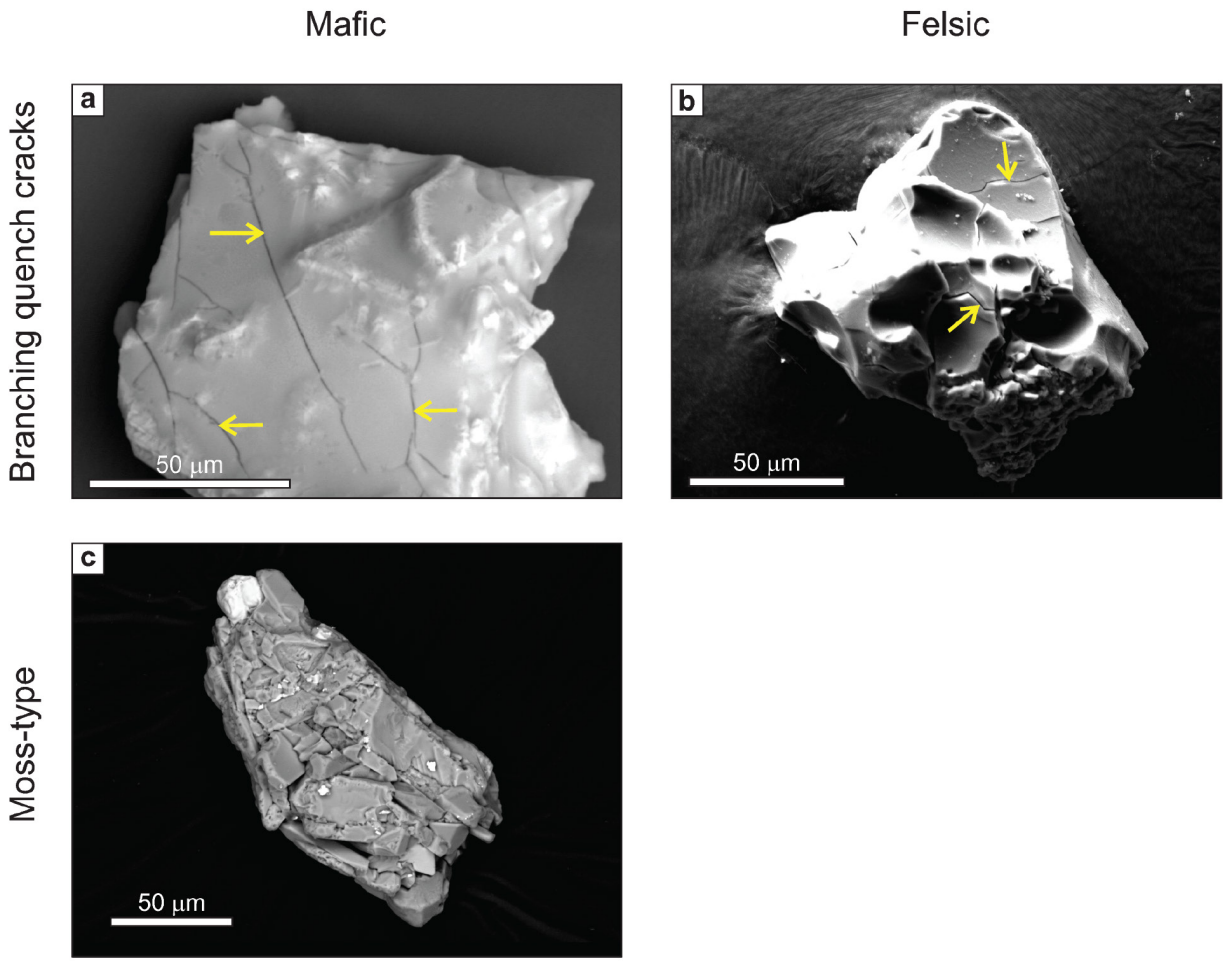

Figure A1.9: SEM images of two types of interactive particles. (a) Branching quench cracks (arrows) in a natural mafic juvenile pyroclast from Ukinrek east maar, Alaska. (b) Branching quench cracks (arrows) in an experimental felsic pyroclast created during an induced fuel-coolant interaction experiment (Dürig et al. 2020b). (c) Moss-type particle created during a MFCI experiment with mafic magma at the University of Würzburg. First two images in secondary electron mode and third one in BSE mode.

We stress again that only glassy (or similar) juvenile fragments should be examined and counted for this exercise, not non-juvenile fragments or free crystals. This is straightforward with the dual mounting procedure since images of the particle interior are available from the epoxy grain mount.

Secondary surface features

Care must be taken to discriminate primary surface features, related directly to fragmentation (described above), from secondary ones, which form later due to transport or sieving, as well as by chemical and thermal alteration. Transport of ash in PDCs allows particle-particle collisions. This produces, particularly for larger particles, rounding (edge abrasion), V-shaped depressions, conchoidal fractures, dish-shaped fractures, grooves, and perhaps some cracks (Wohletz and Krinsley 1978; Heiken and Wohletz 1985).

Transport in plumes and PDCs also allows particles in the micron to sub-micron range to adhere to larger particles; this can happen due to water vapor related to phreatomagmatism, but also because of atmospheric moisture, or electrostatic forces (Schumacher and Schmincke 1995). Adhering particles are common on phreatomagmatic ash (Dellino and LaVolpe 1995), but this alone is not a diagnostic criterion (White and Valentine 2016).

Sieving is likely to modify the ash surface, but we are unaware of any detailed study about this effect. The importance of this effect is expected to be reduced at small grain sizes, and is probably minor at 63 μm (+ 4ϕ) for most materials.

Chemical alteration of ash grains has been proposed to occur in the eruption column and within PDCs (Büttner et al. 2002; Zimanowski et al. 2015), but also more slowly, after deposition (Wohletz and Krinsley 1978; Wohletz 1983b). Alteration produces chemical modification of the surface (including palagonitization and hydration), pitted surfaces, and hydration cracks (Wohletz and Krinsley 1978; Zimanowski et al. 2015).

Archiving the images and data

The original, unmodified, uncompressed SEM images of juvenile fragments should be made available, along with all the measurements. The Excel templates of Online Resource A1.2 can help standardize the data files. Images and data can submitted as supplementary material with each new paper, if the journal allows it, or to one of the existing online data repositories. It might eventually be more convenient to create a common repository for volcanology (or at least for magma fragmentation studies). Archiving the raw SEM images achieves the following: (1) other morphology or textural parameters might be discovered in the future, that are better at discriminating fragmentation styles, or give different important information; (2) anyone can verify that they obtain the same numbers on the same images (reproducibility of scientific results). Archiving the measurements ensures that future workers can easily compile them.

Data analysis

In the interest of space, a review of methods for statistical analysis of morphometric data will be presented elsewhere (Dürig et al. 2021). Future work on data analysis will also have to integrate all types of data discussed here.

Discussion and conclusions

Juvenile pyroclasts contain valuable information on magma state at the time of fragmentation, and about fragmentation processes. At present, no consensus exists in the volcanology community on a standardized methodology to characterize juvenile pyroclasts for comparative fragmentation studies. This makes the data difficult or even impossible to compare among different research groups, for different volcanoes and different eruptions. The methodological variability suggests numerous questions are raised by the various methodologies in use, including:

- Is knowing the geochemical composition of the magma important?
- Should the pyroclastic deposits be sieved or not?
- Which size fraction(s) should be further analyzed?
- Should ultrasonic cleaning of the particles be performed?
- How many grains are needed for each sample and size fraction?
- For 2D morphology quantification, should the grains be imaged using projections of 3D shapes (silhouettes) or in cross-section (polished section/briquette)?
- Should we use a binocular microscope, a petrographic microscope, a particle-sizing device, a scanning electron microscope, or a micro-CT device, or all of them for different purposes?
- What are the resolution and magnification needed to best image the grains?
- Which morphometric parameters should be used, and what is their definition?
- What method should be used to quantify the particle morphologies?
- Should internal textures (crystals and bubbles) also be measured, and how?

Only through acquisition of mutually compatible datasets can our community address process-oriented questions such as:

- Are ash surface features important and diagnostic, and how do we recognize interactive particles?

- Do other particle formation mechanisms also have recognizable fingerprints? If so, what are they? How do they form?

In this paper and a companion one (Chapter 2), we have provided and justified answers for most of these questions, and propose a standardized method for characterizing juvenile particles for comparative fragmentation studies. We stress that our standardized method is not intended to curb academic freedom. Instead, the idea is for workers to include at least our standard steps in their workflows, which can also comprise many other parameters. We intend our proposal to be discussed and extended or refined, and plan an international workshop with this as a focus. We hope that a broad consensus can be reached on a uniform methodology, and that this will become the new standard for studying juvenile particles for comparative fragmentation studies. The community will then be able to accumulate consistent data on juvenile pyroclasts from a range of eruption styles, fragmentation mechanisms, magma compositions, crystallinities and vesicularities, using both natural samples and experiments. When enough data is available, new "fragmentation diagrams" can be developed and we may be able to obtain deeper insights into the full panoply of magma-to-pyroclast processes that drive particle-producing volcanic eruptions. These will allow different styles of particle-forming eruptions to be distinguished based on the particles produced.

Acknowledgements

A number of images presented here (including Online Resource A1.1) show particles generated during magma fragmentation experiments at the University of Würzburg, with the very beneficial involvement and guidance of Bernd Zimanowski and Ralf Büttner. These experiments were funded by the Natural Sciences and Engineering Research Council of Canada (NSERC), using a Discovery Grant to the first author (RGPIN-2015-06782). This is Laboratory of Excellence ClerVolc contribution number 510. A very early draft of the manuscript was read by Emma Liu, Cathy Cashman and Alison Rust, who all made helpful suggestions. We thank Erin Fitch, an anonymous reviewer and associate editor Benjamin Andrews for constructive reviews.

Online Resource A1.1: Recommended and optional steps

The proposed standardized methodology for the analysis of juvenile particles, to be used in comparative studies of primary magma fragmentation, contains standard, recommended and optional steps. The paper describes the standard steps (workflow: Fig. A1.1), whereas this supplementary document describes the recommended steps (workflow: Fig. A1.2) and the

optional steps (not included on flowcharts). Again, the presentation broadly follows the order of the steps on the flowchart (Fig. A1.2), from top to bottom and left to right, focusing on the additional recommended steps (boxes with dashed outlines).

Density, porosity, connectivity and permeability measurements

Lapilli or bombs can be used for several types of density, porosity and permeability measurements. To be complete we also describe similar measurements on ash here.

Dense rock equivalent density (recommended)

Dense rock equivalent (DRE) density is best measured on a several representative lapilli or bomb fragments, which are crushed. The volume of the powders can be precisely measured with gas pycnometers. The DRE density is then deduced by dividing the mass of the powders by their volume (Formenti and Druitt 2003). The DRE density mostly depends on the glass composition and on the crystal phases. Thus, this parameter is important for a global database in order to compare the DRE densities with those given for magma, melt and crystal compositions.

Porosity (recommended)

Porosity is calculated by comparing the bulk density (including voids) of a sample with the DRE density. The bulk density of a section of lapilli or bomb is measured either using the water immersion technique (Houghton and Wilson 1989; Shea et al. 2010) or using envelope density analyzers (Kawabata et al. 2015). These two techniques show very similar results (Thivet al. 2020a).

The average porosity of a selection of ash particles can also be measured using the water pycnometry method (Eychenne and Le Pennec 2012). The porosity/density range of the ash, lapilli and bombs can thus be compared each other (for different grain sizes) and can be also compared to 2D or 3D vesicularity.

Vesicle connectivity (recommended)

Vesicle connectivity is best measured on bomb fragments and lapilli using gas pycnometers following Formenti and Druitt (2013) and Colombier (2017a) procedures, and can bring insights on vesicle nucleation, growth and coalescence processes that might occur within magma storage and conduit areas, as well as crack formation that might occur during magma fragmentation

(Gurioli et al. 2018; Thivet et al. 2020a, 2020b). Thus, vesicle connectivity is an important parameter to measure when dealing with eruptive dynamics and magma fragmentation mechanisms.

Clast permeability (optional)

Permeability can be measured on bomb and lapilli fragments following the Colombier (2017b) procedure, based for instance on the Takeuchi et al. (2008) experiments. Measuring tephra permeability allows estimation of magma permeability at the fragmentation level, hence this is a key physical parameter to measure the efficiency of gas flow within the magma column and thus allow assessment of overpressure-driven fragmentation mechanisms (Thivet et al. 2020a; Bain et al. 2021).

Grain-size distribution

Complete grain size analysis (recommended)

Sieving at half ϕ steps is part of the standardized methodology, both to obtain grain size information and to extract specific size fractions for the analysis of juvenile pyroclasts. Sieving typically yields the grain size distribution down to 63 μm (+ 4ϕ), and the finer particles go to the 'pan'. If additional resolution at the smaller-particle end of the size distribution is required, the contents of pan and several sieve fractions above it (e.g., up 250 μm) can be recombined and analyzed with laser diffraction techniques (e.g., Dellino and La Volpe 1995; Bonadonna et al. 2011; Dellino et al. 2012; Pardo et al. 2014a; Gaunt et al. 2016; Liu et al. 2017). The laser diffraction technique determines the particle size distribution of a dispersed sample in an aqueous solution through the application of the Mie theory (Riley et al. 2003). Results from all techniques are then carefully combined to produce a complete grain size distribution (e.g., Dellino and La Volpe 1995; Manville et al. 2002; Dellino et al. 2012; Eychenne et al. 2012; Pardo et al. 2014a; Jones et al. 2016; Liu et al. 2017).

The particle size distributions obtained by laser diffraction should be binned to half ϕ to be consistent with the sieving data. Assuming that the particle density is constant over the size range analyzed by laser diffraction (reasonable in most deposits, see Eychenne and Le Pennec 2012; Cashman and Rust 2016), the vol. % particle size distributions obtained by laser diffraction are equivalent to wt.% distributions. Sieving and laser diffraction wt.% particle size distributions can

be merged by scaling the laser distribution to the mass fraction (wt.%) finer than 250 μm in the original sieved sample (Eychenne et al. 2012).

The overlap between sieving and laser diffraction data over the 250 to 63 μm size range can be used to evaluate the agreement between the two methods and refine the quality of fit. Because the two methods rely on fundamentally different measurement techniques, they are sensitive to the nature of the sample and the shape(s) of the particles, so can derive different wt.% values for the same grain size fraction. In case of poor agreement between the sieving and laser diffraction data over the 250 to 63 μm size range, an empirical scale factor, minimizing the residual between the wt.% values obtained between 250 and 63 μm by the two methods, can be applied to the laser diffraction data before merging.

Total grain size distribution (optional)

Total grain size distribution (TGSD) of fallout deposits is important for eruption plume models and can yield insights on primary magma fragmentation and eruption intensity (e.g., Bonadonna and Houghton 2005; Costa et al. 2016; Pioli et al. 2019). This requires obtaining grain size distributions at many (from proximal to distal) sites representative of the full extent of the deposit and combining them in a statistically robust manner (Bonadonna and Houghton 2005; Andronico et al., 2014a; Costa et al. 2016; Pioli et al. 2019). However, since TGSDs require a lot of work and the current workflows focus on juvenile particles, we leave this as a completely optional step.

Familiarization (recommended)

Once sieving is complete, it is good practice to look at all size fractions under the binocular microscope. We suggest using a binocular microscope with a magnification range up to 60 times or more. This recommended familiarization step will provide qualitative information on componentry (the proportions of different clast types), the shapes and vesicularities of juvenile pyroclasts, etc. Dust adhering to particles may be a hindrance at this stage, and more-detailed observations can be done on the selected size fractions after the ultrasonic cleaning step (see the paper and Fig. A1.2).

Choice of size fractions: adding medium lapilli

Reasons for our choice of ash fractions are described in the paper. We add a recommended lapilli size fraction here, which allows us to identify the larger vesicles and crystals (e.g., Gurioli et al. 2015). Note, however, that post-fragmentation expansion is likely to have significantly affected

basaltic lapilli (e.g., Fig. 4b in Porritt et al. 2012). Lapilli are commonly used in vesicle-population studies for more-felsic compositions (e.g., Gardner et al. 1996), and analysis is thus useful as a tie-in with that body of work.

We consider that it is best to work on the 5.7 to 4 mm (- 2.5 to - 2ϕ), particles, which are part of the medium lapilli range (White and Houghton 2006; Table A1.1). This keeps the same ϕ spacing as between the other selected fractions (3 ϕ units apart; Fig. A1.2). In the 5.7–4 mm (- 2.5 to - 2ϕ) fraction, there should be enough particles for study in many proximal to medial samples. A similar fraction was previously used by Ersoy et al. (2006).

Detailed componentry of glassy juvenile particles (recommended)

The main paper describes the standard basic componentry (separating grains from a size fraction into juvenile, lithic, ± free crystal, ± composite). *Full* componentry further distinguishes different types of glassy juvenile fragments, different types of lithics, crystals, etc., and is an option for all three size fractions. We specifically recommend detailed componentry on glassy juvenile fragments for the medium lapilli and coarse ash fractions (Fig. A1.2).

Componentry classes

In theory, juvenile clasts can be divided into primary and recycled (Houghton and Smith 1993; White and Houghton 2006; D'Oriano et al. 2014). Recycled clasts have fallen back into the crater and have then been ejected again (D'Oriano et al. 2014). Distinction between primary juvenile clasts and those recycled in this way can be very difficult, but where possible will help investigators distinguish the signatures of primary fragmentation from those of intra-crater recycling (D'Oriano et al. 2013, 2014; Deardorff and Cashman 2017).

In practice, different populations of glassy juvenile clasts can be distinguished based on their colors, lusters, clast shapes, vesicularities, vesicle sizes and shapes, crystallinities, degree of alteration, etc. (e.g., Taddeucci et al. 2002, 2004; Eychenne and Le Pennec 2012; Pardo Villaveces 2012; Suzuki et al. 2013; Andronico et al. 2014b; Cioni et al. 2014; D'Oriano et al. 2014; Eychenne et al. 2015; Gaunt et al. 2016; Liu et al. 2017). It does not appear possible to create a universal standardized scheme for detailed juvenile componentry, but workers should carefully define and illustrate their component classes in publications.

How many grains?

For component abundances of 10–20% or more, counting 200 particles is a reasonable compromise between precision and speed (see the paper, in particular Fig. A1.4c). If there is good reason to quantify components with low abundances (< 5%), larger numbers of clasts must be counted. For a component representing about 3–4% of a sample, a relative 2σ error of 50% can be reached by counting 400–500 clasts (Fig. A1.4c). Such errors can be tolerated if different samples have marked differences in the abundances of these components. For comparison, Houghton and Carey (2015) mention that counting 200 clasts (from the bulk fraction) is 'typical' for each size fraction; Eychenne and Le Pennec (2012), Pardo et al. (2014b), Eychenne et al. (2015), Gaunt et al. (2016), Jones et al. (2016) and Ort et al. (2018) all counted 300 grains or more for each fraction; Andronico et al. (2009, 2014b), Jordan et al. (2016) and Scarpati et al. (2016) counted 500 clasts or more; Taddeucci and Palladino (2002) and Taddeucci et al. (2002) counted "more than 1000" particles per sample. The number of clasts to count depends on the focus of the study, and the abundance of constituents of interest.

In summary and as a general rule, we recommend counting 200+ glassy juvenile grains to quantify the most abundant juvenile components (Fig. A1.2), and 400–500 grains if juvenile components with low abundances are to be studied. Even more grains are needed to be confident at the level of a percent or two. For the 5.7–4 mm (- 2.5 to - 2ϕ) fraction, these glassy juvenile grains can be counted by eye (Eychenne and Le Pennec 2012; Murch et al. 2019a) or under a binocular microscope (Ersoy et al. 2006). For the 0.71–0.5 mm (+ 0.5 to + 1ϕ) fraction, a binocular microscope is used. For both fractions, all glassy juvenile particles separated during basic componentry can first be classified, and then more can be separated from the remaining bulk fraction. If counting several hundred grains, the user can proceed in steps of 100 particles and compare the data between steps, to get an idea of the reproducibility of the results.

Juvenile particle selection and preparation for internal texture analysis (medium lapilli and coarse ash)

After detailed componentry of glassy juvenile particles, a subset is selected for mounting. For the medium lapilli fraction, ~ 15–20 representative particles are selected to make a polished thin section or polished epoxy grain mount, on which internal textures can be studied (Fig. A1.2). These lapilli should be well separated on the mount or thin section. For the coarse ash fraction, 50 representative juvenile particles are selected to manufacture a polished epoxy grain mount (Chapter 2), to be used for morphological and textural measurements.

Image analysis of cross-sectioned single particles (three fractions)

The standard shape and textural parameters to measure on images of cross-sectioned particles of the coarse ash fraction are presented in Appendix I. Recommended and optional steps related to the cross-sections (obtained through polished epoxy grain mounts and/or polished thin sections) of the medium lapilli, coarse ash and very fine ash fractions are presented here.

Crystallinity and vesicularity for the medium lapilli fraction (recommended)

For the medium lapilli fraction, the recommended textural parameters are 2D vesicularity and 2D crystallinity (Fig. A1.2). These are measured exactly as described in the paper for the coarse ash fraction, using the PASTA code. We do not recommend measuring morphology parameters for the lapilli, since it may not give information on primary fragmentation due to factors such as relaxation, aerodynamic drag, and modification during transport (Manga et al. 2011), etc.

Other shape measurements for the coarse ash fraction (optional)

For the coarse ash fraction, based on the acquired SEM images of particle cross-sections, additional morphometric parameters and particle outline characteristics can be measured if the user wishes. This can be particularly useful for comparison with existing studies. This includes the parameters proposed by Cioni et al. (2014), Leibrandt and Le Pennec (2015) or Schmith et al. (2017), which are for example obtained using PARTISAN (Dürig et al. 2019).

Morphology and textural parameters for the very fine ash fraction (recommended)

The dual-mounting procedure for the very fine ash fraction produces a polished epoxy grain mount and SEM images of the same particles' cross-sections. In the figure A1.1 flowchart, this is used only for basic componentry, so in Appendix I, we state that the polishing can be done quickly and that a pixel density of 4000 or 5000 pixels per particle is enough. But the polished epoxy grain mount can also be used for morphology and textural characterization of this size fraction (recommended). In this case, grinding and polishing should be done very carefully to preserve the particle shapes, and SEM-BSE imaging should be done with a pixel resolution of at least 10 000 pixels per particle (Chapter 2). As for the coarse ash fraction, we suggest using PASTA and PARTISAN (see the paper) on images from the very fine ash fraction to obtain the same morphological and textural parameters.

Internal textures: optional measurements

A range of optional measurements are possible to further quantify the internal textures of juvenile pyroclasts, for the medium lapilli and coarse ash fractions. The size of each vesicle and crystal can be measured, to obtain the raw areal, or stereologically calculated volume, vesicle size distribution, vesicle number density, crystal size distribution, crystal number density, etc. (e.g., Mangan et al. 1993; Klug and Cashman 1994; Higgins 2000; Polacci et al. 2001; Taddeucci et al. 2004; Sable et al. 2006; Shea et al. 2010; Murtagh et al. 2011; Stovall et al. 2011, 2012; Murtagh and White 2013; Pardo et al. 2014b). The shapes of vesicles and crystals can also be quantified. These measurements can be done in FOAMS (http://www.soest.hawaii.edu/GG/FACULTY/tshea/foams/foamsintro.html), ImageJ and associated macros, or other image analysis software. The CSDslice database (Morgan and Jerram 2006) and software CSD corrections (Higgins 2000) allow researchers to obtain 3D crystal shapes, 3D crystallinities and associated crystal-size distributions. For crystals in particular, measurements can be facilitated if elemental phase maps are available from EDS chemistry (Hornby et al. 2019). Vesicle size distribution and crystal size distribution can yield important insights into vesicle/crystal nucleation/growth processes, from the magma reservoirs to the surface.

Textural examination of the groundmass of juvenile pyroclasts can also help determine whether reheating, related to hot-state recycling during the eruption, might have taken place (D'Oriano et al. 2013, 2014).

Dual mounting for the very fine ash fraction

In the figure A1.1 flowchart, for the very fine ash fraction, 200+ particles are dual-mounted from the bulk fraction, including 100+ glassy juvenile grains. In the figure A1.2 flowchart, more particles are needed, since we now need 200 glassy juvenile grains for the 3D morphological classification (described below). Thus, enough of the bulk fraction should be mounted to get this number of glassy juvenile particles.

3D morphological classification of the very fine ash fraction (recommended)

The Fig. A1.2 flowchart calls for a step of 3D morphological classification of glassy juvenile grains from the very fine ash fraction. To clarify, the difference between 3D morphological classification and detailed componentry is that for the latter, glassy juvenile grains are classified according to all features observable by eye or with a binocular microscope, including shape but also color,

luster, alteration, etc. (see above). Because very fine ash is studied using SEM images from the carbon tape grain mount, rather than a binocular microscope, 3D particle shapes become the main observable features for this fraction. Hence, for very fine ash, detailed componentry of glassy juvenile particles is replaced by 3D morphological classification. The qualitative 3D work adds information on the third dimension, relative to the standard morphology parameter measurements on silhouettes. For example it provides insights into if a circularly shaped particle (in 2D) is actually spherical or ovoid, or if an angular particle is blocky or plate-like.

The goal is to classify the glassy juvenile clasts into distinct classes or categories based on their overall 3D shapes (e.g., Heiken and Wohletz 1985; Cioni et al. 2008; Andronico et al. 2014b; Jordan et al. 2014; Comida et al. 2017; Murch et al. 2019a). This exercise is partly user-dependent (i.e. subjective), but data from a single user should be internally consistent and should be very useful in comparing different samples. Fig. A1.10 shows typical particle shapes, for a range of magma compositions, vesicularities and fragmentation processes, to help users homogenize the way they classify particles. These SEM images are mostly for fine or very fine ash, but the same shape classes can also be applied to coarse ash.

Fluidal particles

A first group of particles, generally corresponding to the ‘achneliths’ of Walker and Croasdale (1971), has smooth surfaces influenced by surface tension. These fluidal particles might be variably vesicular inside (D’Oriano et al. 2011; Porritt et al. 2012; Pompilio et al. 2017; Clarke et al. 2019), but their external ‘skin’ tends to show few vesicles, except for the irregular variety. Particles of this group are generally thought to result from ductile (hydrodynamic) fragmentation of ultramafic to mafic magmas (Zimanowski et al. 2003; Stovall et al. 2011; Eychenne et al. 2015), although some felsic magmas can show fluidal behavior as well, suggesting anomalously low viscosity (Clarke et al. 2019; Murch et al. 2019b). Ductile fragmentation happens when the characteristic deformation times are greater than the viscous relaxation times (Zimanowski et al. 2003) and can be associated with a range of both magmatic and phreatomagmatic eruptive styles, in subaerial and submarine environments (e.g., Büttner et al. 2002; Dellino and Kyriakopoulos 2003; Stovall et al. 2011; Eychenne et al. 2015; Fitch et al. 2017; Murch et al. 2019a, 2019b; Dürig et al., 2020a, 2020b).

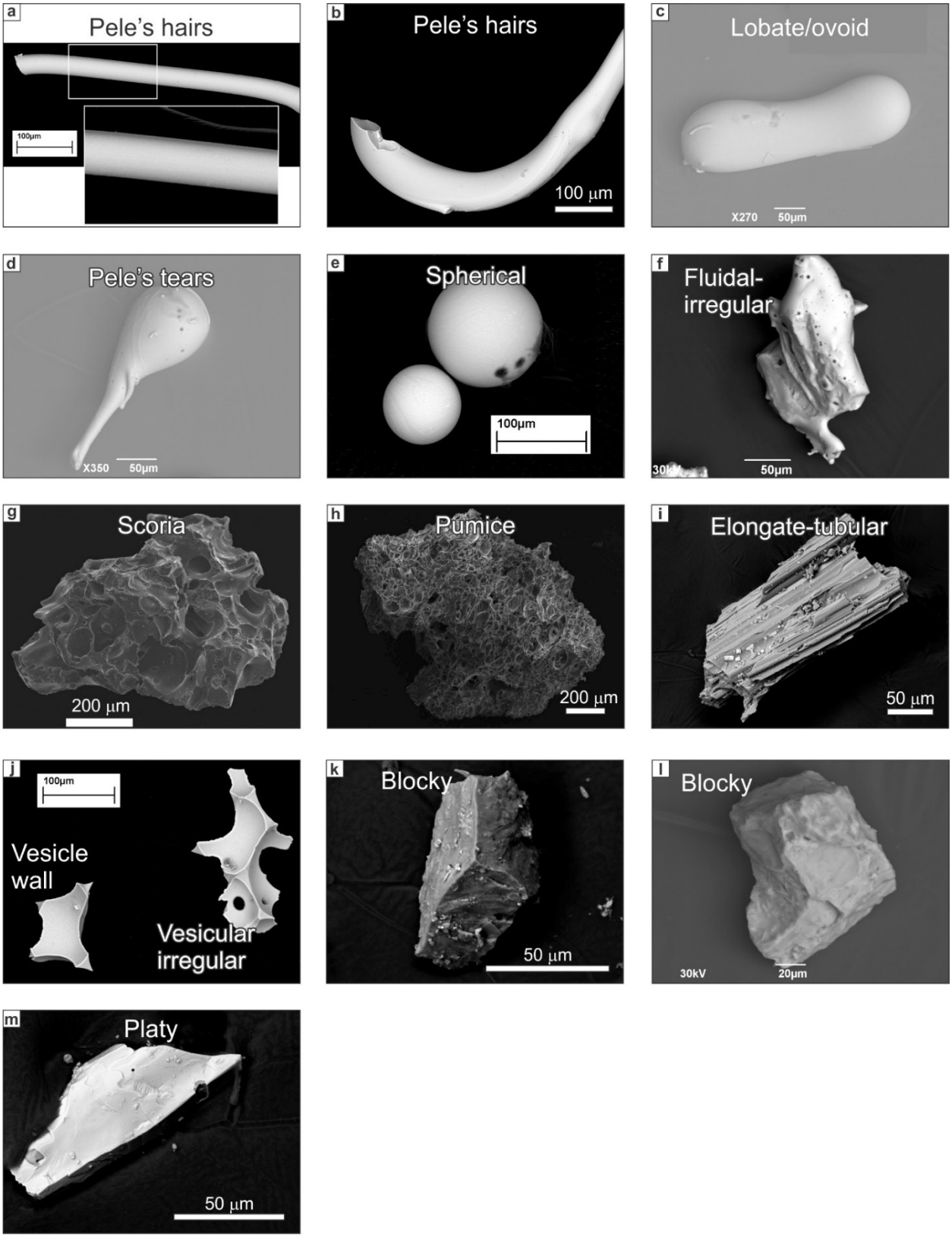
a
Pele's hairs
100µm
b
Pele's hairs
100 µm
c
Lobate/ovoid
X270
50µm
d
Pele's tears
X350
50µm
e
Spherical
100µm
f
Fluidal-
irregular
50µm
g
Scoria
200 µm
h
Pumice
200 µm
i
Elongate-tubular
50 µm
j
100µm
Vesicle
wall
Vesicular
irregular
k
Blocky
50 µm
l
Blocky
30kV
20µm
m
Platy
50 µm

Figure A1.10 (previous page): SEM images of some typical 3D particle shapes, mostly in the fine or very fine ash ranges, from both natural juvenile pyroclasts and products of magma fragmentation experiments at the University of Würzburg: (a)-(f) fluidal group; (g)-(j) vesicle-dominated group; (k)-(m) angular group. (a)-(b) Pele's hairs generated in blowout experiments with mafic magma and intermediate magma, respectively. (c) Lobate/ovoid particle generated in a blowout experiment with ultramafic magma. (d) Pele's tear obtained during the same experiment as for (c). (e) Spherical particle generated in a blowout experiment with mafic magma. (f) Fluidal-irregular particle from the mafic eruption of the Ukinrek maars (Alaska) in 1977. (g) Andesitic scoria from the 2006 Tungurahua eruption (Ecuador). (h) Felsic pumice from the same eruption. (i) Elongate-tubular particle from the submarine felsic Havre eruption of 2012. (j) Vesicle wall and vesicular-irregular particles from the Kilauea Iki (Hawaii) eruption of 1959 (mafic). (k) Blocky fragment from Havre (felsic). (l) Blocky fragment from Ukinrek (mafic). (m) Platy fragment from Havre (felsic).

- **Pele's hairs** are "long thin strands" of glass (Heiken and Wohletz 1985), mostly with diameters of 1–300 μm (Duffield et al. 1977), or sometimes thicker (Cannata et al. 2019); their surfaces are smooth to ribbed (Heiken 1974) (Figs. A1.10a, A1.10b; for other examples, see Heiken 1974's plates 7g and 13b and Cannata et al. 2019's Fig. 1);
- **Ovoid** particles are lobate to ovoid in shape (Fig. A1.10c; ovoids are sometimes grouped with tears, e.g. Porritt et al. 2012);
- **Pele's tears** are "tear-shaped pendants of basaltic glass" (Heiken and Wohletz 1985) (Fig. A1.10d; for other examples, see Porritt et al. 2012's Fig. 3c);
- **Spheres** are smooth spherical particles (Fig. A1.10e) (for other examples, see Heiken 1974's plate 8a; Jordan et al. 2014's Fig. 3, 2nd row);
- **Fluidal-irregular** particles have a smooth, largely continuous skin, but they are more irregular than the other types of fluidal particles, perhaps due to more visible vesicles. Also, not all of the particle surface necessarily needs to look fluidal for it to be classified this way (Murch et al. 2019a) (Fig. A1.10f; for other examples, see Heiken 1974's Plate 2a; Wohletz and Krinsley 1978's Fig. 1-8-3; Cioni et al. 2008's Fig. 4b top; D'Oriano et al. 2011's Fig. 2 left; Andronico et al. 2014b's Fig. 10a; Cioni et al. 2014's Fig. 3 bottom row; Murch et al. 2019a's Fig. 7g). The key feature is that at least part of the particle displays the continuous skin.

Vesicle-dominated particles

A second group of particles have shapes that are controlled by abundant broken vesicles, clearly visible on the particle exterior (Heiken 1974). We call this group "vesicle-dominated" because the bubbles control the overall particle shape and/or the details of the shape. These particles all lack the fluidal aspect (the smoothly curved 'skin') of the first group. This group includes (1) scoria, which is generally ultramafic to mafic; (2) pumice, which is generally intermediate to felsic

(although ‘pumice’ has been used for highly vesicular clasts from basaltic lava fountains in Hawaii, i.e. golden pumice, and for some clasts from the Grímsvötn 2004 eruption in Iceland; Jude-Eton et al. 2012); (3) elongate/tubular particles, again typical of more evolved magmas; (4) vesicle walls/shards, the more finely fragmented version of the first three types; and (5) vesicular-irregular particles.

- **Scoria** has abundant vesicles with walls thicker than that of pumice (Heiken and Wohletz 1985); these fragments are sometimes called spongy (Fig. A1.10g; for other examples, see D’Oriano et al. 2011’s Fig. 2 “spongy”; Cioni et al. 2011’s Fig. 7 “spongy”);
- **Pumice** has very abundant vesicles with thin walls (Heiken and Wohletz 1985) (Fig. A1.10h; for other examples, see Heiken 1974’s plate 20; D’Oriano et al. 2011’s Fig. 2 right);
- **Elongate-tubular** particles contain very long vesicles, and are also known as tube, or woody (Allen et al. 2010), pumice (Fig. A1.10i; for other examples see Heiken 1974’s plate 20; Cioni et al. 2011’s Fig. 7 “tubular”; Murch et al. 2019a’s Figs. 3c, 7k);
- **Vesicle walls**, also known as “bubble walls” or sometimes “glass shards”, are “characterized by highly concave outlines with smooth surfaces from large bounding vesicles” (Liu et al. 2017) (Fig. A1.10j); this includes Y-shaped particles (for other examples see Murtagh and White 2013’s Fig. 12a; Cashman and Rust 2016’s Fig. 11h);
- **Vesicular-irregular** is a poorly defined category for vesicular grains that do not fit in the previous categories (Fig. A1.10j); this includes the “light-colored, glassy, vesicular particles with sub-spherical bubbles and irregular shape” described at Etna by Andronico et al. (2014b) as well as the “vesicular particles of irregular shapes” documented from Eyjafjallajökull by Dellino et al. (2012, see their Fig. 4e).

Angular particles

A third group consists of particles with angular shapes, such as blocky and platy grains. Archetypical blocky and platy clasts have a low vesicularity (Wohletz 1983), but this is not part of the definition here, although such clasts will be easier to recognize if their vesicularity is moderate or less. These particles are produced by brittle fragmentation of magma with any composition (Büttner et al. 2002; Dürig et al. 2012a, 2012b, 2020a, 2020b; Fitch et al. 2017; Murch et al. 2019a). Angular particles can be produced by a variety of eruptive processes, including hyaloclastite formation (thermal granulation), formation of blocky peperite, phreatomagmatic fragmentation, and some explosive magmatic styles such as dome-shattering Vulcanian blasts

and basaltic activity at Etna ranging from “ash explosions” to strombolian activity (Skilling et al. 2002; Taddeucci et al. 2002, 2004; Dellino and Kyriakopoulos 2003; Andronico et al. 2009; Miwa et al. 2009; Dürig et al. 2012b, 2020a; Murtagh and White 2013; Polacci et al. 2019). Depending on the eruptive style and cooling rates, angular particles can have different internal textures; for example, in basalts, hyaloclastite should have glassy (sideromelane) textures (Schipper et al. 2011; White et al. 2015), phreatomagmatic particles can range from sideromelane to tachylite (Andronico et al. 2009), and blocky particles of magmatic origin at Etna are micro- to crypto-crystalline tachylite (Taddeucci et al. 2002, 2004; Polacci et al. 2019).

- **Blocky** particles are generally equant to sub-equant and feature “planar or curviplanar surfaces that intersect nearly at right angles” (Heiken and Wohletz 1985; Figs. A1.10k-l) (for other examples, see Heiken 1974’s plates 23a and 25a; Wohletz and Krinsley 1978’s Fig. 1-8-1; Taddeucci et al. 2004’s Fig. 3 lower left; Cioni et al. 2008’s Fig. 4c; Andronico et al. 2014b’s Fig. 10c);
- **Platy** particles are similar to blocky ones, but are plate-like instead of equant or sub-equant. When their vesicularity is low, platy particles can have “smooth surfaces and angular contours” (Dürig et al. 2012b; Fig. A1.10m). Some small platy particles may represent bubble wall shards (Wohletz 1983; Cashman and Rust 2016) (for other examples, see Pardo Villaveces 2012’s Fig. 4.9b; Dürig et al. 2012b’s Fig. 5, 4th row; Cashman and Rust 2016’s Fig. 11h; Murch et al. 2019a’s Fig. 7c).

Practical details

The appendix describes basic componentry of the very fine ash fraction based on SEM images of the polished epoxy grain mount (Fig. A1.4e). For 3D morphological classification of glassy juvenile particles, the counting method is essentially the same (e.g., manual point counting in JMicroVision) except that SEM images from the carbon tape grain mount are used. Only the particles identified as glassy juvenile fragments on the polished epoxy grain mount should be utilized for the 3D morphology study.

Quantitative shape analysis: alternative methods

As mentioned in Appendix I, methods other than the SEM can also be used to measure particle shapes, including micro-CT and automated particle analyzers. The challenge is that raw shape factors measured by different methods cannot be directly compared at present. In the future, it

might be possible to empirically ‘correct’ or ‘calibrate’ shape factors from different methods to make them comparable to a common standard.

Online Resource A1.2: Methodology steps templates

The templates will be available in the final version of the journal manuscript.

Online Resource A1.3: Sieving of pyroclastic deposits

Sieving is standard in the workflows. Pyroclastic deposits require more care than ‘normal’ sediments when sieving, so we present recommendations for best practices here.

Blocks and bombs

For very coarse pyroclastic deposits containing blocks and bombs, some of the grainsize analysis must be done in the field, by measuring individual fragments, by using coarse sieves in the field (Cas and Wright 1987; Bernard et al. 2014; Houghton and Carey 2015; Scarpati et al. 2016) or from photos of the outcrops (Gurioli et al. 2012; Bernard et al. 2014). Lapilli and ash (see Table A1.1 for grain size terms) are then taken back to the laboratory for further analysis.

One obvious advantage of dealing with blocks and bombs (and perhaps even some lapilli) in the field is to reduce sample weight for transportation back to the laboratory. A more subtle advantage is that eliminating the largest clasts before shipping may reduce secondary breakage during transport (E.P. Fitch, written commun., 2021).

Drying and splitting

In the laboratory, samples are first dried in an oven, typically at 105°C for up to 48 hours (Carter and Gregorich 2008). Then the sample is split (e.g., Andronico et al. 2014) until the starting mass is 500 g or less, to prevent clogging the sieves. For the ash fraction, we recommended to sieve no more than 50–100 g.

Manual dry sieving

Sieving can be destructive, especially for vesicular clasts and for particles with complex or elongate shapes. Gentle manual dry sieving is the least disruptive technique (e.g., Walker 1971; Barberi et al. 1989; Dellino and La Volpe 1995; Parfitt 1998; Gaunt et al. 2016; Avery et al. 2017;

Liu et al. 2017; Schmith et al. 2018; Murch et al. 2019), and motorized sieve shakers should be avoided.

Half-ϕ sieves (Table A1.1) give more detailed grain size information than full-ϕ sieves, and half-ϕ size fractions are easier to mount in epoxy and polish to the middle of grains. But we again stress that manual sieving must be done very gently to minimize breakage and potential morphological modification. More work is needed to check the impact of various sieving techniques on breakage and particle morphologies.

The manual sieving procedure is typically as follows. Use one sieve at a time (i.e. one sieve plus the pan), down to 2 mm (- 1ϕ), for no more than three minutes, to minimize breakage (Jordan et al. 2016). This can be continued down to 63 μm (+ 4ϕ). Alternatively, the 2 mm (- 1ϕ) to 63 μm (+ 4ϕ) sieves can be used as a column (Fig. A1.11a).

Cleaning the sieves

To minimize cross-contamination between samples, sieves should be carefully cleaned using either high pressure air and picks and/or by ultrasonic cleaning in distilled water (with ultrasonic soap) for sieves in the 0.5 mm (+ 1ϕ) to 63 μm (+ 4ϕ) range (Merkus 2009) (Fig. A1.11b). Alternatively, disposable sieve meshes can be used for the fine sieves (Liu et al. 2017), if the budget allows.

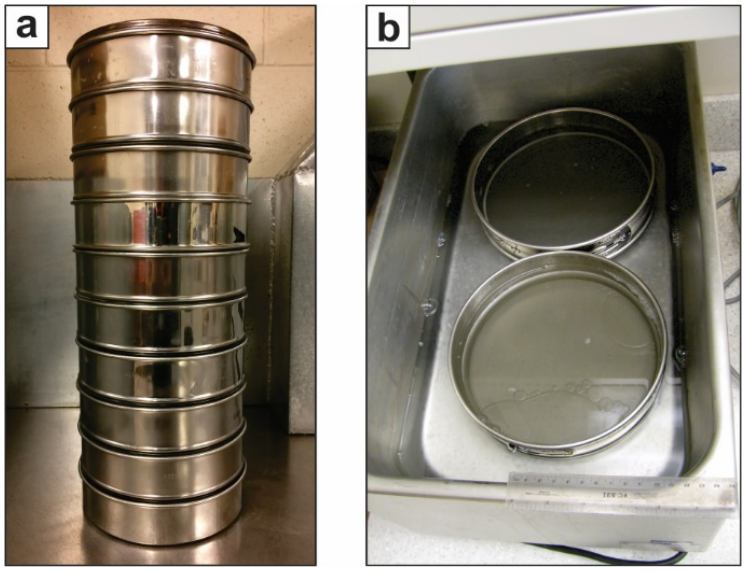

Figure A1.11: Sieving and cleaning the sieves. (a) Column of full-ϕ sieves from - 4ϕ to + 4ϕ. A column of half-ϕ sieves will yield a more detailed grainsize distribution. (b) Cleaning the finer sieves in an ultrasonic bath, after each sample is sieved.

Dealing with aggregates

Particle aggregates (e.g. armored and accretionary lapilli, or aggregates formed during sample drying) are problematic for fragmentation studies. These aggregates mask the properties of the constituent ash particles. One option to retrieve the individual ash particles is to attempt disaggregation in an ultrasonic bath with distilled water (not acid, see Cioni et al. 1992). Sodium hexametaphosphate, a deflocculant commonly used for microfossil preparation, can be useful (Casalbore et al. 2010). The sample can then be dried in an oven at ~ 60°C, checked under a binocular stereo microscope, and re-sieved. This process can be repeated until disaggregation is complete, noting that non-destructive separation of highly cemented aggregates may not be achievable.

Online Resource A1.4: Dual mounting of the very fine ash fraction

Carbon tape grain mount

For the 88–63 µm (+ 3.5 to + 4ϕ) fraction, a carbon tape grain mount (CTGM) is the first stage of the dual mounting procedure (Fig. A1.1). For preparing this CTGM, we offer four particle transfer methods: three quick ones and a slow one.

Preparing the mounting surface

All methods start with a circular double-sided carbon tape being stuck onto an aluminum disk (Fig. A1.5a). The top will be covered by a non-stick paper circle, on which a smaller circle is drawn, corresponding to the internal diameter of the ring form to be used later for the polished epoxy grain mount (Fig. A1.5b). This ensures that there will be no particles mounted near the periphery of the carbon tape later. The non-stick paper circle is then peeled off from the carbon tape (Fig. A1.5c).

Quick particle transfer methods

In the three quick methods, the marked non-stick paper circle is placed at the bottom of a petri dish, and a subsample from the bulk size fraction is spread evenly over it. The distribution of particles can be quickly evened out under the binocular microscope, using a fine brush or a needle. This is the point where the three quick methods differ. In the first one, the sticky (carbon tape) side of the aluminum disc is very gently pressed on the sample (Fig. A1.5d). The disk is then turned back upright and the paper circle taken off. There may be some particles touching

each other, which is a nuisance when performing image analysis, but they can be separated manually with image editing software. It may be prudent to mount more than the minimum number of grains if using this method, to make sure that there are enough non-overlapping grains to work with.

In the second quick method, a moistened thumb (big finger) is used to transfer the particles from the non-stick circle to the sticky side of the carbon tape, making sure to press down very gently to avoid crushing fragile grains. The gesture can be repeated twice on the same position to get a concentrated mount, or applied on adjacent areas of the carbon tape (Fig. A1.5e). Wearing a latex/nitrile glove will prevent finger marks to be left on the tape.

The third quick method involves a fine-tipped paintbrush (E.P. Fitch, written commun., 2021). The paintbrush bristles are cut at a slight angle, so that grains can be easily picked up from the petri dish. The grains are then deposited on the carbon tape “with a gentle angled press of the paintbrush (…) along the cut edge”. The maneuver is repeated a few times, until enough grains have been transferred. It is important to clean the brush thoroughly to avoid contamination between samples. This involves “tapping it over a trash can, with occasional blowing”, and then the cleanliness of the brush is checked under the binocular microscope.

Grain-by-grain transfer method

For the slow method, particles are transferred and deposited one by one onto the carbon tape, under the binocular microscope. The transfer can be done with a metallic probe or a wooden toothpick. Moistening the tool with water can help. This method is ideal to get good particle separation but still mount the particles in a restricted area, which allows fewer SEM images for the same number of grains.

Final steps

With all mounting methods, a linear object with a thickness of ~ 50 µm or more is added to the carbon tape grain mount, to be used as a “horizontal” reference later, during imaging. For example, a long prism of cork, which can be cut with a sharp knife, has been trialed successfully (Fig. A1.5e). Finally, the CTGM is coated with a very thin layer of carbon or gold, under a vacuum. It is then ready to take to the SEM to image particles (Fig. A1.5f).

Polished epoxy grain mount

After SEM imaging of 3D grains at the SEM, the CTGM can be transformed into a polished epoxy grain mount (PEGM). This is the second stage of the dual mounting procedure for the very fine ash fraction.

First, the plastic ring form is glued on the side where particles are present (the carbon tape should still be sticky enough to do this). This ring form should have the same external diameter as the aluminum stub. Then the epoxy is poured (Fig. A1.5g). It is important to apply a lot of weight on top of the ring form during curing to make sure that epoxy does not penetrate under it. After curing, the assembly can be turned upside down (Fig. A1.5h). The aluminum stub and carbon tape are detached (Fig. A1.5i). This may leave a residue, which can be cleaned off with a soft paper tissue moistened with acetone. The epoxy mount is then ready for grinding and polishing, the aim being to expose the center of the smallest particle, which means removing 32 µm of ring form, epoxy and particles. Detailed instructions on this portion of the procedure are available in Chapter 2 (Note that for the Fig. A1.1 flowchart, the polishing does not have to be extremely careful for this particular mount, since only the inside of the particles will be studied, not the outlines, as opposed to the mount of the coarse ash fraction.) This leaves a finished polished epoxy grain mount, which can be coated with carbon (Fig. A1.5j) and taken back to the SEM for imaging (Fig. A1.5k). The raw SEM images of the polished grain mount should constitute mirror images of the carbon tape grain mount.

Online Resource A1.5: SEM imaging settings

Coarse ash fraction

For the polished epoxy grain mount of the 0.71–0.5 mm (+ 0.5 to + 1ϕ) fraction, the SEM is used in backscatter mode. Each particle must contain about 20 000 pixels (see Appendix I and Chapter 2). The following settings have been successfully employed at INRS to obtain 20 000 pixels per particle: 68x magnification, 2048x1536 image resolution. Any combination of magnification and resolution that yields 20 000 pixels per particle is acceptable.

Greyscales for glass, crystals, etc. should be consistent between images within the same sample. Any auto-brightness/contrast function should be disabled so that brightness/contrast are unchanged from image to the next. Any drift in grey levels over time can be compensated by keeping the first image of a sample opened for reference.

Another important factor is the SEM scan speed, which must be set to produce high-quality images, even though this increases acquisition time, in order to optimize the contrast of the image and be able to distinguish small features such as microlites.

Very fine ash fraction

For the 88–63 μm (+ 3.5 to + 4ϕ) fraction, there is a dual mounting procedure (see Appendix I). This means that each mount is imaged twice: once as a carbon tape grain mount (CTGM), and later as a polished epoxy grain mount (PEGM). The backscatter mode of the SEM can be employed in both states.

If following only the standard steps (Fig. A1.1), more pixels per particle are required in the CTGM state, to allow identification of interactive particles (see the paper). For example, 450x magnification and 2048x1556 resolution yields ~ 16 000 pixels per particle in the CTGM state.

Then in the PEMG state, the same magnification should be used to produce a mirror image, but a lower resolution is acceptable to save time, since the only aim is basic componentry (and juvenile identification) in the flowchart with only the standard steps. For the 450x magnification mentioned above, 1024x768 resolution yields ~ 4000 pixels per particle for the PEGM.

References

Agustín-Flores J, Németh K, Cronin SJ, Lindsay JM, Kereszturi G (2015) Construction of the North Head (Maungauika) tuff cone: a product of Surtseyan volcanism, rare in the Auckland Volcanic Field, New Zealand. Bull Volc 77:article 11

Allen SR, McPhie J (2000) Water-settling and resedimentation of submarine rhyolitic pumice at Yali, eastern Aegean, Greece. J Volcanol Geotherm Res 95:285–307

Allen SR, Fiske RS, Tamura Y (2010) Effects of water depth on pumice formation in submarine domes at Sumisu, Izu-Bonin arc, western Pacific. Geology 38:391–394

Alvarado GE, Mele D, Dellino P, de Moor JM, Avard G (2016) Are the ashes from the latest eruptions (2010–2016) at Turrialba volcano (Costa Rica) related to phreatic or phreatomagmatic events? J Volcanol Geotherm Res 327:407–415

Andronico D, Cristaldi A, Del Carlo P, Taddeucci J (2009) Shifting styles of basaltic explosive activity during the 2002–03 eruption of Mt. Etna, Italy. J Volcanol Geotherm Res 180:110–122

Andronico D, Scollo S, Cristaldi A, Lo Castro MD (2014a) Representivity of incompletely sampled fall deposits in estimating eruption source parameters: a test using the 12–13 January 2011 lava fountain deposit from Mt. Etna volcano, Italy. Bull Volc 76:article 861

Andronico D, Scollo S, Lo Castro MD, Cristaldi A, Lodato L, Taddeucci J (2014b) Eruption dynamics and tephra dispersal from the 24 November 2006 paroxysm at South-East Crater, Mt Etna, Italy. J Volcanol Geotherm Res 274:78–91

Andronico D, Taddeucci J, Cristaldi A, Miraglia L, Scarlato P, Gaeta M (2013) The 15 March 2007 paroxysm of Stromboli: video-image analysis, and textural and compositional features of the erupted deposit. Bull Volc 75:733

Andronico D, Di Roberto A, De Beni E, Behncke B, Bertagnini A, Del Carlo P, Pompilio M (2018) Pyroclastic density currents at Etna volcano, Italy: The 11 February 2014 case study. J Volcanol Geotherm Res 357:92–105

Austin-Erickson A, Büttner R, Dellino P, Ort MH, Zimanowski B (2008) Phreatomagmatic explosions of rhyolitic magma: experimental and field evidence. J Geophys Res 113:paper B11201

Austin-Erickson A, Ort MH, Carrasco-Núñez G (2011) Rhyolitic phreatomagmatism explored: Tepexitl tuff ring (Eastern Mexican Volcanic Belt). J Volcanol Geotherm Res 201:325–341

Avery MR, Panter KS, Gorsevski PV (2017) Distinguishing styles of explosive eruptions at Erebus, Redoubt and Taupo volcanoes using multivariate analysis of ash morphometrics. J Volcanol Geotherm Res 332:1–13

Bagheri GH, Bonadonna C, Manzella I, Vonlanthen P (2015) On the characterization of size and shape of irregular particles. Powder Tech. 270:141–153.

Bain AA, Kendrick JE, Lamur A, Lavallée Y, Calder ES, Cortés JA, Cortés GP, Gómez Martinez D, Torres RA (2021) Micro-textural controls on magma rheology and vulcanian explosion cyclicity. Front Earth Sci 8:611320

Barberi F, Cioni R, Rosi M, Santacroce R, Sbrana A, Vecci R (1989) Magmatic and phreatomagmatic phases in explosive eruptions of Vesuvius as deduced by grain-size and component analysis of the pyroclastic deposits. J Volcanol Geotherm Res 38:287–307

Barberi F, Bertagnini A, Landi P, Principe C (1992) A review on phreatic eruptions and their precursors. J Volcanol Geotherm Res 52:231–246

Beget JE, Larsen JF, Neal CA, Nye CJ, Schaefer JR (2005) Preliminary volcano-hazard assessment for Okmok volcano, Umnak Island Alaska. *In*: Alaska Department of Natural Resources, Division of Geological & Geophysical Surveys, Report of Investigations 2004-3

Bernard B (2013) Homemade ashmeter: a low-cost, high-efficiency solution to improve tephra field-data collection for contemporary explosive eruptions. J Appl Volc 2:article 1

Bernard J, Le Pennec JL (2016) The milling factory: Componentry-dependent fragmentation and fines production in pyroclastic flows. Geology 44:907–910

Bernard J, Kelfoun K, Le Pennec JL, Vallejo Vargas S (2014) Pyroclastic flow erosion and bulking processes: comparing field-based vs. modeling results at Tungurahua volcano, Ecuador. Bull Volc 76:article 858

Bonadonna C, Houghton BF (2005) Total grain-size distribution and volume of tephra-fall deposits. Bull Volc 67:441–456

Bonadonna C, Cioni R, Costa A, et al. (2016) MeMoVolc report on classification and dynamics of volcanic explosive eruptions. Bull Volc 78:article 84

Bonadonna C, Genco R, Gouhier M, Pistolesi M, Cioni R, Alfano F, Hoskuldsson A, Ripepe M (2011) Tephra sedimentation during the 2010 Eyjafjallajökull eruption (Iceland) from deposit, radar, and satellite observations. J Geophys Res Solid Earth 116(B12202)

Brand BD, Gravley DM, Clarke AB, Lindsay JM, Bloomberg SH, Agustin-Flores J, Németh K (2014) A combined field and numerical approach to understanding dilute pyroclastic density current dynamics and hazard potential: Auckland Volcanic Field, New Zealand. J Volcanol Geotherm Res 276:215–232

Buckland HM, Eychenne J, Rust AC, Cashman KV (2018) Relating the physical properties of volcanic rocks to the characteristics of ash generated by experimental abrasion. J Volcanol Geotherm Res 349:335–350

Bursik M, Kuehn S, Pouget S, Wallace K, et al. (2015) Tephra 2014: summary and consensus document; Appendix I – Checklist for tephra collection. Downloaded from https://vhub.org/resources/3860/supportingdocs on December 3, 2018

Bustillos J, Romero JE, Troncoso L, Guevara A (2016) Tephra fall at Tungurahua volcano (Ecuador) – 1999–2014: An example of tephra accumulation from a long-lasting eruptive cycle. Geofis Intl 55:55–67

Büttner R, Dellino P, Zimanowski B (1998) Physics of thermohydraulic explosions. Phys Rev E 57, 5726–5729

Büttner R, Dellino P, Zimanowski B (1999) Identifying magma-water interaction from the surface features of ash particles. Nature 401:688–690

Büttner R, Dellino P, La Volpe L, Lorenz V, Zimanowski B (2002) Thermohydraulic explosions in phreatomagmatic eruptions as evidenced by the comparison between pyroclasts and products from Molten Fuel Coolant Interaction experiments. J Geophys Res 107:Art. 2277

Cannata CB, De Rosa R, Donato P, Donato S, Lanzafame G, Mancini L, Houghton BF (2019) First 3D imaging characterization of Pele's hair from Kilauea volcano (Hawaii). Sci Rep 9:1711

Caracciolo A, Gurioli L, Marianelli P, Bernard J, Harris AJL (2021) Textural and chemical features of a "soft" plug emitted during Strombolian explosions: A case study from Stromboli volcano. Earth Planet Sci Lett 559:116761

Carey S, Sparks RSJ (1986) Quantitative models of the fallout and dispersal of tephra from volcanic eruption columns. Bull Volc 48:109–125

Carter MR, Gregorich EG (2008) Soil sampling and methods of analysis, second edition. Canadian Society of Soil Science, Taylor & Francis Group

Cas RAF, Wright JV (1987) Volcanic successions, modern and ancient. Allen & Unwin, London, 528 p.

Casalbore D, Romagnoli C, Chiocci F, Frezza V (2010) Morpho-sedimentary characteristics of the volcaniclastic apron around Stromboli volcano (Italy). Marine Geol 269:132–148

Cashman KV, Scheu B (2015) Magmatic fragmentation. *In*: Sigurdsson H, Houghton B, McNutt SR, Rymer H, Stix J (eds) Encyclopedia of Volcanoes, Second edition. Academic Press, London, pp 459–471

Cashman K, Rust A (2016) Volcanic ash: Generation and spatial variations. *In*: Mackie S, Cashman K, Ricketts H, Rust A, Watson M (eds) Volcanic Ash. Elsevier, pp 5–22

Chamberlain KJ, Barclay J, Preece K, Brown RJ, Davidson JP (2016) Origin and evolution of silicic magmas at ocean islands: Perspectives from a zoned fall deposit on Ascension Island, South Atlantic. J Volcanol Geotherm Res 327:349–360

Cioni R, Sbrana A, Vecci R (1992) Morphologic features of juvenile pyroclasts from magmatic and phreatomagmatic deposits of Vesuvius. J Volcanol Geotherm Res 51:61–78

Cioni R, Sulpizio R, Garruccio N (2003) Variability of the eruption dynamics during a Subplinian event: the Greenish Pumice eruption of Somma–Vesuvius (Italy). J Volcanol Geotherm Res 124:89–114

Cioni R, Bertagnini A, Santacroce R, Andronico D (2008a) Explosive activity and eruption scenarios at Somma-Vesuvius (Italy): Towards a new classification scheme. J Volcanol Geotherm Res 178:331–346

Cioni R, D'Oriano C, Bertagnini A (2008b) Fingerprinting ash deposits of small scale eruptions by their physical and textural features. J Volcanol Geotherm Res 177:277-287

Cioni R, Bertagnini A, Andronico D, Cole PD, Mundula F (2011) The 512 AD eruption of Vesuvius: complex dynamics of a small scale subplinian event. Bull Volc 73:789–810

Cioni R, Pistolesi M, Bertagnini A, Bonadonna C, Hoskuldsson A, Scateni B (2014) Insights into the dynamics and evolution of the 2010 Eyjafjallajökull summit eruption (Iceland) provided by volcanic ash textures. Earth Planet Sci Lett 394:111–123

Clarke B, Calder ES, Dessalegn F, Fontijn K, Cortés JA, Naylor M, Butler I, Hutchison W, Yirgu G (2019) Fluidal pyroclasts reveal the intensity of peralkaline rhyolite pumice cone eruptions. Nat Commun 10:article 2010

Colo' L, Ripepe M, Gurioli L, Harris AJL (2020) Fragmentation processes during strombolian explosions revealed using particle size distribution mapping. Front Earth Sci 8:356

Colombier M, Wadsworth FB, Gurioli L, Scheu B, Kueppers U, Di Muro A, Dingwell DB (2017a) The evolution of pore connectivity in volcanic rocks. Earth Planet Sci Lett 462:99–109

Colombier M, Gurioli L, Druitt TH, Shea T, Boivin P, Miallier D, Cluzel N (2017b) Textural evolution of magma during the 9.4-ka trachytic explosive eruption at Kilian Volcano, Chaîne des Puys, France. Bull Volc 79:article 17

Comida PP, Ross P-S, Zimanowski B, Büttner R (2017) Artificial juvenile pyroclasts from wet and dry "eruptions": impact of magma composition on grain sizes and particle shapes. IAVCEI 2017, Portland, Oregon, USA

Comida PP, Ross P-S, Lefebvre N, Zimanowski B, Büttner R (2018) Phreatomagmatic versus magmatic fragmentation: Insights from juvenile particle analysis. Cities on Volcanoes 10, Naples, Italy

Colucci S, Palladino DM, Mulukutla GK, Proussevitch AA (2013) 3-D reconstruction of ash vesicularity: Insights into the origin of ash-rich explosive eruptions. J Volcanol Geotherm Res 255:98–107

Costa A, Pioli L, Bonadonna C (2016) Assessing tephra total grain-size distribution: Insights from field data analysis. Earth Planet Sci Lett 443:90–107

Deardorff N, Cashman K (2017) Rapid crystallization during recycling of basaltic andesite tephra: timescales determined by reheating experiments. Sci Rep 7:1–8

Dellino P, La Volpe L (1995) Fragmentation versus transportation mechanisms in the pyroclastic sequence of Monte Pilato-Rocche Rosse (Lipari, Italy). J Volcanol Geotherm Res 64:211–231

Dellino P, La Volpe L (1996) Image processing analysis in reconstructing fragmentation and transportation mechanisms of pyroclastic deposits. The case of Monte Pilato-Rocche Rosse eruptions, Lipari (Aeolian islands, Italy). J Volcanol Geotherm Res 71:13–29

Dellino P, Kyriakopoulos K (2003) Phreatomagmatic ash from the ongoing eruption of Etna reaching the Greek island of Cefalonia. J Volcanol Geotherm Res 126:341–345

Dellino P, Isaia R, La Volpe L, Orsi G (2001) Statistical analysis of textural data from complex pyroclastic sequences: implications for fragmentation processes of the Agnano-Monte Spina Tephra (4.1 ka), Phlegraean Fields, southern Italy. Bull Volc 63:443–461

Dellino P, Gudmundsson MT, Larsen G, Mele D, Stevenson JA, Thordarson T, Zimanowski B (2012) Ash from the Eyjafjallajökull eruption (Iceland): Fragmentation processes and aerodynamic behavior. J Geophys Res Solid Earth 117:B00C04

Devine JD, Gardner JE, Brack HP, Layne GD, Rutherford MJ (1995) Comparison of microanalytical methods for estimating H2O contents of silicic volcanic glasses, Am Mineral 80:319-328

Dioguardi F, Mele D, Dellino P, Dürig T (2017) The terminal velocity of volcanic particles with shape obtained from 3D X-ray microtomography. J Volcanol Geotherm Res 329:41–53

D’Oriano C, Bertagnini A, Pompilio M (2011) Ash erupted during normal activity at Stromboli (Aeolian Islands, Italy) raises questions on how the feeding system works. Bull Volc 73:471–477

D’Oriano C, Pompilio M, Bertagnini A, Cioni R, Pichavant M (2013) Effects of experimental reheating of natural basaltic ash at different temperatures and redox conditions. Contrib Min Pet 165:863–883

D'Oriano C, Bertagnini A, Cioni R, Pompilio M (2014) Identifying recycled ash in basaltic eruptions. Sci Rep 4:article 5851

Doubik P, Hill BE (1999) Magmatic and hydromagmatic conduit development during the 1975 Tolbachik Eruption, Kamchatka, with implications for hazards assessment at Yucca Mountain, NV. J Volcanol Geotherm Res 91:43–64

Duffield WA, Gibson E, Heiken G (1977) Some characteristics of Pele’s hair. J Res US Geol Surv 5:93-10

Dürig T, Zimanowski B (2012) “Breaking news” on the formation of volcanic ash: Fracture dynamics in silicate glass. Earth Planet. Sci Lett 335:1–8

Dürig T, Bowman HM (2021) lsschmidt/PARTISAN (Version 2.0, March 10, 2021), https://github.com/lsschmidt/PARTISAN/tree/v2.0, DOI 10.5281/zenodo.4593833

Dürig T, Sonder I, Zimanowski B, Beyrichen H, Büttner R (2012a) Generation of volcanic ash by basaltic volcanism. J Geophys Res 117, B01204.

Dürig T, Mele D, Dellino P, Zimanowski B (2012b) Comparative analyses of glass fragments from brittle fracture experiments and volcanic ash particles. Bull Volc 74:691–704

Dürig T, Bowman MH, White JDL, Murch A, Mele D, Verolino A, Dellino P (2019) PARTIcle Shape ANalyzer PARTISAN – an open source tool for multi-standard two-dimensional particle morphometry analysis. Ann Geophys-Italy 61: AC31, DOI:10.4401/ag-7865

Dürig T, Schmidt LS, White JDL, Bowman MH (2020a) DendroScan: an open source tool to conduct comparative statistical tests and dendrogrammatic analyses on particle morphometry. Sci Rep 10: article 21682

Dürig T, White JDL, Murch AP, Zimanowski B, Büttner R, Mele D, Dellino P, Carey RJ, Schmidt LS, Spitznagel N (2020b) Deep-sea eruptions boosted by induced fuel–coolant explosions. Nature Geosci 13:498–503

Dürig T, White JDL, Zimanowski B, Büttner R, Murch A, Carey RJ (2020c) Deep-sea fragmentation style of Havre revealed by dendrogrammatic analyses of particle morphometry. Bull Volc 82: article 67

Dürig T, Ross P-S, Dellino P, White JDL, Mele D, Comida PP (2021) A review of statistical tools for morphometric analysis of juvenile pyroclasts. Bull Volc 83:79

Engwell S, Eychenne J (2016) Contribution of fine ash to the atmosphere from plumes associated with pyroclastic density currents. *In*: Shona M, Cashman K, Ricketts H, Rust A, Watson M (eds) Volcanic Ash, Elsevier, pp 67–85

Ersoy O, Chinga G, Aydar E, Gourgaud A, Evren Cubukcu H, Ulusoy I (2006) Texture discrimination of volcanic ashes from different fragmentation mechanisms: A case study, Mount Nemrut stratovolcano, eastern Turkey. Computers & Geosciences 32:936–946

Eychenne J, Le Pennec J-L (2012) Sigmoidal particle density distribution in a subplinian scoria fall deposit. Bull Volc 74:2243–2249

Eychenne J, Le Pennec J.-L, Troncoso L, Gouhier M, Nedelec J-M (2012) Causes and consequences of bimodal grain-size distribution of tephra fall deposited during the August 2006 Tungurahua eruption (Ecuador). Bull Volc 74:187–205

Eychenne J, Houghton BF, Swanson DA, Carey RJ, Swavely L (2015) Dynamics of an open basaltic magma system: The 2008 activity of the Halemaʻumaʻu Overlook vent, Kīlauea Caldera. Earth Planet Sci Lett 409:49–60

Freret-Lorgeril V, Donnadieu F, Eychenne J, Soriaux C, Latchimy T (2019) In situ terminal settling velocity measurements at Stromboli volcano: Input from physical characterization of ash. J Volcanol Geotherm Res 374:62-79

Fisher RV, Schmincke H-U (1984) Pyroclastic Rocks. Springer-Verlag, Berlin, 472 p.

Fitch EP, Fagents SA (2020) Characteristics of rootless tephra emplaced by high-energy lava–water explosions. Bull Volc 82:article 62

Fitch EP, Fagents SA, Thordarson T, Hamilton CW (2017) Fragmentation mechanisms associated with explosive lava–water interactions in a lacustrine environment. Bull Volc 79:12

Formenti Y, Druitt T (2003) Vesicle connectivity in pyroclasts and implications for the fluidisation of fountain-collapse pyroclastic flows, Montserrat (West Indies). Earth Planet Sci Lett 214:561–574

Gardner JE, Thomas RME, Jaupart C, Tait S (1996) Fragmentation of magma during Plinian volcanic eruptions. Bull Volc 58:144–162

Gaunt HE, Bernard B, Hidalgo S, Proaño A, Wright H, Mothes P, Criollo E, Kueppers U (2016) Juvenile magma recognition and eruptive dynamics inferred from the analysis of ash time series: The 2015 reawakening of Cotopaxi volcano. J Volcanol Geotherm Res 328:134–146

Genareau K, Mulukutla GK, Proussevitch AA, Durant AJ, Rose WI, Sahagian DL (2013) The size range of bubbles that produce ash during explosive volcanic eruptions. Journal of Applied Volcanology 2:article 4

Giordano D, Russell JK, Dingwell DB (2008) Viscosity of magmatic liquids: A model. Earth Planet Sci Lett 271:123-134

Goldstein JI, Newbury DE, Michael JR, Ritchie NW, Scott, JHJ, Joy, DC (2017) Scanning electron microscopy and X-ray microanalysis. Springer.

Graettinger AH, Valentine GA (2017) Evidence for the relative depths and energies of phreatomagmatic explosions recorded in tephra rings. Bull Volc 79:article 88

Graettinger AH, Skilling I, McGarvie D, Höskuldsson Á (2013) Subaqueous basaltic magmatic explosions trigger phreatomagmatism: A case study from Askja, Iceland. J Volcanol Geotherm Res 264:17–35

Gurioli L, Harris AJL, Houghton BF, Polacci M, Ripepe M (2008) Textural and geophysical characterization of explosive basaltic activity at Villarrica volcano. J Geophys Res Solid Earth 113, doi 10.1029/2007JB005328

Gurioli L, Sulpizio R, Cioni R, Sbrana A, Santacroce R, Luperini W, Andronico D (2010) Pyroclastic flow hazard assessment at Somma–Vesuvius based on the geological record. Bull Volc 72:1021–1038

Gurioli L, Zanella E, Gioncada A, Sbrana A (2012) The historic magmatic-hydrothermal eruption of the Breccia di Commenda, Vulcano, Italy. Bull Volc 74:235–1254

Gurioli L, Andronico D, Bachelery P, Balcone-Boissard H, Battaglia J, Boudon G, Burgisser A, Burton MR, Cashman K, Cichy S, Cioni R, et al. (2015) MeMoVolc consensual document: a review of cross-disciplinary approaches to characterizing small explosive magmatic eruptions. Bull Volc 77:49

Gurioli L, Di Muro A, Vlastélic I, Moune S, Thivet S, et al. (2018) Integrating field, textural, and geochemical monitoring to track eruption triggers and dynamics: a case study from Piton de la Fournaise. Solid Earth 9:431–455

Harris AJL, Battaglia J, Donnadieu F, Gurioli L, Kelfoun K, Labazuy P, Sawyer G, Valade S, Bombun M, Barra V, Delle Donne D, Lacanna G (2013) Full bandwidth remote sensing for total parameterization of volcanic plumes. Eos 94:321–322

Hayward C (2011) High spatial resolution electron probe microanalysis of tephras and melt inclusions without beam-induced chemical modification. The Holocene 22:119–125

Heiken G (1972) Morphology and petrography of volcanic ashes. Geol Soc Am Bull 83:1961–1988

Heiken G (1974) An atlas of volcanic ash. Smithsonian Contributions to the Earth Sciences 12, 101 p.

Heiken G, Wohletz K (1985) Volcanic ash. University of California Press, Berkeley, California, 246 p.

Heiken G, Wohletz K (1987) Tephra deposits associated with silicic domes and lava flows. In: Fink JH (ed) The Emplacement of Silicic Domes and Lava Flows. Geol Soc Am, Special Paper 212, pp 55–76

Heiken G, Wohletz K (1991) Fragmentation processes in explosive volcanic eruptions. *In*: Fisher RV, Smith GA (eds) Sedimentation in volcanic settings. Society of Economic Paleontologists and Mineralogists, Special Publication 45, pp 19–26

Higgins MD (2000) Measurement of crystal size distributions. American Mineralogist 85:1105–1116

Hornby AJ, Lavallée Y, Kendrick JE, Rollinson G, Butcher AR, Clesham S, Kueppers U, Cimarelli C, Chigna G (2019) Phase partitioning during fragmentation revealed by QEMSCAN Particle Mineralogical Analysis of volcanic ash. Sci Rep 9:126

Houghton B, Hackett W (1984) Strombolian and phreatomagmatic deposits of Ohakune Craters, Ruapehu, New Zealand: a complex interaction between external water and rising basaltic magma. J Volcanol Geotherm Res 21:207–231

Houghton B, Wilson CJN (1989) A vesicularity index for pyroclastic deposits. Bull Volc 51:451–462

Houghton BF, Smith RT (1993) Recycling of magmatic clasts during explosive eruptions: estimating the true juvenile content of phreatomagmatic volcanic deposits. Bull Volc 55:414–420

Houghton BF, Gonnermann HM (2008) Basaltic explosive volcanism: Constraints from deposits and models. Chemie der Erde - Geochemistry 68:117–140

Houghton B, Carey RJ (2015) Pyroclastic fall deposits. *In*: Sigurdsson H, Houghton B, McNutt SR, Rymer H, Stix J (eds) The Encyclopedia of Volcanoes, Second Edition. Academic Press, London, pp 599–616

Houghton BF, Wilson CJN, Fierstein J, Hildreth W (2004) Complex proximal deposition during the Plinian eruptions of 1912 at Novarupta, Alaska. Bull Volc 66:95–133

Houghton BF, Swanson DA, Rausch J, Carey RJ, Fagents SA, Orr TR (2013) Pushing the Volcanic Explosivity Index to its limit and beyond: Constraints from exceptionally weak explosive eruptions at Kīlauea in 2008. Geology 41:627–630

Hunt JB, Hill PG (1993) Tephra geochemistry: a discussion of some persistent analytical problems. The Holocene 3:271–278

Jerolmack DJ, Reitz MD, Martin RL (2011) Sorting out abrasion in a gypsum dune field. J Geophys Res 116:F02003

Jones TJ, Russell JK (2017) Ash production by attrition in volcanic conduits and plumes. Sci Rep 7:article 5538

Jones TJ, McNamara K, Eychenne J, Rust AC, Cashman KV, Scheu B, Edwards R (2016) Primary and secondary fragmentation of crystal-bearing intermediate magma. J Volcanol Geotherm Res 327:70–83

Jordan SC, Dürig T, Cas RAF, Zimanowski B (2014) Processes controlling the shape of ash particles: Results of statistical IPA. J Volcanol Geotherm Res 288:19–27

Jordan SC, Le Pennec JL, Gurioli L, Roche O, Boivin P (2016) Highly explosive eruption of the monogenetic 8.6ka BP La Vache et Lassolas scoria cone complex (Chaîne des Puys, France). J Volcanol Geotherm Res 313:15–28

Jude-Eton TC, Thordarson T, Gudmundsson MT, Oddsson B (2012) Dynamics, stratigraphy and proximal dispersal of supraglacial tephra during the ice-confined 2004 eruption at Grímsvötn Volcano, Iceland. Bull Volc 74:1057–1082

Kapelanczyk L, Rose WI, Jicha B (2012) An eruptive history of Maderas volcano using new 40Ar/39Ar ages and geochemical analyses. Bull Volc 74:2007–2021

Kawabata, E, Cronin SJ, Bebbington MS, Moufti MRH, El-Masry N, Wang T (2015) Identifying multiple eruption phases from a compound tephra blanket: an example of the AD1256 Al-Madinah eruption, Saudi Arabia. Bull Volc 77:article 6.

Klug C, Cashman KV (1994) Vesiculation of May 18, 1980, Mount St. Helens magma. Geology 22:468–472

Krumbein WC (1934) Size frequency distributions of sediments. J Sedim Res 2:65–77

Kuenen PH (1960) Experimental abrasion; 4, Eolian action. J Geol 68:427–449

Lautze NC, Taddeucci J, Andronico D, Cannata C, Tornetta L, Scarlato P, Houghton B, Lo Castro MD (2012) SEM-based methods for the analysis of basaltic ash from weak explosive activity at Etna in 2006 and the 2007 eruptive crisis at Stromboli. Physics and Chemistry of the Earth 45–46:113–127

Lautze NC, Taddeucci J, Andronico D, Houghton B, Niemeijer A, Scarlato PG (2013) Insights into explosion dynamics and the production of ash at Stromboli from samples collected in real-time, October 2009. In: Rose WI, Palma JL, Delgado Granados H, Varley N (eds) Understanding open-vent volcanism and related hazards, GSA Special Paper 498, pp 125–139

Leibrandt S, Le Pennec J-L (2015) Towards fast and routine analyses of volcanic ash morphometry for eruption surveillance applications. J Volcanol Geotherm Res 297:11–27

Lindoo A, Larsen JF, Cashman KV, Dunn AL, Neill OK (2016) An experimental study of permeability development as a function of crystal-free melt viscosity. Earth Planet Sci Lett 435:45–54

Liu EJ, Cashman KV, Rust AC (2015a) Optimising shape analysis to quantify volcanic ash morphology. GeoResJ 8:14–30

Liu EJ, Cashman KV, Rust AC, Gislason SR (2015b) The role of bubbles in generating fine ash during hydromagmatic eruptions. Geology 43:239–242

Liu EJ, Cashman KV, Rust AC, Höskuldsson A (2017) Contrasting mechanisms of magma fragmentation during coeval magmatic and hydromagmatic activity: the Hverfjall Fires fissure eruption, Iceland. Bull Volc 79:68

Lorenz V, Zimanowski B, Fröhlich G (1994) Experiments on explosive basic and ultrabasic, ultramafic, and carbonatitic volcanism. Proc 5th Int Kimb Conf, Araxa, Brazil, CPRM Special Publication 1, p. 270–284.

Manga M, Patel A, Dufek J (2011) Rounding of pumice clasts during transport: field measurements and laboratory studies. Bull Volc 73:321–333

Mangan MT, Cashman KV, Newman S (1993) Vesiculation of basaltic magma during eruption. Geology 21:157–160

Manville V, Segschneider B, White JDL (2002) Hydrodynamic behaviour of Taupo 1800a pumice: implications for the sedimentology of remobilized pyroclasts. Sedimentology 49:955–976

Maria A, Carey S (2002) Using fractal analysis to quantitatively characterize the shapes of volcanic particles. J Geophys Res Solid Earth 107:ECV 7-1-ECV 7–17

Mele D, Dioguardi F (2018) The grain size dependency of vesicular particle shapes strongly affects the drag of particles. First results from microtomography investigations of Campi Flegrei fallout deposits. J Volcanol Geotherm Res 353:18–24

Mele D, Dellino P, Sulpizio R, Braia G (2011) A systematic investigation on the aerodynamics of ash particles. J Volcanol Geotherm Res 203:1–11

Mele D, Dioguardi F, Dellino P (2018) A study on the influence of internal structures on the shape of pyroclastic particles by X-ray microtomography investigations. Ann Geophys-Italy 61:AC27

Merkus HG (2009) Sieves and sieving. In: Particle size measurements - fundamentals, practice, quality. Springer, pp 219–240

Miwa T, Toramaru A (2013) Conduit process in vulcanian eruptions at Sakurajima volcano, Japan: Inference from comparison of volcanic ash with pressure wave and seismic data. Bull Volc 75:685

Miwa T, Toramaru A, Iguchi M (2009) Correlations of volcanic ash texture with explosion earthquakes from vulcanian eruptions at Sakurajima volcano, Japan. J Volcanol Geotherm Res 184:473–486

Moitra P, Gonnermann HM, Houghton BF, Giachetti T (2013) Relating vesicle shapes in pyroclasts to eruption styles. Bull Volc 75:691

Moitra P, Sonder I, Valentine GA (2018) Effects of size and temperature-dependent thermal conductivity on the cooling of pyroclasts in air. Geochemistry, Geophysics, Geosystems 19:3623–3636

Morgan GB, London D (1996) Optimising the electron microprobe analysis of hydrous alkali aluminosilicate glasses. Am Mineral 81:1176–1185

Morgan DJ, Jerram DA (2006) On estimating crystal shape for crystal size distribution analysis. J Volcanol Geotherm Res 154:1–7

Mosley MP, Tindale DS (1985) Sediment variability and bed material sampling in gravel-bed rivers. Earth Surf Proc Land 10:465–482

Mueller SB, Houghton BF, Swanson DA, Fagents SA, Klawonn M (2018) Intricate episodic growth of a Hawaiian tephra deposit: case study of the 1959 Kīlauea Iki eruption. Bull Volc 80:article 73

Mueller SB, Houghton BF, Swanson DA, Poret M, Fagents SA (2019) Total grain size distribution of an intense Hawaiian fountaining event: case study of the 1959 Kīlauea Iki eruption. Bull Volc 81:article 43

Murch AP, White JDL, Carey RJ (2019a) Unusual fluidal behavior of a silicic magma during fragmentation in a deep subaqueous eruption, Havre volcano, southwestern Pacific Ocean. Geology 47: 487–490

Murch AP, White JDL, Carey RJ (2019b) Characteristics and deposit stratigraphy of submarine-erupted silicic ash, Havre Volcano, Kermadec arc, New Zealand. Front Earth Sci 7:article 1

Murtagh RM, White JDL, Sohn YK (2011) Pyroclast textures of the Ilchulbong 'wet' tuff cone, Jeju Island, South Korea. J Volcanol Geotherm Res 201:385–396

Murtagh RM, White JDL (2013) Pyroclast characteristics of a subaqueous to emergent Surtseyan eruption, Black Point volcano, California. J Volcanol Geotherm Res 267:75–91

Németh K, Cronin SJ, Smith IEM, Agustin Flores J (2012) Amplified hazard of small-volume monogenetic eruptions due to environmental controls, Orakei Basin, Auckland Volcanic Field, New Zealand. Bull Volc 74:2121–2137

Nurfiani D, Bouvet de Maisonneuve C (2018) Furthering the investigation of eruption styles through quantitative shape analyses of volcanic ash particles. J Volcanol Geotherm Res 354:102–114

Ort MH, Lefebvre NS, Neal CA, McConnell VS, Wohletz KH (2018) Linking the Ukinrek 1977 maar-eruption observations to the tephra deposits: New insights into maar depositional processes. J Volcanol Geotherm Res 360:36–60

Osman S, Beckett F, Rust A, Snee E (2020) Sensitivity of volcanic ash dispersion modelling to input grain size distribution based on hydromagmatic and magmatic deposits. Atmosphere 11:567

Pardo Villaveces N (2012) Andesitic Plinian eruptions at Mt. Ruapehu (New Zealand): from lithofacies to eruption dynamics. PhD thesis, Massey University, New Zealand

Pardo N, Cronin SJ, Wright HMN, Schipper CI, Smith I, Stewart B (2014a) Pyroclast textural variation as an indicator of eruption column steadiness in andesitic Plinian eruptions at Mt. Ruapehu. Bull Volc 76:822

Pardo N, Cronin SJ, Németh K, Brenna M, Schipper CI, Breard E, White JDL, Procter J, Stewart B, Agustín-Flores J, Moebis A, Zernack A, Kereszturi G, Lube G, Auer A, Neall V, Wallace C (2014b) Perils in distinguishing phreatic from phreatomagmatic ash; insights into the eruption mechanisms of the 6 August 2012 Mt. Tongariro eruption, New Zealand. J Volcanol Geotherm Res 286:397–414

Pardo N, Avellaneda JD, Rausch J, Jaramillo-Vogel D, Gutiérrez M, Foubert A (2020) Decrypting silicic magma/plug fragmentation at Azufral crater lake, Northern Andes: insights from fine to extremely fine ash morpho-chemistry. Bull Volc 82:article 79

Parfitt EA (1998) A study of clast size distribution, ash deposition and fragmentation in a Hawaiian-style volcanic eruption. J Volcanol Geotherm Res 84:197–208

Piercey SJ (2014) Modern analytical facilities 2. A review of quality assurance and quality control (QA/QC) procedures for lithogeochemical data. Geoscience Canada 41:75–88

Pioli L, Bonadonna C, Pistolesi M (2019) Reliability of total grain-size distribution of tephra deposits. Sci Rep 9:article 10006

Pioli L, Erlund E, Johnson E, Cashman K, Wallace P, Rosi M, Delgado Granados H (2008) Explosive dynamics of violent Strombolian eruptions: The eruption of Parícutin Volcano 1943–1952 (Mexico). Earth Planet Sci Lett 271:359–368

Pistolesi M, Bertagnini A, Di Roberto A, Isaia R, Vona A, Cioni R, Giordano G (2017) The Baia-Fondi di Baia eruption at Campi Flegrei: stratigraphy and dynamics of a multi-stage caldera reactivation event. Bull Volc 79:article 67

Polacci M, Corsaro RA, Andronico D (2006) Coupled textural and compositional characterization of basaltic scoria: Insights into the transition from Strombolian to fire fountain activity at Mount Etna, Italy. Geology 34:201–204

Polacci M, Andronico D, de' Michieli Vitturi M, Taddeucci J, Cristaldi A (2019) Mechanisms of ash generation at basaltic volcanoes: the case of Mount Etna, Italy. Front Earth Sci 7:article 193

Pompilio M, Bertagnini A, Del Carlo P, Di Roberto A (2017) Magma dynamics within a basaltic conduit revealed by textural and compositional features of erupted ash: the December 2015 Mt. Etna paroxysms. Sci Rep 7:4805

Porritt LA, Russell JK, Quane SL (2012) Pele's tears and spheres: examples from Kilauea Iki. Earth Planet Sci Lett 333:171–180

Prival J-M, Thouret J-C, Japura S, Gurioli L, Bonadonna C, Mariño J, Cueva K (2019) New insights into eruption source parameters of the 1600 CE Huaynaputina Plinian eruption, Peru. Bull Volc 82:article 7

Quinn GD (2020) Fractography of ceramics and glasses. NIST Special Publication 960-16e3, doi 10.6028/NIST.SP.960-16e3

Rausch J, Grobéty B, Vonlanthen P (2015) Eifel maars: Quantitative shape characterization of juvenile ash particles (Eifel Volcanic Field, Germany). J Volcanol Geotherm Res 291:86–100

Riley CM, Rose WI, Bluth GJS (2003) Quantitative shape measurements of distal volcanic ash. J Geophys Res Solid Earth 108(B10)

Roduit N (2007) JMicroVision : un logiciel d'analyse d'images pétrographiques polyvalent. PhD thesis, Université de Genève.

Ross P-S, White JDL (2012) Quantification of vesicle characteristics in some diatreme-filling deposits, and the explosivity levels of magma-water interactions within diatremes. J Volcanol Geotherm Res 245-246:55–67

Ross P-S, Giroux B, Latutrie B (2021) Precision and accuracy of modal analysis methods for clastic deposits and rocks: A statistical and numerical modeling approach. Geosphere 17: doi 10.1130/GES02374.1

Rust AC, Cashman KV (2011) Permeability controls on expansion and size distributions of pyroclasts. J Geophys Res Solid Earth 116 doi:10.1029/2011JB008494

Sable JE, Houghton BF, Del Carlo P, Coltelli M (2006) Changing conditions of magma ascent and fragmentation during the Etna 122 BC basaltic Plinian eruption: Evidence from clast microtextures. J Volcanol Geotherm Res 158:333–354

Sahagian DL, Proussevitch AA (1998) 3D particle size distributions from 2D observations: stereology for natural applications. J Volcanol Geotherm Res 84:173–196

Saxby J, Rust A, Cashman K, Beckett F (2020) The importance of grain size and shape in controlling the dispersion of the Vedde cryptotephra. J Quartern Sci 35:175–85

Scarpati C, Sparice D, Perrotta A (2016) Comparative proximal features of the main Plinian deposits (Campanian Ignimbrite and Pomici di Base) of Campi Flegrei and Vesuvius. J Volcanol Geotherm Res 321:149–157

Schipper CI, White JDL, Zimanowski B, Büttner R, Sonder I, Schmid A (2011) Experimental interaction of magma and “dirty” coolants. Earth Planet Sci Lett 303:323-336

Schipper CI, Castro JM, Tuffen H, James MR, How P (2013) Shallow vent architecture during hybrid explosive-effusive activity at Cordón Caulle (Chile, 2011-12): evidence from direct observations and pyroclast textures. J Volcanol Geotherm Res 262:25–37

Schmith J, Höskuldsson Á, Holm PM (2017) Grain shape of basaltic ash populations: implications for fragmentation. Bull Volc 79:article 14

Schmith J, Höskuldsson Á, Holm PM, Larsen G (2018) Large explosive basaltic eruptions at Katla volcano, Iceland: Fragmentation, grain size and eruption dynamics. J Volcanol Geotherm Res 354:140–152

Schumacher R., Schmincke, HU (1995) Models for the origin of accretionary lapilli. Bull Volc 56:626–639

Shea T, Houghton BF, Gurioli L, Cashman KV, Hammer JE, Hobden BJ, Stovall W, Carey R (2009) SEM image processing with Photoshop. Report published in support of the Fast Object Analysis and Measurement System (FOAMS) program: http://www2.hawaii.edu/~tshea/foams/methodsimrec.html

Shea T, Houghton BF, Gurioli L, Cashman KV, Hammer JE, Hobden BJ (2010) Textural studies of vesicles in volcanic rocks: an integrated methodology. J Volcanol Geotherm Res 190:271–289

Shimano T, Nishimura T, Chiga N, Shibasaki Y, Iguchi M, Miki D, Yokoo A (2013) Development of an automatic volcanic ash sampling apparatus for active volcanoes. Bull Volc 75:article 73

Skilling IP, White JDL, McPhie J (2002) Peperite: a review of magma-sediment mingling. J Volcanol Geotherm Res 114:1–17

Sparks RSJ, Wilson L, Sigurdsson H (1981) The pyroclastic deposits of the 1875 eruption of Askja, Iceland. Philosophical Transactions of the Royal Society of London. Series A, Mathematical and Physical Sciences 299:241–273

Stovall W, Houghton B, Hammer J, Fagents S, Swanson D (2012) Vesiculation of high fountaining Hawaiian eruptions: episodes 15 and 16 of 1959 Kīlauea Iki. Bull Volc 74:441–455

Suda Y, Grebennikov AV, Kuzmin YV, Glascock MD, Wada K, Ferguson JR, Kim JC, et al. (2018) Inter-laboratory validation of the WDXRF, EDXRF, ICP–MS, NAA and PGAA analytical techniques and geochemical characterisation of obsidian sources in northeast Hokkaido Island, Japan. Journal of Archaeological Science: Reports 17:379–392

Sulpizio R, Cioni R, Di Vito MA, Mele D, Bonasia R, Dellino P (2010) The Pomici di Avellino eruption of Somma-Vesuvius (3.9 ka bp). Part I: stratigraphy, compositional variability and eruptive dynamics. Bull Volc 72:539–558

Suzuki Y, Nagai M, Maeno F, Yasuda A, Hokanishi N, Shimano T, Ichihara M, Kaneko T, Nakada S (2013) Precursory activity and evolution of the 2011 eruption of Shinmoe-dake in Kirishima volcano – insights from ash samples. Earth, Planets and Space 65:11

Swanson D, Wooten K, Orr T (2009) Buckets of ash track tephra flux from Halema'uma'u crater, Hawai'i. Eos, Transactions American Geophysical Union 90:427–427

Szramek L, Gardner JE, Hort M (2010) Cooling-induced crystallization of microlite crystals in two basaltic pumice clasts. American Mineralogist 95:503–509

Taddeucci J, Palladino DM (2002) Particle size-density relationships in pyroclastic deposits: inferences for emplacement processes. Bull Volc 64:273–284

Taddeucci J, Pompilio M, Scarlato P (2002) Monitoring the explosive activity of the July-August 2001 eruption of Mt. Etna (Italy) by ash characterization. Geophys Res Lett 29:71–74

Taddeucci J, Pompilio M, Scarlato P (2004) Conduit processes during the July–August 2001 explosive activity of Mt. Etna (Italy): inferences from glass chemistry and crystal size distribution of ash particles. J Volcanol Geotherm Res 137:33–54

Takeuchi S, Nakashima S, Tomiya A (2008) Permeability measurements of natural and experimental volcanic materials with a simple permeameter: Toward an understanding of magmatic degassing processes. J Volcanol Geotherm Res 177:329–339

Thivet S, Gurioli L, Di Muro A, et al. (2020a) Evidences of plug pressurization enhancing magma fragmentation during the September 2016 basaltic eruption at Piton de la Fournaise (La Réunion Island, France). Geochemistry, Geophysics, Geosystems 21:1–30

Thivet S, Gurioli L, Di Muro A (2020b) Basaltic dyke eruptions at Piton de La Fournaise: characterization of the eruptive products with implications for reservoir conditions, conduit processes and eruptive dynamics. Contrib Mineral Petrol 175:article 26

Thivet S, Gurioli L., Di Muro A, Eychenne J, Besson P, Nedelec J-M (2020c) Variability of ash deposits at Piton de la Fournaise (La Reunion Island): insights into fragmentation processes at basaltic shield volcanoes. Bull Volc 82:article 63

Thivet S, Harris AJL, Gurioli L, Bani P, Barnie T, Bombrun M, Marchetti E (2021) Multi-Parametric Field Experiment Links Explosive Activity and Persistent Degassing at Stromboli. Front Earth Sci 9 https://doi.org/10.3389/feart.2021.669661

Valentine GA (2012) Shallow plumbing systems for small-volume basaltic volcanoes, 2: Evidence from crustal xenoliths at scoria cones and maars. J Volcanol Geotherm Res 223-224:47–63

Valentine GA, Groves KR (1996) Entrainment of country rock during basaltic eruptions of the Lucero volcanic field, New Mexico. J Geol 104:71–90

Valentine GA, White JDL, Ross P-S, Graettinger AH, Sonder I (2017) Updates to concepts on phreatomagmatic maar-diatremes and their pyroclastic deposits. Front Earth Sci, DOI 10.3389/feart.2017.00068

Verolino A, White JDL, Dürig T, Cappuccio F (2019) Black Point – Pyroclasts of a Surtseyan eruption show no change during edifice growth to the surface from 100 m water depth. J Volcanol Geotherm Res 384:85–102

Vonlanthen P, Rausch J, Ketcham RA, Putlitz B, Baumgartner LP, Grobéty B (2015) High-resolution 3D analyses of the shape and internal constituents of small volcanic ash particles: The contribution of SEM micro-computed tomography (SEM micro-CT). J. Volcanol. Geotherm. Res. 293:1–12

Walker GPL (1971) Grain-size characteristics of pyroclastic deposits. J Geol 79:696–714

Walker GPL (1973) Explosive volcanic eruptions: a new classification scheme. Geologische Rundschau 62:431–446

Walker GPL (1981) Plinian eruptions and their products. Bull Volc 44:223–240

Webster JD, Burt DM, Aguillon RA (1996) Volatile and lithophile trace-element geochemistry of Mexican tin rhyolite magmas deduced from melt inclusions. Geochimica et Cosmochimica Acta 60:3267–3283

White JDL (1991) Maar-diatreme phreatomagmatism at Hopi Buttes, Navajo Nation (Arizona), USA. Bull Volc 53:239–258

White JDL (1996a) Impure coolants and interaction dynamics of phreatomagmatic eruptions. J Volcanol Geotherm Res 74:155–170

White JDL (1996b) Pre-emergent construction of a lacustrine basaltic volcano, Pahvant Butte, Utah. Bull Volc 58:249–262

White JDL, Houghton BF (2006) Primary volcaniclastic rocks. Geology 34:677–680

White JDL, Ross P-S (2011) Maar-diatreme volcanoes: a review. J Volcanol Geotherm Res 201:1–29

White JDL, Valentine GA (2016) Magmatic versus phreatomagmatic fragmentation: absence of evidence is not evidence of absence. Geosphere 12:1478–1488

White JDL, McPhie J, Soule SA (2015) Submarine lavas and hyaloclastite. *In*: Sigurdsson H, Houghton B, McNutt SR, Rymer H, Stix J (eds) Encyclopedia of Volcanoes, Second edition. Academic Press, London, pp. 363–375

Wohletz KH (1983a) Mechanisms of hydrovolcanic pyroclast formation: grain-size, scanning electron microscopy, and experimental studies. J Volcanol Geotherm Res 17:31–63

Wohletz KH (1983b) Chemical and textural features of pyroclasts from hydrovolcanic eruption sequences. Los Alamos National Laboratory, report LA-UR-83-250

Wohletz KH (1986) Explosive magma-water interactions: Thermodynamics, explosion mechanisms, and field studies. Bull Volc 48:245–264

Wohletz K, Krinsley D (1978) Scanning electron microscopy of basaltic hydromagmatic ash. Los Alamos National Laboratory, report LA-UR-82-1433

Wohletz KH, Sheridan MF, Brown WK (1989) Particle size distribution and sequential fragmentation/transport theory applied to volcanic ash. J Geophys Res 94:15 703–15 721

Wohletz K, Orsi G, de Vita S (1995) Eruptive mechanisms of the Neapolitan Yellow Tuff interpreted from stratigraphic, chemical, and granulometric data. J Volcanol Geotherm Res 67:263–290

Yoshimoto M, Shimano T, Nakada S, Koyama E, Tsuji H, Iida A, Kurokawa M, Okayama Y, Nonaka M, Kaneko T, Hoshizumi H, Ishizuka Y, Furukawa R, Nogami K, Onizawa S, Niihori K, Sugimoto T, Nagai M (2005) Mass estimation and characteristics of ejecta from the 2004 eruption of Asama volcano. Bull Volc. Soc. Jpn 50:519–533 (in Japanese with English abstract)

Zimanowski B, Büttner R, Lorenz V, Häfele H-G (1997) Fragmentation of basaltic melt in the course of explosive volcanism. J Geophys Res 102:803–814

Zimanowski B, Wohletz K, Dellino P, Büttner R (2003) The volcanic ash problem. J Volcanol Geotherm Res 122:1–5

Zimanowski B, Büttner R, Delino P, White JDL, Wohletz K (2015) Magma-water interaction and phreatomagmatic fragmentation. *In*: Sigurdsson H, Houghton B, McNutt SR, Rymer H, Stix J (eds) Encyclopedia of Volcanoes, Second Edition. Academic Press, London, pp 473–484

APPENDIX II: CONFERENCE ABSTRACTS

Poster session at IAVCEI[5] (2017), Portland, USA

Artificial juvenile pyroclasts from wet and dry "eruptions": impact of magma composition on grain sizes and particle shapes

Pier Paolo Comida[1], Pierre-Simon Ross[1], Bernd Zimanowski[2], Ralf Büttner[2]

[1]Institut National de la Recherche Scientifique, Centre Eau Terre Environnement, 490 Rue de la Couronne, Québec (QC), G1K 9A9, Canada

[2]Physikalisch-Vulkanologisches Labor, Universität Würzburg, Pleicherwall 1, Würzburg, 97070, Germany

Maar-diatremes are the second most common volcanic landform on continents and a direct expression of phreatomagmatic explosions, characterized by high explosivity and commonly associated with potentially devastating pyroclastic density currents. Beyond the hazard implications, some diatremes are associated with major ore deposits. Yet eruptive processes especially for the diatreme portion are still poorly understood as they occur largely underground.

Juvenile pyroclasts in maar-diatreme volcanoes come in a range of sizes, shapes, surface features and internal textures (e.g., for basalt, sideromelane versus tachylite). These parameters are influenced by how magma deforms, fragments and cools, which is controlled by factors such as magma viscosity, surface tension, crystallinity, volatile content, and interaction with external water, including Molten Fuel Coolant Interactions (MFCI) and less explosive interactions.

To understand how both silica content and interaction with external water impact on magma fragmentation and the resulting juvenile pyroclasts, a series of laboratory scale experiments were performed at the Physikalisch Vulkanologisches Labor in Würzburg (Germany). In each run, 200–250 g of volcanic rock was re-melted to 1200°C within 1–2 hours using an induction furnace. The melt was fragmented and expelled from the steel crucible through the use of compressed argon (~ 500 cm^3, 10 MPa driving pressure) injected from the base; this is known informally as a "dry blowout". In wet blowouts, a layer of liquid water (~ 100–250 ml) was added on top of the magma about 2 s before the start of deformation. Dry and wet blowouts were performed on four melt compositions ranging from olivine-melilitite to rhyolite and the artificial pyroclasts collected. The next steps are to analyze the size, texture and shape of particles. These results will be compared

[5] International Association of Volcanology and Chemistry of the Earth's Interior

to data on artificial pyroclasts from classic “water entrapment” MFCI experiments on the same and similar melts, as well as with data from natural juvenile pyroclasts from selected diatremes and maars. This will hopefully allow us to better link processes and products in maar-diatreme volcanoes.

Keywords: juvenile pyroclasts, magma fragmentation, experiments, shapes

Poster session at COV10[6] (2018), Naples, Italy

Phreatomagmatic versus magmatic fragmentation: Insights from juvenile particle analysis

Pier Paolo Comida[1], Pierre-Simon Ross[1], Nathalie Lefebvre[2], Bernd Zimanowski[3], Ralf Büttner[3]

[1]Institut National de la Recherche Scientifique, Centre Eau Terre Environnement, 490 Rue de la Couronne, Québec (QC), G1K 9A9, Canada

[2]ETH Zurich, Institute of Geochemistry and Petrology, Clausiusstrasse 25, 8092 Zurich, Switzerland

[3]Physikalisch-Vulkanologisches Labor, Universität Würzburg, Pleicherwall 1, Würzburg, 97070, Germany

Juvenile pyroclasts offer unique insights on the style of magma fragmentation. Observed variations in their morphology (e.g., fluidal versus blocky), crystallinity, vesicularity, and surface features (e.g., stepped features, etc.) have been used to distinguish phreatomagmatic from magmatic explosive activity. This distinction is of primary importance in hazard assessment. However, there is no widely accepted methodology for the characterization of juvenile pyroclasts to investigate magma fragmentation. To contribute to the development of such a unified methodology, we characterize known phreatomagmatic and magmatic juvenile pyroclasts from fragmentation experiments and the well-observed 1977 Ukinrek maar eruption in Alaska.

A test was carried out on phreatomagmatic and strombolian samples from the Ukinrek eruption in order to identify which grain sizes best record the fragmentation signature. Polished grain mounts were produced for size fractions from 0 to + 4ϕ, and observed with optical and electronic microscopy. Selected 2D shape parameters such as axial ratio (form), solidity (morphological roughness) and convexity (textural roughness), along with crystallinity and vesicularity, were quantified from particle cross-sections for each size fraction and the results compared.

Experiments at the Physikalisch Vulkanologisches Labor in Würzburg (Germany) allowed us to reproduce both magmatic and phreatomagmatic fragmentation processes, using volcanic material of olivine-melilitite to basaltic trachyandesite composition, remelted at magmatic temperatures. High-speed video recordings allowed direct investigation of free air expansion of the melt. Artificial pyroclasts collected from each run were prepared for 3D and 2D image analysis. Preliminary results show that during magmatic fragmentation, magmas having similar equilibrium viscosities behave quite differently due to non-Newtonian behavior, and this has major influence

[6] Cities on Volcanoes 10

on particle shape. Work on both the Ukinrek test and the experimental products is currently in progress, and the results will be presented at the conference.

Keywords: juvenile pyroclasts, magmatic fragmentation, phreatomagmatic fragmentation, experiments, shapes, vesicularity, crystallinity, surface features, maar

Oral session at GAC-MAC-IAH[7] (2019), Quebec City, Canada

Non-Newtonian behavior influences pyroclast shapes in lava fountains: experimental evidence

Pier Paolo Comida[1], Pierre-Simon Ross[1], Bernd Zimanowski[2], Ralf Büttner[2]

[1]Institut National de la Recherche Scientifique, Centre Eau Terre Environnement, 490 Rue de la Couronne, Québec (QC), G1K 9A9, Canada

[2]Physikalisch-Vulkanologisches Labor, Universität Würzburg, Pleicherwall 1, Würzburg, 97070, Germany

Hawaiian lava fountains are mildly explosive eruptions where low viscosity magma is fragmented in the conduit and ejected as juvenile fragments, along with gasses. Juvenile pyroclasts produced by lava fountains include spatter, scoria, Pele's spheres, Pele's tears, Pele's hairs, and reticulite. We are particularly interested by the smaller pyroclasts, i.e. the spheres, tears and hairs, which cool completely before landing. In the literature, the shapes of these pyroclasts are thought to be controlled by ejection velocity, magma surface tension, and magma viscosity. The composition of the magma has not typically been cited as an important parameter, except indirectly through its influence on viscosity.

A series of laboratory scale "blowout" experiments were performed at the Physikalisch Vulkanologisches Labor in Würzburg (Germany). These experiments are partly similar to natural lava fountains. In each run, 200 g of volcanic rock was re-melted to 1200°C within 1 hour using an induction furnace. The melt was fragmented and expelled from the steel crucible through the use of compressed argon injected from the base. Blowouts were performed on three melt compositions ranging from olivine-melilitite (ultramafic) to basaltic trachy-andesite (intermediate); these three compositions have approximately the same equilibrium viscosity for low shear rates at 1200°C.

The artificial pyroclasts were collected and hand-sieved in order to obtain grain-size distribution, then different size fractions were examined under the binocular microscope. Particles in the 0ϕ size fraction were assigned to different classes based on shapes and other visual features. Major differences in the particle shapes were observed between the three magmas, despite using the same experimental conditions, comparable magma surface tensions, and equilibrium viscosities.

[7] Geological Association of Canada - Mineralogical Association of Canada - International Association of Hydrogeologists

Therefore, instantaneous viscosity and non-Newtonian behavior probably play a role in controlling particle shapes in lava fountains and other styles of explosive eruptions.

Keywords: non-Newtonian behavior, magma fragmentation, experiments, shapes, lava fountains, viscosity

Oral session at IUGG[8] (2019), Montreal, Canada

Understanding magma fragmentation in lava fountains: evidence from laboratory experiments and juvenile particle analysis

Pier Paolo Comida[1], Pierre-Simon Ross[1], Bernd Zimanowski[2], Ralf Büttner[2]

[1]Institut National de la Recherche Scientifique, Centre Eau Terre Environnement, 490 Rue de la Couronne, Québec (QC), G1K 9A9, Canada

[2]Physikalisch-Vulkanologisches Labor, Universität Würzburg, Pleicherwall 1, Würzburg, 97070, Germany

Hawaiian fire fountains are spectacular examples of magma fragmentation involving low viscosity, volatile-rich magmas. Associated juvenile products range in shape from perfect spheres to very elongated Pele's hairs. In the literature, these shape variations are described as controlled by ejection velocity, magma surface tension and viscosity, and particle size. Magma composition has not typically been cited as an important parameter, except indirectly through its influence on viscosity.

In order to investigate the relevance of magma composition in controlling particle shapes in lava fountains, a series of laboratory scale "blowout" experiments were performed at the Physikalisch Vulkanologisches Labor in Würzburg (Germany). In each run, 200 g of volcanic rock was re-melted to 1200°C within 1 hour using an induction furnace. Compressed argon was injected from the base of the crucible, which fragmented and ejected the melt. The dynamics were partly comparable to a single lava fountain pulse. Experiments used three different melt compositions (olivine-melilitite, alkali basalt, basaltic trachy-andesite).

The 0ϕ size fraction from each experimental sample was used for a 3D morphology examination. Particles were assigned to different classes based on shapes and other visual features. Major differences in particle shapes were observed between the three magma compositions, despite using the same experimental conditions, comparable magma surface tensions and equilibrium viscosities. Therefore, instantaneous viscosity and non-Newtonian behaviour probably play a role in controlling particle shapes in lava fountains.

Keywords: lava fountains, experiments, magma fragmentation, juvenile particle analysis, non-Newtonian behavior

[8] 27th International Union of Geodesy and Geophysics – General Assembly

Oral session at IUGG[9] (2019), Montreal, Canada

Magmatic versus phreatomagmatic: finding the best size fractions for juvenile particle analysis

Pier Paolo Comida[1], Pierre-Simon Ross[1], Nathalie Lefebvre[2], Bernd Zimanowski[3], Ralf Büttner[3]

[1]Institut National de la Recherche Scientifique, Centre Eau Terre Environnement, 490 Rue de la Couronne, Québec (QC), G1K 9A9, Canada

[2]ETH Zurich, Institute of Geochemistry and Petrology, Clausiusstrasse 25, 8092 Zurich, Switzerland

[3]Physikalisch-Vulkanologisches Labor, Universität Würzburg, Pleicherwall 1, Würzburg, 97070, Germany

Distinction between phreatomagmatic and magmatic fragmentation is of primary importance in hazard assessment. Variations of juvenile pyroclasts in terms of shape, crystallinity and vesicularity offer insights on fragmentation processes, yet there is no widely accepted methodology of investigation for quantifying juvenile pyroclasts. As part of the development of such a uniform protocol, a test is being carried out in order to identify which grain sizes best record the magma fragmentation signature. The test is based on phreatomagmatic and magmatic juvenile pyroclasts from fragmentation experiments and from the well-observed 1977 Ukinrek maar eruption in Alaska. The laboratory experiments were performed at the Physikalisch Vulkanologisches Labor in Würzburg (Germany) and involved volcanic material of olivine-melilitite to basaltic trachyandesite composition, remelted at magmatic temperatures, and fragmented in various ways.

Pyroclasts from the experiments and from Ukinrek are currently being processed to quantify shape parameters (i.e., axial ratio (form), solidity (morphological roughness), convexity (textural roughness)), 2D crystallinity and 2D vesicularity for size fractions from 0ϕ to + 4ϕ. This involves manufacturing polished grain mounts to obtain particle cross-sections. These are imaged using electronic microscopy. The manually refined, pre-processed SEM images are then automatically processed in order to extract the desired data. Data acquisition for the whole set of samples is currently ongoing. Preliminary shape factor data, for both strombolian and phreatomagmatic samples from Ukinrek, reveals a sensible separation for all the size fractions. Complete results will be presented at the conference.

[9] 27th International Union of Geodesy and Geophysics – General Assembly

Keywords: phreatomagmatic fragmentation, magmatic fragmentation, juvenile pyroclasts, experiments, maar, juvenile particle analysis, shapes